Interfacial phenomena between bacterial or mammalian cells and orthopaedic biomaterials

A thesis submitted in accordance with the conditions governing candidates for the degree

of

Philosophiae Doctor in Cardiff University

by

Emily Callard Preedy

July 2015

Cardiff School of Pharmacy and Pharmaceutical Science

Cardiff University

Thesis summary

Adhesion as a scientific phenomenon has been researched for the past 70 years, as the notion of two entities contacting effects a huge expanse of daily activities, from writing to sophisticated cellular and bacterial interactions essential for growth and survival.

Inherently, a robust and adequate model of adhesion was acquired, one in which biological aspects were considered. Initially, the methodology required was optimised using the atomic force microscope (AFM) by testing a model bone substrate against ultra-high molecular weight polyethylene (UHMWPE), a material commonly found in the articulating acetabular cup. Once a force mapping technique was established experimentation continued to bacterial adhesion against model bone samples of various roughness, establishing that the adhesion phenomena occurs at a scale dependency due to the alterations in the topography of the surface at the micro to nano level.

Aseptic loosening and osteolysis are major causes of failures in implanted biomedical devices at the hip. These issues are governed by the deterioration of the moving components, producing particles known as wear debris associated with the metals, bone cement, and UHMWPE materials initiating an immune response which is detrimental to the surrounding cells and tissues adjacent to the implant. The notion of mechanical aspects altering the health of mammalian cells has been ignored throughout the research of implantations and their effect on the cells by foreign bodies; the only concept studied to date is the viability and functionality post exposure. Therefore, this thesis aims at observing

mesenchymal and osteoblast (both rodent and human) cells associated to wear debris (metal and polymeric particles of various sizes and compositions) exposure and the effect this has on cell nanomechanical and adhesive properties using the AFM techniques. The data obtained indicated that Cobalt nanoparticles were more damaging on all cell types than Titanium and polymeric particles.

DECLARATION

This work has not been submitted in substance for any other degree or award at this or any other university or place of learning, nor is being submitted concurrently in candidature for any degree or other award.

Signed …… 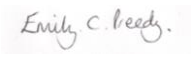 … (candidate) Date …29/10/2015……

STATEMENT 1

This thesis is being submitted in partial fulfilment of the requirements for the degree of PhD (insert MCh, MD, MPhil, PhD etc, as appropriate)

Signed ……… 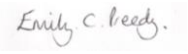 … (candidate) Date …29/10/2015……

STATEMENT 2

This thesis is the result of my own independent work/investigation, except where otherwise stated. Other sources are acknowledged by explicit references. The views expressed are my own.

Signed …… 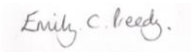 …… (candidate) Date .29/10/2015……

STATEMENT 3

I hereby give consent for my thesis, if accepted, to be available online in the University's Open Access repository and for inter-library loan, and for the title and summary to be made available to outside organisations.

Signed …… 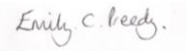 … (candidate) Date …29/10/2015……

Table of Contents

List of Figures

List of Tables

Acknowledgments

They say that curiosity killed the cat; however, I'm sure others have noted that they possess 9 lives; in addition, a great amount of curiosity successfully got Alice through her Wonderland.

From acknowledging this aspect of my character, I am extremely grateful and indebted to my primary supervisor Dr Polina Prokopovich for allowing me this great opportunity in pursuing my ambition, and obviously curiosity, to such a great feat. From our initial encounter as a nervous but determined candidate, we have both blossomed throughout the past three years of trials and tribulations; not only has Dr Prokopovich continuously encouraged, guided, and advised my academic investigations but also supported me at times of need. I would also like to thank Dr Stefano Perni for his invaluable knowledge and patience when asked for advice, equipment, and occasional help to prepare samples allowing for my work to continue smoothly. Last but not least, appreciation also extends to Professor Sam Evans for his continuous support throughout my research.

An extension of my gratitude goes towards the funding bodies, Arthritis UK and Cardiff School of Pharmacy and Pharmaceutical Sciences, for supplying financial support allowing for vital research to take place.

Other users of AFMs will understand when I say a big thank you to my new found friend and ally over the past three years for being stable and not giving up the ghost, especially when my patience was wearing thin, although your light would dim occasionally to my frustration.

I would also like to give my appreciation to all the technical advice I have received from supporting staff in engineering, within the AFM lab, engineering workshop, as well as SEM users. Without your abilities and promptness in helping would have delayed my progress. So I am very thankful for your support.

The final thanks goes to my family and friends for their continuous support and encouragement, and although my family always do provide this support especially when my computer fails on me, or doesn't save the work, or decides to lose documents, then I get the same response from my sister 'well I know you're doing well, but I don't have a clue what you're doing! So you'll get it sorted'. My parents on the other hand always have more belief in me than I do in myself at times, and I need to thank them for their continuous patience after my tantrums with said computer! Behind any success story there is always a team behind the lead to offer support in troubling times, and most importantly laughs.

Research outputs:

Peer reviewed journal publications:

E. Callard Preedy, S. Perni, P. Prokopovich "Cobalt, Titanium and PMMA Bone Cement debris Influence on Mouse Osteoblasts Cell Elasticity, Spring constant and Calcium Production Activity" under review *Chem Phy Phys Chem*

E. Callard Preedy, S. Perni, P. Prokopovich "Nanomechanical and surface properties of rMSCs post exposure to CAP treated UHMWPE wear particles" under review *Nanomedicine: nanotechnology, Biology and Medicine*

E. Callard Preedy, S. Perni, D. Nipiĉ, K. Bohinc, P. Prokopovich “Surface Roughness Mediated Adhesion Forces between Borosilicate Glass and Gram Positive Bacteria” *Langmuir* 2014;30(31), 9466-9476

E. Callard Preedy, S. Perni, P. Prokopovich "Application of AFM Techniques to Study the Adhesion Phenomena in Pharmaceutical Field" *Rev. Adhesion Adhesives* 2014;2(2):226-252

E. Callard Preedy, E. Brousseau, S. Evans, S. Perni, P. Prokopovich “Adhesive Forces and Surface Properties of Cold Gas Plasma Treated UHMWPE” *Coll. Surfaces A* 2014;460:83-89

S. Perni, E. Callard Preedy, P. Prokopovich “Success and Failure of Colloidal Approached in Bacterial Adhesion” *Adv. Coll. Interface Sci.* 2014;206:265-274

Peer reviewed conference contributions:

S. Perni, E. Callard Preedy, P. Prokopovich "Cobalt and Titanium Nanoparticle Influence on Mesenchymal Stem Cell Elasticity and Turgidity" Proceeding from Smart and Green Interfaces Meeting, 30 March-1 April 2015, Belgrade, Serbia

E. Callard Preedy, S. Perni, P. Prokopovich “Curli Expression Genes Influence on Spatial Distribution of Forces of Adhesion on the Cell Surfaces of *E. coli*” Proceeding from *27th Conference of European Colloids and Interface Society – ECIS,* 1-6 September 2013, Sofia, Bulgaria (accepted for oral presentation)

E.C. Preedy, S. Perni, E. Brousseau, S. Evans, P. Prokopovich “Curli Expression Genes Influence on Spatial Distribution of Forces of Adhesion on Cell Surfaces of *E. coli*” Proceeding from *14th European Student Colloid Conference*, 10-13 June 2013, Potsdam, Germany

Chapter 1 - Introduction

Joint replacement surgeries are ever increasing in number with 211,312 operations performed in England and Wales in 2014 [1]. To date, 2015 has already seen 92,393 joint replacements in England and Wales between the NHS and private sector [2]; with this number expecting to increase by the end of the year. 93% of these cases requiring a joint replaced was due to osteoarthritis, and is the most common type of arthritis affecting around 1 million people in England and Wales [1]; it is a disabling condition and costly [3]. Other causes may include hip fractures, septic arthritis, avascular necrosis, Paget's disease of the bone, bone tumours, hip dysplasia; as well as Perthes disease and slipped upper femoral epiphysis another childhood hip problem leading to long term issues, eventually resulting in hip replacement requirements. In order to decrease the suffering, to eradicate the pain of patients, and to improve their quality of life, then joint replacement is the only solution [4].

It is well documented that the majority of hip implants (as sketched in Figure 1-1) have a life expectancy of 10-15 years, commonly caused by the aseptic loosening of the implanted biomedical device. Loosening will be evident due to the return of pain as well as instability in the movement of the joint will occur. Another issue to arise is wear and tear of the socket of the hip, the constant rubbing and loading of the joint will produce wear debris i.e. particles of the bulk material coming away and being adsorbed into the surrounding cells and tissues. A more severe problem, although a small risk, is bacterial infections post-surgery; which can also affect the surrounding environment of the biomedical device.

That being said, demonstrates an inherent need to understand the cause and implications of these issues which are responsible for revision surgeries. By developing an in depth knowledge of these problems could potentially lead onto solutions aimed at improving the quality of life for the patient as well as minimising the costs associated with the initial operation, after care, and further surgical procedures.

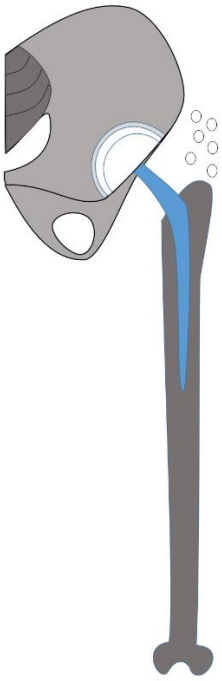

Figure 1-1. Schematic representation of a hip replacement generating debris.

Usually only after 5 days after an operation the implant will be completely covered in biological fluids, protein, and cells in order to achieve successful osseointegration. Cells present near a biomedical device will often include immune cells due to inflammation, as well as bone cells for growth of new bone

to incorporate the implant; these mammalian cells include mesenchymal stem cells which develop into osteoblasts depending on their stimuli.

However, during this preliminary phase bacterial cells may interfere and adhere to the implantation. The severity of an infection post-surgery can damage the healthy tissue encasing the implantation, and in the worst case, even death if left untreated i.e. sepsis. Initially (Figure 1-2), bacterial cells will need to attach themselves to the device or substrate (Figure 1-2a) and establish a colony for survival; once a bacterial cell has attached other bacterial cells will anchor themselves to the conditioning layer i.e. the biological fluid (Figure 1-2b), whereby further attachment (Figure 1-2c) and maturation (Figure 1-2d) of the colony is achieved with irreversible binding; a biofilm is now present allowing cells to grow within this protective layer (Figure 1-2e). Finally, a colony of cells will detach (Figure 1-2f), to find another surface or location to establish themselves to begin the cycle again.

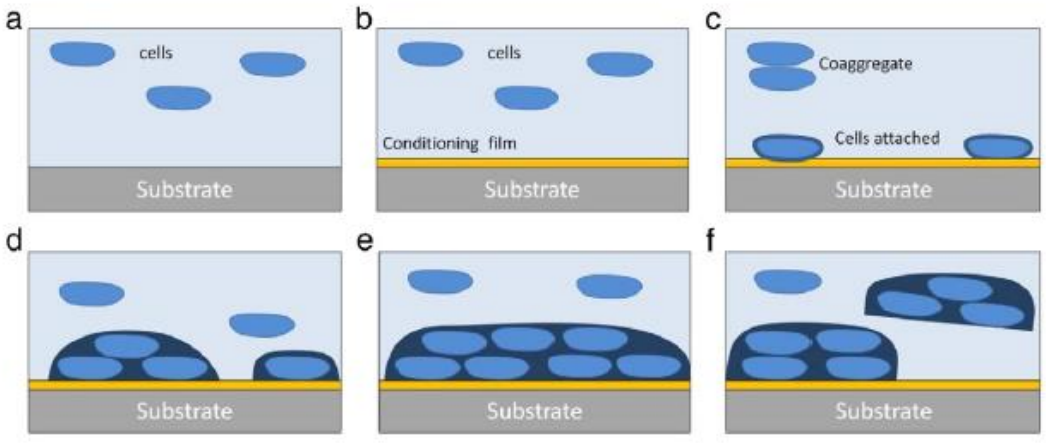

Figure 1-2. Schematic representation of the biofilm formation steps.

Not only can infections spread to the tissues surrounding the implanted biomedical device, but the wear debris produced from the hip implant components can also accumulate in these tissues as well as the new developing bone cells. Debris can adhere to the external membrane of bone cells, such as the parent mesenchymal stem cells and osteoblasts, which can potentially alter the growth through the prevention of the cell coaggregating with other cells. If the wear debris is internalised, this can affect the structure and function of the cell through changes in their mechanical properties. It is therefore important to determine whether the physicochemical composition of the wear debris produced has an effect on the overall health of the bone forming cells.

The viability of cells is constantly under scrutiny especially when concerned with the internalisation of foreign materials. Throughout the past decade the biological responses [5-6] to wear debris, and cells surrounding hip implantations has been investigated however, there is a lack of information regarding the mechanical aspects which can also govern the normal function of cells.

This evident gap in the literature, concerning physical changes to cells through stresses and strains, has led to this investigation of alterations to the nanomechanics of a cell after exposure to wear debris. This is the first time any exploratory work of this nature has been conducted for cells found at/near biomedical implantations such as mesenchymal stem cells, and osteoblasts that have been exposed to nano sized particles of wear debris to understand the full

extent of potential damage and adversity that regularly occurs post-surgery of biomedical devices.

The **aims of the thesis** were to achieve a greater depth of knowledge into the adhesive interactions and nanomechanical aspects of cells surrounding implantations which have not been investigated previously, and will require research into adhesion concepts adaptable to biological systems. Considerations for the influence of surface parameters and surface treatments along with their impact on cells nanomechanical and adhesive properties caused by implant debris have been investigated.

The **objectives** of this thesis were to:

- Employ cold atmospheric gas plasma (CAP) to improve performance of
- UHMWPE, a commonly used polymer for use in the acetabular cup;
- Study the surface topography and roughness of UHMWPE pre and post
- CAP treatment;
- Characterise the surface properties of CAP treated UHMWPE investigating the contact angles and surface energy parameters; further characterisation of the size and composition of wear debris particles to assess bone cells (osteoblasts) viability;
- Understand how surface roughness influences adhesion of bacteria that currently induce infections post-surgery;
- Determine the impact on viability, nanomechanical, adhesive properties and functionality of mesenchymal stem cells and osteoblasts from rodents exposed to wear debris particles including the metals used in hip

implants such as Cobalt and Titanium, as well as UHMWPE particles and polymethylmethacrylate (PMMA) bone cement particles often used as a fixative in joint surgeries;

- Determine the validity of the murine model by comparing the nanomechanical, adhesive and cell functionality data using human osteoblast cells.

A general overview of each chapter content is given below:

Chapter 2 is a literature review regarding current models of adhesion, their limitations, and applications; and how to apply these to real living biological systems.

Chapter 3 describes the main techniques of analysis using the atomic force microscope (AFM) and how the data collected are transformed into useful information concerning the adhesive properties, nanomechanical characteristics such as the elasticity, and spring constant of cells.

Chapter 4: The adhesive forces of model bone material, borosilicate glass functionalised AFM tips, were analysed along with the surface properties of modified ultra-high molecular weight polyethylene (UHMWPE) with cold atmospheric gas plasma (CAP).

Chapter 5: Using a model bone material to investigate the surface roughness and its relation to scanned areas comparable to the bacterial adhesion, using functionalised AFM tips to determine the adhesive forces.

Chapter 6: Moving on from bacterial aspects of adhesion, chapter 6 investigates the detrimental aspects of wear debris, namely Cobalt and Titanium, which were exposed to the osteoprogenitor cells i.e. mesenchymal stem cells. This chapter quantifies the nanomechanical properties of these mammalian cells post exposure to metal nanoparticles of various size and composition using the atomic force microscope, with supporting biological information regarding the cells viability throughout the experimentations.

Chapter 7: Following on from chapter 4, the CAP treated UHMWPE was used as wear debris particles. These particles were exposed to the mesenchymal stem cells as no investigation has been made to date concerning the effect of this material to the surrounding tissues and cells of an implanted biomedical device.

Chapter 8: In this chapter, metal nanoparticles (Cobalt and Titanium) and PMMA bone cement particles were exposed to osteoblasts, the progenitor cells, which develop into new bone. These cells were analysed as to whether the wear debris influences the nanomechanical properties and calcium production of the osteoblast cells.

Chapter 9: Following on from chapter 8, this chapter observes whether the same metal nanoparticles have a similar influence on human osteoblasts to validate the information already recovered throughout the thesis.

Conclusions and suggestions for Future work are given in Chapter 10.

1.1 References

[1] BORROFF, M. 2014. National Joint Registry 11th Annual Report. In: NJR (ed.) Annual Report. NJR.

[2] REGISTRY, N. J. 2015. NJR StatsOnline. Annual. NJR online: NJR.

[3] FRANKEL, L., SANMARTIN, C., CONNER-SPADY, B., MARSHALL, D. A., FREEMAN-COLLINS, L., WALL, A. & HAWKER, G. A. 2012. Osteoarthritis patients' perceptions of “appropriateness” for total joint replacement surgery. Osteoarthritis and Cartilage, 20, 967-973.

[4] GEETHA, M., SINGH, A. K., ASOKAMANI, R. & GOGIA, A. K. 2009. Ti based biomaterials, the ultimate choice for orthopaedic implants – A review. Progress in Materials Science, 54, 397-425CHIU, R. & GOODMAN, S. B. 2012. Biological Response of Osteoblasts and Osteoprogenitors to Orthopaedic Wear Debris. In: YUNFENG, L. (ed.) Osteogenesis - Biochemistry, Genetics and Molecular Biology. CC BY.

[5] CHIU, R., MA, T., SMITH, R. L. & GOODMAN, S. B. 2008. Polymethylmethacrylate particles inhibit osteoblastic differentiation of MC3T3-E1 osteoprogenitor cells. Journal of Orthopaedic Research, 26, 932-936.

[6] GOODMAN, S. B., MA, T., CHIU, R., RAMACHANDRAN, R. & LANE SMITH, R. 2006. Effects of orthopaedic wear particles on osteoprogenitor cells. Biomaterials, 27, 6096-6101.

Chapter 2 - Adhesion

Adhesion may be defined as an attraction action which causes two different materials to join (1). For years, there has been much interest in adhesion stemming from its presence in many daily activities, from the mundane to the extraordinary; for example writing to walking, spreading to more complex elastic material adhesion which is required for many industrial and medical applications. When two bodies join, this becomes the point of contact or contact zone, the extent of which plays an important role in understanding the contact as well as non-contact interactions in many natural and industrial processes. Such interactions include cell-cell and cell-material interactions; microfluidics; drug delivery systems (2-5) (essential in the pharmaceutical industry); and medical prostheses (6) whereby adhesion can influence friction and wear performance of the contacting surfaces in which biomedical applications are concerned. This subject is of utmost importance when considering aspects at the mesoscopic scale and may be beneficial or even detrimental for certain applications. Research into adhesion has a long track record, dating back to 1930's (6); regardless, complete understanding of adhesion remains in its infancy. Moreover, there are numerous industrial as well as medical applications which require the control of adhesive and cohesive properties, with a drive aimed at improving formulations in many pharmaceutical products such as inhaled medications within drug delivery systems. Not only is it sufficient to consider the device for inhaled formulations, but it is essential to consider the pharmaceutical particles and excipients in inhaled formulations. It is fundamental that an understanding of the adhesive and cohesive properties is

known for the respirable particles, as these forces can affect the stability and aggregation of the active material from the carrier particle. Commonly, lactose is used as a carrier particle especially in dry powder inhalers and often aides the active particle delivery on actuation from the particle interacting with the carrier particles.

Despite the fact that the study of adhesion reaches back over 70 years (4, 7, 8), and many models of adhesion have been famously produced and accepted that attempt to explain the adhesion phenomena. Yet, many of these models do not predict adhesion in real systems to any degree of accuracy; therefore this research will focus on developing a current complex multi-asperity adhesion model, and applying this model to pharmaceutical and biomedical applications.

2.1 Models of Adhesion

There are many models of adhesion that have been used to describe the physical and mechanical procedures behind the complexities of this phenomenon. Namely, Derjaguin, Landau, Verwey and Overbeek (DLVO); the extended DLVO (XDLVO); Johnson, Kendall, Roberts (JKR); Derjaquin, Muller and Toporov (DMT); and Maugis-Dugdale (MD) and more recently (6) viewing asperities to develop a further understanding of these theories.

2.1.1 Physical models (DLVO and XDLVO)

Firstly, the physical aspects of adhesion must be addressed. Thereby, applying the commonly used DLVO theory has been sufficient in many areas of research (9, 10). DLVO forms the basis of modern colloid interface science (9). The

principal concept of the theory of stability of lyophobic colloids was developed over 50 years ago by four famous scientists: Derjaguin, Landau, Verwey and Overbeek. With added research the theory was refined for the calculation of electrostatic and dispersion forces and their direct measurement (9). Famously, the Derjaguin School has dealt with the physical aspects of the theory and colloid stability, whereas the Rehbinder School (9) concerned themselves with the colloid chemistry and physicochemical mechanics. This resulted in both schools accounting for the same problems concerning the main factor of the theory, colloid stability. From Derjaguin, this main effect was thought to be secured by electrostatic repulsive forces; however, Rehbinder considered an absorption-solvation barrier as the main factor (9). Thanks to the discussions between these schools with both notions being in fact correct; these developments have allowed for further application of the DLVO theory.

Further developments came about when Derjaguin introduced the disjoining pressure as a measure of forces acting between two plane interfaces. Resulting in the DLVO theory being employed to measure the energy of interaction of flat surfaces directly using spherical bodies or crossed cylinders (9).

Derjaguin and Landau used the complete Debye-Huckel equations for electrical potential distributions between two similarly charged plates when applied to strong electrolytes. In general, the DLVO theory has been used to describe the balance between attractive forces, V_A, due to van der Waals (vdW) forces of attraction; and repulsive interactions, V_R, which arise due to the overlap of the electrical double layers of the cell as well as the substratum; all expressed as the total interaction (V_{TOT}) of a sample and a flat surface (11), e.g. cell and

substratum. The substratum's electrical double layer is usually negative in charge due to the charge on the cells, resulting in a repulsive interaction force.

$$V_{TOT} = V_A + V_R \quad (2\text{-}1)$$

And V_A may be defined as:

$$V_A = -Ar/6d \quad (2\text{-}2)$$

Where *A* is the Hamaker constant, *d* is the separation distance between the cell or sample and the substratum, *r* is the radius of the cell or sample (assuming cells/samples are spherical). V_R, the double layer interaction originates from Coulomb interactions.

This interaction relies on the strength and range of ions in its vicinity and the charged particles, however regardless of these interactions; the charging mechanisms of any surface are balanced in electroneutrality, which acts independently of other external interactions, as the surface charge is balanced by an equal but oppositely charged region of counterions (11). The Hamaker constant *A*, in Eq. 2-2, is proportional to the vdW interaction. It is a material property which describes the strength of the interaction between a surface and medium, and between two interacting bodies; relying on the dielectric properties of the medium, substratum and the cell. As a general rule of thumb, *A* is positive between like particles, resulting in a negative interaction potential i.e. attractive interaction (11). Normally due to the shrinkage of the electrical double layer (EDL) results in a reduction in the distance between particles and being attracted via the short-range vdW forces of attraction.

This theory proposes that the binding strength between colloidal particles, such as micro-organisms, as they are about 0.5-2 μm in size (12) and substratum surfaces may be calculated on the basis of Lifshitz–Van der Waals (LW), electrostatic, acid-base (AB) and electrical double layer interactions (DL) (12-15). According to this theory, the total interaction between a surface and a particle is the summation of their vdW and Coulomb interactions (12, 16). In addition, as the Lifshitz-van der Waals attractive forces are dominant close to the surface, and defined as shown in Eq. 2-2 (V_A = -Ar/6d) (11, 17). According to Dorobantu et al (2009) (18) the following equation represents the non-retarded vdW force between a sphere and an infinite planar surface, which is based on the Hamaker's approach and Derjaguin's approximation:

$$F_{LW} = A_{132}/6\ [-a/h^2 – a/(h+2a)^2 + 2a/h(h+2a)] \quad (2\text{-}3)$$

Where A_{132} is the effective Hamaker constant of interaction between 1-bacteria; 2-tip material; and 3-medium used; *a* is the radius of an atomic force tip, and *h* the surface to surface distance between the substrate and the AFM tip.

Then the particles are unable to detach or separate from the surface by Brownian motion and therefore adhere irreversibly; as Brownian motion governs the deposition, sedimentation and hydrodynamic forces (13, 14, 19).

Additionally, outside of the Stern layer is the diffuse layer, where interactions occur with the un-neutralized surface and ions which causes an accumulation of counterions and depleted co-ions. With increasing distance from the surface the atmosphere reaches the same ion concentration as that of a bulk solution; and if these ions are in rapid thermal motion are known as the diffuse electric double

layer. In contrast, the Coulomb interaction becomes dominant at a distance away from the surface because the vdW force decreases sharply with distance (12). As the counterions which are responsible for this interaction and are only transiently bound to the surface and build up forming the Stern layer (11). As a result the repulsive interaction forces originate from the repulsive osmotic pressure between these ions of the overlapping double layers; therefore, V_R is also associated with the surface potential, Ψ, the distance d (between cell and surface) and the Debye length, κ. κ in the following equation (11):

$$V_R \propto \Psi^2 e^{-\kappa d} \qquad (2\text{-}4)$$

Alternatively, if the surface potentials of the two surfaces are different then Ψ_1, Ψ_2 are often used. In order to calculate the thickness of the diffuse layer, then the inverse of the Debye length is required, i.e. 1/κ, where κ is defined as the following:

$$\kappa = \sqrt{(2000 e^2 N_A c / \varepsilon \varepsilon_0 kT)} \qquad (2\text{-}5)$$

N_A represents Avogadro's constant, c the concentration of the electrolyte ions (mol l^{-1}), ε is the dielectric constant of the solution and ε_0 the dielectric permittivity of free space, k is the Boltzmann constant, e the electronic charge, and T is the absolute temperature.

On the other hand, as the ionic strength (I) directly affects the inverse Debye length, then at high ionic strength the interaction of the double layer as well as the thickness are compressed, then the net interaction may be attractive i.e. due to the vdW forces even if both surfaces are negative in charge. Yet at an intermediate ionic strength can cause reversible attachment of cells at certain

distances from the surface; hence, at low ionic strength repulsion is at large (11).

Earlier calculations using the Poisson-Boltzmann equation was used to derive the electrostatic double-layer energy between two macro-bodies (20, 21), yet is limited to the case of two parallel infinitely flat plates, which is not the case when microbes are in question. Therefore the Derjaguin approximation was employed in order to estimate these interaction forces between two curved surfaces. Unfortunately, this approximation was not without its own limitations, as it assumes that the range of interaction energy is shorter than that of the radii of curvature of the particles (20) in question, and so was only applicable to larger particles and not ideal at the nanoscale.

This theory has been used both qualitatively and quantitatively to calculate the adhesion free energy changes which aid in the explanation of microbial adhesion (11). As well as being widely used to describe interfacial interactions between charged surfaces in liquid media (20), and characterises the total interaction energy as a combination of vdW and electrostatic double-layer interactions. The DLVO theory describes bacterial adhesion to surfaces as a balance between Lifshitz–van der Waals and electrostatic interactions while accounting for their dependence on the distance of separation between bacterium and substratum surfaces (22). Basically, microbial adhesion is the transfer of cells from an unbound state to a firm attached state at an interface (11).

The vdW interactions have also been used to describe the overall interaction (V_{TOT}) between a cell and substratum as a balance between two additive factors

(V_A) which results from vdW attractive interactions and repulsive interactions (V_R) which is from the overlap between the electrical double layer of the cell and the substratum (11). The repulsive interactions are due to the negative charge of cells and substratum, shown in the equation 1 and 2. Where *A* is the haymaker constant, *d* is the separation distance between the cell and the substratum, and *r* is the radius of the cell (as the cells are assumed to be spherical). Also, the double layer interaction (V_R) originates from the Coulomb interaction between charged molecules; with its strength and range strongly affected by the presence of surrounding ions (11, 23), and is a far more complex function as shown in the equation below:

$$V_R = 2\pi\varepsilon a\zeta^2 \exp(-\kappa d) \qquad (2\text{-}6)$$

Where *a* is the radius of the particle, π is the solvent permeability, κ is a function of the ionic composition and ζ is the zeta potential.

When a particle is further from a deposited surface then the vdW forces which only apply to the short-range interactions, compared to Lewis acid-base and electrostatic interactions which are weaker interactions, therefore will become unbound. Furthermore, in the DLVO theory, the total interaction energy between a particle and a solid surface is the sum of the non-covalent Lifshitz-van der Waals (LW) and Electrostatic interactions (EL) or double layer forces (DL); due to the separation distance increasing between particle-particle interaction (24), and the DL forces exponentially decay, but on the other hand the LW forces decay more gradually.

At normal ionic strength the attraction and repulsive forces are shown in Figure 2-1, this is the physiological ionic strength. However, at higher ionic strengths the electrical double layer of materials decreases which affects the repulsive electrostatic force but does nothing to the attractive van der Waals forces. The increased ionic strength reduces the electrostatic repulsion so the two surfaces may get closer i.e. as the ionic strength increases reduces the repulsion this is demonstrated in Figure 2-1.

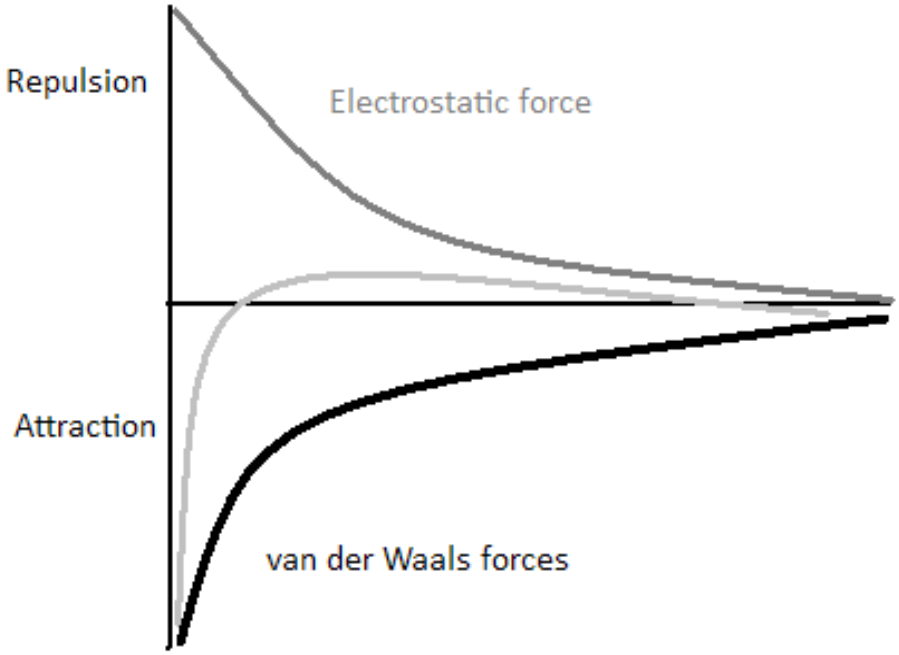

Figure 2-1. DLVO theory of attraction at normal ionic strength.

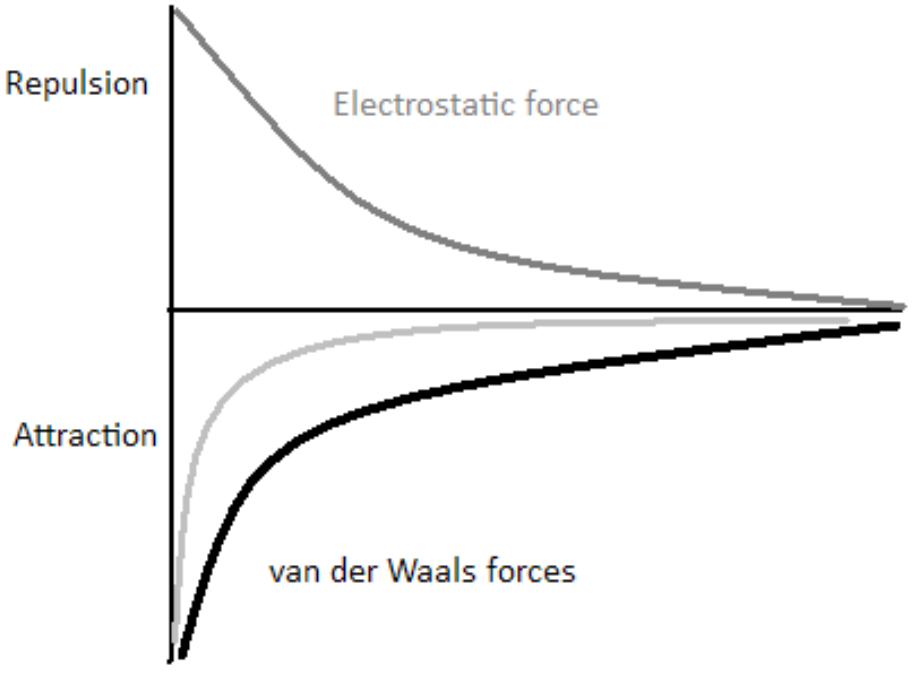

Figure 2-2. DLVO theory of attraction at high ionic strength reduces the repulsive forces.

Although the DLVO theory has been, and is useful for the qualitative description of particle adhesion to a solid surface; its experimental results do not always coincide with the theoretical predictions (18, 25). It has been mentioned that these deviations are attributed to a number of factors included the complexity and heterogeneity of surfaces i.e. it does not consider asperities; therefore it has been proven that there is a difficulty in generalizing the mechanisms of adhesion as these complexities reach across the numerous surfaces let alone the variability of different manufacturing processes (24).

Therefore, as adhesion is a very complex notion, the extended DLVO theory was considered, yet still has limitations and restrictions (26, 27).

The theories explained have limitations, for example, the DLVO theory assume perfectly smooth surfaces which may not be realistic in certain applications especially biological problems. The DLVO theory focused mainly on two kinds of forces, electrostatic double layer and weak van der Waals attractive forces acting between solid surfaces; and along with the Smoluchoski theory of coagulation, some statistical mechanics of two phase equilibrium were enough to account for the model for systems in which the theory was devised. Indeed, it is known that Derjaguins students were taught that DLVO only worked between approximately 10^{-3} and 10^{-2} M i.e. the Debye length which measures the range of the double layer and varies from 100 A (10^{-3} M), 30 A (10^{-2} M) to 10 A (10^{-1} M) (28). However, added complications were noticed when applied to cell biology where the Debye length is < 8 A; further complications came to light with micellar chemistry at high salt, and in ionic microemulsions, as well as

polyelectrolytes where the screening length is often the same order as hydrated ions (28).

However, the XDLVO theory attempts to right the wrongs of the classic DLVO yet remains shortened in its applicability of real life particles. This novel approach considers the total free energy of interactions between two surfaces immersed in an aqueous environment, and is the sum of the Lifshitz-van der Waals (LW) forces; polar interactions or acid-base (AB) which determine the hydrophobicity (or hydrophilicity) of the surface; electrical double layer (DL) interactions, as well as Brownian motion (BR) (26, 29), shown in the following equations:

$$\triangle G^{TOT} = \triangle G^{LW} + \triangle G^{AB} + \triangle G^{DL} + \triangle G^{BR} \quad (2\text{-}7)$$

The interaction energies in this case are divided into LW, AB, and electrostatic contribution of the double layer (DL); according to Boks et al (2008) (13) the distance dependence of the LW of interaction energies ($\Delta G^{LW}(d)$) were calculated assuming a sphere plane geometry:

$$\Delta G^{LW}(d) = -A/6\,[(2r(d+r)/(d(d+2r))-\ln(d+2r/d)] \quad (2\text{-}8)$$

Whereby *d* is the separation distance, again A is the Hamaker constant, and the distance dependence of the AB interaction energies ($\Delta G^{AB}(d)$):

$$\Delta G^{AB}(d) = 2\pi r \Delta G_{slb}{}^{AB} \lambda \exp(d_0-d/\lambda) \quad (2\text{-}9)$$

In which λ denotes the correlation length of molecules in liquid, and $\Delta G_{slb}{}^{AB}$ is the AB component of free energy of interaction at contact. Also, the distance-dependence EL interaction energies ($\Delta G^{DL}(d)$):

$$\Delta G^{DL}(d) = \pi\varepsilon\varepsilon_0 r\,(\varphi_b^2 + \varphi_s^2)[(2\varphi_b\varphi_s/\varphi_b^2)\,\ln[1\exp(-\kappa d)/1-\exp(-2\,\kappa d)] \quad (2\text{-}10)$$

$\varepsilon\varepsilon_0$ is the dielectric permittivity of the medium, φ_b φ_s, are the surface (zeta) potentials of the bacterial surface and collector surface respectively, and κ is the Debye length (13).

When both the classic DLVO and extended DLVO theory are concerned, then surface tension of colloid-size particles are mainly composed of apolar or Lifshitz-van der Waals components (15, 30); polar, or Lewis acid-base, as well as electrostatic components. Whereby the Lifshitz-van der Waals element of the surface tension is initiated by the even distribution of the electron cloud surrounding the molecules or particles (31-33). On the other hand, the Lewis acid-base component is governed by the potential formation of coordinate covalent bonds by Lewis acids i.e. electron pair acceptors, and Lewis bases i.e. electron donors. Acid–base interactions play the most important role in bacterial attachment to surfaces and can be quantified based on electron donor/electron acceptor data from contact angle measurement according to the XDLVO theory (22). The electrostatic element of surface tension is often described by zeta potentials, given the symbol ζ, and is measured by the electrical surface charge.

Evidence also suggests that the mechanisms of adhesion are significantly influenced by the surface free energy, Zhao et al (2007) (14) explain that there exists an optimum surface free energy of substrates by which bacterial adhesion is minimal (14, 34). Explanations in the literature also suggest that with certain surface coatings of substrates, such as corrosion resistant properties on coatings, have an advantageous outlook for reducing biofouling in medical devices as well as industrial equipment (14, 35).

However, further reading reveals that discrepancies between the XDLVO predictions and experimental attachment (22, 34) may be due to the complexity of bacterial cells and living organisms which is far from the ideal colloidal particles that these theories are based on. Therefore a physicochemical approach is needed as the XDLVO theory is unlikely to explain all aspects of attachment to surfaces (11, 22). Also, it has been pointed out that from inaccurate determination of cell physicochemical properties and the estimation of their interaction energies makes for difficult predictions when using the XDLVO theory.

Adhesion to a surface is often influenced by electrostatic forces, and from the origins of XDLVO, DLVO theory, the colloidal interaction which are caused by van der Waals potential and the electrical double layer are concerned with the colloids stability (14, 36). Moreover the Lifshitz-van der Waals attraction interaction potential for a sphere interacting with a surface is related to the geometries given by:

$$\Phi_{vdw} = - Ad_p/12a \qquad (2\text{-}11)$$

Where A is the Hamaker constant, d_p the diameter of the particle and a represents the distance between the surfaces. The following equation is used to calculate the Hamaker constant from the surface free energies according to Van Oss (2007) (37):

$$A_{123}=24\pi_0^2 (\sqrt{\gamma_1}^{LW}-\sqrt{\gamma_3}^{LW})(\sqrt{\gamma_2}^{LW}-\sqrt{\gamma_3}^{LW}) \qquad (2\text{-}12)$$

Where particles (1) interact with the surface (2) immersed in water (3), where γ_i^{LW} is the Lifshitz-van der Waals element for the surface free energy of the

material represented by i and H_0=0.158nm represents the minimum separation distance (37, 38).

Once particles are immersed in the media, an electrical double layer forms, and naturally with particles of like electrical charge the double layer will inherently be repulsive. Furthermore, the attractive hydrophobic interactions can surpass the DLVO forces and arise due to the electron donor-electron acceptor interaction in polar media (35). It is the addition on the non-DLVO force hydrophobic attractive interactions of the van der Waals and electrical double layer which give rise to the extended DLVO, as adhesion is determined by the balance between attractive and repulsive forces (35). This balance is calculated as a sum of the interaction potentials according to the XDLVO theory:

$$\Phi_r \varphi_{vdw} + \varphi_{edl} + \varphi_{AB} \quad (2\text{-}13)$$

Although the XDLVO has been used successfully for aqueous systems, experimentally however, values for the interaction energy may be too high for regions of a few nanometres from the surface (38); therefore by the addition of the effect of the electrical double layer on the water permittivity, this will decrease the XDLVO theory for the estimated interaction energy i.e. when the EDL is in close quarters to the particle, it affects the polarization of the medium, and so changes the permittivity of the media, which depends on the distance to the surface. Results revealed that the interaction energy obtained using the methods described above, were sensitive to the ionic strength of the medium as well as the size of the particle i.e. the smaller the particle and the higher the ion strength, then the lower energy is required to overcome the energy barrier near the surface; whereas the electrostatic forces are governed by the salt content of

the medium and the zeta potential, along with the Debye length which decreases with increasing ionic strength (35). In turn these effects will decrease the repulsion forces, which give rise to the lower energy barrier, making fouling an easy process to take place. Experiments also revealed when applying the XDLVO that larger particles adhere to surfaces only when the ion strength is high, therefore this evidence suggests that fouling is dependent on particle size.

2.1.2 Mechanical models (JKR and DMT)

Alternative or additive theories have therefore been observed, which aim to combat the short falls of the previous adhesion models. Johnson, Kendall and Roberts, in 1971, developed a theory of adhesion of two sols in contact (4, 39-41) i.e. the JKR theory. DMT on the other hand, Derjaguin, Muller and Toporov, in 1975 came about their theory of contact (39) whereby tensile stress exists as an annular zone around the contact area without deforming the profile. Basically the JKR model based its theory on the short-range surface forces that act in the contact area; and the DMT model takes into consideration the non-contact area forces, such as molecular attraction which are at large outside of the contact area.

There are always of course many hurdles and barriers to overcome when it comes to science, however, the impact of adhesive particles with a surface or other particles is a fundamental physical process that applies to a wide range of scientific conundrums and engineering applications. The list of applications may include particle deposition; filtration; coagulation and breakage (42). As adhesion plays a fundamental role at the contact area, and the dynamic process may result in either two ways; then first the particle may be

rebounded/repelled from the surface; or it may be captured which leads to particle deposition and biofilm formation.

Liu et al (2011) (42) decided that a dynamic model was needed to help understand these complex issues of adhesion. Analytically however, these models proposing the theoretical aspects of impact are divided into 2 categories: first is the kinetic model; the second being the dynamic model. According to Liu et al (2011) (42), the kinetic model focuses on predicting the capture velocity, or the relationship between restitution coefficient and incident velocity; further explanations reveal that a kinetic model is advantageous as it's simple and has been extensively studied for hard spheres. On the other hand, kinetic models do not reveal the dynamic aspects of impact i.e. in terms of time-variant contact force, particle velocity, deformation and the relationship in between the surface and contact area. Whereas dynamic models predict these lacking in the kinetic model, such as the restitution coefficient and capture velocity; whilst concentrating on the contact mechanics, as well as establishing the inter-particle interactions. Dynamic models generally describe the impact process through the combination of the static contact theory and appropriate dissipation mechanisms (42). The theory on static contact usually serves as the fundamental description of the impact, while energy dissipation accounts for the dynamic effects such as viscoelasticity of materials (42). JKR model predicts the critical pull-off force given by $3/2\pi\sigma R$ and a contact area larger than Hertzian contact due to the presence of adhesion (42).

This theory has been utilized by Liu et al (2011) (42) to explain the dynamic model, yet better understanding is still required for the improvement of energy

dissipation mechanisms for the dynamic model. Rundlöf et al (2000) (43) concentrates on the adhesion between poly(dimethylsiloxane) (PDMS) caps and Langmuir-Blodgett cellulose surfaces including the substrate, hydrophobized mica, and two flat mineral surfaces (bare mica and glass) (43). The study revealed a similarity in self-adhesion for PDMS caps and oxidised PDMS caps, as long as the systems showed little or no hysteresis between the loading and unloading force curves. Yet, in some force curves there was large hysteresis between the loading and unloading curves, and showed a larger adhesion measurement compared to the pull-off force than from the JKR-curve determined loading. JKR method utilises the deformation of surfaces (which is a limitation concerned with the AFM as these are difficult to account for) under zero or applied loads to accurately determine the adhesion between two bodies (43).

The JKR theory is commonly used as the experimental data recovered often agrees with the theory, and according to the JKR theory of adhesion, the radius of the contact area between solids may be related to the work of adhesion:

$$F = \frac{Ea^3}{R} - \sqrt{6\pi\sigma E a^3} \tag{2-14}$$

$$\delta = \frac{a^2}{R} - \frac{2}{3}\sqrt{\frac{6\pi\sigma a}{E}} \tag{2-15}$$

$$a^3 = R/K\ [F+3\pi\sigma R+\sqrt{((6\sigma RF+(3\pi\sigma R)^2)}] \tag{2-16}$$

where R = the equivalent radius of curvature of the tip, F = the applied load/force, and, E = the elastic constant of the system i.e. Young's modulus; δ is the deformation; α = the contact area radius, and σ = the work of adhesion. In

order to calculate *R*, then the radius of curvature of two materials (materials 1 and 2) are needed:

$$1/R = 1/R_1 + 1/R_2 \quad (2\text{-}17)$$

K is calculated from the Young's modulus, *E*, and the Poisson ratio, *v*, of material 1 and 2:

$$1/K = ¾ ((1-v_1^2/E_1) + (1-v_2^2/E_2)) \quad (2\text{-}18)$$

Also, when applying the JKR theory, the negative load required to separate the two contacting surfaces, must overcome the action of the adhesive forces between the surfaces, and is related to the work of adhesion, *σ*:

$$F = - 3/2\ \pi\ \sigma R \quad (2\text{-}19)$$

The interfacial energies in a medium, 3, is related to the work of adhesion, *σ*, between materials 1 and 2 as shown:

$$\sigma = \gamma_{1,3} + \gamma_{2,3} - \gamma_{1,2} \quad (2\text{-}20)$$

So, the adhesion energy, *σ*, and the modulus *K* are obtained by the cube of contact radius a^3, and when plotted against the load, *F* are fitted to the first equation $a^3 = R/K\ [F+3\pi\sigma R+\sqrt{((6\sigma RF+(3\pi\sigma R)^2)}]$; and the adhesion energy which corresponds to the pull-off force is calculated using the fourth equation: $F = - 3/2\ \pi\ \sigma R$.

However, the JKR theory may only be applied to thermodynamically equilibrated conditions; this is where the loading data and unloading data are reversible. On the contrary, when no equilibrium, then the loading and unloading curves are hysteretic, therefore $\sigma_{unloading} > \sigma_{loading}$; this means that the

loading curve will be under the unloading curve, and the rate at which this occurs is thoroughly dependent on a number of factors such as the loading/unloading rate; temperature; relative humidity, and the sample itself (43).

It is common when using the loading and unloading curves, that the $\sigma_{loading}$ will often give data values that are similar to the thermodynamic work, whereas the $\sigma_{unloading}$ will be larger and equal to the $\sigma_{pull\text{-}off}$ and is commonly due to the large adhesion hysteresis (43). Frequently the work of adhesion is larger in unloading curves as a result of a few factors which include: viscoelastic deformations, interpenetration of the surface layer, surface roughness, formation of chemical bonds by reactive groups, and reorientation of polar groups.

JKR may be applied to higher adhesion and deformability when the adhering surfaces in question are subject to a separating force (44). It is an analytical model which extends the non-adhesive Hertzian contact theory (45). JKR theory relates the pull off force F_s and the adhesion energy σ_{adh} through the radii of curvature of the materials. For example, when considering an ideal solid homogenous sphere, then:

$$\sigma_{adh} = 2F_s / (3\pi R_m) \quad (2\text{-}21)$$

Where R_m is the harmonic mean of the radii of the two spheres, and more recently the relation between F_s and σ_{adh} has been derived for spherical shells (44):

$$\sigma_{adh} = F_s / (\pi R_m) \quad (2\text{-}22)$$

It has been noted throughout research into bacterial adhesion that from the thermodynamic model of adhesion of small particles from a suspension onto a solid substratum is governed by the surface properties of three phases i.e. (i) the surface tensions of the adhering particles; (ii) the substrate; (iii) the suspending liquid medium (46, 47). It has also been brought to attention that adhesion is more extensive to hydrophilic substrata, of which have a relatively high surface tension; compared to their hydrophobic counterpart; whereby the surface tension of the bacteria is larger than that of the suspending media; therefore the reverse would occur i.e. no adhesion.

Recently Bayoudh et al (2009) (25), stated that adhesion or attraction between two interacting surfaces occurs when the total free energy is negative, and repulsion will occur if it is positive, supporting the earlier claims of researches. This can also be observed as the total interaction energy may be evaluated as a function of the separation distance between the interacting surfaces, therefore once an interaction energy profile is predicted this indicates the type of interaction (attraction or repulsion) as the microbial particle approaches a substrate surface (25, 46).

Furthermore, Lin et al (2008) (48) mentions the contact/adhesion test based on JKR theory, and has been extensively used to quantify the work of adhesion between 2 soft elastic materials; and only applies when the contact radius is small when compared to the radius of the spheres e.g. can't be applied to thin elastic lenses. JKR theory only assumes small strains and material linearity; and so there are many problems with this theory in practice, especially when concerned with micro- or nano-indenters on thin and compliant coatings. So

when the contact radius is not small in comparison with the radius of the spheres, the Hertz assumption is no longer valid. And as deformation is large, the strains are not linear. Li and Chen (2012) (20) developed a theory which models large-deformation adhesive contact of hyperelastic lenses based on energy balance. They calculated the energy release rate of a large-deformation JKR (LDJKR) problem using the solution of the corresponding large-deformation Hertz (LDH) problem. Two problems were studied in their work (20) a rigid spherical indenter in contact with a Neo-Hookean half space, and a Neo-Hookean hemisphere in contact with a rigid substrate (48).

Commonly, the JKR, DMT, Maugis-Dugdale models and Tabor parameter for contact under normal loading have been developed based on solid-solid interactions i.e. vdW; and in the study by Xu et al (2007) (49), the characteristic length scale for the adhesive forces in the Tabor parameter is the equilibrium interatomic spacing (41, 49). But, a more realistic approach is needed when considering biological specimens as contact tends to be in humid environments, therefore long range capillary forces are in action and it has been noted by Xu et al (2007) (49) that these forces may be related and dominated by the Kelvin radius. Many researchers have delved into this notion and some have introduced parameters which include the Kelvin radius for the JKR-DMT transition, as well as observing the capillary effects; and are collectively known as the Tabor parameter. The introduction of this modified Tabor parameter with the Kelvin radius has allowed quantitative description of the JKR-DMT transition in terms of relative humidity (49). Tabor defined a dimensionless parameter μT representing the ratio between the gap outside the contact zone and the

equilibrium distance between atoms. The parameter established the range of applicability of the 2 models, and suggested that interactions within and outside of the contact zone needed to be accounted for (49).

Further research (49) demonstrated a continuous transition from DMT to JKR as the Tabor parameter increased by using a Lennard-Jones potential. It has also come to light that the adhesive contact models of JKR, DMT and Maugis are not sensitive to the origin of mechanism of the adhesive interaction. But, that the time period of contact is dependent on the origin of adhesion.

When two surfaces make contact in a vapour, absorbed and condensed liquid molecules are present and constrained between these surfaces (49). At certain distances such as these described, then the surfaces will be attracted, yet repulsion still exists between the absorbed molecules as this repulsion equalises the external adhesive forces. The forces which occur during the adhesion process are described in the following equations:

$$F = \frac{Ea^3}{R} - 2\pi R\sigma \tag{2-23}$$

$$\delta = \frac{a^2}{R} \tag{2-24}$$

Where *F* is the force applied to the system; *E* is the Young's modulus; and δ is the deformation occurring in the system; *a* is the contact area radius, *R* is the tip curvature radius; and σ the work of adhesion.

However contradictory this may appear, then one must assume that within the contact area the absorbed molecules are solid. It has also been noted that films less than 10 molecular diameters thick will become more viscous; and that films

of 4 molecular diameters will undergo a phase transition to a liquid-crystalline phase. Xu et al (2007) (49) observed ice-like water on mica surfaces by using sum-frequency-generation (SFG) vibrational spectroscopy, and scanning polarisation force microscopy (SPFM). Moreover, it was noted that outside the contact area then bulk liquid behaviour returned, therefore Xu et al (2007) (49) explain that it is important therefore to determine an appropriate limit to the contact zone as the behaviour from bulk changes, and are consistent with the stress distributions proposed in the Maugis model (49).

Woerdeman et al (1999) (50) explain of different techniques to test adhesion, which include; peeling, blister and fibre fragmentation tests. Mentioned also in the text is the adhesion test based on the JKR theory, and has been applied to a number of systems in order to determine the intrinsic work of adhesion required to separate two surfaces. Also an important aspect of the JKR technique is that it enables the assessment of the interfacial contributions to the adhesive strength, as the test is usually performed at low crack velocities. The JKR technique involves a convex elastomer coming into contact with another solid substrate which causes the adhesive forces to deform the solid and increases their interfacial contact area. It has been described by many as an extension to the classic Hertz result whereby the deformation of two elastic bodies when in contact affect the interfacial adhesion energy at work.

Further explanations (50) reveal that typical adhesion experiments are performed in 3 parts:

1-The loading process- compresses the elastomeric lens against a flat surface with a specified load under controlled conditions;

2-Elastomer remains in contact with the surface for a set time- allowing for the physical and chemical interactions to evolve and can lead to enhanced adhesion energy;

3-The unloading process- this involves the rapid decompression of the elastomer lens, whilst monitoring the applied load, the deformation of the contact area, and the contact area itself as a function of time.

This theory however relies on the assumption that an equilibrium state is reached at each loading stage, yet Woerdeman et al (1999) (50) claim that this theory should be tested as the time it takes for equilibrium can vary substantially between systems. AFM was also used to study the adhesion failure from peeling an elastomeric film from a glass substrate, and is achieved as the AFM can simultaneously observe and characterize surfaces (50).

A model proposed by Tabor after comparing the results of both models, introduced a non-dimensional parameter μT (Tabor's parameter) which explained the inconsistencies (51). This was known as the Maugis-Dugdale model (M-D). The Maugis-Dugdale (M-D) model was first proposed to determine the adhesive contact of elastic spheres. In this model, the step cohesive stress (σ_0) is randomly chosen to be the theoretical stress (σ_{th}) which matches that of the Lennard-Jones potential indicated by:

$$F^*(h) = 8\Delta\gamma/3z_0 [(h/z_0)^{-9}-(h/z_0)^{-3}] \quad (2\text{-}25)$$

Where *h* represents the local separation related to the gap $h(r) = z_0 + [w(r/a]$

Zheng and Yu (2007) (52) point out an alternative more reasonable model, where the Maugis model is initially extended to an axisymmetric elastic object

with a random surface adhesive interaction which is then applied to a power-law shape function and a step cohesive stress (52). The discussion of these models is significant in relation to the developments within the area of contact mechanisms, as some aspects such as characterising the consistent relation of deformation and the interaction have been problematic. Not only has the subject developed quickly since the JKR and DMT model, but on the other hand has also been limited by the natural limitations these models lack.

The third model, the Maugis-Dugdale (M-D) theory considers the frictionless adhesive contact between two axisymmetric elastic objects. This is where an assumption is made that a small deformation occurs when two spheres are in contact, and the distribution of the stress and deformation is regarded as an elastic half-space and is performed with a Hankel transform (52). Maugis-Dugdale (M-D) concentrates mainly on deriving the load-displacement relation that characterises the contact behaviour. The surface shape has been described by Zheng and Yu (2007) (52) by:

$$F(\varsigma) \equiv z(r) = z_1(r) + z_2(r), \varsigma = r/a \quad (2\text{-}26)$$

where r is the radius, a represents the contact radius, with z_1 and z_2 representing two objects, and this surface contact may be divided into three regions: an intimate contact region r<a; a cohesive region a<r<c; and a non-interaction region r>c.

As these theories are complex, a simplified explanation is given by Zheng and Yu (2007) (52) which considers the power-law shape function, and the adhesive

interaction of the Dugdale approximation; the power-law shape function is described by:

$$F(\varsigma) = a^n \varsigma^n / nQ \quad (2\text{-}27)$$

where *n* and *Q* represent two shape parameters; whereby *n* is for all positive numbers i.e. n=1 for a cone; n=2 for a sphere; and n = ∞ represents a flat punch. Also *Q* is given by the dimension ℓ^{n-1}, with ℓ being the length; and if n=1, then Q = tanφ, where φ is a semi-angle; otherwise Q is denoted by R^{n-1}, and R is the equivalent radius. The Dugdale approximation is therefore a rough calculation of the step cohesive pressure distribution:

$$p(\varsigma) = -\sigma_0,\ 1<\varsigma<m \quad (2\text{-}28)$$

where σ_0 represents a constant stress.

To calculate the M-D-n model, its simplified, as when the load is sufficiently high, the adhesive component may be neglected, which is an extended Hertz theory (Hertz-n) for power-law axisymmetric elastic objects (52).

As discussed in the above models of adhesion, DLVO and XDLVO, both lack in the fundamentals of asperities associated with bacterial surfaces and appendages. These single-asperity micro- and nanoscale contact behaviours are important for the performance of many small-scale mechanical systems, such as the AFM (53). Usually, when analysing such aspects of cells, an assumption to their shape is made that they are parabolic and therefore the familiar adhesive contact models such as Johnson-Kendall-Roberts (JKR); Derjaguin-Muller-Toporov (DMT); and Maugis-Dugdale (M-D) may be applied.

Recently Grierson et al (2013) (53) investigated the use of this M-D-n model to investigate the behaviour of nanoscale adhesive contacts with non-paraboloidal geometries; specifically observing the pull-off force, work of adhesion. It was pointed out that adhesive forces that act between two surfaces play a critical role in determining the behaviour of small-scale mechanical systems that have a naturally high surface to volume ratio, For example, the AFM relies on the adhesion and friction between the tip and the sample surface in order to image and manipulate the sample in question. Therefore the tip is assumed a paraboloid shape and is able to be analysed using techniques such as JKR and DMT which extend the Hertzian contact model. However, this is not always the case as AFM tips are often of different geometry due to varying manufacturing methods as well as wear and tear after use.

Results revealed an uncanny large adhesion range which may be due to the long range vdW forces or a deviation in the theory caused by atomic-scale roughness of the tip (53).

Figure 2-3 highlights the three proposed models highlighting the Force versus the penetration depth for the different amount of adhesion.

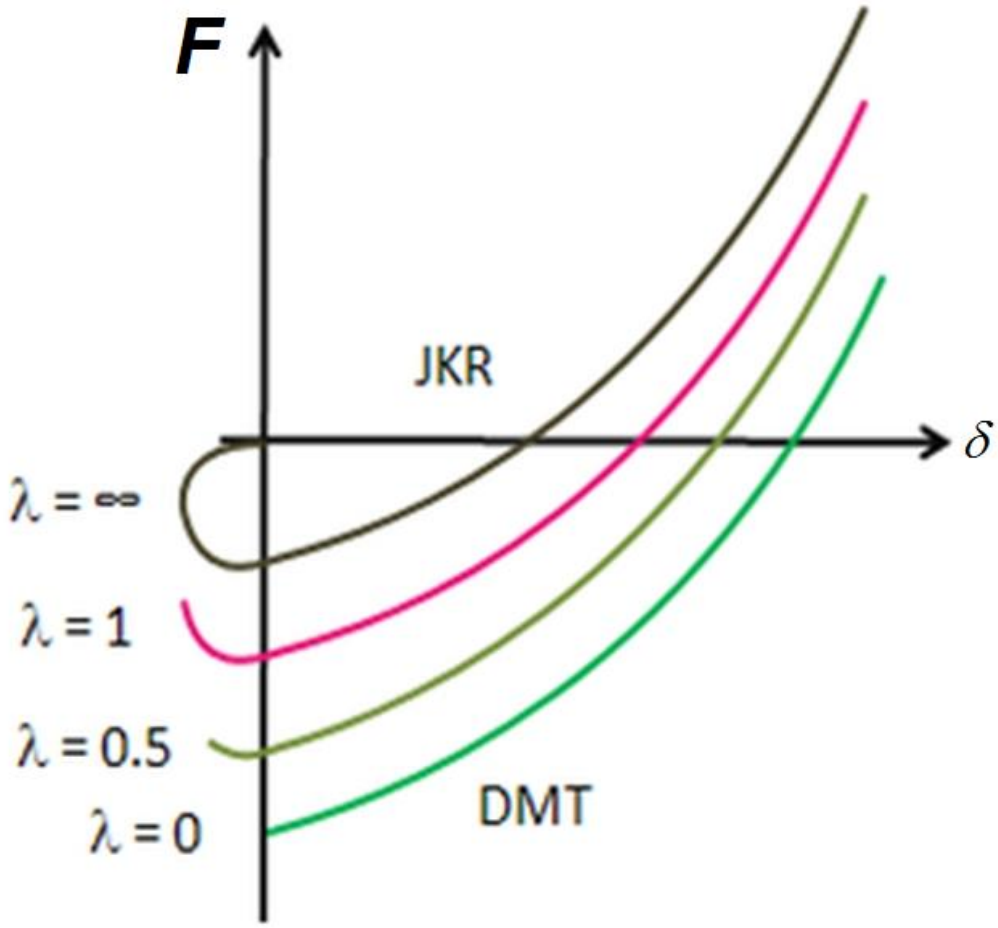

Figure 2-3. Adhesion models shown in graphical form.

2.2 Importance of surface topography

The theories described consider many surfaces; however, there is lack of knowledge when applying the theories to real surfaces. As is evident not all surfaces are ideal, many exhibit irregularities (6), and additions on an otherwise flat surface. For example, the highest points on any surface may sometimes be known as peaks, but in this case they are known as asperities, with the lower points denoted as valleys.

It’s important to note that the effect of topographical heterogeneity on colloidal DLVO interactions has shown discrepancies between experimental deposition rates to the theoretical particle deposition when using the Derjaguin approximation showing the latter to be significantly smaller. Also the same DLVO model has attributed to the roughness of particles and surface, as asperities on both interacting surfaces decrease the total interacting energy and the height of the energy barrier that particles must overcome in order to adhere. Furthermore, the decrease in repulsion was attributed to the surface roughness therefore greater deposition occurs which is larger than predicted using the DLVO theory for smooth surfaces, as this does not account for ‘real’ surfaces. Computations of DLVO interactions between rough particles and a smooth plate and two rough surfaces have confirmed that roughness can significantly decrease the energy barrier, suggesting that deposition rates could be larger on rough surfaces (54).

Single asperity adhesion models are more commonly viewed as sphere-sphere or sphere-flat plane approaches, and most techniques to understand and predict interactions are commonly based on vdW adhesion which utilize the vdW forces of attraction which inevitably leads to adhesion. Asperities tend to be modelled as a sphere with a radius equivalent to the radius of curvature of the asperity of the tip (6).

Alternatively surface energy approaches are used, for example, the JKR, DMT and MD models; these consider the elastic response of the interacting subjects. Originally, an adhesionless contact model for a circular point was developed by Hertz, which described the deformation and contact radius. A further model

introduced later by Maugis and Dugdale (M-D) proposed the effects of surface forces which are involved at the Hertzian region of contact between two hemispherical asperities, and so Prokopovich and Starov (2011) (6) indicate that this model may be used for materials of both high and low adhesion (6).

Through many years of research into the theories of contact, there has been much debate over which theory or combination of theories is most accurate. Evidence suggests that for small loads, the asperity models predicts a linear relation between the area of true contact and the applied load (55). As stated, the Coulombs friction law describes the fiction force as being proportional to the load due to a direct proportionality between the applied load and the area of real contact. Further explanation indicate that asperities of rough solid surfaces are deformed as soon as they are in contact, and as the yield stress is constant, the asperities end up with a direct proportionality between the load and the area on intimate contact. For example, Carbone and Bottiglione (2008) (55) performed wear experiments in which the contact of asperity was believed to be formed under elastic not plastic deformation i.e. initially plastic deformation occurs, but with time once a steady state condition the load is then supported elastically. Another point made by Carbone and Bottiglione (2008) (55) is that rubber materials undergo no plastic deformation and instead the area of intimate contact is determined by its viscoelastic properties of the material itself, the surface energies as well as their roughness (55). An interest in this area has arisen due to the requirement of manufacturing smaller mechanical and electrical devices from micro- to even nanoscale i.e. microelectromechanical systems (MEMS).

Basically, the multi asperity model is a generalized Hertz contact theory which accounts for the surface statistics. The notion developed from research into modelling the roughness of surfaces assuming identical spherical asperities with randomly distributed height, as all surfaces are not ideal, and most are uneven and so contact must be through asperities. Two models of multi asperity have been proposed (6). The first is the un-coupled model, and in general each asperity contributes but estimated independently, and the overall adhesion is the sum of all contributing asperities. The second model explained by Prokopovich and Starov (2011) (6) is the coupled model, whereby the surface in question is considered in its entirety. The coupled model is far more complex according to Prokopovich and Starov (2011) (6), which is rarely used, due to its mathematical difficulty. This model concentrates on the periodic interface profiles and does not consider the random distribution of asperity heights.

2.3 References

1. Dos Santos Ferreira O, Gelinck E, de Graaf D, Fischer H. Adhesion experiments using an AFM--Parameters of influence. Applied Surface Science. 2010;257(1):48-55.

2. Rogueda PGA, Price R, Smith T, Young PM, Traini D. Particle synergy and aerosol performance in non-aqueous liquid of two combinations metered dose inhalation formulations: An AFM and Raman investigation. Journal of Colloid and Interface Science. 2011;361(2):649-55.

3. Young PM, Price R, Lewis D, Edge S, Traini D. Under pressure: predicting pressurized metered dose inhaler interactions using the atomic force microscope. Journal of Colloid and Interface Science. 2003;262(1):298-302.

4. Johnson KL, Kendall K, Roberts AD. Surface Energy and the Contact of Elastic Solids. Mathematical and Physical Sciences. 1971;324:301-13.

5. Preedy EC, Brousseau E, Evans S, Perni S, Prokopovich P. Adhesive Forces and Surface Properties of Cold Gas Plasma Treated UHMWPE. Colloids and Surfaces B: Biointerfaces. 2014.

6. Prokopovich P, Starov V. Adhesion models: From single to multiple asperity contacts. Advances in Colloid and Interface Science. 2011;168(1–2):210-22.

7. Derjaguin B. Kolloid Z. 1934;69:155.

8. Johnson DJ, Al Malek SA, Al-Rashdi BAM, Hilal N. Atomic force microscopy of nanofiltration membranes: Effect of imaging mode and environment. Journal of Membrane Science. 2012;389(0):486-98.

9. Churaev NV. The DLVO theory in Russian colloid science. Advances in Colloid and Interface Science. 1999;83(1–3):19-32.

10. van Oss CJ, Docoslis A, Wu W, Giese RF. Influence of macroscopic and microscopic interactions on kinetic rate constants: I. Role of the extended DLVO theory in determining the kinetic adsorption constant of proteins in aqueous media, using von Smoluchowski's approach. Colloids and Surfaces B: Biointerfaces. 1999;14(1–4):99-104.

11. Hermansson M. The DLVO theory in microbial adhesion. Colloids and Surfaces B: Biointerfaces. 1999;14(1–4):105-19.

12. Hori K, Matsumoto S. Bacterial adhesion: From mechanism to control. Biochemical Engineering Journal. 2010;48(3):424-34.

13. Boks NP, Norde W, van der Mei HC, Busscher HJ. Forces involved in bacterial adhesion to hydrophilic and hydrophobic surfaces. Microbiology. 2008;154(10):3122-33.

14. Zhao Q, Wang C, Liu Y, Wang S. Bacterial adhesion on the metal-polymer composite coatings. International Journal of Adhesion and Adhesives. 2007;27(2):85-91.

15. Hamadi F, Latrache H. Comparison of contact angle measurement and microbial adhesion to solvents for assaying electron donor–electron acceptor (acid–base) properties of bacterial surface. Colloids and Surfaces B: Biointerfaces. 2008;65(1):134-9.

16. Vincent B. Early (pre-DLVO) studies of particle aggregation. Advances in Colloid and Interface Science. 2012;170(1–2):56-67.

17. Shao W, Zhao Q, Abel EW, Bendavid A. Influence of interaction energy between Si-doped diamond-like carbon films and bacteria on bacterial adhesion under flow conditions. Journal of Biomedical Materials Research Part A. 2010;93A(1):133-9.

18. Dorobantu LS, Bhattacharjee S, Foght JM, Gray MR. Analysis of Force Interactions between AFM Tips and Hydrophobic Bacteria Using DLVO Theory. Langmuir. 2009;25(12):6968-76.

19. Schwegmann H, Ruppert J, Frimmel FH. Influence of the pH value on the photocatalytic disinfection of bacteria with TiO2 – Explanation by DLVO and XDLVO theory. Water research. 2013;47(4):1503-11.

20. Li K, Chen Y. Evaluation of DLVO interaction between a sphere and a cylinder. Colloids and Surfaces A: Physicochemical and Engineering Aspects. 2012;415(0):218-29.

21. Chidlow SJ, Chong WWF, Teodorescu M. On the two-dimensional solution of both adhesive and non-adhesive contact problems involving functionally graded materials. European Journal of Mechanics - A/Solids. 2012(0).

22. Nguyen VT, Chia TWR, Turner MS, Fegan N, Dykes GA. Quantification of acid–base interactions based on contact angle measurement allows XDLVO predictions to attachment of Campylobacter jejuni but not Salmonella. Journal of microbiological methods. 2011;86(1):89-96.

23. Sharp JM, Dickinson RB. Direct Evaluation of DLVO Theory for Predicting Long-Range Forces between a Yeast Cell and a Surface. Langmuir. 2005;21(18):8198-203.

24. Eydelnant IA, Tufenkji N. Cranberry Derived Proanthocyanidins Reduce Bacterial Adhesion to Selected Biomaterials. Langmuir. 2008;24(18):10273-81.

25. Bayoudh S, Othmane A, Mora L, Ben Ouada H. Assessing bacterial adhesion using DLVO and XDLVO theories and the jet impingement technique. Colloids and Surfaces B: Biointerfaces. 2009;73(1):1-9.

26. Azeredo J, Visser J, Oliveira R. Exopolymers in bacterial adhesion: interpretation in terms of DLVO and XDLVO theories. Colloids and Surfaces B: Biointerfaces. 1999;14(1–4):141-8.

27. Wiącek A, Chibowski E. Application of an extended DLVO theory for the calculation of the interactions between emulsified oil droplets in alcohol solutions. Colloids and Surfaces B: Biointerfaces. 1999;14(1–4):19-26.

28. Ninham BW. On progress in forces since the DLVO theory. Advances in Colloid and Interface Science. 1999;83(1–3):1-17.

29. Hoek EMV, Agarwal GK. Extended DLVO interactions between spherical particles and rough surfaces. Journal of Colloid and Interface Science. 2006;298(1):50-8.

30. Strevett KA, Chen G. Microbial surface thermodynamics and applications. Research in Microbiology. 2003;154(5):329-35.

31. Vennapusa RR, Binner S, Cabrera R, Fernandez-Lahore M. Surface Energetics to Assess Microbial Adhesion onto Fluidized Chromatography Adsorbents. Engineering in Life Sciences. 2008;8(5):530-9.

32. Farahat M, Hirajima T, Sasaki K. Adhesion of Ferroplasma acidiphilum onto pyrite calculated from the extended DLVO theory using the van Oss–Good–Chaudhury approach. Journal of Colloid and Interface Science. 2010;349(2):594-601.

33. Farahat M, Hirajima T, Sasaki K, Doi K. Adhesion of Escherichia coli onto quartz, hematite and corundum: Extended DLVO theory and flotation behavior. Colloids and Surfaces B: Biointerfaces. 2009;74(1):140-9.

34. Chrysikopoulos CV, Syngouna VI. Attachment of bacteriophages MS2 and ΦX174 onto kaolinite and montmorillonite: Extended-DLVO interactions. Colloids and Surfaces B: Biointerfaces. 2012;92(0):74-83.

35. Ojaniemi U, Riihimäki M, Manninen M, Pättikangas T. Wall function model for particulate fouling applying XDLVO theory. Chemical Engineering Science. 2012;84(0):57-69.

36. van Oss CJ. Chapter Five The interfacial tension/free energy of interaction between water and identical condensed-phase entities, i, immersed in water, w. In: Carel JvO, editor. Interface Science and Technology. Volume 16: Elsevier; 2008. p. 59-72.

37. van Oss CJ. Development and applications of the interfacial tension between water and organic or biological surfaces. Colloids and Surfaces B: Biointerfaces. 2007;54(1):2-9.

38. Bower MJD, Bank TL, Giese RF, van Oss CJ. Nanoscale forces of interaction between glass in aqueous and non-aqueous media: A theoretical and empirical study. Colloids and Surfaces A: Physicochemical and Engineering Aspects. 2010;362(1–3):90-6.

39. Espinasse L, Keer L, Borodich F, Yu H, Jane Wang Q. A note on JKR and DMT theories of contact on a transversely isotropic half-space. Mechanics of Materials. 2010;42(4):477-80.

40. Ebenstein DM, Wahl KJ. A comparison of JKR-based methods to analyze quasi-static and dynamic indentation force curves. Journal of Colloid and Interface Science. 2006;298(2):652-62.

41. Prokopovich P, Perni S. Comparison of JKR- and DMT-based multi-asperity adhesion model: Theory and experiment. Colloids and Surfaces A: Physicochemical and Engineering Aspects. 2011;383(1–3):95-101.

42. Liu G, Li S, Yao Q. A JKR-based dynamic model for the impact of micro-particle with a flat surface. Powder Technology. 2011;207(1–3):215-23.

43. Rundlöf M, Karlsson M, Wågberg L, Poptoshev E, Rutland M, Claesson P. Application of the JKR Method to the Measurement of Adhesion to Langmuir–Blodgett Cellulose Surfaces. Journal of Colloid and Interface Science. 2000;230(2):441-7.

44. Chu Y-S, Dufour S, Thiery JP, Perez E, Pincet F. Johnson-Kendall-Roberts Theory Applied to Living Cells. Physical Review Letters. 2005;94(2):028102.

45. Sauer RA, Li S. An atomic interaction-based continuum model for adhesive contact mechanics. Finite Elements in Analysis and Design. 2007;43(5):384-96.

46. Absolom DR, Lamberti FV, Policova Z, Zingg W, Van Oss CJ, Neumann W. Surface Thermodynamics of Bacterial Adhesion. Appl Environ Microbiol. 1983;46(1):90-7.

47. Shi X, Polycarpou AA. Adhesive transition from noncontacting to contacting elastic spheres: extension of the Maugis–Dugdale model. Journal of Colloid and Interface Science. 2005;281(2):449-57.

48. Lin Y-Y, Chang C-F, Lee W-T. Effects of thickness on the largely-deformed JKR (Johnson–Kendall–Roberts) test of soft elastic layers. International Journal of Solids and Structures. 2008;45(7–8):2220-32.

49. Xu D, Liechti KM, Ravi-Chandar K. On the modified Tabor parameter for the JKR–DMT transition in the presence of a liquid meniscus. Journal of Colloid and Interface Science. 2007;315(2):772-85.

50. Woerdeman DL, Amouroux N, Ponsinet V, Jandeau G, Hervet H, Léger L. Characterization of glass–epoxy adhesion using JKR methods and atomic force microscopy. Composites Part A: Applied Science and Manufacturing. 1999;30(1):95-109.

51. Prokopovich P, Perni S. Multiasperity Contact Adhesion Model for Universal Asperity Height and Radius of Curvature Distributions. Langmuir. 2010;26(22):17028-36.

52. Zheng Z, Yu J. Using the Dugdale approximation to match a specific interaction in the adhesive contact of elastic objects. Journal of Colloid and Interface Science. 2007;310(1):27-34.

53. Grierson DS, Liu J, Carpick RW, Turner KT. Adhesion of nanoscale asperities with power-law profiles. Journal of the Mechanics and Physics of Solids. 2013;61(2):597-610.

54. Bendersky M, Davis JM. DLVO interaction of colloidal particles with topographically and chemically heterogeneous surfaces. Journal of Colloid and Interface Science. 2011;353(1):87-97.

55. Carbone G, Bottiglione F. Asperity contact theories: Do they predict linearity between contact area and load? Journal of the Mechanics and Physics of Solids. 2008;56(8):2555-72.

Chapter 3 - Atomic Force Microcopy (AFM) and AFM related methodologies

3.1 Introduction

The Atomic Force Microscope (AFM) was initially developed to overcome the problems associated with Scanning Electron Microscopes, whereby samples must be conducting or semiconducting in order to be imaged. Inherently, some samples, such as biological samples must be coated in carbon or gold which could damage the integrity of the sample itself.

Yet, AFM is a very powerful technique, allowing samples to be imaged *in situ* in physiological conditions (1, 2), and it is also used quantitatively to study cell elasticity and molecular interaction forces (3). It can also be used to image the topography of materials in their native environments, giving significant information about surface features with unprecedented clarity (4). One aspect which enables this microscope to effectively produce accurate representations of the topography is the ability for three-dimensional mapping of the surface (2, 4). AFM creates images by scanning a microscale cantilever with a sharp tip across its surface, in a non-destructive manner; and can be performed on bulk samples to reveal nanoscale topographical information about fragile materials and molecules, without the need for complex sample preparation (5). Figure 3-1 is a simplified schematic adapted from the diagram produced by Last et al (2010) (1) and Braga and Ricci (2004) (4), illustrating the components needed for the AFM.

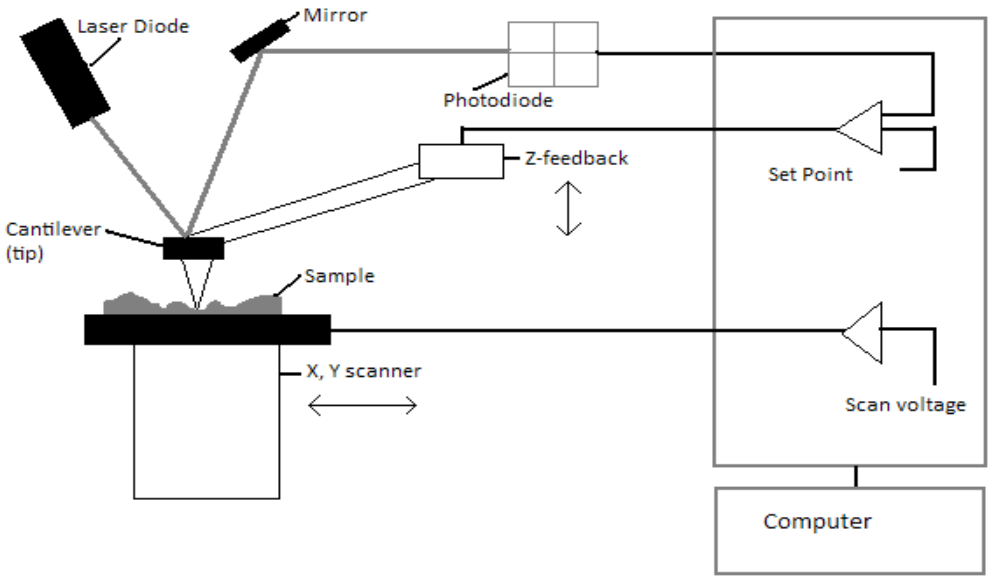

Figure 3-1. Schematic diagram of the operation of the AFM, illustrating the components required to obtain an image; a cantilever is scanned over the sample surface; and a laser beam is deflected off the back of the cantilever, monitored using a photodiode detector.

The tip is the heart of the instrument (4), giving rise to the image through force interactions; it's mounted to the end of the cantilever. Essential parameters of the tip are governed by the sharpness of the apex, the radius of curvature, and the aspect ratio of the whole tip (4), which are depicted in Figure 3-2. The images of the AFM are formed by the interaction forces that are recorded between the tip and the sample; and a feedback loop is essential for the accuracy of the images produced. Principally, the AFM utilizes the tip to raster scan across a surface in a horizontal pattern and back, controlled by the AFM electronics, the scanner then steps in a perpendicular direction (4), scans the second line horizontally and back; it continues in this manner until a topographic

image is formed containing the pre-selected number of scan lines. An image is achieved from these vertical movements (6) and in turn controls the signals sent by the feedback circuit to the scanner to move it up or down depending on the morphology of the sample and maintains the interaction forces applied.

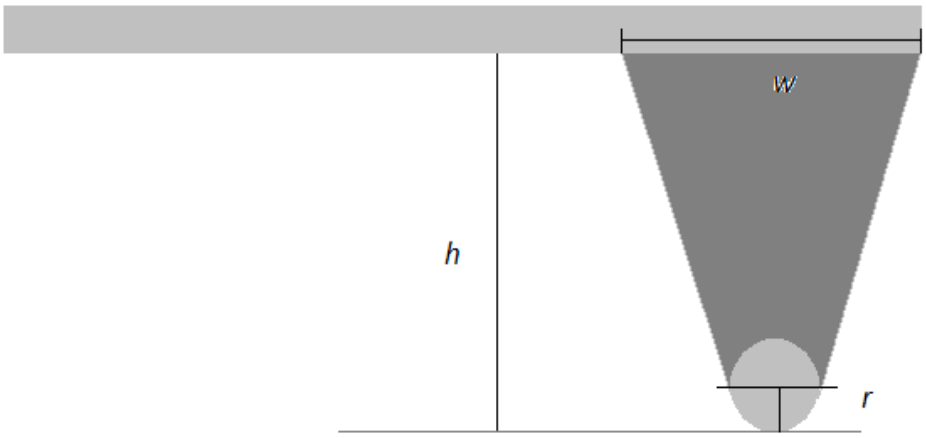

Figure 3-2. Scheme of the three essential parameters of the tip: r, the radius of curvature; the aspect ratio h, height to w, width of the tip.

Normally, the AFM cantilever has three modes of operation; contact, non-contact, and tapping mode. Jalili and Laxminarayana (2004) (7) point out that in order to probe electric, magnetic, and/or atomic forces of a selected sample; the non-contact mode is utilized by moving the cantilever away from the sample surface and oscillating the cantilever at/near its natural resonance frequency. Contact mode monitors the interaction forces while the cantilever tip is in contact with the sample. Tapping mode combines qualities of both contact and non-contact modes by gleaning sample data and oscillating the cantilever tip at/near its natural resonance frequency while allowing the cantilever tip to

impact the target sample for a minimal amount of time (7). Figure 3-3 illustrates an idealised plot of the relationship of the forces between the tip and sample, and also highlights the three common modes of operation, as modified from Braga and Ricci (2004) (4); and Jalili and Laxminarayana (2004) (7).

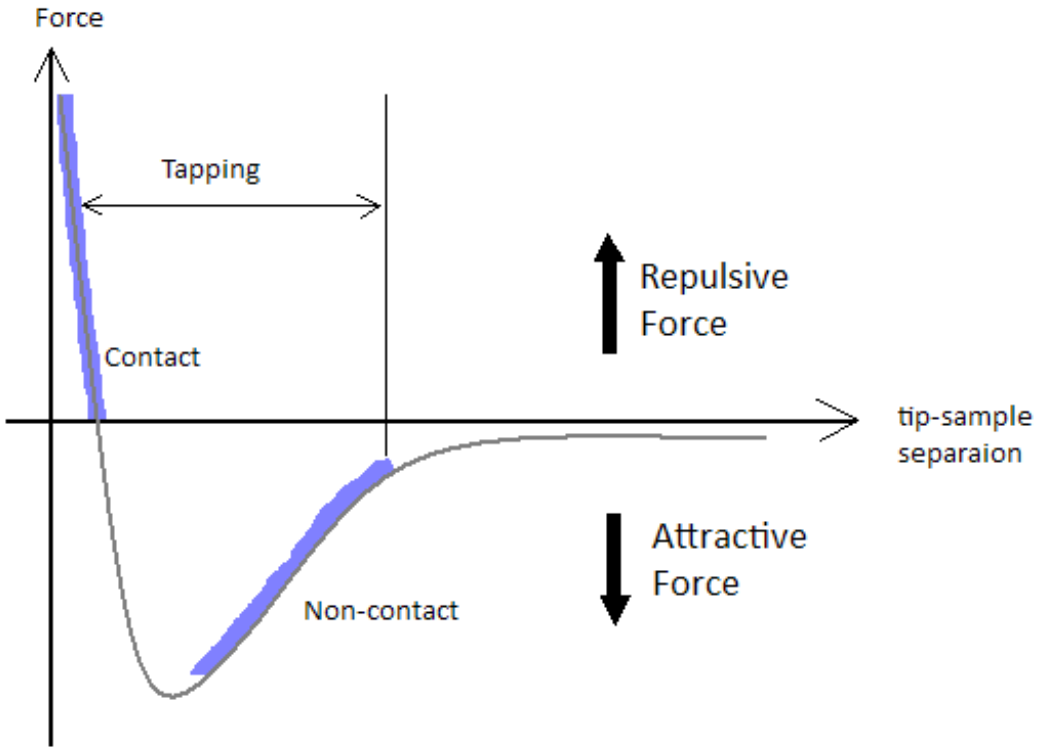

Figure 3-3. Simple profile of the force separation plot, highlighting in blue the different modes of operation of an AFM (Contact, Non-contact and Tapping), indicating the forces of attraction of each.

The reality and quality of AFM images depends greatly on operation, tip state, hardness of the sample surface, including the roughness and height (2, 8). In some cases, images that look perfect may be distorted, which could have been

influenced by the state of the tip, and any flattening or contamination of the tips must be avoided in order to obtain real images of the sample surfaces (8).

3.2 Equipment

The AFM used for the following experiments is the commercially available XE-100 Advanced Scanning Probe Microscope (Park Systems, Korea), in contact mode, using a tip manufactured by NT-MDT, a CSG30 tip with a Gold coating, tip height of 14 µm, curvature of radius of 10nm with a spring constant of 0.6 N/m and sensitivity of 37.388 V/µm; resonant frequency of 48kHz.

3.3 Calibration

The data obtained using AFM are z-piezo displacement (nm) and the tip deflection (mV), therefore, a calibration procedure is essential to maintain the integrity of the information gained from the tip to sample images. A simple equation:

$$F = kx \tag{3-1}$$

Describes the normal force applied by the tip to a sample according to Hooke's law. Whereby, F is the force at the tip (N); k the normal spring constant of the cantilever (Nm^{-1}), and *x* being the deflection of the cantilever along the direction of F at the tip (m); furthermore the deflection is the product of the measured voltage and the device sensitivity (mV^{-1}). Given these parameters enables accuracy in applying the normal force through calculating the exact spring constant as well as the sensitivity of the photodiode, as shown in Figure 3-4.

This is to accurately convert the voltage measurements given by the reflection of the laser beam from the cantilever on the AFM photodiode into the corresponding vertical deflection of the probe at the tip position. Hence, two consecutive calibrations are required.

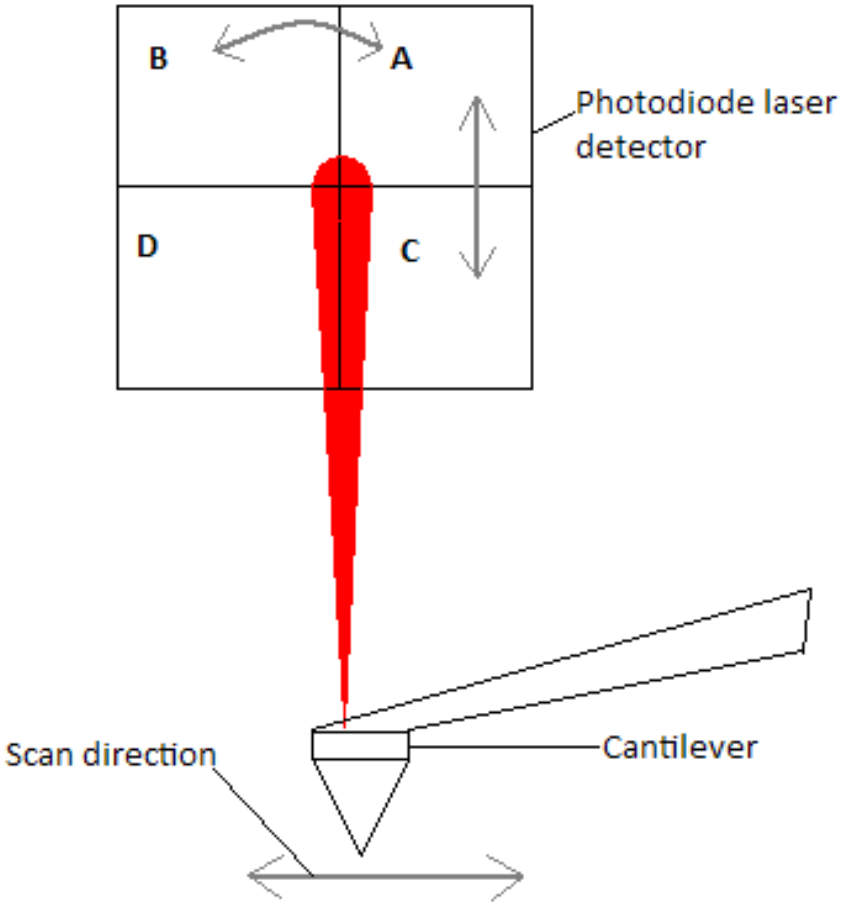

Figure 3-4. Effects of the lateral forces that affect the cantilever due to frictional characteristics on the surface of the ample by illustrating the change in movement of the photodiode laser detector.

The calculation used to determine the spring constant for a given cantilever depend on its shape i.e. whether the tip is V-shaped or rectangular. Sader method is employed for rectangular cantilevers; and the Neumeister and Ducker method is utilised for V-shaped cantilevers. The Sader method is a 2 step process; when using the Sader method, the following parameters are required to obtain the spring constant k for the first step: width, length and quality factor (this is obtained by vibrating the cantilever); these parameters are then used along with the Sader equation [3-2]:

$$K = 7.5246\rho b^2 L Q \gamma i(Re) f^2 \qquad (3\text{-}2)$$

Where:

K = spring constant (N/m)

ρ = fluid density (kg/m^3)

b = width of the cantilever (µm)

L = length of the cantilever (µm)

Q = quality factor characterises the stability of an oscillator, usually calculated by dividing the resonance frequency by its resonance width (9); and generally the higher the frequency and smaller the resonance width gives a large Q which governs the resolution measurements (determined using the AFM software).

γi(Re) = imaginary component of hydrodynamic function which accounts for the loading on the vibrating cantilever by taking into consideration the effects of fluid surroundings and using the Q factor and natural frequency to determine the stiffness (10) (this can effect imaging and the sensitivity of the AFM).

f = resonant frequency (kHz)

Using the calculated spring constant in the calibration mode of the AFM software allows for the sensitivity of the cantilever to be determined by utilising the Force-Distance Spectroscopy function to obtain a force-distance curve. This technique consists of lowering the tip to contact the surface (usually a silicon wafer), then the Z scanner moves down; the cantilever will deflect while the tip remains static to the hard surface. Therefore the reflection of the laser beam from the cantilever onto the photodiode gives an output voltage which is a function of the vertical distance moved by the Z scanner. Hence, the sensitivity of the photodiode is defined by the slope of the force-distance curve. This knowledge allows for accurate measurements of the displacement of the probe at the tip position.

3.4 Surface topography analysis

Surface coordinates of the tested materials were obtained using AFM in contact mode. For all the sample types, the scan was performed on an area size of 40 x 40 μm, at scan velocity of 40 μm/s and at scan frequency equal to 1.0 Hz. Asperities were located using an in-house written FORTRAN code under the following condition: a point on the surface is an asperity if the 8 bordering points (in x and y directions) are lower and the z- coordinates bordering further away from the initial x,y point are lower (Figure 3-5), mathematically expressed as:

$$z(i,j) \in asperities \Leftrightarrow z(i,j) > z(m,n)$$
$$\text{with} \quad m = i-2, i-1, i, i+1, i+2 \quad n = j-2, j-1, j, j+1, j+2 \quad and \quad m,n \neq i,j$$

Once an asperity had been located, its height was determined against a reference plane based on the average of all coordinates. The asperity density was determined calculating the number of asperities observed in the scanned area.

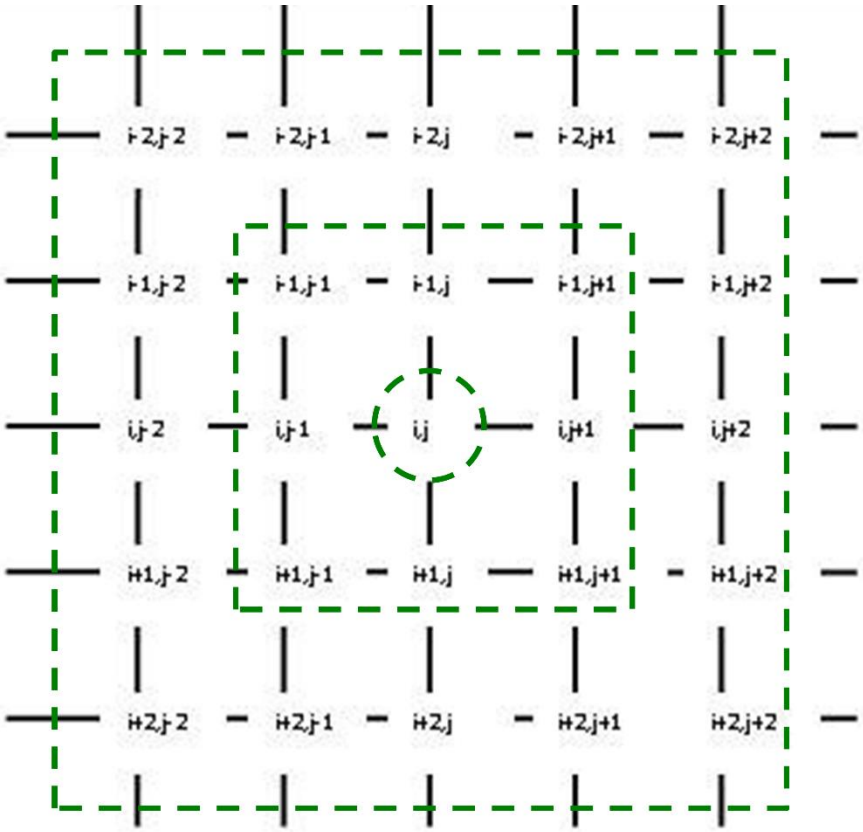

Figure 3-5. Representation of the process used to identify asperities on surfaces.

The asperity curvature radius in the x direction (*Rx*) was determined fitting the coordinates of the five points bordering the asperity, along the x axis, with a parabola (Figure 3-6) and using the following equation:

$$R_{x,i} = \frac{\left[1+\left(\frac{\partial z}{\partial x}\right)^2\right]^{3/2}}{\frac{\partial^2 z}{\partial x^2}}$$

(3-3)

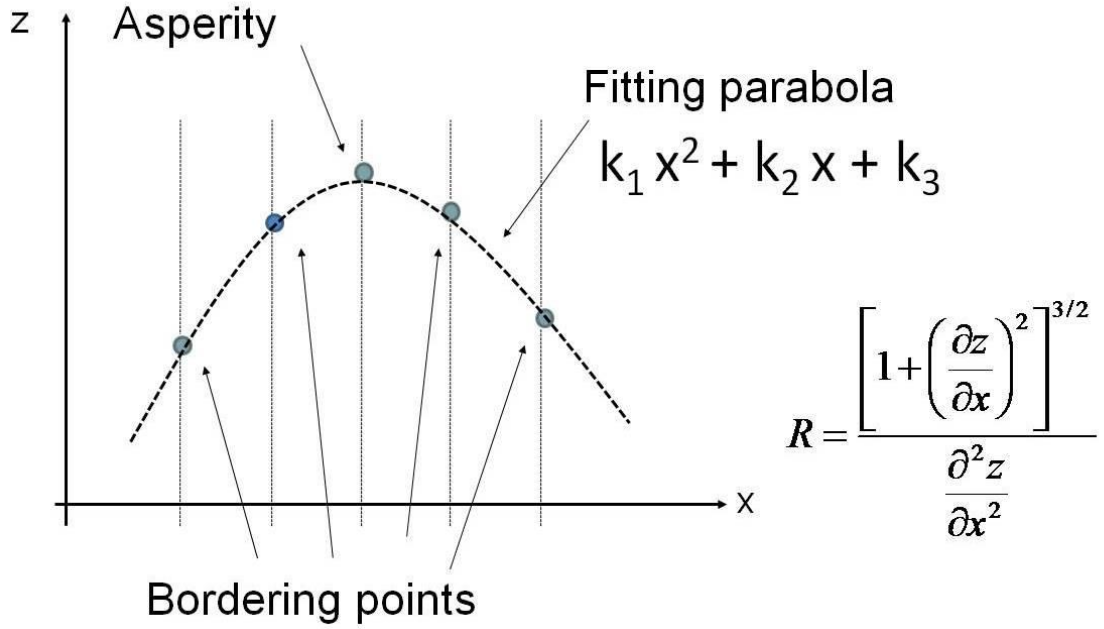

Figure 3-6. Schematic description of the process used to determine the radius of curvature of each asperity.

In the same way, for the radius of curvature in the y direction (*Ry*), the bordering points on the y axis were used.

Asperity heights and radii of curvature (*Rx* and *Ry*) cumulative distributions were estimated and fitted with the Gaussian model (Eq. (3-4).

$$\Phi(R) = \frac{1}{\sigma\sqrt{2\pi}} \int_{-\infty}^{R} \exp\left(-\frac{(\mu-\xi)^2}{2\sigma^2}\right) d\xi \qquad (3\text{-}4)$$

3.5 Surface forces mapping analysis

All adhesive force measurements were conducted in an open liquid cell made of polychlorofluoroethylene, PCTFE (Park Systems, Korea) which is a homopolymer with high compressive strength and low deformation under load, using phosphate buffer solution (PBS) as the aqueous environment. A rectangular silicone cantilever with a borosilicate colloid sphere, 20 µm in diameter, attached (Novoscan, USA) was used with a spring constant 14 N/m calibrated using Craig and Neto's in situ calibration of colloidal probe cantilevers (9, 11, 12), with Au surface (no reflex). The calibration method uses the force-distance function of the AFM and simply uses the gradient of the force curve to determine the spring constant (*k)* using the following equation [3-5]:

$$K = 6\pi\eta b^2 m \qquad (3\text{-}5)$$

Where:

k = the spring constant (N/m)

η = viscosity of the solution (mPa s)

b = radius of the sphere (µm) as stated by the manufacturers

m = slope of the line

In order to gain comprehensive data for the adhesive interactions of the given samples, the surface mapping feature of the AFM was employed. Using a 40 x 40 µm scan size, the mapping function was selected in force-distance

spectroscopy mode, enabling the repetition of measurements; this case is demonstrated in Figure 3-7.

.

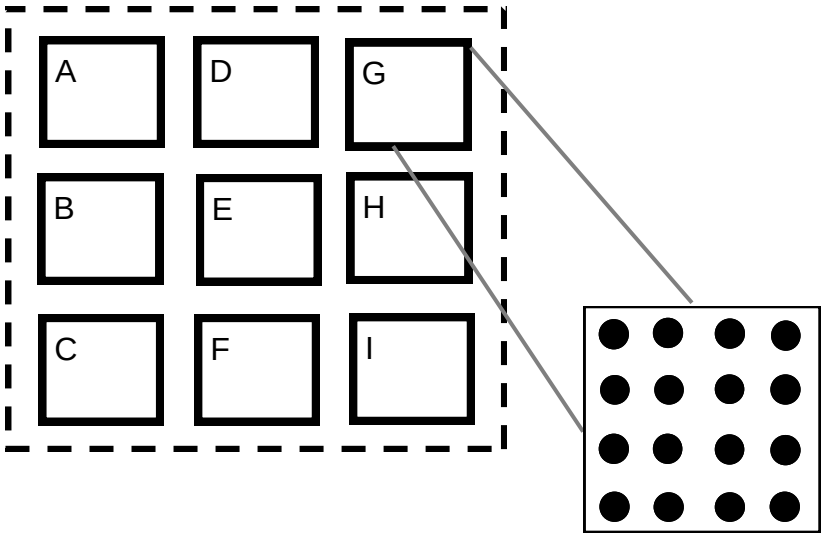

Figure 3-7. Mapping function of the AFM depicted to determine the surface forces.

The larger image, (dotted outline) containing 9 smaller boxes with letters, represents an area (40 x40 µm) on the surface of the UHMWPE; inside of which are smaller (bold lines) boxes containing letters, A-I, these demonstrate the mapping function available on the AFM. From each of these 9 boxes, 16 adhesive force measurements are applied to one box at a time, these 16 points are shown to the right of the area (dotted line square). This type of mapping allows the user to gain 144 force curves per area (dotted line square) of UHMWPE, and as three areas from the three different samples were measured

for all untreated and cold atmospheric pressure plasma (CAP) treated UHMWPE, then a total of 1296 force curves were analysed for this work.

3.6 References

1. Last JA, Russell P, Nealey PF, Murphy CJ. The Applications of Atomic Force Microscopy to Vision Science. Investigative Ophthalmology & Visual Science. 2010;51(12):6083-94.

2. Alonso JL, Goldmann WH. Feeling the forces: atomic force microscopy in cell biology. Life Sciences. 2003;72(23):2553-60.

3. Zhang YQ, Ren SX, Li HL, Wang YX, Fu G, Yang J, et al. Genome-based analysis of virulence genes in a non-biofilm-forming Staphylococcus epidermidis strain (ATCC 12228). Mol Microbiol. 2003;49(6):1577-93.

4. Braga PC, Ricci D. Atomic Force Microscopy: Biomedical Methods and Applications. Braga PC, Ricci D, editors. Totowa, New Jersey: Humana Press; 2004 2004. 394 p.

5. Tilley JMR, Carr AJ, Czernuszka JT. Atomic Force Microscopy of bulk tendon samples: Affect of location and fixation on tissue ultrastructure. Micron. 2011;42(5):531-5.

6. Fotiadis D, Scheuring S, Müller SA, Engel A, Müller DJ. Imaging and manipulation of biological structures with the AFM. Micron. 2002;33(4):385-97.

7. Jalili N, Laxminarayana K. A review of atomic force microscopy imaging systems: application to molecular metrology and biological sciences. Mechatronics. 2004;14(8):907-45.

8. Li LX, Liu RP, Xu Z, Xu Y, Wang WK, Fan CZ. Distorted surface topography observed by atomic force microscopy. Measurement. 2006(39):12-5.

9. Sader JE, Larson I, Mulvaney P, White LR. Method for the calibration of atomic force microscope cantilevers. Review of Scientific Instruments. 1995;66(7):3789-98.

10. Frentrup H. Uncertainty Quantication in Calibration of AFM Probes Due to Non-uniform Cantilevers. Department of Engineering Physics - College of Engineering. 2010 11/21/.

11. Sader JE, Sanelli JA, Adamson BD, Monty JP, Wei X, Crawford SA, et al. Spring constant calibration of atomic force microscope cantilevers of arbitrary shape. Review of Scientific Instruments. 2012;83(10):103705--16.

12. Craig VSJ, Neto C. In Situ Calibration of Colloid Probe Cantilevers in Force Microscopy: Hydrodynamic Drag on a Sphere Approaching a Wall. Langmuir. 2001;17(19):6018-22.

1. Last JA, Russell P, Nealey PF, Murphy CJ. The Applications of Atomic Force Microscopy to Vision Science. Investigative Ophthalmology & Visual Science. 2010;51(12):6083-94.

2. Alonso JL, Goldmann WH. Feeling the forces: atomic force microscopy in cell biology. Life Sciences. 2003;72(23):2553-60.

3. Zhang YQ, Ren SX, Li HL, Wang YX, Fu G, Yang J, et al. Genome-based analysis of virulence genes in a non-biofilm-forming Staphylococcus epidermidis strain (ATCC 12228). Mol Microbiol. 2003;49(6):1577-93.

4. Braga PC, Ricci D. Atomic Force Microscopy: Biomedical Methods and Applications. Braga PC, Ricci D, editors. Totowa, New Jersey: Humana Press; 2004 2004. 394 p.

5. Tilley JMR, Carr AJ, Czernuszka JT. Atomic Force Microscopy of bulk tendon samples: Affect of location and fixation on tissue ultrastructure. Micron. 2011;42(5):531-5.

6. Fotiadis D, Scheuring S, Müller SA, Engel A, Müller DJ. Imaging and manipulation of biological structures with the AFM. Micron. 2002;33(4):385-97.

7. Jalili N, Laxminarayana K. A review of atomic force microscopy imaging systems: application to molecular metrology and biological sciences. Mechatronics. 2004;14(8):907-45.

8. Li LX, Liu RP, Xu Z, Xu Y, Wang WK, Fan CZ. Distorted surface topography observed by atomic force microscopy. Measurement. 2006(39):12-5.

9. Sader JE, Larson I, Mulvaney P, White LR. Method for the calibration of atomic force microscope cantilevers. Review of Scientific Instruments. 1995;66(7):3789-98.

10. Frentrup H. Uncertainty Quantication in Calibration of AFM Probes Due to Non-uniform Cantilevers. Department of Engineering Physics - College of Engineering. 2010 11/21/.

11. Sader JE, Sanelli JA, Adamson BD, Monty JP, Wei X, Crawford SA, et al. Spring constant calibration of atomic force microscope cantilevers of arbitrary shape. Review of Scientific Instruments. 2012;83(10):103705--16.

12. Craig VSJ, Neto C. In Situ Calibration of Colloid Probe Cantilevers in Force Microscopy: Hydrodynamic Drag on a Sphere Approaching a Wall. Langmuir. 2001;17(19):6018-22.

Chapter 4 - Adhesive Forces and Surface Properties of Cold Gas Plasma Treated UHMWPE

The content of this chapter has been published in:

E. Callard Preedy, E. Brousseau, S. Evans, S. Perni, P. Prokopovich “Adhesive Forces and Surface Properties of Cold Gas Plasma Treated UHMWPE” *Coll. Surfaces A* 2014;460:83-89

4.1 Abstract

Total joint replacement (TJR) has become common practice for osteoarthritis sufferers. Many materials from ceramics, metals and alloys, to polymers have been used based on certain desirable properties which include: low friction coefficient; resistance to bearing damage and wear; generates small amounts of wear debris and biocompatibility to reduce adverse cellular responses; it is also beneficial for the surface to have decreased hydrophobicity, as this allows for ease of osseointegration, and increased adhesive properties associated with asperities on the material to allow extracellular materials to effectively attach minimising rejection. Cold atmospheric pressure plasma (CAP) treatment was used on ultra-high molecular weight polyethylene (UHMWPE), a common articulating counter material employed in hip and knee replacements. UHMWPE is a biocompatible polymer with low friction coefficient, yet does not have robust wear characteristics. CAP effectively cross-links the polymer chains of the UHMWPE improving wear performance (Perni et al, 2012) (1).

In this work, interactions between CAP treated UHMWPE and spherical borosilicate sphere (representing model material for bone) is considered employing AFM technique. CAP increased the adhesive forces in the presence of phosphate buffer solution (PBS), after treatment with Helium and Helium/Oxygen cold gas plasmas. Furthermore, a more hydrophilic surface of UHMWPE was observed after both treatments, determined through a reduction of up to a third in the contact angles of water. On the other hand, the asperity density also decreased by half, yet the asperity height had a three-fold decrease. This work shows that CAP treatment can be a very effective

technique at enhancing the adhesion between bone and UHMWPE implant material as aided by the increased adhesion forces. Moreover, the hydrophilicity of the CAP treated UHMWPE can lead to proteins and cells adhesion to the surface of the implant stimulating osseointegration process.

4.2 Introduction

Osteoarthritis is also known as “degenerative joint disease” and occurs as a result of loss in articular cartilage which lines the bone of synovial joints (2). Articular cartilage minimises stress on subchondral bone and provides low friction surfaces (3, 4) playing an essential role at these lubricating junctions. Furthermore, it is a resilient tissue, demonstrating features of durability (4) through compression and shear. However, once the cartilage fractures, it has limited or no ability to heal. These injures are often caused by mechanical twisting and direct impact/loading, including: direct injury to the articular cartilage (e.g. osteochondral fractures); abnormal mechanical stress on the joint (e.g. in poor joint alignment) and impaired subchondral bone support and blood supply (e.g. avascular necrosis). These events can alter the composition, along with the structure, and mechanical properties of the cartilage impairing its ability to perform the required functions (4, 5).

In many cases if the medical management i.e. drug intervention of the joints has failed then many patients are recommended for total joint arthroplasty (TJA) (6). It is well accepted, since its development in the 1960s (7), that total hip and total knee replacement surgery is a reliable method to relieve pain and return lower limb function, generally to improve the quality of life for the patient. Ultra

high molecular weight polyethylene (UHMWPE) has been commonly used for over four decades (8, 9) as an articulating counter surface for TJA. For example, UHMWPE is used in spine disk replacement (10) and as a concave bearing material in the acetabular cup in the hip and as the tibial tray in the knee; with the opposite bearing surface traditionally made of hard but very smooth ceramic (Alumina, Zirconia, hydroxyapatite/calcium phosphate) or metal (stainless steel, Titanium and alloys, Cobalt and alloy materials. Other polymers (polyethylene, polypropylene, polyurethane, poly-methyl methacrylate) (11) in combination with metal/alloys (Nickel-Titanium; Cobalt-Chromium) are also used as they have good mechanical and surface properties when employed together (12). However, the true success of UHMWPE lies in the fact that it is biocompatible (12), with good low friction properties, chemical inertness, high impact strength and sufficient mechanical performance (1, 13, 14).

Regardless of the hype associated with UHMWPE, it does not display robust wear performance on dynamic load (15) as the energy builds up and accumulates forming cracks (15); therefore decreases the longevity of the device for TJA (1). Research has suggested that some wear particles, of polyethylene in particular, are the result of the sterilisation treatment pre-surgery which introduces free radicals (1, 16) and is often achieved through gamma radiation (15). Certain techniques have already been used as an attempt at improving the wear performance of UHMWPE, for example: gamma or electron beam irradiation with thermal stabilisation (1, 17); ion bombardement (18); proton radiation (14); argon plasma surface modification (19) and addition of Vitamin E to the polymer (20). Irradiation of the polymer was introduced to

overcome the initial problem of fragility; gamma radiation effectively produced free carbon radicals on the backbone chain of the polymer which caused cross-linking (desirable) chain scission, and oxidation (undesirable) of the polymer (15, 16). Cross-linking increases the wear resistance, abrasion resistance, and even improve the thermal stability (14, 15); on the other hand oxidation has a negative effect by decreasing the properties listed as well as lowering the molecular weight and chain length governing the fragility (15).

Surface processing with gas plasma effectively alters the surface chemistry of the material by the bombardment of ions, electrons UV radiation and other chemically reactive species (radicals) present in the plasma plume (1). Developments in gas plasma technology allow generating gas plasmas at room temperature without the need for vacuum, these have been called “cold atmospheric pressure plasmas” (CAP) (1, 21); this is a cheaper alternative than other plasma techniques as it is performed in air and without a vacuum chamber; it also aids as a sterilising technique. Cold gas plasma technology has been successfully employed to enhance the wear performance of UHMWPE (1); untreated UHMWPE had a wear factor of 2.7×10^{-7} mm^3 N^{-1} m^{-1}, yet after just 7 minutes of treatment with the plasma, it had a wear factor of almost half the untreated material at 1.4×10^{-7} mm^3 N^{-1} m^{-1}; further benefits were also seen after XRD diffraction patterns demonstrated that the treatments did not affect the crystallinity of the UHMWPE, therefore maintaining its integrity and in retaining cytocompatible properties of untreated UHMWPE (1). Although, treatment improved the wear performance of the UHMWPE, no evidence of the CAP on the adhesive properties outcome of the material has been studied

which inherently cause wear particles. On the other hand, adhesion plays an essential role when applied to osseointegration; which is the process of bone adhering to the implanted device to improve function and overall health of the patient (22). In this study therefore, these characteristics of the new materials (CAP modified UHMWPE) were investigated by delving further into the role of adhesive force interactions focusing on the comparison of the untreated and CAP treated UHMWPE and by presenting comprehensive surface topography analysis along with adhesive force mapping, using atomic force microscopy (AFM); the impact of the treatment on the UHMWPE properties was also characterised by contact angle measurements and surface energy parameters determination.

4.3 Materials and Methods

4.3.1 Polymers

Selections of UHMWPE (GUR 1020, Hoechst, Germany) were employed in this study.

4.3.2 Cold gas plasma treatment

The CAP device was made of two electrodes: a capillary powered electrode, situated within a quartz tube of 1.5 mm inner diameter; and a downstream ring electrode, this is wrapped around the outside of the quartz tube near a nozzle. This set up (Figure 4-1) allows for the axial separation of the electrodes producing an axially directed electrical field upon an external voltage (1). Using CAP generated in Helium and Helium with varying amounts of Oxygen, were able to demonstrate an effective and beneficial method of treating UHMWPE.

The flow of gas was achieved by applying 5 slm (standard litre per minute) of 99.99% Helium and 10 sccm (standard cubic centimetre per minute) of Oxygen were combined before passing through the capillary electrode i.e. doubling as the gas inlet (1). Power was supplied by an alternative current (A.C.) supply with a peak voltage of 8 kV and an excitation frequency of 20 kHz (1). Due to the alignment of the electrodes and hence the electrical field, then the gas flow is also in an axial direction and is sometimes known as linear field devices (1, 23, 24). The resulting applied voltage governs the breakdown of the gas (Helium/Oxygen mixture) to produce an electrical discharge inside the quartz tube, which appears as a light emitting plume or plasma jet from the quartz (23).

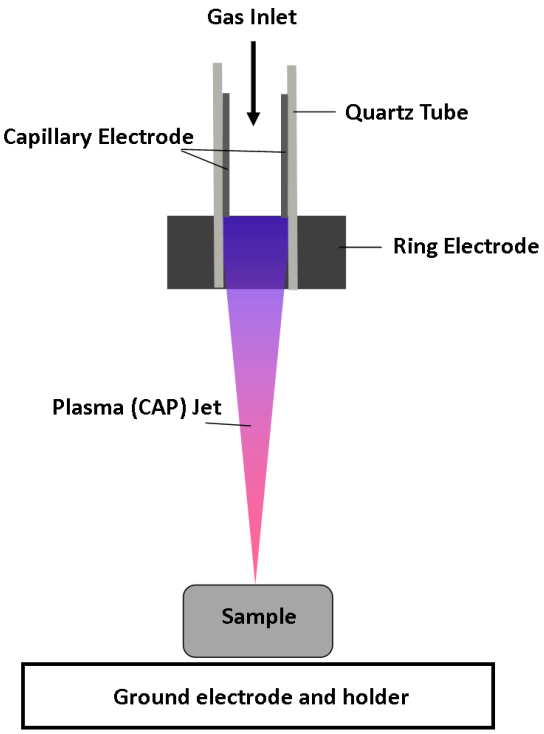

Figure 4-1. CAP equipment set up.

4.3.3 Surface analysis

Atomic Force Microscope (AFM) (XE-100 Advanced Scanning Probe Microscope (Park Systems, Korea) was used for surface topography analysis, as well as for adhesion force measurements.

4.3.3.1 Topography

In order to image all three samples (untreated UHMWPE, Treated UHMWPE-Helium, Helium and Oxygen mix), a contact rectangular tip, CSG30 (NT-MDT, Russia), with reflective Au side, was used with a spring constant of 3.3 N/m, a tip height of 14µm and a tip curvature of radius of 10nm. This probe was calibrated using the Sader method (25).

The scan parameters used were as follows: Scan size of 40x40 µm; resolution at 1024x1024; Scan rate was maintained between 0.8-1.0 Hz and an applied load of 21.34 nN. Three independent samples for each of the material used were scanned and around 10 images for each sample were taken.

Asperities were located using an in-house written FORTRAN code under the following condition: a point on the surface is an asperity if the 8 bordering points (in x and y directions) are of lower height and the z- coordinates bordering these are further away as well as lower in height (26). Once located, the asperity height, density and the radius of curvature were determined using the in-house built FORTRAN code, as described in detail in other work (26).

4.3.3.2 Surface Energy

The surface energy components for each material were determined by contact angle measurements of water (θ_w), ethylene glycol (θ_{et}) and hexadecane (θ_h). A

drop of each liquid, 5µl, was gently placed onto the UHMWPE sample and imaged using a digital camera; 10 replicates were performed on each sample. The contact angle of both the right and left side of the liquid drop (Figure 4-2) were measured using ImageJ software (NIH, USA).

The mean values were used to calculate the surface energy parameters: Lifshitz-Van der Waals interactions (γ^{LW}), Lewis acid-base interactions γ^{AB}, the electron-acceptor (γ^{+}) and the electron-donor (γ^{-}) molecular interaction through the following equation [4-1]

$$\gamma_L(1-cos\theta) = 2\left(\sqrt{\gamma_S^{LW}\gamma_L^{LW}} + \sqrt{\gamma_S^{+}\gamma_L^{-}} + \sqrt{\gamma_S^{-}\gamma_L^{+}}\right) \quad (4\text{-}1)$$

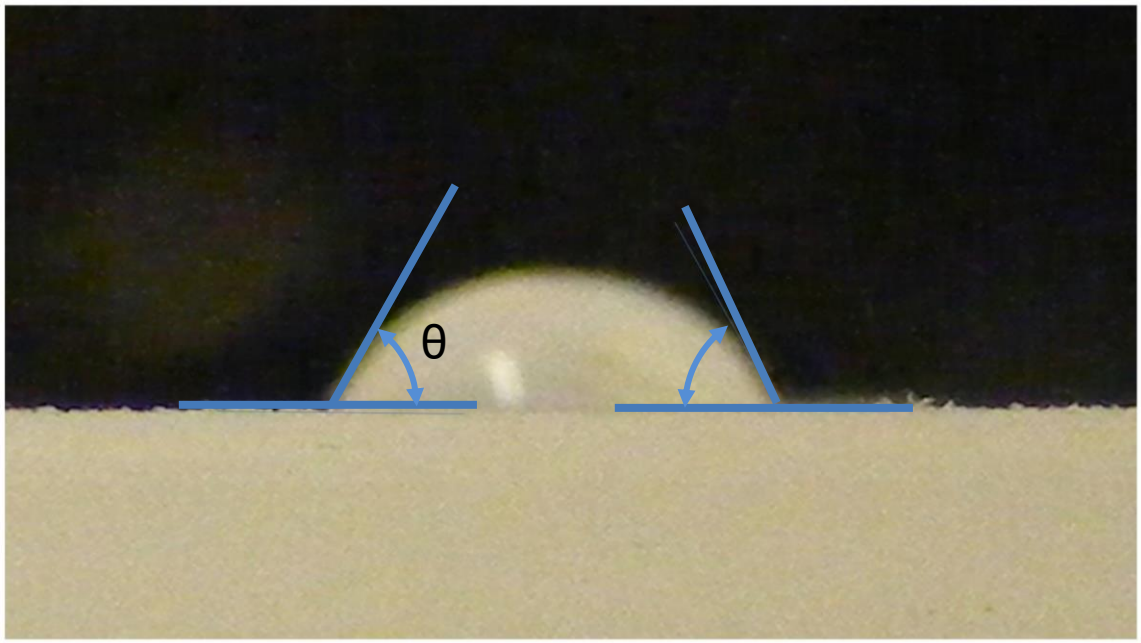

Figure 4-2. Image taken of a liquid drop used to determine the contact angle as well as the surface free energy of the UHMWPE samples.

4.3.3.3 Adhesive Force Measurements

All adhesive force measurements were conducted in an open liquid cell made of polychlorofluoroethylene, PCTFE (Park Systems, Korea) which is a homopolymer with high compressive strength and low deformation under load, using PBS as the aqueous environment. A rectangular silicone cantilever with a borosilicate colloid sphere, 20 µm in diameter, attached (Novoscan, USA) was used with a spring constant 14 N/m calibrated using Craig and Neto's in situ calibration of colloidal probe cantilevers (25, 27, 28), with Au surface (no reflex).

In order to gain comprehensive data for the adhesive interactions of the given samples, the surface mapping feature of the AFM was employed. Using a 40 x 40 µm scan size, 144 force curves were obtained on each UHMWPE samples, as three different samples were measured for each of untreated and CAP treated UHMWPE, a total of 1296 force curves were analysed for every material for this work.

4.3.4 Statistical analysis

The effect of the cold gas plasma treatment on the asperity heights distribution was investigated through the one-way ANOVA test followed by the Bonferroni *post hoc* test ($p < 0.05$). The difference on asperity curvature radii was analysed with Kruskal-Wallis test followed *post hoc* with a Dunn's test for individual pairs of data sets.

4.4 Results

4.4.1 Surface topography

Analysis of the 40 x40 µm scanned areas of both untreated and CAP treated UHMWPE Helium and Helium/Oxygen mixture (Figure 4-3) estimated that the average asperity density for untreated UHMWPE was 15.2 x 10^{10} asp/m^2 almost twice the value after CAP treatment of both Helium and the Helium and Oxygen mix samples, 9.3 x 10^{10} asp/m^2 and 6.7 x 10^{10} asp/m^2 respectively (Table 4-1).

Another parameter which attributes to the surface roughness of the samples is the asperity height, (µm) again it is clear from the results that a three-fold reduction of asperity height has occurred post-CAP treatment of the samples with no significant difference between the CAP-treated samples; as the untreated UHMWPE had an average asperity height of 652 nm yet the Helium treated UHMWPE had an average asperity height of 223 nm, while the Helium and Oxygen mixture treated samples average asperity height reduced to 180 nm. All samples of UHMWPE both treated and untreated had asperity heights normally distributed (Figure 4-4).

Table 4-1. Surface topography analysis data recovered from each of the three UHMWPE samples.

			X and Y direction Radius of curvature percentile		
UHMWPE Samples	Asperity density (Asp/m^2)	Average Asperity height (nm)	25th (μm)	50th (μm)	75th (μm)
untreated	15.2±0.3 E+10	652 ± 25	1.55 ± 0.11	2.33 ± 0.05	3.66 ± 0.05
He	9.3 ± 1.1 E+10	223 ± 47	0.64 ± 0.26	1.12 ± 0.13	2.37 ± 0.84
He/O_2	6.7 ± 0.9 E+10	180 ± 53	1.13 ± 0.42	2.46 ± 0.54	3.49 ± 0.76

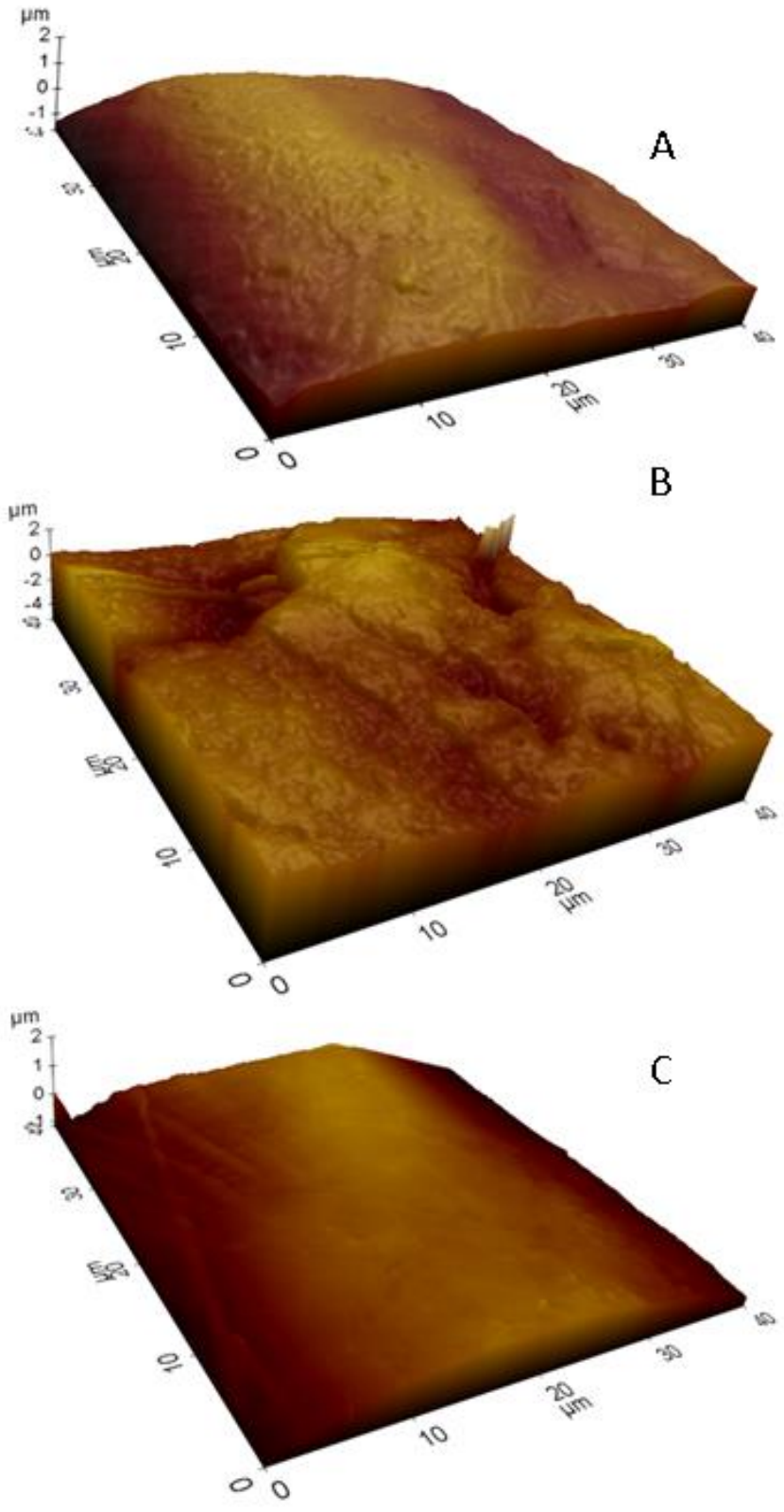

Figure 4-3. AFM 3D images of UHMWPE pre- (a) and post-CAP treatment with Helium (b) and Helium Oxygen mix (c).

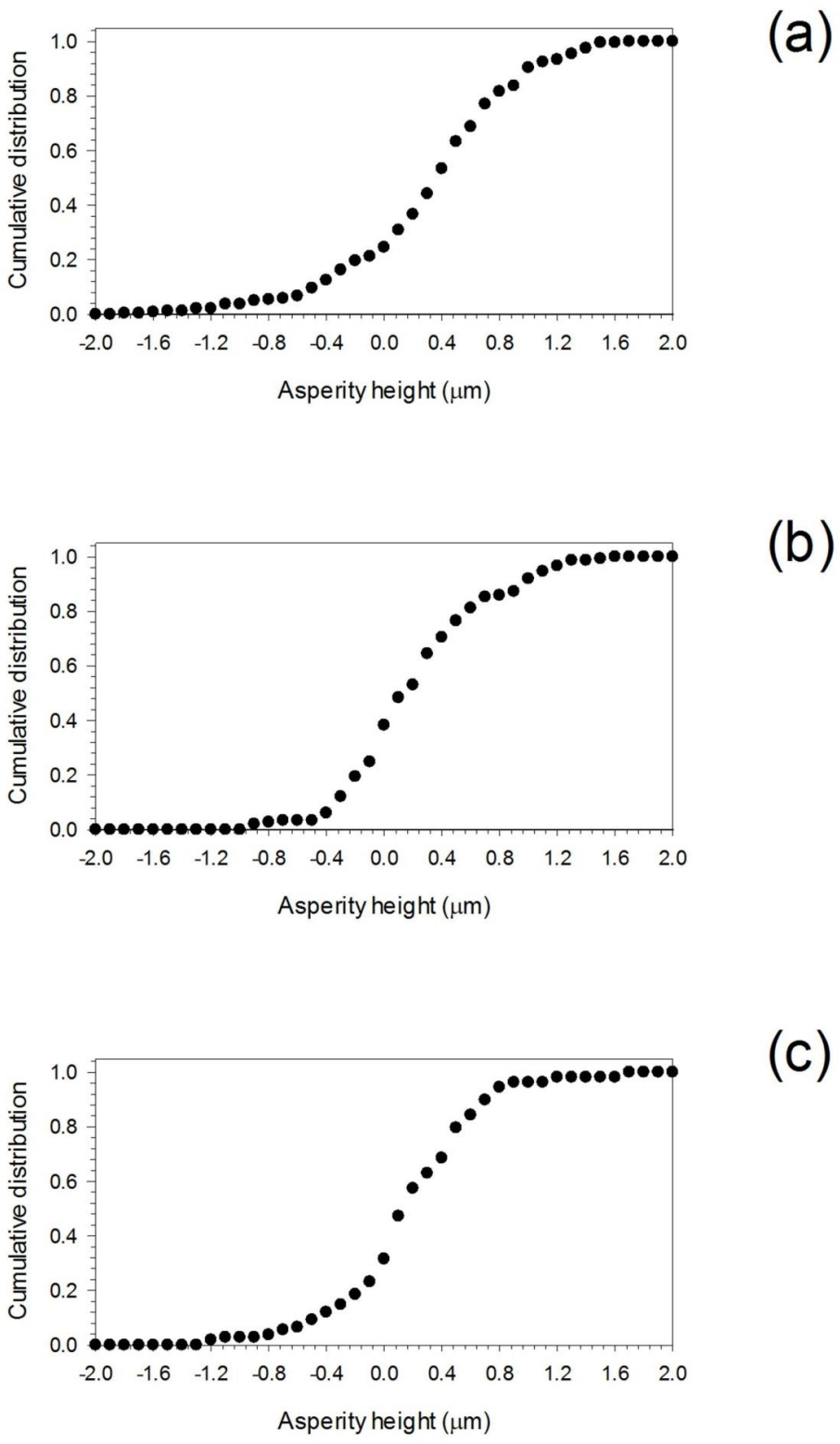

Figure 4-4. Cumulative frequency distribution data of the asperity heights, before CAP treatment (a) post-CAP treatment with Helium (b) and Helium Oxygen mix (c).

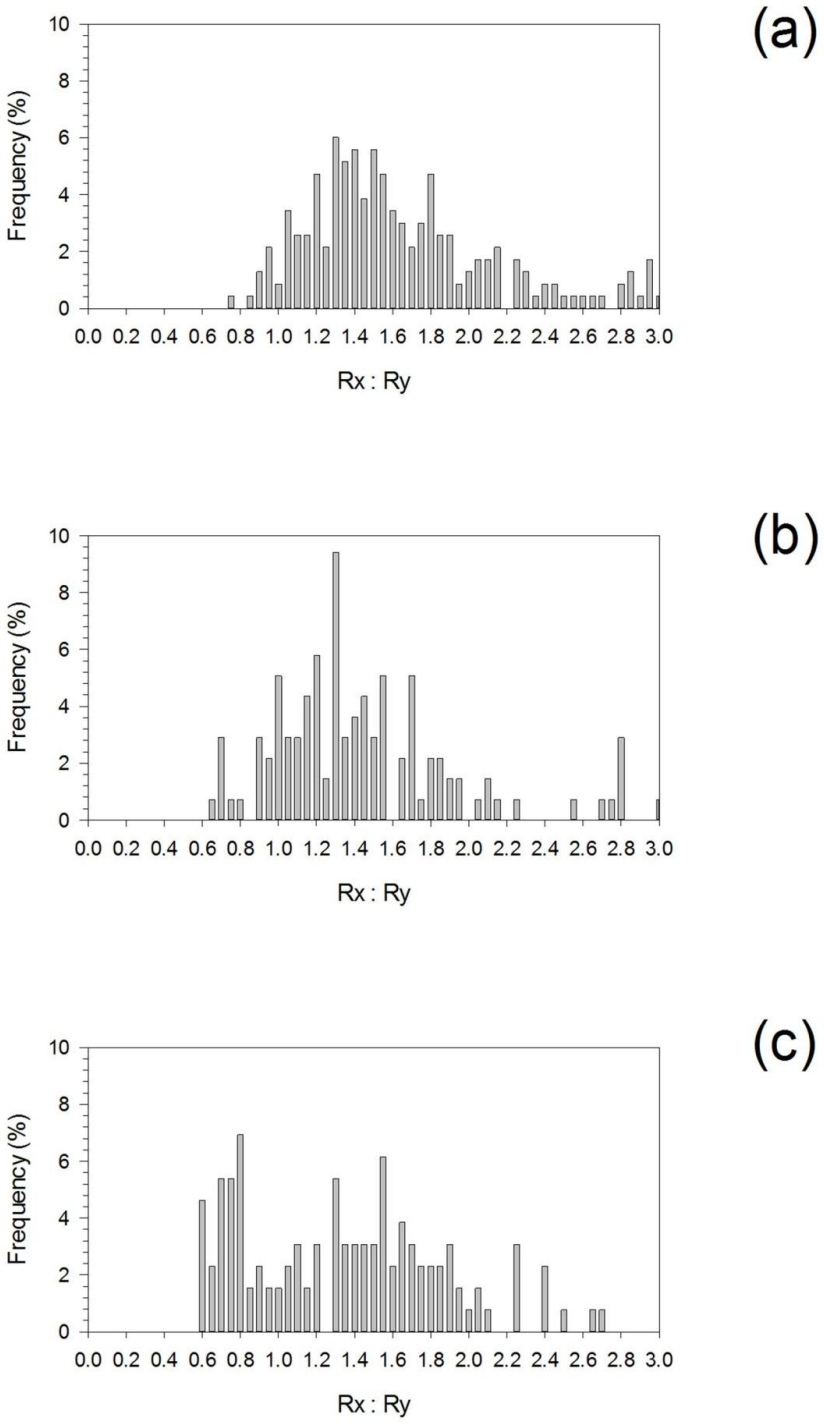

Figure 4-5. Distribution for the curvature of radii for the hemispherical theory based on the ratio of the curvature in the x and y direction (Rx/Ry) for all samples of UHMWPE: Untreated (a); Helium Treated (b) and Helium Oxygen mix treated (c).

A further surface topographical aspect which has been investigated was the radii of curvature of asperities. The distribution of the ratios of the asperity radii in the x and y directions (Rx to Ry) were investigated to determine the hemisphericity of the asperities. On comparison with the untreated UHMWPE (Figure 4-5) the curvature of radii ratio (Rx:Ry) demonstrated a hemispherical shape as the higher frequency of the distribution is at ratios of about 1; similarly this is also the case for Helium and Helium/Oxygen CAP treated UHMWPE. When considering the percentile results, it emerged that in all cases the curvature radii were not normally distributed. Moreover, the He/O_2 cold gas plasma treatment did not present a statistical difference compared to untreated samples, whereas the He cold gas plasma caused a reduction of the curvature asperity radii.

4.4.2 Contact Angles and Surface Energy

All surface energy parameters, including the contact angles measured for each liquid used, are given in Table 4-2. The contact angle measurements display great changes as there is a decrease in contact angle for both CAP treated samples compared to the untreated UHMWPE. For example, contact area of water drop, θ_w, was found to be 70.4^o for untreated UHMWPE, but for Helium and Helium/Oxygen CAP treated UHMWPE the angle was measured at 46.1^o and 58.0^o, respectively. This decreasing trend is also given for the contact angles for ethylene glycol, θ_{et}, for example, θ_{et}: 51.2^o for untreated UHMWPE; 35.3^o and 50.2^o for Helium and Helium/Oxygen CAP treated UHMWPE, indicating that the CAP treated surfaces have become hydrophilic. On the other hand the surface energy data clearly demonstrates that there is little difference of the electron-donor and electron-acceptor parameters (γ^{AB}), with results

varying by a few mJ/m^2: 7.89, 8.38 and 6.54 mJ/m^2 for untreated UHMWPE and CAP-treated UHMWPE with Helium and Helium/Oxygen mixture, respectively. As the dispersive surface free energies (γ^{LW}) are also calculated also had little difference between the samples, for untreated UHMWPE, 25.58 mJ/m^2; 26.61 mJ/m^2 for the Helium treated sample and for the Helium and Oxygen mix sample that was tested was 30.23 mJ/m^2. Therefore due to the small difference, the overall total of the surface free energies for the tested samples not surprisingly had little variation of 33.47 mJ/m^2; 34.99 mJ/m^2; and 36.77 mJ/m^2 for untreated UHMWPE, and CAP-treated UHMWPE with Helium, and Helium Oxygen mix respectively.

Table 4-2. Contact angles of water (θ_w), ethylene glycol (θ_{et}), hexadecane (θ_h) and surface energy parameters of UHMWPE samples.

	θ_w	θ_{et}	θ_h	γ^{LW} (mJ/m^2)	γ^+ (mJ/m^2)	γ^- (mJ/m^2)	γ^{AB} (mJ/m^2)	γ^{tot} (mJ/m^2)
untreated	70.4±1.5	51.2±1.9	19.7±2.4	25.58	0.92	16.93	7.89	33.47
He	46.1±2.5	35.3±2.6	12.4±1.7	26.61	1.04	17.00	8.38	34.99
He/O_2	58.0±3.6	50.2±3.8	15.0±3.1	30.23	0.33	32.73	6.54	36.77

4.4.3 Adhesion Force Measurements

Adhesion force measurements results for dry case samples are set in Figure 4-6. Generally for the dry case samples a normal distribution was observed.

However, for the untreated dry case UHMWPE the distribution is very wide with possibly three populations at 250, 1250, and 1900 nN; this may be associated with the distribution of asperities on the surface governed by the mechanical properties of adhesion phenomenon. For Helium dry case treated sample had an average adhesion distribution around 500 nN; as well as the Helium/Oxygen treated UHMWPE at around 600 nN, from this decrease in adhesive force measurements compared to the untreated UHMWPE in dry case suggests that the CAP treatment has altered the surface properties as the adhesion has reduced. On the other hand when observing the results collected for adhesive force measurements in PBS there is no normal distribution (Figure 4-7). Also there appears to be a significant decrease in adhesion force measured compared to those measured in a dry environment. This decreasing trend of adhesion force measurements may be attributed to the relative permittivity phenomenon (29, 30).The resulting adhesion measurements for untreated UHMWPE in PBS exhibited an average adhesion force measurement of around 10nN, (Figure 4-7a), whereas both treated samples had a five-fold increase in adhesion force averaging 50nN (Figure 4-7b and c).

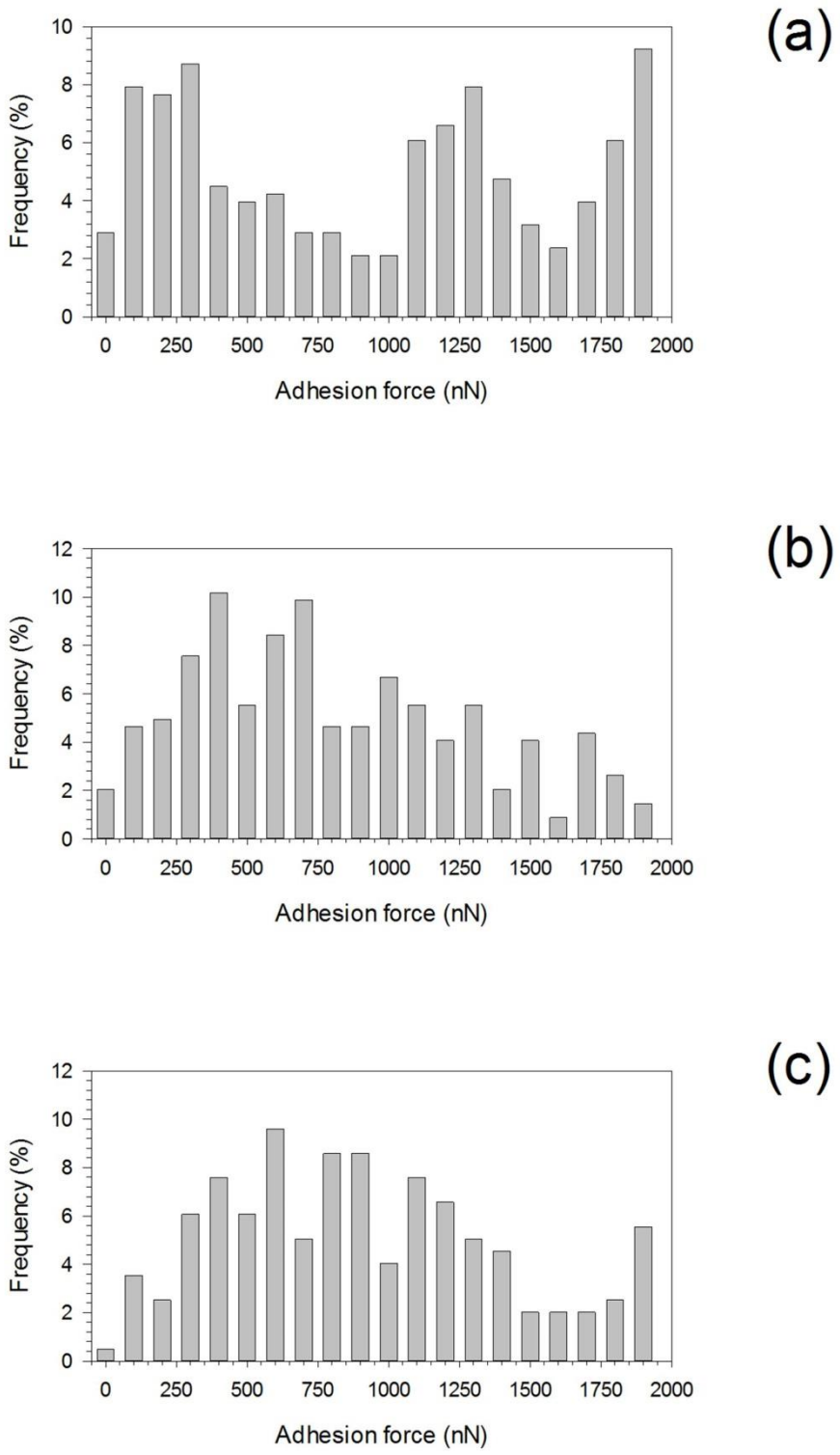

Figure 4-6. Adhesion force measurements for all tested samples of UHMWPE; a) Untreated; b) Helium treated and c) Helium/Oxygen treated.

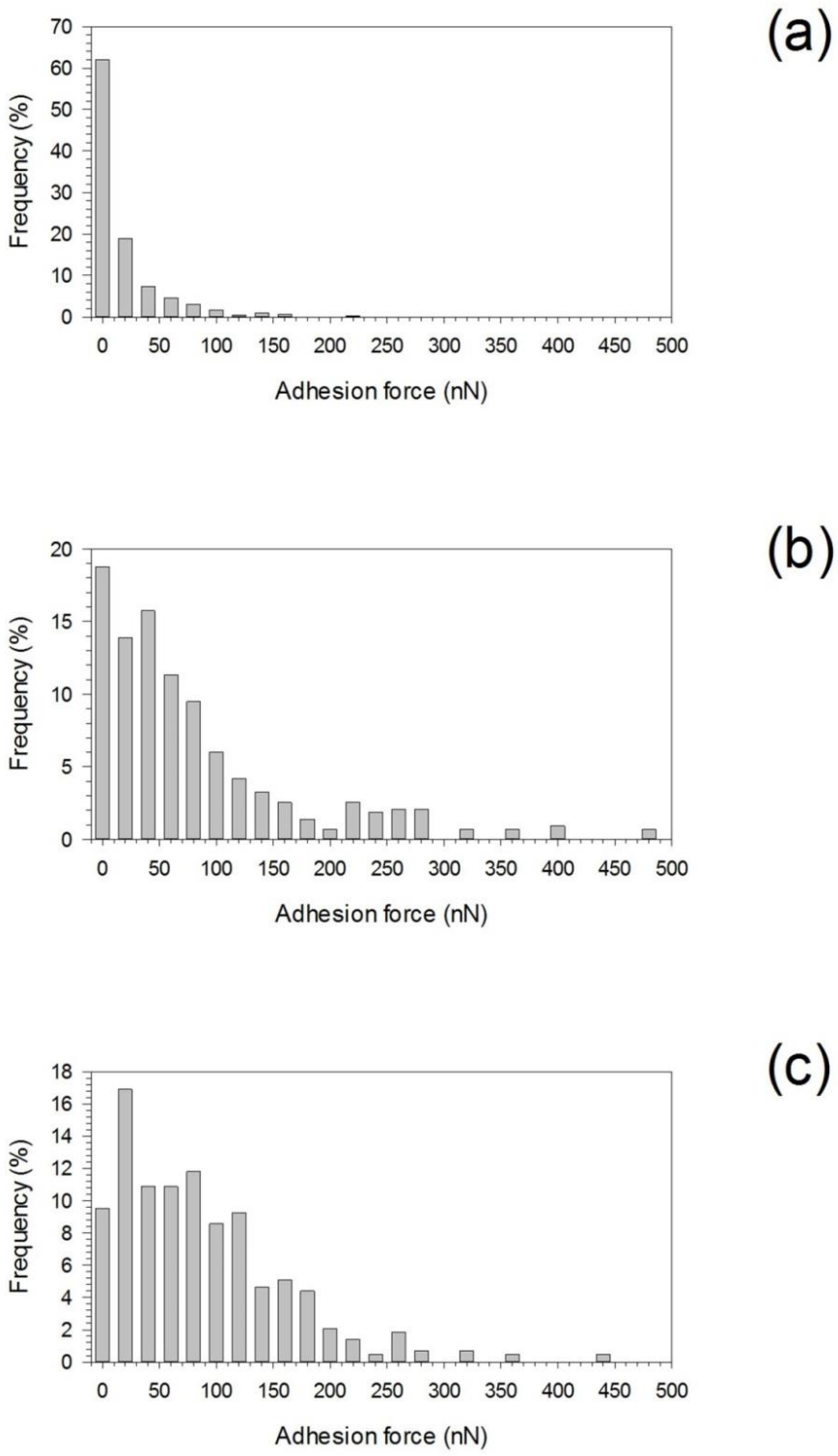

Figure 4-7. The adhesion force measurement results for all tested samples of UHMWPE; a) Untreated; b) Helium treated and c) Helium Oxygen mix in PBS.

4.5 Discussion

Irregularities on the material surface are features exhibited by all solid materials; these are denoted "asperities". For decades adhesion has been of interest in research (31-34) and is a complex phenomenon applied to a vast range of activities from walking to bacterial attachment (33). Generally, there are many aspects which govern the adhesion process, for example, the surface topography may influence the extent of adhesion due to variations in the real area of contact (26).

Moreover, the physicochemical properties associated with the surface of UHMWPE are strongly influenced by the chemical and functional groups of the polymer. In this case, polyethylene polymer is a long chain consisting of the monomer ethylene ($(C_2H_4)_n$) (35), variations exist in the density and amount of branching. However as has been discussed that UHMWPE has a disadvantage in regards to wear leading to aseptic loosening (9, 13, 35). It has been highlighted that highly cross-linked polyethylene (XLPE) (35) has a higher density and usually achieved through costly process such as thermal treatment and irradiation. However, it has been noted that these procedures introduce another problem of oxidation (15, 16) causing long-term damage and failure of the device. The CAP treatment therefore has the advantages of these techniques through introducing free radicals such as Nitrogen free radicals from the surrounding environment which promote further cross-linking across multiple polymer chains effectively increasing the density and strength of the polymer (35). It is has been demonstrated (1) that the CAP introduce Nitrogen groups on the surface of UHMWPE. Furthermore, these groups have a clear

effect on the surface properties of the samples post-CAP treatment increasing the hydrophilicity of the material.

As was observed in this work, the changes in the surface topography are inherent of plasma etching which explains the decreased asperity density by almost half that of the untreated UHMWPE compared to both CAP treated UHMWPE, as well as the reduction in height. As the plasma is volatile on production it bombards the surface with highly charged ions/radicals that etch away parts of the surface, some of these parts may embed to the surface through chemical reactions therefore disrupting the topography; such as shaving the height of asperities, thereby reducing the number of asperities per given area. Also this may affect the curvature of radii, although it has been noted (26) that normal contact models have a random anisotropic distribution, especially when considering the surface roughness, asperity radii (36) and asperity heights are traditionally assumed to have a Gaussian distribution (26) yet when applied to engineering applications, many machining process produce surface with asperity heights non normally distributed (26). The variations in height and shape of asperity play an essential role in the adhesion phenomena and influence the resulting adhesion force measurements along for a closer apposition of bone to the implanted device (37).

The small adhesive forces observed in PBS compared to the dry case results are due to the different relative permittivity of water and air, ε_r of water ranges from 4 to 88 Fm^{-1} and ε_r of air is much less at 1.000536 Fm^{-1} at room temperature. The higher permittivity of water impacts on the extent of the

interaction between UHMWPE and borosilicate sphere reducing the contribution to the contact forces (30, 38)

It is evident (39) that the mechanical and physicochemical interactions between the implant and lubricant is a necessity, especially when considering osseointegration (40) and the formation of molecular layers to the implant to minimise friction and potential wear. Osseointegration has been defined as direct structural and functional connection between ordered living bone and implant (22). Nanoseconds into TJR surgery water forms a layer facilitating proteins that adsorb onto the surface of the implant i.e. the extracellular matrix (ECM) proteins (22) which initiates cellular adhesion. Normally a duration of at least 5 days post implantation is essential for new bone formation (22) which is governed by the surface properties and adsorption rate of the polymer, which determines the proliferation of osteoblasts and acceptance or rejection of the implant as implant bone interface has an essential role in prolonging the longevity and function of the prostheses (40). It has also been pointed out (41) that the biocompatibility of the implant can influence the cell behaviour and, therefore, attachment; as well as the surface characteristics such as topography, chemistry and surface energy have an important role an adhesion which has been highlighted in this work. Moreover, these results indicate that the increased adhesion and hydrophilicity of the polymers surface after treatment with CAP could lead to improved osseointegration (40, 42).

4.6 Conclusions

This work aimed at comparing the effects of CAP-treatment with He and He/Oxygen cold gas plasmas on medical grade UHMWPE surface properties and forces of adhesion. Results showed that CAP treatment decreased the asperity density of both treated samples by half that of the untreated UHMWPE; the treatment also reduced the height of these asperities due to plasma etching. Furthermore, the etching also affected the asperity curvature radii which were generally smaller after CAP treatment. However, the CAP-treatment did not affect the overall surface energy of the tested samples as there was little difference in the parameters, although a decrease in contact angle of water was noticed in the treated UHMWPE samples, thereby improving the hydrophilicity. From the decrease in hydrophobicity after CAP treatment to the UHMWPE increased the resulting adhesion forces measured. These results have shown that CAP-treated UHMWPE has advantageous properties at improving the characteristics associated with successful prostheses such as improved wear and increased adhesion which is essential for improved osseointegration for the longevity of the implanted devices.

4.7 Abbreviations

A.C. – Alternative Current

AFM – Atomic Force Microscopy

CAP – Cold Atmospheric Pressure Plasma

ECM – Extracellular Matrix

PBS – Phosphate Buffer Solution

PCTFE – Polychlorofluoroethylene

slm – standard litre per minute

sccm – standard cubic centimetre per minute

TJA – Total Joint Arthroplasty

TJR – Total Joint Replacement

UHMWPE – Ultra-high Molecular Weight Polyethylene

XLPE – Highly cross-linked polyethylene

4.8 References

1. Perni S, Kong MG, Prokopovich P. Cold atmospheric pressure gas plasma enhances the wear performance of ultra-high molecular weight polyethylene. Acta Biomaterialia. 2012;8(3):1357-65.

2. Dressler MR, Strickland MA, Taylor M, Render TD, Ernsberger CN. Predicting wear of UHMWPE: Decreasing wear rate following a change in direction. Wear. 2011;271(11–12):2879-83.

3. Jeffery AK. Articular cartilage and the orthopaedicsurgeon. Part 2: Degeneration, injury and repair. Current Orthopaedics. 1994;8(2):108-15.

4. Suh J-K, Scherping S, Mardi T, Richard Steadman J, Woo SLY. Basic science of articular cartilage injury and repair. Operative Techniques in Sports Medicine. 1995;3(2):78-86.

5. Goldring SR, Goldring MB. Clinical aspects, pathology and pathophysiology of osteoarthritis. Journal of musculoskeletal & neuronal interactions. 2006;6(4):376-8.

6. Frankel L, Sanmartin C, Conner-Spady B, Marshall DA, Freeman-Collins L, Wall A, et al. Osteoarthritis patients' perceptions of “appropriateness” for total joint replacement surgery. Osteoarthritis and Cartilage. 2012;20(9):967-73.

7. Katz JN. Total joint replacement in osteoarthritis. Best Practice & Research Clinical Rheumatology. 2006;20(1):145-53.

8. Brach Del Prever EM, Bistolfi A, Bracco P, Costa L. UHMWPE for arthroplasty: past or future? Journal of orthopaedics and traumatology : official journal of the Italian Society of Orthopaedics and Traumatology. 2009;10(1):1-8.

9. Fisher J. Wear of ultra high molecular weight polyethylene in total artificial joints. Current Orthopaedics. 1994;8(3):164-9.

10. Prokopovich P, Perni S, Fisher J, Hall RM. Spatial variation of wear on Charité lumbar discs. Acta Biomaterialia. 2011;7(11):3914-26.

11. Davis JR. Handbook of Materials for Medical Devices. Overview of Biomaterials and Their Uses in Medical Devices: ASM International; 2003.

12. Wilches LV, Uribe JA, Toro A. Wear of materials used for artificial joints in total hip replacements. Wear. 2008;265(1–2):143-9.

13. Lapcikova M, Slouf M, Dybal J, Zolotarevova E, Entlicher G, Pokorny D, et al. Nanometer size wear debris generated from ultra high molecular weight polyethylene in vivo. Wear. 2009;266(1–2):349-55.

14. Cummings CS, Lucas EM, Marro JA, Kieu TM, DesJardins JD. The effects of proton radiation on UHMWPE material properties for space flight and medical applications. Advances in Space Research. 2011;48(10):1572-7.

15. Turos A, Abdul-Kader AM, Grambole D, Jagielski J, Piątkowska A, Madi NK, et al. The effects of ion bombardment of ultra-high molecular weight polyethylene. Nuclear Instruments and Methods in Physics Research Section B: Beam Interactions with Materials and Atoms. 2006;249(1–2):660-4.

16. Goldman M, Pruitt L. Comparison of the effects of gamma radiation and low temperature hydrogen peroxide gas plasma sterilization on the molecular structure, fatigue resistance, and wear behavior of UHMWPE. Journal of Biomedical Materials Research. 1998;40(3):378-84.

17. Bracco P, Brunella V, Luda MP, Zanetti M, Costa L. Radiation-induced crosslinking of UHMWPE in the presence of co-agents: chemical and mechanical characterisation. Polymer. 2005;46(24):10648-57.

18. Bieliński DM, Tranchida D, Lipiński P, Jagielski J, Turos A. Ion bombardment of polyethylene—influence of polymer structure. Vacuum. 2007;81(10):1256-60.

19. Liu H, Pei Y, Xie D, Deng X, Leng YX, Jin Y, et al. Surface modification of ultra-high molecular weight polyethylene (UHMWPE) by argon plasma. Applied Surface Science. 2010;256(12):3941-5.

20. Bracco P, Brunella V, Zanetti M, Luda MP, Costa L. Stabilisation of ultra-high molecular weight polyethylene with Vitamin E. Polymer Degradation and Stability. 2007;92(12):2155-62.

21. Tendero C, Tixier C, Tristant P, Desmaison J, Leprince P. Atmospheric pressure plasmas: A review. Spectrochimica Acta Part B: Atomic Spectroscopy. 2006;61(1):2-30.

22. Chug A, Shukla S, Mahesh L, Jadwani S. Osseointegration—Molecular events at the bone–implant interface: A review. Journal of Oral and Maxillofacial Surgery, Medicine, and Pathology. 2013;25(1):1-4.

23. Walsh JL, Kong MG. Contrasting characteristics of linear-field and cross-field atmospheric plasma jets. Appl Phys Lett. 2008;93(11):111501-3.

24. Cao Z, Nie Q, Bayliss DL, Walsh JL, Ren CS, Wang DZ, et al. Spatially extended atmospheric plasma arrays. Plasma Sources Science and Technology. 2010;19(2):025003.

25. Sader JE, Larson I, Mulvaney P, White LR. Method for the calibration of atomic force microscope cantilevers. Review of Scientific Instruments. 1995;66(7):3789-98.

26. Prokopovich P, Perni S. Multiasperity Contact Adhesion Model for Universal Asperity Height and Radius of Curvature Distributions. Langmuir. 2010;26(22):17028-36.

27. Sader JE, Sanelli JA, Adamson BD, Monty JP, Wei X, Crawford SA, et al. Spring constant calibration of atomic force microscope cantilevers of arbitrary shape. Review of Scientific Instruments. 2012;83(10):103705--16.

28. Craig VSJ, Neto C. In Situ Calibration of Colloid Probe Cantilevers in Force Microscopy: Hydrodynamic Drag on a Sphere Approaching a Wall. Langmuir. 2001;17(19):6018-22.

29. Gongadze E, Velikonja A, Slivnik T, Kralj-Iglič V, Iglič A. The quadrupole moment of water molecules and the permittivity of water near a charged surface. Electrochimica Acta. 2013;109(0):656-62.

30. Gongadze E, Iglič A. Decrease of permittivity of an electrolyte solution near a charged surface due to saturation and excluded volume effects. Bioelectrochemistry. 2012;87(0):199-203.

31. Johnson KL, Kendall K, Roberts AD. Surface Energy and the Contact of Elastic Solids. Mathematical and Physical Sciences. 1971;324:301-13.

32. Derjaguin KL, Muller VM, Toporov YP. Effect of Contact Deformation on the Adhesion of Particles. Journal of Colloid and Interface Science. 1975;53(2):314-26.

33. Prokopovich P, Starov V. Adhesion models: From single to multiple asperity contacts. Advances in Colloid and Interface Science. 2011;168(1–2):210-22.

34. Prokopovich P, Perni S. Comparison of JKR- and DMT-based multi-asperity adhesion model: Theory and experiment. Colloids and Surfaces A: Physicochemical and Engineering Aspects. 2011;383(1–3):95-101.

35. Patel S, Hossain FS, Haddad FS. Focus On Bearing Surfaces in Lower Limb Total Joint Arthroplasty. The Journal of Bone and Joint Surgery. 2010;357(3):1-4.

36. Bush AW, Gibson RD, Thomas TR. The elastic contact of a rough surface. Wear. 1975;35(1):87-111.

37. Hunter A, Archer CW, Walker PS, Blunn GW. Attachment and proliferation of osteoblasts and fibroblasts on biomaterials for orthopaedic use. Biomaterials. 1995;16(4):287-95.

38. Nalaskowski J, Drelich J, Hupka J, Miller JD. Adhesion between Hydrocarbon Particles and Silica Surfaces with Different Degrees of Hydration As Determined by the AFM Colloidal Probe Technique. American Chemical Society. 2003(19):5311-7.

39. Wang N, Trunfio-Sfarghiu A-M, Portinha D, Descartes S, Fleury E, Berthier Y, et al. Nanomechanical and tribological characterization of the MPC phospholipid polymer photografted onto rough polyethylene implants. Colloids and Surfaces B: Biointerfaces. 2013;108(0):285-94.

40. Khan SN, Ramachandran M, Senthil Kumar S, Krishnan V, Sundaram R. Osseointegration and more–A review of literature. Indian Journal of Dentistry. 2012;3(2):72-6.

41. Anselme K. Osteoblast adhesion on biomaterials. Biomaterials. 2000;21(7):667-81.

42. Goda T, Konno T, Takai M, Ishihara K. Photoinduced phospholipid polymer grafting on Parylene film: Advanced lubrication and antibiofouling properties. Colloids and Surfaces B: Biointerfaces. 2007;54(1):67-73.

Chapter 5 - Surface Roughness Mediated Adhesion Forces between Borosilicate Glass and Gram Positive Bacteria

The content of this chapter has been published in:

E. Callard Preedy, S. Perni, D. Nipiĉ, K. Bohinc, P. Prokopovich "Surface Roughness Mediated Adhesion Forces between Borosilicate Glass and Gram Positive Bacteria" *Langmuir* 2014;30(31), 9466-9476

E. Callard Preedy, S. Perni, P. Prokopovich "Curli Expression Genes Influence on Spatial Distribution of Forces of Adhesion on the Cell Surfaces of *E. coli*" Proceeding from *27th Conference of European Colloids and Interface Society – ECIS,* 1-6 September 2013, Sofia, Bulgaria (accepted for oral presentation)

E.C. Preedy, S. Perni, E. Brousseau, S. Evans, P. Prokopovich "Curli Expression Genes Influence on Spatial Distribution of Forces of Adhesion on Cell Surfaces of *E. coli*" Proceeding from *14th European Student Colloid Conference*, 10-13 June 2013, Potsdam, Germany

5.1 Abstract

It is well known that a number of surface characteristics affect the extent of adhesion between two adjacent materials. One such parameter is the surface roughness as surface asperities at the nanoscale level govern the overall adhesive forces. For example, the extent of bacterial adhesion is determined by the surface topography, also once a bacteria colonizes a surface, proliferation of that species will take place and a biofilm may form increasing the resistance of bacterial cells to removal.

In this study, borosilicate glass was employed with varying surface roughness and coated with bovine serum albumin (BSA) in order to replicate the proteins layer that covers orthopaedic devices on implantation. As roughness is a scale dependent process, relevant scan areas were analysed using atomic force microscope (AFM) to determine surface roughness (Ra), furthermore appropriate bacterial species were attached to the tip to measure the adhesion forces between cells and substrates. The bacterial species chosen (Staphylococci and Streptococci) are common pathogens associated with a number of implant related infections that are detrimental to the biomedical devices and patients. Correlation between adhesion forces and surface roughness (Ra) was generally better when the surface roughness was measured through scanned areas with size (2x2 μm) comparable to bacteria cells. Furthermore, the BSA coating altered the surface roughness without correlation with the initial values of such parameter; therefore, better correlations were found between adhesion forces and BSA coated surfaces when actual surface roughness was used instead of the initial (nominal) values.

It was also found that BSA induced a more hydrophilic and electron donor characteristic to the surfaces; in agreement with increasing adhesion forces of hydrophilic bacteria (as determined through Microbial Adhesion to Solvents test) on BSA coated substrates.

5.2 Introduction

Biofilms are defined as a layer or layers of cells, adhered to a substratum which are generally embedded in an organic biological matrix i.e. extracellular polymeric substances (EPS) (1-5). It is due to biofilm formation that many bacteria survive in highly diverse and adverse environments as a result of the polymicrobial ecosystem. Not surprisingly, biofilms have formed on a variety of surfaces and are not only restricted to attachment at a solid-liquid interface, but have been observed at solid-air and liquid-liquid interfaces (1-4, 6, 7), with some having beneficial results as well as detrimental; for example, in industry biofilms are used successfully to separate coal particles from mineral matter (8, 9).

On the other hand, biofilms have been known to cause biofouling reducing mass and heat transfer and effectively increasing corrosion (10, 11); yet from a medical point of view, biofilms colonizing implanted medical devices often lead to implant failure (7). Furthermore, the food industry have had a major interest in biofilms as a result of their resistance to cleaning and disinfection because spoilage and pathogenic bacteria pose a risk to public health and product quality (11-13). Also in the paper industry, biofilms can trap certain particles, calcium carbonate, cellulose fibres, causing problems with the formation of a

thick slimy deposit which clogs wires resulting in sheet breakages and reduction in paper quality because of holes, odours and even discoloration (14).

The formation of biofilms is a complex multistep process which is dependent on a number of variables such as: the type of microorganism, the surface of attachment and the surrounding environment (6). Initially, microorganisms attachment to an abiotic surface occurs mainly through hydrophobic interactions; yet adhesion in living tissue takes place through specific molecular mechanisms such as ligands. In the first stage of attachment, cells are reversibly bound to a surface; this step is governed by the repulsive energy barrier, when occurring and resulting from the overlap of the negatively charged substratum surface produced by the electrical double layer formed in an aqueous environment (13). Nevertheless, many bacteria can overcome the repulsive energy barrier by effectively penetrating this obstacle using features such as: nanofibers, for example flagella, whilst others produce EPS to bridge the cell to the substratum surface effectively forming the conditioning layer (6, 9, 13). As well as these effective bridging effects, these crucial initial stages of attachment are mediated by a number of other interactions, namely van der Waals attractive forces, electrostatic repulsive forces and surface hydrophobicity (14, 15). The predominance of these forces is dependent on the distance between the microorganism and the surface; usually at distances greater than 50 nm van der Waals (vdW) forces are the main factor, whilst at closer distance (10-20 nm) a combination of both vdW and electrostatic interactions controls cell adhesion (6).

A conditioning film is often provided by body fluids, this has also been noted to play a role in biofilm formation; for instance, in dentistry, teeth can be coated by a protein layer made of albumin, lysosomes, glycoproteins, lipids and gingival crevice fluid (9) allowing for anchoring points to which flagella can attach. The conditioning film may be very complex and often results in chemical modification of the substratum surface which effectively influences the rate and extent of attachment of the bacteria (6, 16), these result from the conditioning film effectively creating a foundation base that masks the surface features. The adhesion process on a coated substratum is, therefore, dominated by this conditioning film (6).

Certain parameters such as: the surface hydrophobicity/hydrophilicity (15, 17), topography and roughness (18-20) are known to have a dominating role in the extent of adhesion that is essential for the biofilm growth phase to be successful. At large and intermediate separation distances between cell and substrate, macroscopic cell surface properties (such as: surface free energy, surface charge and hydrophobicity/hydrophilicity) control the initial attachment; whilst at small separation distances (below 5 nm) microscopic molecular short-range interactions mediate bacterial adhesion (5, 21). It has been hypothesized (21, 22) that asperities or peaks and other surface structures on both interacting surfaces may result in a decrease in the total interacting energy as well as the height of the energy barrier that the microbial cell must overcome before adhering to the substratum surface; hence there may be a greater rate of adhesion on rougher surfaces (18) with a positive correlation with the rate of colonization, especially in oral implants (18, 19, 23). Additionally, surface

roughness is a scale dependent process i.e. results from undulations and imperfections on the surface of a material in relation to the observed or scanned area, therefore, average surface roughness (Ra) or root-mean-squared (RMS) values may be different at the macroscale compared to the micro- and even at the nanoscale (24, 25).

Atomic force microscopy (AFM) is a technique that employs the deflection of a cantilever in proximity of a surface to determine the topography and/or the interfacial forces between two surfaces; cantilevers have also been functionalized with cells to quantify forces acting between surfaces and bacteria (26).

The aim of this study was to investigate the role of surface roughness, in relation to a scanned area comparable with the size of bacteria, on the forces of adhesion between the material and cells. Borosilicate glasses, uncoated and coated with bovine serum albumin (BSA, of different micro- and nanoscale roughness have been used in this work against various bacterial species: *Staphylococcus epidermidis*, *Staphylcoccus aureus* and *Streptococcus mutants*, employing AFM to analyse the adhesive forces associated with these bacterial species and substrates. These bacteria are some of the common causes of infections associated with medical devices; specifically *Staphylococci* in orthopaedic implanted devices (where borosilicate glass mimics orthopaedic materials), whilst *S. mutant* in oral cavity related applications (where glass has been used to coat Titanium dental implants (27)).

5.3 Materials and Methods

5.3.1 Borosilicate Glass

Samples of borosilicate glass (size 2x2cm^2 with thickness of 2mm) were cut from TEMPAX sheet glass obtained from Schott under constant temperature of 510^{o}C and the surfaces of glass pieces were fused using a gas burner. Increasing roughness of the glass was achieved by grinding to specific gradation using abrasive particles of varying sizes. After polishing the edges of the glass plates were then fused again; untreated glass samples were used as a control. In total five glass materials were employed: A – control (untreated), B, C, D, and E of increasing roughness.

5.3.2 Macroscale roughness measurements

The macro scale roughness of the sample was determined using a mechanical profilometer (Talysurf Series 2, Taylor-Hobson Ltd., Leicester, UK).

5.3.3 Bacteria and AFM tip functionalisation

Staphylococcus epidermidis RP62 and ATCC 12228; *Staphylococcus aureus* ATCC 25923 and *Streptococcus mutants* NCTC 10449 were cultured statically in brain heart infusion (BHI, Oxoid, UK) broth overnight at 37°C, before placing a 100 µl drop of bacteria suspension onto a previously poly-L-lysine (0.1% w/v solution, Sigma, UK) coated AFM tips. The drop was left for 30 minutes before attaching the functionalized tip to the liquid head of the AFM. Each functionalized tip was used only once.

5.3.4 Bovine Serum Albumin coating (BSA)

A 1% w/v solution of bovine serum albumin (BSA) (Sigma-Aldrich, UK) was used to coat the glass samples. Samples were immersed in 10 ml solution for 30 minutes at room temperature prior to analysis.

5.3.5 Scanning Electron Microscopy (SEM)

Bacterial functionalized AFM tips were fixed with 2% glutaraldehyde for 2 hours, then dehydrated in alcohol solutions of progressive concentrations, 70, 90 and 100 %. Each tip was gold coated using a sputter coater (Agar Model 109A, Stansted, Essex, UK), with a mixture of Gold and Palladium (80% and 20%, respectively) in Argon gas; all tips were exposed for 15 seconds, this was repeated four times to achieve an even coating. Once coated, the tips were transferred to the scanning electron microscope (SEM) sample holder, and imaged (XB1540, Carl Zeiss, Germany).

5.3.6 Atomic Force Microscopy (AFM)

Atomic Force Microscope (AFM) (XE-100 Advanced Scanning Probe Microscope (Park Systems, Korea) was used to analyse the surface roughness, surface topography and adhesion forces.

5.3.6.1 Surface Topography Analyses

Contact mode was employed for all AFM analysis; the micro-scale roughness was measured using scanned areas of 10 x 10 µm. Whereas areas of 2 x 2 µm were scanned for the nanoscale roughness. Images were obtained using a contact rectangular tip, CSG30 (NT-MDT, Russia), with reflective Au side, a spring constant of 3.3 N/m, tip height of 14 µm and a tip curvature radius of 10 nm; each tip was calibrated using the Sader method (28). The scan parameters

used were as follows: resolution at 1024x1024; scan rate between 0.8 and 1.0 Hz and applied load of 10 nN. For each glass sample, six replicate scans were made and the average surface roughness (Ra) determined.

5.3.6.2 Adhesion forces measurements

All adhesive force measurements were conducted in an open liquid cell made of polychlorofluoroethylene, PCTFE (Park Systems, Korea) using phosphate buffer solution (PBS) as the aqueous environment. In order to gain comprehensive data for the adhesive interactions of the given samples, the surface mapping feature of the AFM was employed with a tip functionalized with the chosen bacteria species. Using 2 x 2 µm scan size, 100 curves per area and three areas were scanned on separate occasions on each sample using three functionalized cantilever with three independent cultures of the same bacteria, therefore at least 300 curves were collected per glass sample and bacteria as well as control experiments.

Retraction of the bacterial probe from a composite surface with and without BSA was done without delay (0 sec) in order to avoid possible bond strengthening.

Scanning electron micrographs were taken at the end of the experiments to confirm that no visual damage occurred to the bacterial probe as results of the measurements; for this study no force–distance curves had to be discarded due to a damaged probe.

5.3.7 Microbial Adhesion to Solvents (MATS)

MATS protocol, a two phases partitioning assay, was developed by (29) to determine physico-chemical properties of bacterial surfaces. The cell suspensions, prepared as previously described, were centrifuged for 10 minutes at 6037 × g (HERMLE centrifuge Z-383 K, LabPlant, Huddersfield, UK) at 4 ºC. Cells were washed with a NaCl (sodium chloride) solution (0.15 M) and centrifuged three more times. The final suspension was diluted with the same NaCl solution to a final cell concentration of about 10^8 CFU/ml. 2.0 ml of this cell suspension and 0.5 ml of one of the solvents (chloroform, hexadecane, ethyl-acetate and decane (Sigma, UK) were vortexed together for 1 minute. The emulsion was left to stand for 15 minutes to allow the two phases to separate.

The absorbance of the aqueous phase was evaluated at 450 nm with a spectrophotometer (UV-1201, Shimadzu (UK), Milton Keynes). The affinity of the bacterial species for each solvent was determined using the following equation:

$$\%\,\text{Affinity} = 100 \cdot \left(1 - \frac{A}{A_0}\right) \qquad (5\text{-}1)$$

where A_0 is the absorbance at 450 nm of the suspension before mixing and A is the absorbance of the suspension after mixing with one of the solvents. This protocol was carried out on cells that originated from four independent cultures and the results are presented as mean values ± standard deviation.

5.3.8 Contact angles and surface energy

The surface energy components of the samples were determined using the thermodynamic approach, based on contact angle measurements (30). Three probe liquids, with different polarities, were used: distilled water, glycerol and hexadecane (Sigma Aldrich, UK). A drop of 5 μl of each liquid was deposited on the sample and images were immediately recorded. Contact angles at both the right and the left side were measured using ImageJ (NIH, USA). The mean value of 10 readings was calculated for each sample and for each liquid.

5.4 Results

5.4.1 Surface Topography

The roughness measurements at the macroscale level, measured using the profilometer, are shown in Table 5-1 demonstrating that glass sample A was the smoothest with an increase in roughness up to glass sample E, with Ra values of 100 nm and 6000 nm, respectively.

All borosilicate glass samples were imaged to reveal the topography of their bare surface at the microscale level (Figure 5-1 and Figure 5-2) using a 10 x 10 μm scan area, and at the nanoscale level (Figure 5-3 and Figure 5-4), 2 x 2 μm scan area. Samples were imaged again once coated with BSA (see supplementary material). From these images the average roughness (Ra) measurements were gained and presented in Table 5-1.

Table 5-1. Average roughness (Ra) measurements of each glass sample (A-E) at varying scales before and after BSA coating.

Roughness Scale (nm)	Glass Samples				
	A	B	C	D	E
Macro	100	500	1000	2500	6000
Micro	0.250±0.12	20.00±0.05	34.6±0.15	56.10±0.12	94.40±0.54
Nano	0.259±0.04	21.90±7.65	37.0±16.29	56.30±10.82	62.15±9.04
Micro after BSA coating	1.54±0.19	52.62±0.03	81.87±0.02	103.63±0.02	145.8±-0.02
Nano after BSA coating	1.35±0.57	3.04±-0.93	4.78±1.22	2.93±0.68	4.25±1.42

At the microscale level glass, sample A was the smoothest (Ra = 0.250 nm); the Ra measurements gradually increased to the roughest sample, glass sample E, showing a Ra value of 94.4 nm. It can be seen that there is an obvious correlation between surface images (Figure 5-1) and Ra values (Table 5-1); both demonstrating a roughness pattern Glass A < Glass B < Glass C < Glass D < Glass E. Similar observations could be made on the BSA coated glass samples at microscale level, demonstrating the same pattern in roughness of A < B < C < D < E; moreover Table 5-1 demonstrated Glass A was still the smoothest with Ra of 1.54 nm, whilst Glass E was the roughest at Ra of 145.88 nm.

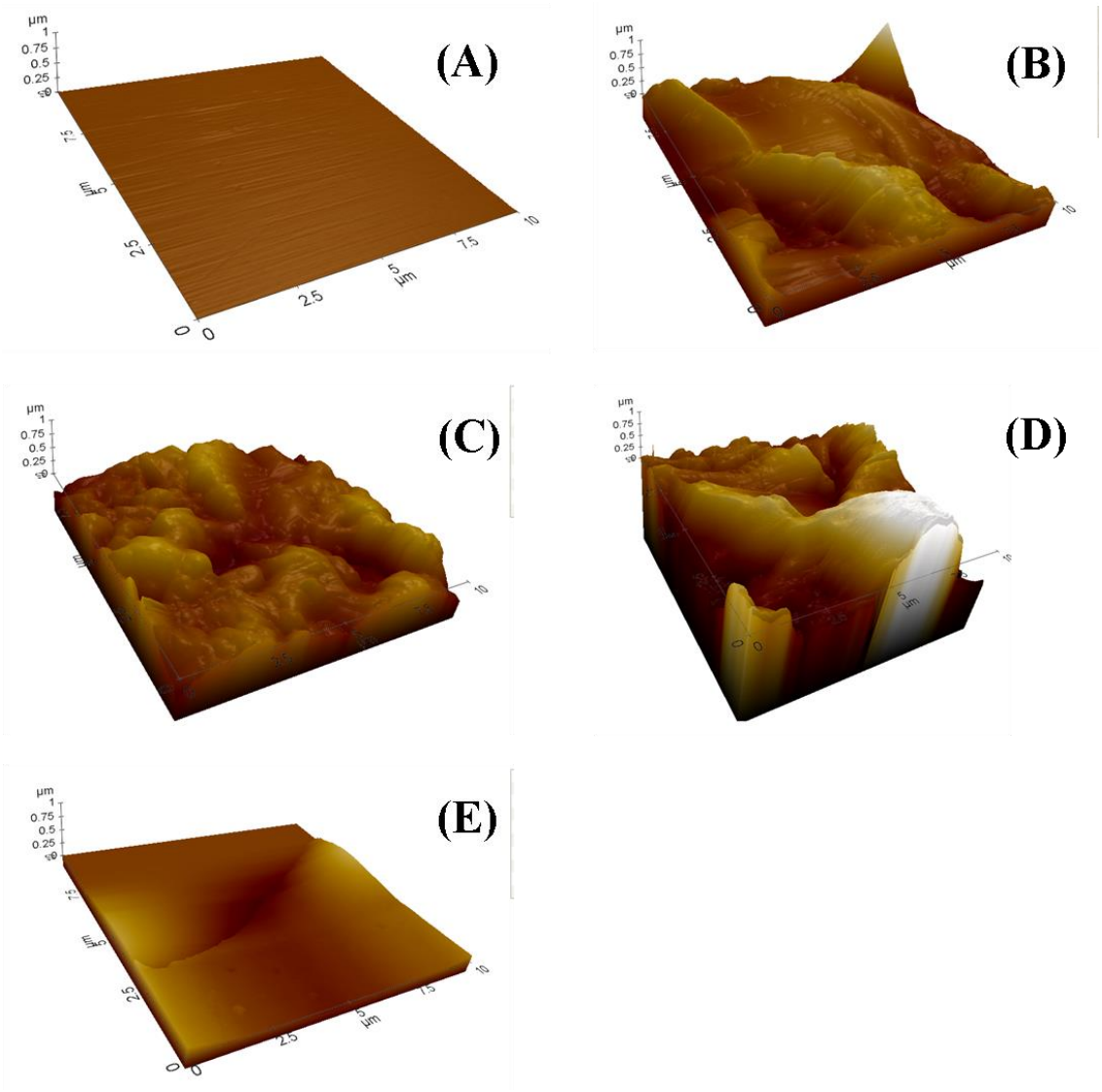

Figure 5-1. Microscale images of bare glass samples, A-E.

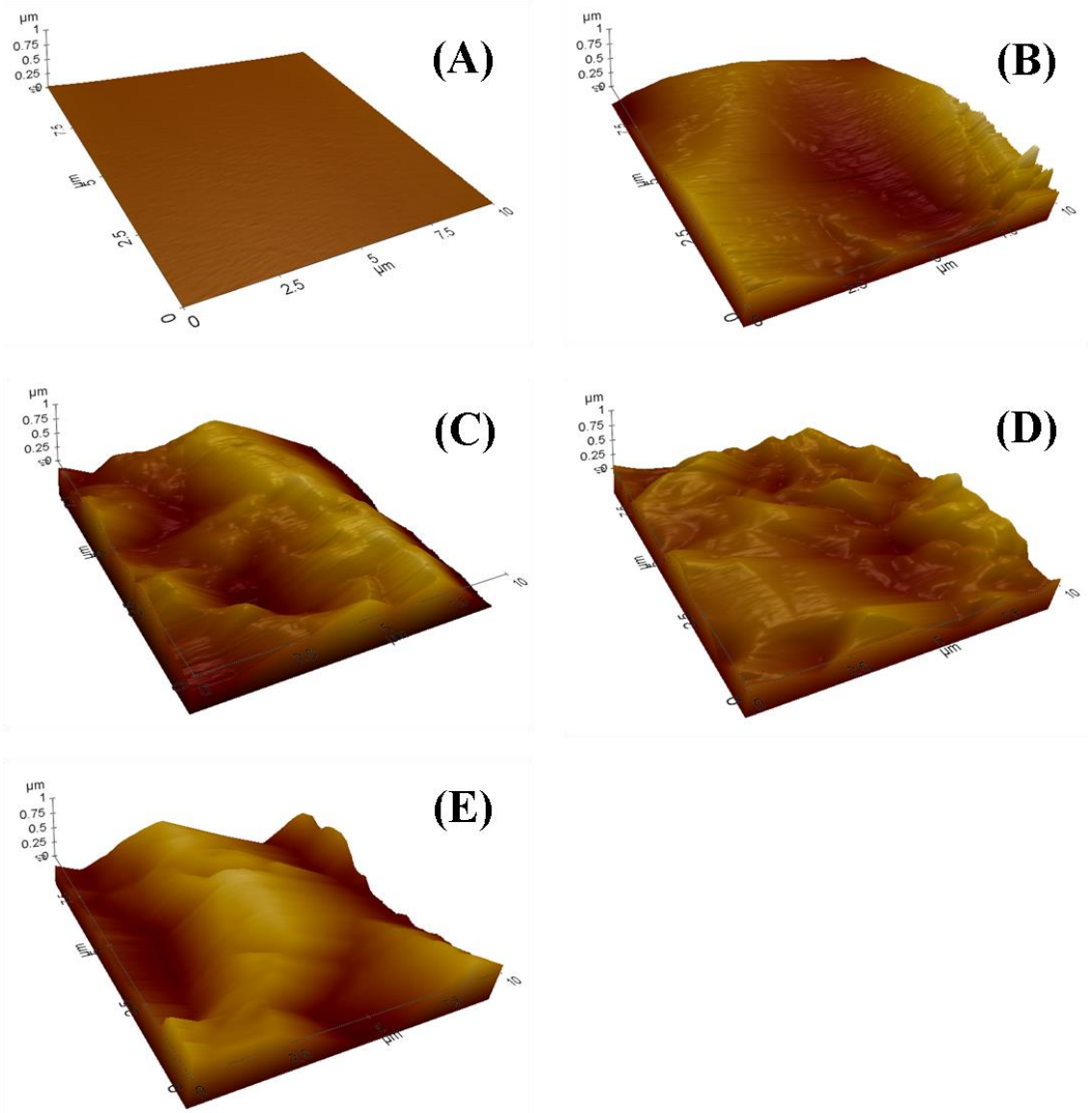

Figure 5-2. Microscale images of all glass samples A-E, coated with BSA.

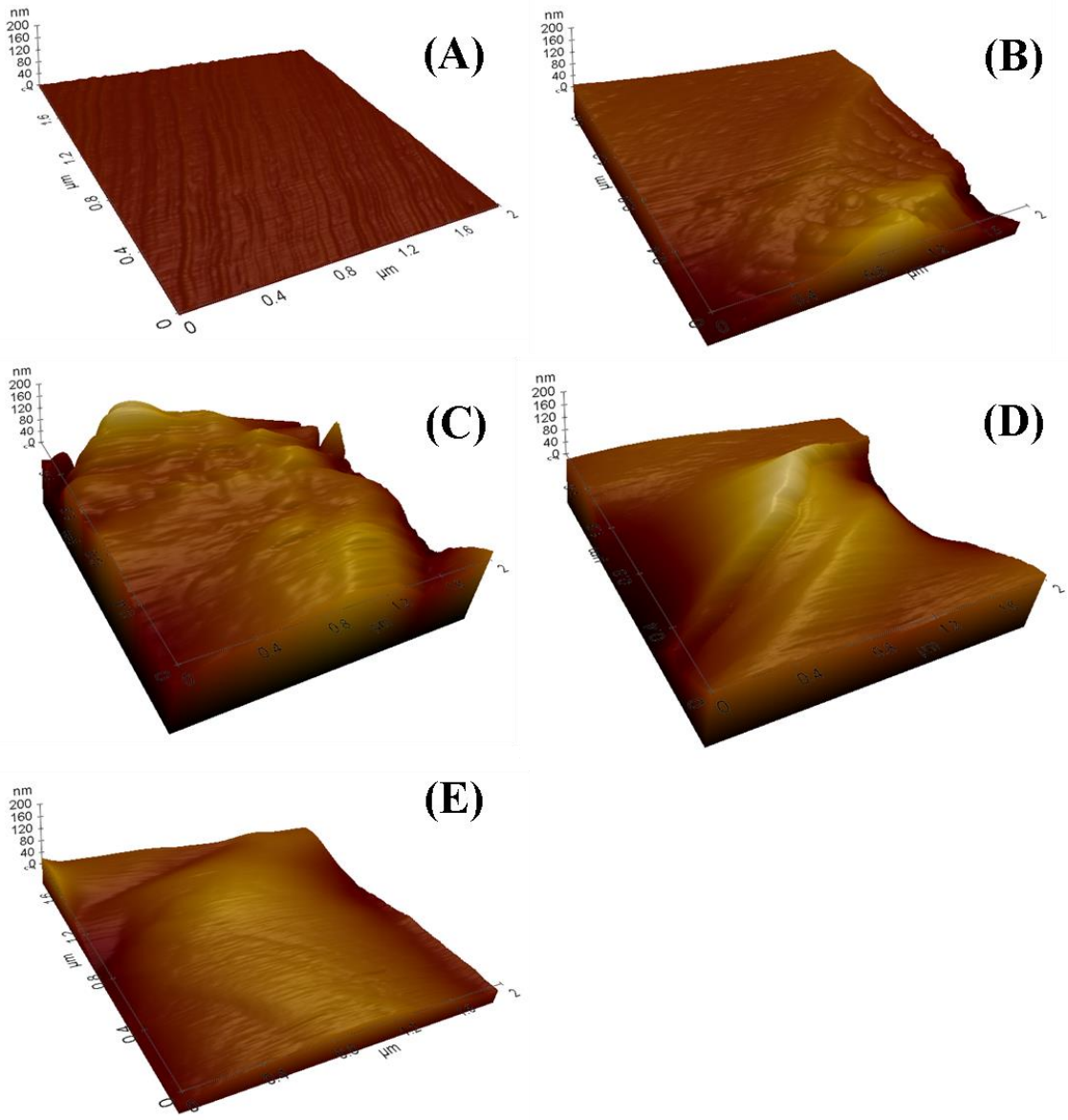

Figure 5-3. Nanoscale images of all bare glass samples A-E.

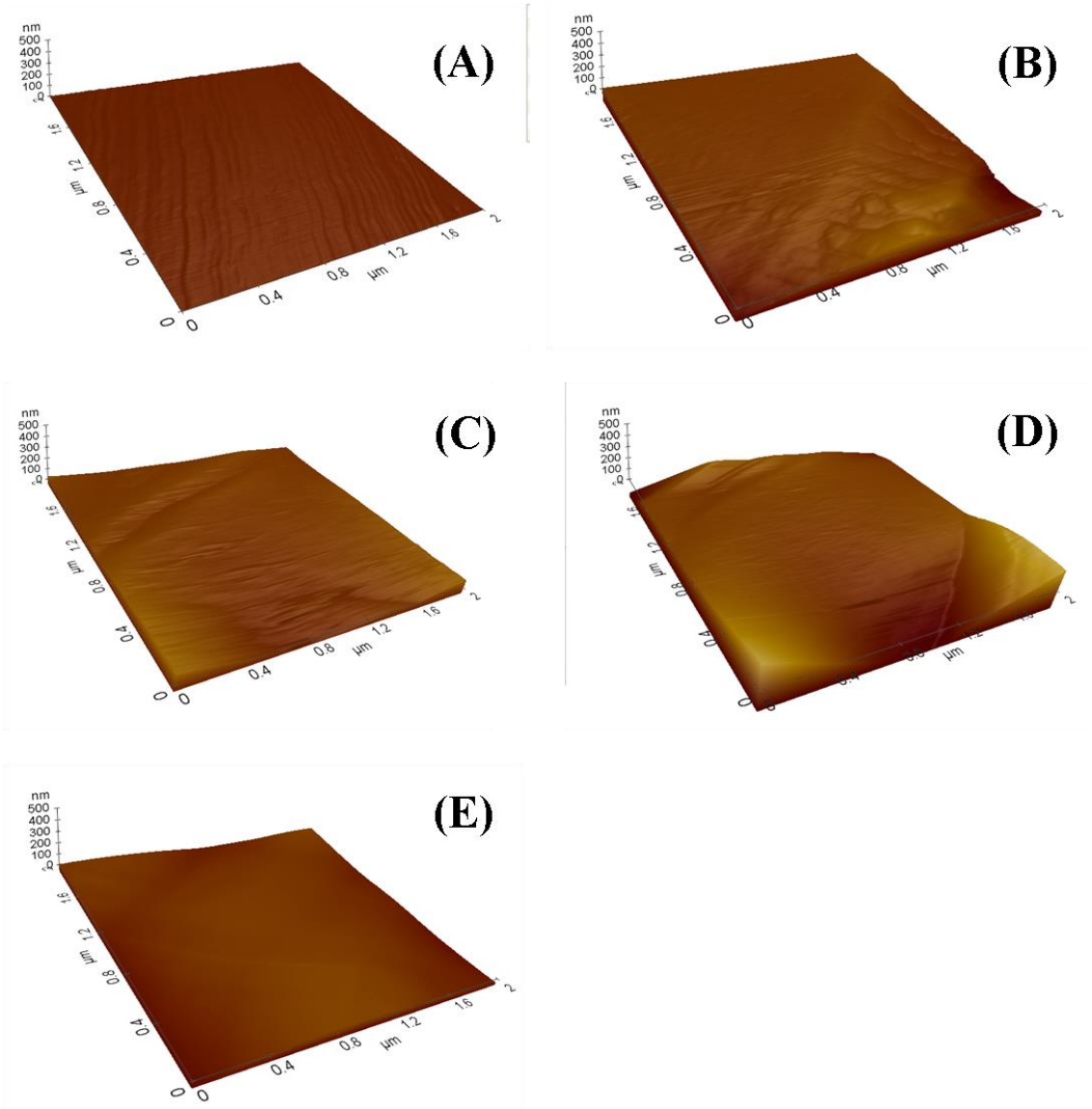

Figure 5-4. Nanoscale images of all glass samples A-E coated with BSA.

At the nanoscale level the pattern in roughness of sample A < B < C < D < E was maintained for the clean samples, but Ra values were closer to their corresponding microscale values for the smooth sample. After BSA coating the pattern of surface roughness was altered (Table 5-1) as sample C was rougher than D and E.

5.4.2 AFM tip functionalization

In order to observe the positive functionalization of the AFM tips with bacteria, SEM was employed (Figure 5-5). It is clear from these images that functionalization of the tips was successful as cells are clustered on the AFM tip for each species of bacteria.

5.4.3 Contact angles and surface energy parameters

The contact angles for all three liquids on each glass sample are shown in Table 5-2. For water, the contact angle was lowest on glass sample A, almost half the value as glass samples B-E that had contact angles ranging between 43 and 50^{o}. The contact angles of glycerol demonstrated a slight increase from 59^{o} for glass sample A, with the other samples in the range of 61-67^{o}. There was no change in the contact angle for hexadecane on any of the glass samples as this measurement remained at 4^{o}. Contact angle measurements were also obtained for all glass samples coated with BSA and the result are shown in Table 5-3; there was a difference in contact angles of water that ranged between 3 and 5^{o} after BSA was applied. No changes were noticed for the contact angles of glycerol and the same can be said regarding the measurements using hexadecane.

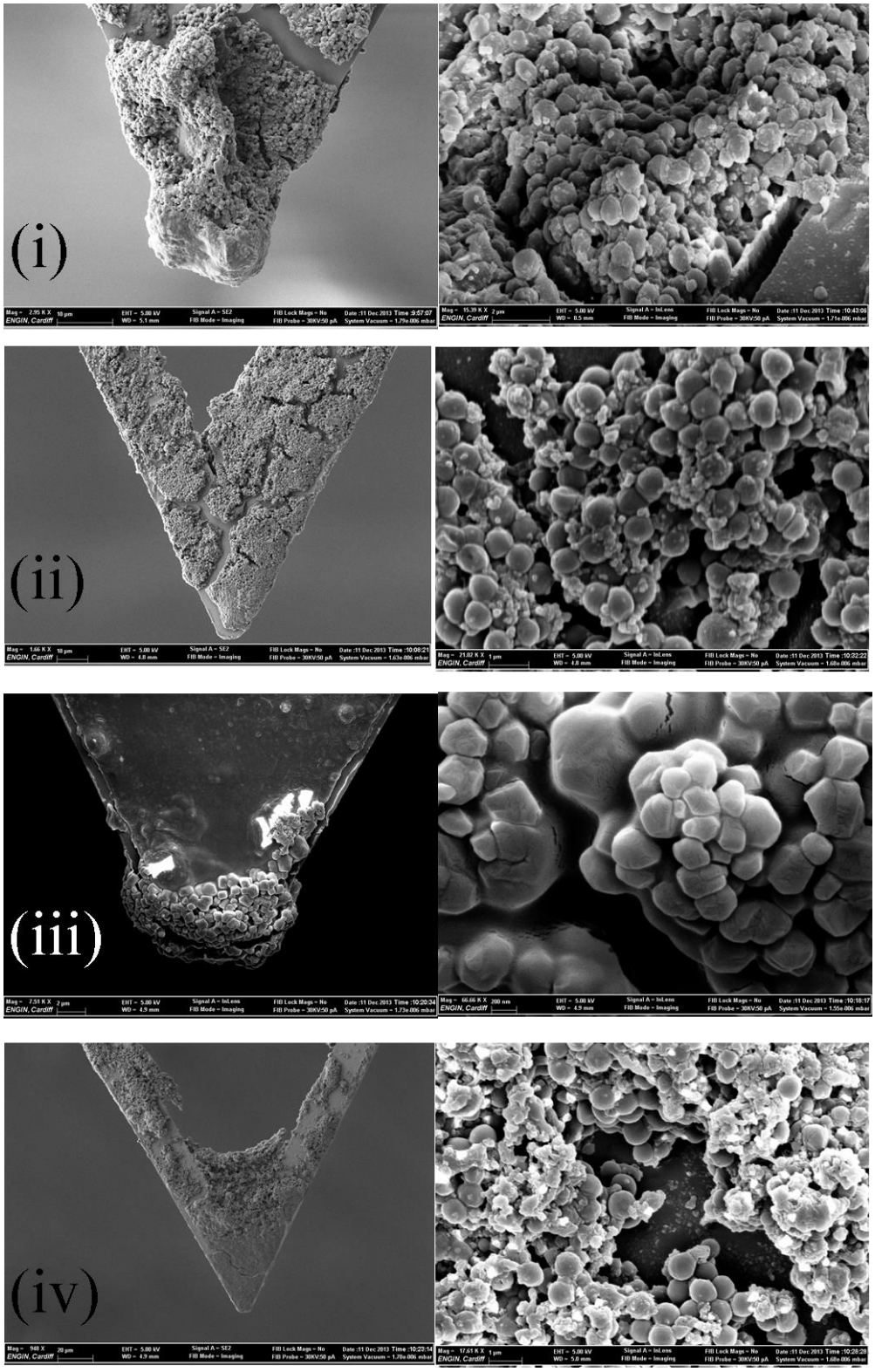

Figure 5-5. SEM images demonstrating bacterial attachement on an AFM tip: (i) *S. epidermidis* RP62a; (ii) *S. epdermidisi* ATCC12228; (iii) *S. aureus*; and (iv) *S. mutants.*

The contact angles were used to calculate the surface energy parameters of the samples that are given in Table 5-2 for uncoated glass samples and in Table 5-3 for all BSA coated glass. Overall, there was little difference in the electron-donor and electron-acceptor parameters (γ^{AB}), with a variation of a few mJ/m^2. Also, the Lifshitz-Van der Waals surface free energy component (γ^{LW}) remained consistent throughout the glass samples at 27.2 mJ/m^2. Due to these small variations, it is obvious that the total surface free energies for all untreated bare glass samples had little difference and was in the range 29-34 mJ/m^2.

Table 5-2. Contact angles of water (ϑ_w), glycerol (ϑ_g), hexadecane (ϑ_h) on borosilicate glass samples (mean ± standard deviation) and surface energy parameters.

Sample	ϑ_w	ϑ_g	ϑ_h	γ_S^{LW} (mJ/m^2)	γ_S^+ (mJ/m^2)	γ_S^- (mJ/m^2)	γ_S^{AB} (mJ/m^2)	γ_S^{TOT} (mJ/m^2)
A	27±4	59±7	4±1	27.2	0.1	72.4	5.4	32.5
B	47±5	65±5	4±1	27.2	0.1	49.0	4.4	31.6
C	50±2	68±7	4±1	27.2	0.0	48.0	1.4	28.5
D	44±3	65±4	4±1	27.2	0.0	55.0	2.6	29.7
E	43±5	62±3	4±1	27.2	0.2	52.0	6.9	34.1

Similarly, once the BSA coating was applied to each glass sample, the Lifshitz-Van der Waals surface energy component remained the same as previously

stated for the bare glass sample at 27.2 mJ/m^2. There was a slight increase in the electron-donor and electron acceptor parameter when compared to the bare glass; however, there was no significant change between samples with the range increasing slightly to 4.4-5.9 mJ/m^2. Also, these calculations have shown a more consistent total surface free energy over all samples ranging from 31-33 mJ/m^2.

Table 5-3. Contact angles of water (ϑ_w), glycerol (ϑ_g), hexadecane (ϑ_h) on BSA coated borosilicate glass samples (mean ± standard deviation) and surface energy parameters.

Sample	ϑ_w	ϑ_g	ϑ_h	γ_S^{LW} (mJ/m^2)	γ_S^+ (mJ/m^2)	γ_S^- (mJ/m^2)	γ_S^{AB} (mJ/m^2)	γ_S^{TOT} (mJ/m^2)
A	4±1	56±5	4±1	27.2	0.1	86.0	5.9	33.0
B	3±2	51±4	4±1	27.2	0.5	79.0	4.4	31.5
C	4±1	56±4	4±1	27.2	0.1	87.0	4.4	31.5
D	4±1	56±3	4±1	27.2	0.1	85.8	5.9	33.0
E	3±1	56±8	4±1	27.2	0.1	86.0	5.9	33.0

5.4.4 Microbial Adhesion to Solvent (MATS)

The results of the MATS analysis are given in Figure 5-6 and demonstrated that *S. epidermidis* RP62a had the highest affinity to both non-polar solvents i.e. hexadecane and decane (around 64%); *S. epidermidis* ATCC12228 also had high affinity for these non-polar solvents with values of 52% and 64% for hexadecane and decane, respectively. From this, it could be deduced that both *S. epidermidis* strains were more hydrophobic compared to the other bacterial

strains (*S. aureus* and *S. mutants*); with *S. aureus* having a relative affinity at around 40% for hexadecane and 48% for decane, whereas *S. mutants* had the lowest affinity for both non-polar solvents at around 8% for hexadecane and 20% for decane; suggesting hydrophilic properties.

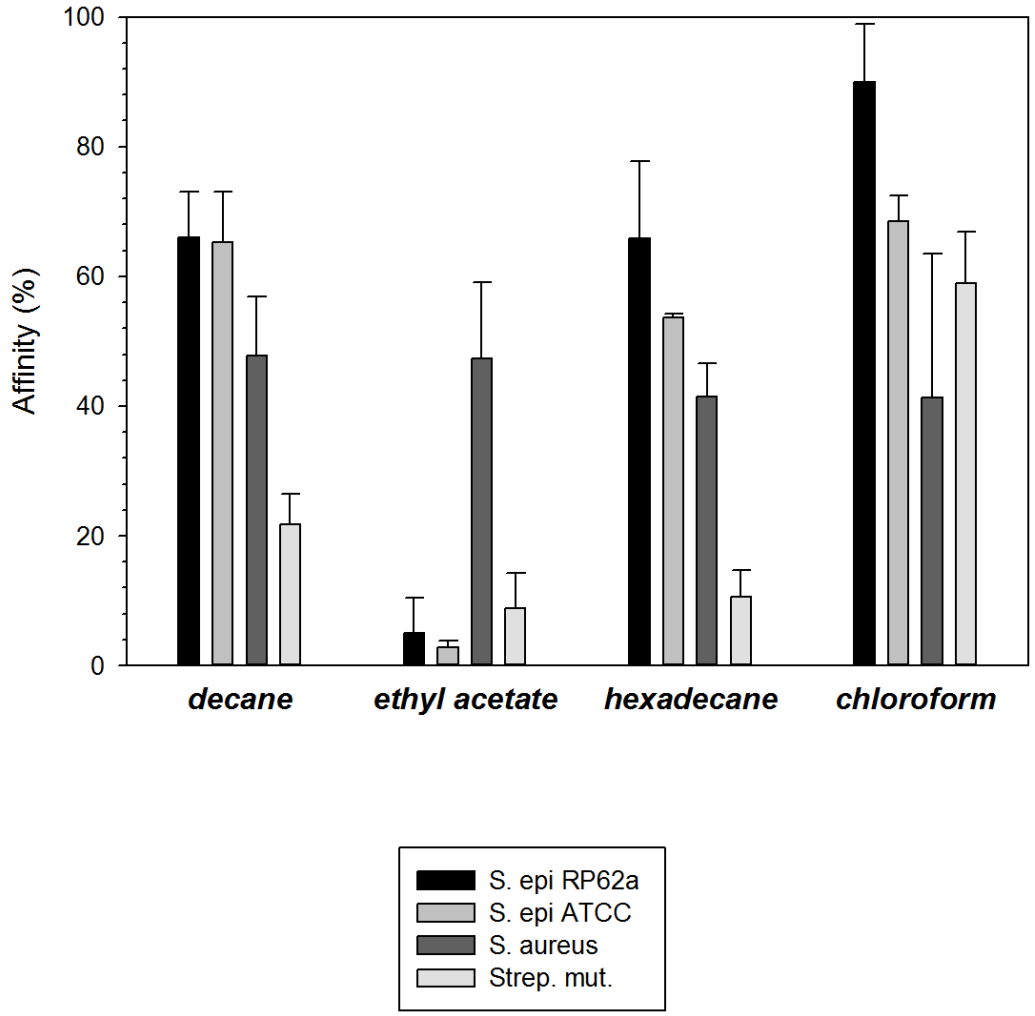

Figure 5-6. Affinity towards solvents of bacteria (Microbial Adhesion to Solvents - MATS)

It is obvious that *S. epidermidis* RP62a demonstrated the greatest affinity towards chloroform (92%) suggesting that *S. epidermidis* RP62a had affinity towards electron acceptor materials, whilst the markedly lower affinity (4%) for ethyl acetate indicating low attraction to electron donor surfaces. This is also the case for *S. epidermidis* ATCC12228; however, *S. aureus* had a strong affinity for ethyl acetate (electron donor) (48%) and for chloroform (40%), therefore, this bacterium had a moderate attraction to either electron donor or acceptor materials. Instead, *S. mutants* had a relatively high affinity for chloroform (60%) and low for ethyl acetate demonstrating this bacterium has high affinity towards electron acceptor materials.

5.4.5 Adhesion Force Measurements

Cumulative distribution of the adhesion forces measured for each bacteria on all substrates are shown in Figure 5-7 and Figure 5-8. Almost in all cases these distribution did not appear to follow a Gaussian profile therefore, median values were extracted in order to make comparisons (Table 5-4 and Table 5-5).

It was observed that *S. mutants* had the lowest adhesion force regardless of the roughness on uncoated glass surfaces in PBS (Figure 5-7). However, there was not a great difference in adhesion forces among *S. epidermidis* RP62a, *S. epidermidis* ATCC12228 and *S. aureus* to sample A with all having similar adhesion force of about 4-5 nN. *S. epidermidis* RP62a demonstrated the highest overall adhesion forces against the glass in PBS, with increasing adhesion with increasing surface roughness of the glass (Figure 5-7).

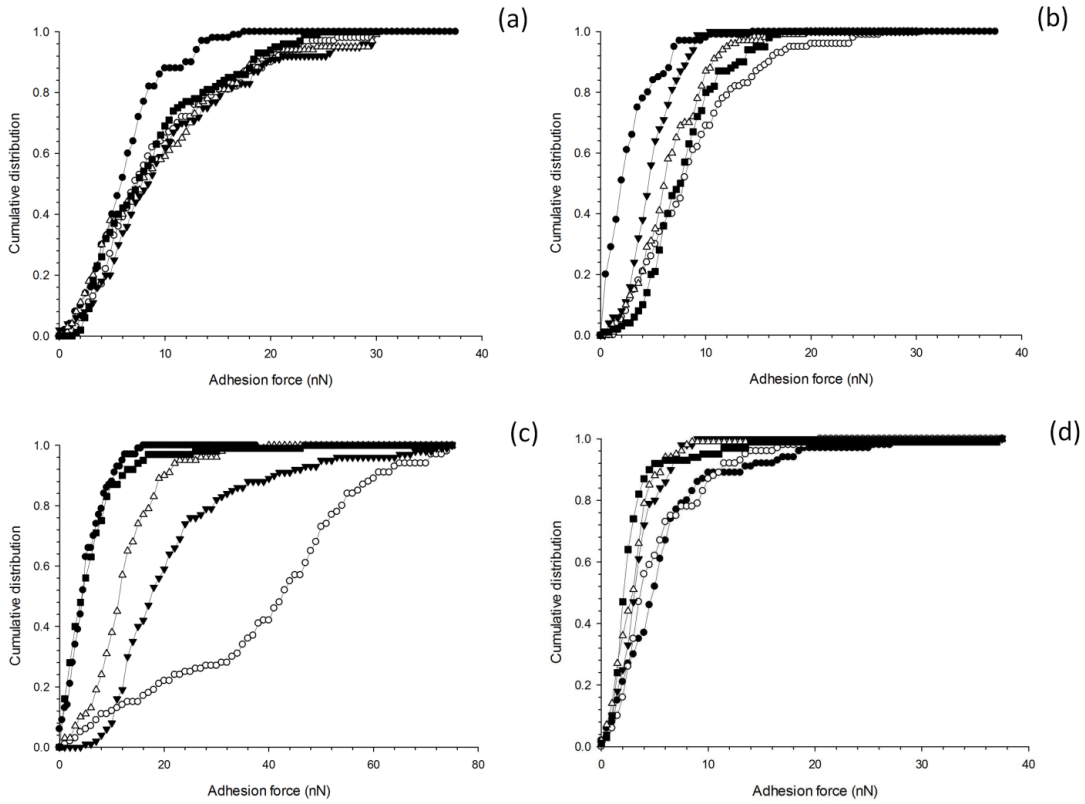

Figure 5-7. Cumulative distribution of adhesion force measurements of (a) *S. aureus,* (b) *S. epidermidis* ATCC12228, (c) *S. epidermidis* RP2a and (d) *S. mutants* against borosilicate glass in PBS.

● A ■ B △ C ▼ D ○ E

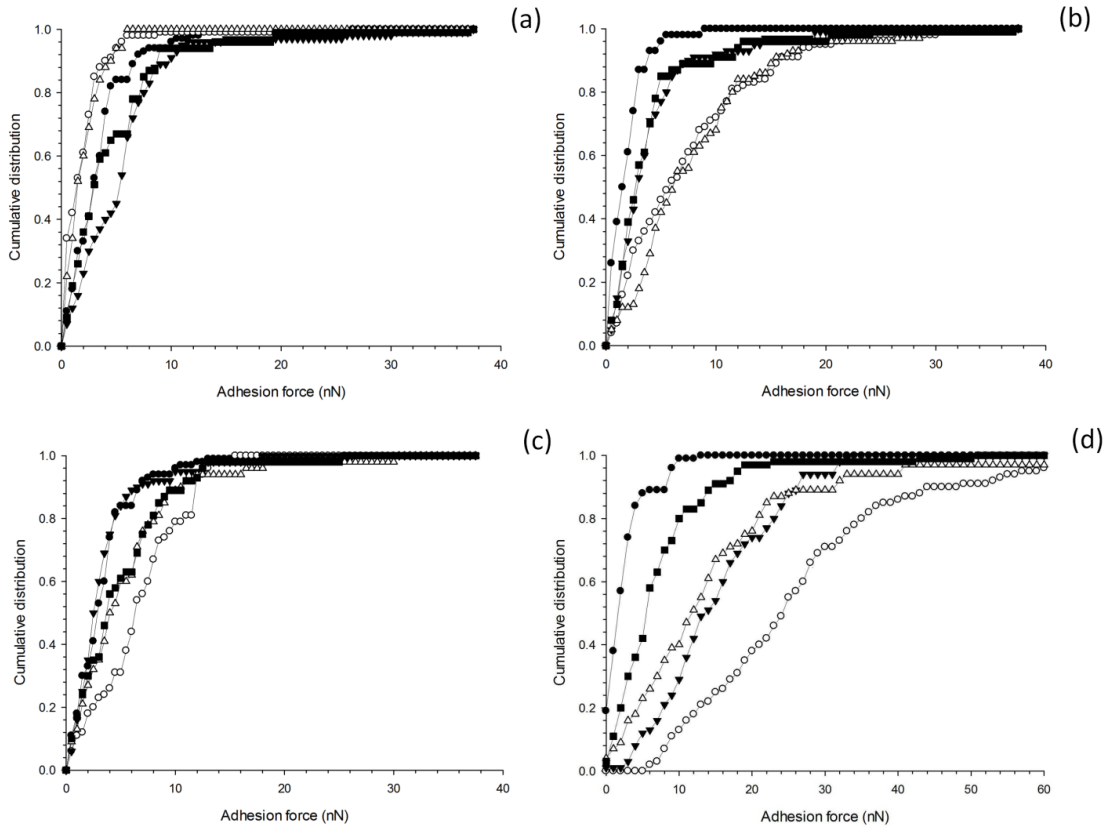

Figure 5-8. Cumulative distribution of adhesion force measurements of (a) *S. aureus,* (b) *S. epidermidis* ATCC12228, (c) *S. epidermidis* RP2a and (d) *S. mutants* against BSA coated borosilicate glass.

● A ■ B △ C ▼ D ○ E

Also, *S. epidermidis* ATCC12228 had a similar pattern of adhesion forces increase with increasing roughness, although not reaching the same values as *S. epidermidis* RP62a; moreover, samples B and C had higher adhesive forces compared to their rougher counterparts D and E (Figure 5-7). Interestingly, the adhesion forces measured for *S. aureus* had little change over the range of

glass samples regardless of the topography. This was also similar for *S. mutants* on uncoated samples (Figure 5-7).

Table 5-4. Median values of bacterial adhesion forces (nN) against clean glass samples.

	S. epidermidis RP62a	*S. epidermidis* ATCC12228	*S. aureus*	*S. mutants*
A	4.25	2.0	5.75	4.75
B	4.2	7.6	9.25	2.5
C	11.5	6.0	9.75	3.0
D	17.5	4.6	10.5	3.2
E	42	7.8	9.0	3.75

Table 5-5. Median values of bacterial adhesion forces (nN) against BSA coated glass samples.

	S. epidermidis RP62a	*S. epidermidis* ATCC12228	*S. aureus*	*S. mutants*
A	2.75	1.5	2.75	0.75
B	3.25	2.75	3.0	5.5
C	4.0	6.0	1.5	12
D	2.5	2.75	5.25	14
E	6.25	5.5	1.25	24

When BSA coating was applied to all glass samples, *S. mutants* had the greatest adhesion to glass surfaces sample C, D and E exhibiting median values of 24 nN (Figure 5-8). When considering the adhesion of all bacteria with BSA coated glass, there was not much difference in adhesion forces for *S. epidermidis* RP62a, as forces were much of an extent regardless of the surface of roughness (Figure 5-8). For *S. epidermidis* ATCC 12228, similar results were observed compared to uncoated samples with adhesion forces increasing with increasing roughness, however, sample C and E had similar adhesion (Figure 5-8).

Because of the altered pattern of roughness caused by the BSA coating (Table 5-1), the possible influence of roughness on adhesion forces was studied through the coefficient of correlation (R^2) between median adhesion force (Table 5-4 and Table 5-5) and surface roughness. The coefficients of correlations increased using surface roughness values obtained from the nanoscale level (scanned areas equal 2 x 2 µm); furthermore, BSA coated surfaces demonstrated greater R^2 values when the actual roughness values (post BSA coating) were used (Table 5-6, Table 5-7 and Table 5-8). Interestingly, bacteria that demonstrated higher R^2 values generally had greater adhesive forces; any negative R^2 values on the rougher surfaces have lower adhesion forces.

Table 5-6. Coefficients of correlation (R^2) for the bacteria adhesion forces in PBS against values of surface roughness obtained from varying scanned areas.

	S. epidermidis RP62a	*S. epidermidis* ATCC12228	*S. aureus*	*S. mutants*
correlation macro	0.995394	0.617702	0.446555	-0.01364
correlation micro	0.98856	0.520074	0.387439	0.077206
correlation nano	0.801811	0.701453	0.777379	-0.35493

Table 5-7. Coefficients of correlation for the bacteria adhesion forces with BSA coated surface against values of surface roughness obtained from varying scanned areas before BSA deposition.

	S. epidermidis RP62a	*S. epidermidis* ATCC12228	*S. aureus*	*S. mutants*
correlation macro	0.755864	0.535618	-0.22737	0.941964
correlation micro	0.688002	0.516285	-0.17544	0.935404
correlation nano	0.458064	0.618088	0.029452	0.941385

Table 5-8. Coefficients of correlation for the bacteria adhesion forces on BSA coated surface against values of surface roughness obtained from varying scanned areas after BSA deposition.

	S. epidermidis RP62a	*S. epidermidis* ATCC12228	*S. aureus*	*S. mutants*
correlation micro	0.626158	0.707773	-0.1518	0.98173
correlation nano	0.611871	0.964164	-0.5494	0.722775

5.5 Discussion

It was found in this study that the scanned area of the sample affects the value of the roughness parameter, for example, sample E had a roughness (Ra) of 6000 nm at the macroscale that decreased at the microscale to 94 nm; this was further reduced at the nanoscale to 62 nm. The results showed that roughness parameters are scale dependent, such phenomenon had also been presented by Perni et al. (31, 32), who determined the roughness of photo-activated materials. This gradual decrease in the overall roughness parameter is important to consider when concerned with the contact area of bacteria and establishing correlation between adhesion forces and roughness. It is noteworthy to mention that the roughness measurements decreased significantly at the nanoscale once a BSA coating was applied; as sample E after BSA coating exhibited an Ra of just 4.2 nm.

Adhesion can be considered as a multifaceted phenomenon, which involves a variety of aspects supplied by both contacting surfaces. Surface topography has been considered (33) an influential feature governing the extent of adhesion due to variations of the physicochemical nature of the surface (1). Bacteria, for example, are known to associate with a wide range of surfaces, natural or synthetic (5) mainly as a survival technique. An advantage of adhesion to a surface is the accumulation of nutrients (34-36); therefore, attaching to a surface has a positive effect compared to free floating (planktonic bacteria). Remarkably, the environment surrounding the bacteria and the nutrients will have an effect on the structure of the adhering microorganisms (35) thereby allowing for adaptation and flexibility to survive.

Although this strategy is beneficial for the bacteria in question, it can cause a number of problems in humans, for example, in biomaterials (prosthetic hip and knee joints), as well as vascular grafts and dental implants (2, 27, 34-36) as bacteria can induce adverse biological responses. Any surface in contact with biological fluids will become coated by a layer of the proteins present in the fluid in a very short period of time; therefore, the subsequent cell adhesion will occur on such coated surface and not on the original substrate (3, 6, 9). Despite reports of possible anti-biofilm formation properties of BSA (36), in order to mimic the presence of this layer, BSA is often used because of its biological relevance (17, 37, 38).

Generally, in biofilm formation, the bacteria will produce EPS consisting of polysaccharides, proteins, nucleic acids and lipids (2, 39), this matrix has a protective function providing mechanical stability. It is this matrix that aids the resistance to antibiotics (2, 6), affecting the success or failure of implanted medical devices and causing endless, costly problems to the healthcare system as well as the patients (2). The main bacteria responsible for failures in implants are *S. epidermidis* ATCC12228, RP62a; *S. aureus* ATCC25923; and *S. mutants (40-42)* and for this reason they were selected for this work.

Immobilization of cells on a support for imaging, or to prepare colloidal probes, inevitably induces some changes on the cells (26, 43). Protocols are based on different approaches, for example entrapment and covalently binding; each method presents advantages and disadvantages; for example, poly-L-lysine can have antimicrobial activity but it is simple and suitable for almost any type of cell, whilst the formation of covalent bonds between the cell and the substrate

leads to chemical changes of the cell surface (43). As demonstrated by Colville et al. (44), although cell adhering to poly-L-lysine coated substrate presented signs of stress, they remained for the majority viable when immersed in buffer.

Despite the unavoidable variation in the colonization extent of the AFM cantilever, the results showed that the forces of adhesion across three cantilevers colonized, in different occasions, with cells originated from independent cultures exhibited little variation. This is likely to be the consequence of the fact that adhesion forces measurements are only influenced by the cells present on the tip and not by cells in other locations on the cantilever.

Some of the variations in overall adhesion forces can be attributed to the bacterial strain (45, 46), which are the most common gram-positive pathogens. The opportunistic pathogen *S. epidermidis* often forms biofilms that enable the bacteria to colonize many medical devices, this is enabled by adhesion factors such as proteins and intracellular adhesion (42). However, *S. epidermidis* RP62A is a biofilm producing strain, yet the ATCC 12228 is a non-biofilm former (42), with a gene cluster associated with methicillin-resistant *Staphylococcus aureus* (MRSA). It has been noted that the difference between *S. epidermidis* and *S. aureus* is the lack of staphylococcal enterotoxins, leukocides, α-toxins, protein A and adherence factors in *S. epidermidis (45)*, all of which aid in the survival and virulence of the strain. However, it is important to note that *S. aureus* tends to be more virulent than *S. epidermidis* due to its ability to acquire foreign DNA and enriched immune response (45). Most biofilms develop in

niches and cracks within implanted devices, but adhesion to the surfaces is also facilitated by the hydrophobic attraction and electrostatic repulsion (47).

It has been highlighted that initial bacterial adhesion to a surface occurs at defects on the surface such as: cracks or grooves (45-48), this is due to the primitive survival instinct of bacteria as these points provide protection from external factors, such as shear forces (48). Also, the transition from reversible to irreversible adhesion is governed by these peaks and troughs on a surface (48), therefore, a rougher surface effectively increases the area available for adhesion to take place. However, the role of surface roughness on bacterial adhesion is still without general consensus; a possible reason for this is that, as we have shown in this work, the parameter indicating the roughness of a surface is scale dependent (25) and, consequently, the correlation between surface forces and *Ra* vary according to the size of the area scanned to calculate the roughness value. Additionally, on BSA coated surfaces, the value of roughness post-coating is different from the "nominal" value pre-coating; furthermore, the BSA coating was not a layer of perfectly uniform thickness as the pattern of surface roughness was altered the protein adsorption. All these phenomena contribute to the uncertainty regarding the effect of surface roughness and bacterial adhesion. Adhesion forces between two contacting bodies can be assumed to be the sum of all individual forces generated by the peaks in contact, hence the rougher a surface the higher the adhesion forces as more peaks are in contact. However, when the roughness of a surface is measured on a scale much bigger than the contacting object (in this work a bacteria cell), it is likely that the object could be smaller than the measured

peaks and thus no correlation between roughness and adhesion found. On the contrary, when surface roughness is measured on a scale comparable to the contacting object, an increase in roughness could result in higher adhesion forces as the contacting area between the two surfaces increases as shown by Verran et al. (49). Similar trends were found by Waerhaug (50) who demonstrated that roughening subgingival enamel increased the deposition of dental plaque. Also, the adhesion of bacterial cells on Titanium and polymer surfaces was promoted by the presence of nanoscale topographical features (51, 52). Moreover, the importance of the scale of the roughness on cell adhesion was highlighted by Taylor et al. (53) who found that a small increase in surface roughness resulted in a significant increase in bacterial adhesion while a large increase in surface roughness did not result in a very significant increase in adhesion.

Adhesion forces between bacteria and substrates present both nonspecific and specific contributions, the latter specially when a protein coating is present on the surface (54); at the same time, when only non specific interactions are present, the adhesion forces are in the range of a few nN, whilst they are two to three times higher for specific interactions (54); adhesion could also be subjected to "bond maturation" (55), we have avoided this phenomenon measuring the adhesion forces without delay. Also, adhesion force between bacteria cells and substrates generally do not follow a normal distribution (55-57) as in this work.

The results showed adhesion forces mainly in the range of 4-5 nN for uncoated glass samples, corroborating previous results (58) apart from *S. epidermidis*

RP62a. Additionally, *S. mutants* on BSA coated had the highest adhesion forces reinforcing the role of this protein in *Streptococci* adhesion as found previously, despite the BSA non specific contribution to adhesion forces (55).

Many bacteria possess MSCRAMMs (Microbial Surface Components Recognizing Adhesive Matrix Molecules) (59) that allow them specific interactions with fibronectin and not BSA, however, the latter remains a wide spread model protein for surface contamination and our work focused on the role of surface roughness on bacterial adhesion forces and how a protein layer on the surface could alter this through changes in surface roughness and surface energy of the substrate. The results showed that an increase of surface roughness resulted in an increase of adhesion forces mainly for *S. epidermidis* RP62a on clean glass samples and *S. mutants* on BSA coated samples; the latter trend found also for other *Streptococci* species (55).

MATS compares the affinity of microbial cells towards varying organic solvents through a partitioning method (29, 30); the protocol requires four solvents: an electron donor, an electron acceptor and two non-polar solvents; chloroform was employed as the electron acceptor, ethyl-acetate as the electron donor, as well as hexadecane and decane as the non-polar solvents. A simple analogy, therefore, to understand the results is that if the cells affinity is greater towards the electron donor solvent than the non-polar solvent it can be concluded that the cell has electron acceptor characteristics and vice versa, i.e. if the cells affinity is higher for electron acceptor solvents compared to the non-polar solvents then the cell is said to have electron donor characteristics. Also, the hydrophobicity of the cell can be measured; the higher the affinity towards the

hydrophobic solvents i.e. hexadecane and decane, the higher the hydrophobicity of the cells surface. *S. epidermidis* RP62a and ATCC 12228 both have a high affinity for hydrophobic surfaces, whereas *S. aureus* and *S. mutants* have more hydrophilic tendencies. These differences suggest and support the claim that certain characteristics of the cell surface such as: fatty acids govern bacteria surface properties (30, 60).

S. epidermidis RP62a had the highest adhesion forces for bare glass and also exhibited an electron donor surfaces as well as the highest affinity towards hydrophobic materials. However, after BSA coating was applied to the glass, *S. mutants* exhibited the highest adhesion forces; this bacterium demonstrated affinity towards hydrophilic surfaces; these considerations match the results of contact angles of uncoated and BSA coated samples (Table 5-3) that showed more hydrophilic surfaces after protein deposition (lower contact angles of water on glass samples after BSA coating).

The glass samples exhibited strong electron donor behaviour (high γ^-), whilst only *S. aureus* presented high affinity towards electron donor solvents. It appears, therefore, that Lewis acid-base interactions did not play a significant role in bacteria adhesion forces to glass substrates; the negligible role of Lewis acid-base interactions in bacterial adhesion was also found in other works (30, 61).

5.6 Conclusions

The surface topography has a crucial role in the adhesion phenomena between bacterial cells and substrates in the biofilm formation process. Not only is the bare surface a consideration, but also the fact that proteins will form a conditioning layer on the surface within seconds. This protein layer can effectively mask the real surface and determine the overall adhesion that takes place due to the alterations in the surface chemistry such as hydrophobicity. This investigation, therefore, demonstrates that surface roughness is a critical factor influencing the extent of adhesion forces between glass substrates and bacteria. Furthermore, in virtue of being a scale dependent parameter, better correlations between adhesion forces and surface roughness measurements were obtained when roughness parameters (*Ra*) were determined from areas with sizes comparable to bacterial cells.

5.7 References

1. Bos R, van der Mei HC, Busscher HJ. Physico-chemistry of initial microbial adhesive interactions – its mechanisms and methods for study. FEMS Microbiology Reviews. 1999;23(2):179-230.

2. Busscher HJ, Van Der Mei RBHC. Initial microbial adhesion is a determinant for the strength of biofilm adhesion. FEMS Microbiology Letters. 1995;128(3):229-34.

3. Muszanska AK, Nejadnik MR, Chen Y, van den Heuvel ER, Busscher HJ, van der Mei HC, et al. Bacterial adhesion forces with substratum surfaces and the susceptibility of biofilms to antibiotics. Antimicrobial agents and chemotherapy. 2012;56(9):4961-4.

4. Crawford RJ, Webb HK, Truong VK, Hasan J, Ivanova EP. Surface topographical factors influencing bacterial attachment. Advances in Colloid and Interface Science. 2012;179–182(0):142-9.

5. Busscher HJ, Weerkamp AH. Specific and nonspecific interactions in bacterial adhesion to solid substrata. FEMS Microbiol Rev. 1987;46(2):165-73.

6. Percival S, Malic S, Cruz H, Williams D. Introduction to Biofilms. In: Percival S, Knottenbelt D, Cochrane C, editors. Biofilms and Veterinary Medicine. Springer Series on Biofilms. 6: Springer Berlin Heidelberg; 2011. p. 41-68.

7. Cateau E, Berjeaud J-M, Rodier M-H, Imbert C. Fungal biofilm inhibition by a component naturally produced by Candida albicans yeasts growing as a biofilm. International Journal of Antimicrobial Agents. 2008;31(2):166-70.

8. Piñeres J, Barraza J. Energy barrier of aggregates coal particle–bubble through the extended DLVO theory. International Journal of Mineral Processing. 2011;100(1–2):14-20.

9. Walker JT, Marsh PD. A review of biofilms and their role in microbial contamination of dental unit water systems (DUWS). International Biodeterioration & Biodegradation. 2004;54(2–3):87-98.

10. Van Houdt R, Michiels CW. Role of bacterial cell surface structures in Escherichia coli biofilm formation. Research in Microbiology. 2005;156(5–6):626-33.

11. Jaglic Z, Červinková D, Vlková H, Michu E, Kunová G, Babák V. Bacterial Biofilms Resist Oxidising Agents Due to the Presence of Organic Matter. Czech Journal of Food Science. 2012;30(2):178-87.

12. Shi X, Zhu X. Biofilm formation and food safety in food industries. Trends in Food Science & Technology. 2009;20(9):407-13.

13. Hori K, Matsumoto S. Bacterial adhesion: From mechanism to control. Biochemical Engineering Journal. 2010;48(3):424-34.

14. Rochex A, Lebeault JM. Effects of nutrients on biofilm formation and detachment of a Pseudomonas putida strain isolated from a paper machine. Water Research. 2007;41(13):2885-92.

15. Hu Y, Ulstrup J, Zhang J, Molin S, Dupres V. Adhesive properties of Staphylococcus epidermidis probed by atomic force microscopy. Physical Chemistry Chemical Physics. 2011;13(21):9995-10003.

16. Poulsen LV. Microbial Biofilm in Food Processing. LWT - Food Science and Technology. 1999;32(6):321-6.

17. Boks NP, Norde W, van der Mei HC, Busscher HJ. Forces involved in bacterial adhesion to hydrophilic and hydrophobic surfaces. Microbiology. 2008;154(10):3122-33.

18. Tsang CSP, Ng H, McMillan AS. Antifungal susceptibility of Candida albicans biofilms on Titanium discs with different surface roughness. Clin Oral Invest. 2007;11(4):361-8.

19. Percival SL, Knapp JS, Wales DS, Edyvean RGJ. The effect of turbulent flow and surface roughness on biofilm formation in drinking water. J Ind Microbiol Biotech. 1999;22(3):152-9.

20. Fröjd V, Linderbäck P, Wennerberg A, Chávez de Paz L, Svensäter G, Davies J. Effect of nanoporous TiO2 coating and anodized Ca2+ modification of Titanium surfaces on early microbial biofilm formation. BMC Oral Health. 2011;11(1):1-9.

21. Cao T, Tang H, Liang X, Wang A, Auner GW, Salley SO, et al. Nanoscale investigation on adhesion of E. coli to surface modified silicone using atomic force microscopy. Biotechnology and Bioengineering. 2006;94(1):167-76.

22. Bendersky M, Davis JM. DLVO interaction of colloidal particles with topographically and chemically heterogeneous surfaces. Journal of Colloid and Interface Science. 2011;353(1):87-97.

23. Bohinc K, Dražić G, Fink R, Oder M, Jevšnik J, Nipič D, et al. Available surface dictates microbial adhesion capacity. International journal of adhesion and adhesives. 2014;50((1)):265-72.

24. Homola AM, Israelachvili JN, McGuiggan PM, Gee ML. Fundamental experimental studies in tribology: The transition from “interfacial” friction of undamaged molecularly smooth surfaces to “normal” friction with wear. Wear. 1990;136(1):65-83.

25. Blau PJ. Scale Effects in Steady-State Friction. Tribology Transactions. 1991;34(3):335-42.

26. Allen S, Davies MC, Roberts CJ, Tendler SJB, Williams PM. Atomic force microscopy in analytical biotechnology. Trends in Biotechnology. 1997;15(3):101-5.

27. Mistry S, Kundu D, Datta S, Basu D. Comparison of bioactive glass coated and hydroxyapatite coated Titanium dental implants in the human jaw bone. Australian dental journal. 2011;56(1):68-75.

28. Sader JE, Larson I, Mulvaney P, White LR. Method for the calibration of atomic force microscope cantilevers. Review of Scientific Instruments. 1995;66(7):3789-98.

29. Bellon-Fontaine MN, Rault J, van Oss CJ. Microbial adhesion to solvents: a novel method to determine the electron-donor/electron-acceptor or Lewis acid-base properties of microbial cells. Colloids and Surfaces B: Biointerfaces. 1996;7(1–2):47-53.

30. Prokopovich P, Perni S. An investigation of microbial adhesion to natural and synthetic polysaccharide-based films and its relationship with the surface energy components. Journal of materials science Materials in medicine. 2009;20(1):195-202.

31. Perni S, Prokopovich P, Piccirillo C, Pratten J, Parkin IP, Wilson M. Toluidine blue-containing polymers exhibit potent bactericidal activity when irradiated with red laser light. Journal of Materials Chemistry. 2009;19(18):2715-23.

32. Perni S, Piccirillo C, Pratten J, Prokopovich P, Chrzanowski W, Parkin IP, et al. The antimicrobial properties of light-activated polymers containing methylene blue and gold nanoparticles. Biomaterials. 2009;30(1):89-93.

33. Prokopovich P, Starov V. Adhesion models: From single to multiple asperity contacts. Advances in Colloid and Interface Science. 2011;168(1–2):210-22.

34. Fletcher M. Bacterial biofilms and biofouling. Curr Opin Biotechnol. 1994;5(3):302-6.

35. Hall-Stoodley L, Costerton JW, Stoodley P. Bacterial biofilms: from the Natural environment to infectious diseases. Nat Rev Micro. 2004;2(2):95-108.

36. Huang TT, Sturgis J, Gomez R, Geng T, Bashir R, Bhunia AK, et al. Composite surface for blocking bacterial adsorption on protein biochips. Biotechnol Bioeng. 2003;81(5):618-24.

37. Xu CP, Boks NP, de Vries J, Kaper HJ, Norde W, Busscher HJ, et al. Staphylococcus aureus-fibronectin interactions with and without fibronectin-binding proteins and their role in adhesion and desorption. Applied and environmental microbiology. 2008;74(24):7522-8.

38. Xu L-C, Logan BE. Interaction Forces between Colloids and Protein-Coated Surfaces Measured Using an Atomic Force Microscope. Environmental Science & Technology. 2005;39(10):3592-600.

39. Flemming HC, Wingender J. The biofilm matrix. Nature reviews Microbiology. 2010;8(9):623-33.

40. Valour F, Trouillet-Assant S, Rasigade J-P, Lustig S, Chanard E, Meugnier H, et al. Staphylococcus epidermidis in Orthopedic Device Infections: The Role of Bacterial Internalization in Human Osteoblasts and Biofilm Formation. PLoS pathogens. 2013;8(6):1-11.

41. Widmer AF. New Developments in Diagnosis and Treatment of Infection in Orthopedic Implants. Clinical Infectious Diseases. 2001;33(Supplement 2):S94-S106.

42. Rosenthal ME, Dever LL, Moucha CS, Chavda KD, Otto M, Kreiswirth BN. Molecular characterization of an early invasive Staphylococcus epidermidis prosthetic joint infection. Microbial drug resistance (Larchmont, NY). 2011;17(3):345-50.

43. Kuyukina MS, Korshunova IO, Rubtsova EV, Ivshina IB. Methods of microorganism immobilization for dynamic atomic-force studies (review). Appl Biochem Microbiol. 2014;50(1):1-9.

44. Colville K, Tompkins N, Rutenburg AD, Jericho MH. Effects of Poly(L-lysine) Substrates on Attached *Escherichia coli* Bacteria. Langmuir. 2010;26(4):2639-44.

45. Fey PD, Olson ME. Current concepts in biofilm formation of Staphylococcus epidermidis. Future microbiology. 2010;5(6):917-33.

46. Fredheim EGA, Klingenberg C, Rohde H, Frankenberger S, Gaustad P, Flægstad T, et al. Biofilm Formation by Staphylococcus haemolyticus. Journal of Clinical Microbiology. 2009;47(4):1172-80.

47. Loosdrecht MM, Norde W, Lyklema J, Zehnder AB. Hydrophobic and electrostatic parameters in bacterial adhesion. Aquatic Science. 1990;52(1):103-14.

48. Gharechahi M, Moosavi H, Forghani M. Effect of Surface Roughness and Materials Composition on Biofilm Formation. Journal of Biomaterials and Nanobiotechnology. 2012;230(3):541-6.

49. Verran J, Packer A, Kelly PJ, Whitehead KA. Use of the Atomic Force Microscope to Determine the Strength of Bacterial Attachment to Grooved Surface Features Carre A, Mittal KL, editors. The Netherlands: VSP Leiden; 2010.

50. Waerhaug J. Effect of Rough Surfaces Upon Gingival Tissue. Journal of dental research. 1956;35(2):323-5.

51. Truong VK, Lapovok R, Estrin YS, Rundell S, Wang JY, Fluke CJ, et al. The influence of nano-scale surface roughness on bacterial adhesion to ultrafine-grained Titanium. Biomaterials. 2010;31(13):3674-83.

52. Bakker DP, Busscher HJ, van Zanten J, de Vries J, Klijnstra JW, van der Mei HC. Multiple linear regression analysis of bacterial deposition to polyurethane coatings after conditioning film formation in the marine environment. Microbiology. 2004;150(Pt 6):1779-84.

53. Taylor RL, Verran J, Lees GC, Ward AJ. The influence of substratum topography on bacterial adhesion to polymethyl methacrylate. Journal of materials science Materials in medicine. 1998;9(1):17-22.

54. Busscher HJ, Norde W, van der Mei HC. Specific Molecular Recognition and Nonspecific Contributions to Bacterial Interaction Forces. Applied and environmental microbiology. 2008;74(9):2559-64.

55. Mei L, Busscher HJ, van der Mei HC, Ren Y. Influence of surface roughness on streptococcal adhesion forces to composite resins. Dent Mater. 2011;27(8):770-8.

56. van der Mei HC, de Vries J, Busscher HJ. Weibull analyses of bacterial interaction forces measured using AFM. Colloids and Surfaces B: Biointerfaces. 2010;78(2):372-5.

57. Mei L, Busscher HJ, Van Der Mei HC, Chen Y, De Vries J, Ren Y. Oral bacterial adhesion forces to biomaterial surfaces constituting the bracket–adhesive–enamel junction in orthodontic treatment. European Journal of Oral Sciences. 2009;117(4):419-26.

58. Busscher HJ, van de Belt-Gritter B, Dijkstra RJB, Norde W, van der Mei HC. Streptococcus mutans and Streptococcus intermedius Adhesion to Fibronectin Films Are Oppositely Influenced by Ionic Strength. Langmuir. 2008;24(19):10968-73.

59. Perkins S, Walsh EJ, Deivanayagam CCS, Narayana SVL, Foster TJ, Höök M. Structural Organization of the Fibrinogen-binding Region of the Clumping Factor B MSCRAMM of Staphylococcus aureus. Journal of Biological Chemistry. 2001;276(48):44721-8.

60. Mastronicolis SK, Berberi A, Diakogiannis I, Petrova E, Kiaki I, Baltzi T, et al. Alteration of the phospho- or neutral lipid content and fatty acid composition in Listeria monocytogenes due to acid adaptation mechanisms for hydrochloric, acetic and lactic acids at pH 5.5 or benzoic acid at neutral pH. Antonie van Leeuwenhoek. 2010;98(3):307-16.

61. Perni S, Preedy EC, Prokopovich P. Success and failure of colloidal approaches in adhesion of microorganisms to surfaces. Advances in Colloid and Interface Science. 2014;206(0):265-74.

Chapter 6 - Cobalt and Titanium Nanoparticles Influence on Mesenchymal Stem Cell Nanomechanics

The content of this chapter has been presented and partially published at:

S. Perni, E. Callard Preedy, P. Prokopovich "Cobalt and Titanium Nanoparticle Influence on Mesenchymal Stem Cell Elasticity and Turgidity" Under review to Public Library of Science One and proceeding from Smart and Green Interfaces Meeting, 30 March-1 April 2015, Belgrade, Serbia

6.1 Abstract

Bone cells are often reported as being damaged by inflammatory responses due to wear particles originating from total joint replacement implants. Generally, investigations on nanoparticles influence on mammalian cells are focused on the assessment of cell viability, cytokines release and gene up/down regulation. However, cell nanomechanical properties such as elasticity and turgor pressure have been shown to be involved in biological responses to both chemical and physical cues and therefore, wear particles induced changes in cell mechanical properties, could lead to further understanding of interactions between cells and nanoparticles.

Mesenchymal stem cells (MSCs) elasticity and turgidity were investigated when exposed to Cobalt and Titanium nanoparticles of different sizes for up to 3 days. AFM nanoindentation was carried out on multiple locations on each cell to determine the spatial variation of the mechanical properties whilst viability was assessed using flowcytometry and MTT assay. The results demonstrated that cells exposed to increasing concentrations of nanoparticles had a lower value of elasticity and spring constant without significant effect on cell metabolic activity and viability as shown by MTT assay and flowcytometry. Cobalt induced greater effect than Titanium and this is consistent with the general knowledge of cytocompatibility of the latter. Moreover, lower elasticity is physiologically linked to a lower turgor pressure as cells can sustain only small size variations, in response to osmotic pressure changes, without irreversible damage.

This work demonstrates for the first time that metal nanoparticles do not only influence cell enzyme activity but also cell structure; however, they do not result

in full membrane damage. Furthermore, the mechanical changes are concentration and particles composition dependent but little influence by the particle size.

6.2 Introduction

It is now widely accepted that cells physically interact with their surrounding in multiple ways and that these mechanical cues can be as important as biochemical ones. Cells are sensitive to forces, stiffness and adhesion [1] such as the stresses (forces) and strains (deformation) of their environment [1, 2]; therefore, cells can respond to internal as well as external forces, for example, detecting the mechanics of interacting substrates will generate internal forces which depend on the mechanical properties of the cell [3].

These mechanical properties of cells have been of interest [2, 4] in the understanding of certain pathological disorders including cancer, osteoporosis, atherosclerosis, and osteoarthritis [3]. As these stresses and strains exerted on cells can generate signals similar to chemical stimuli which initiates cell growth, promoting cell survival and differentiation, as well as apoptosis [1]. This is of particular interest when considering bone cells and its behaviour as a result of exposure to wear particles.

Articulating surfaces of medical implants, resulting from total joint replacement surgeries, generate a large number of particles (macro, micro and nano sizes) as a result of wear process over time [5]. Wear particles originate from the relative motion of two contacting surfaces under loading [5]. The smaller the

particle, the greater its surface area relative to its volume and thus the greater its physical interaction and chemical reactivity. Damage from wear can directly affect the implanted device causing loss of tolerance, friction and therefore the expected longevity of the device is minimised [6].

On the other hand, wear particles also initiate an immune response inducing aseptic loosening, and osteolysis [6-8] which disrupts the integrity of the implant and bone surface [6]. Wear particles-induced osteolysis is the principal cause of aseptic loosening. The cellular mechanism of the response to wear particles involves macrophages, monocytes, osteoblasts, and osteoclasts cells [9, 10]. Osteolysis is a result of an inflammatory response to these foreign particles activating macrophage defence mechanism in the periprosthetic tissues and the surrounding joint replacement [8]. The issues highlighted have an inherent affect disrupting the normal bone remodelling process and implant acceptance [11, 12]. Disruptions commonly occur due to the uptake of nano-sized metal particles to surrounding cells which are biologically active causing greater inflammation, DNA and chromosome damage, cytokine release and cytotoxicity in cells than their micro-sized counterparts [8, 13-15]; and has been recognised as a current problem in orthopaedic implants as metal-on-polyethylene and metal-on-metal (MoM) implants generate large numbers of particles (such as Cobalt chromium, Titanium, and polyethylene) [12, 16, 17]. These particles tend to be in the size range that appeal to macrophages during phagocytosis [12], resulting in inflammatory cell response thereby often causing aseptic loosening of the implant. Osteoprogenitor cells have been implicated as another target in particle-mediated osteolysis [18-26]. Multipotent mesenchymal stem cells

(MSCs) in trabecular bone [27-29] and adjacent to implants have osteoprogenitor activities and are critical contributors to maintaining osseous tissue integrity. Perturbation of MSC osteogenic activity may thus affect bony ingrowth and interface stability, leading to increased risk of loosening.

While many studies have focused on the effect of particles on macrophages [30] or osteoprogenitor cells [18-20], in terms of reduced osteogenic differentiation, proliferation and enhanced apoptosis; differential and combined effects of cell mechanical properties after exposure to wear particles have not been studied. The function of a cell is closely linked to its structure [31]. The cell cytoskeleton, to a large extent, is responsible for the structural and mechanical integrity of cells and takes an active role in signalling pathways (i.e. mechanotransduction). Thus, any changes in the cell structure will result in changes to the mechanical properties of the cell and consequently its functionality. Hence, the ability to measure mechanical properties of cells at different levels, in particular the nano-level, might be considered a powerful method to assess cell and tissue functionality. Recently, there has been a significant increase in number of studies investigating mechanical properties of cell/tissue. Investigations of the impact of diverse physiological conditions on the mechanical properties of various cells, expressed mainly as stiffness, and quantified by the Young's modulus have given us a new understanding of the cell; leading to discoveries of complex pathways that govern cell responses and functionality [31-37].

In this study, we hypothesised that exposure to Cobalt and Titanium nanoparticles will modify MSC cells nanomechanical and adhesive properties.

Therefore, the aim of this study was to directly quantify the elasticity, turgidity and adhesiveness of MSCs after exposure for different periods of time to Cobalt and Titanium nanoparticles of various compositions, sizes and charges employing advanced AFM techniques. The findings from cell nanomechanical and adhesive properties also were supported by cells viability and metabolic activity studies.

6.3 Materials and Methods

6.3.1 Cell Culture

28 days old, male Wistar rats were obtained from the colony maintained by Charles River European Suppliers (Charles River UK Ltd., Kent, UK). The animals were housed with free access to water and were maintained with treatment and care protocols conformed to UK Animals (Scientific Procedures) Act 1986, in accordance to the European Convention for the Protection of Vertebrate Animals Used for Experimental and Other Scientific Purposes (Strasbourg, Council of Europe). Bone marrow stem cells were isolated from rat femur and humerus, using plastic adherence [38], followed by fibronectin adherence techniques [39]. After 7 days, merged colonies were expanded (passage 0). This study was conducted on cells obtained from early population doubling level.

The cells were routinely cultured in α-MEM (Minimum Essential Medium) (Life Technologies), supplemented with 20% (v/v) FBS (Foetal Bovine Serum), 1% (v/v) of solution penicillin (5000 U/mL) and streptomycin (5000 mg/mL) (Gibco Invitrogen) and 1% (v/v) of L-ascorbic acid 2-phosphate solution at 50 mg/ml

(Sigma, UK). Accutase (Gibco Invitrogen) was used when cells were 70% confluent in order to passage and count. The cells were maintained at 37° C in a humidified atmosphere containing 5% CO_2.

For atomic force microscopy experiments, cells were seeded in 24-well plates at a density of 6000 cells per well and cultured for 24 hours on sterilised polystyrene slides placed inside the well before exposure to nanoparticles. For each type of nanoparticles a stock solution of the nanoparticles suspended in culture media was prepared at 5 mg/ml and appropriate amount was added to each well to reach final concentrations of 5; 12.5; 25 and 50 µg/ml and incubated from 24h up to 3 days. Control samples consisting of cells not exposed to nanoparticles and cultured in the same conditions were used for comparison with treated cells.

For the MTT assay, flowcytometry and cell uptake experiments cells were cultured as described above.

6.3.2 Nanoparticles

Commercially available nanoparticles were obtained of various sizes and compositions from Sigma Aldrich, UK. For Cobalt (Co) nanoparticles (NPs), two samples were employed:

- Co elemental, 30nm diameter (referred as ‘Co 30nm’ throughout the text);
- Co (II,III) oxide, 50nm diameter (referred as ‘Co 50nm’ throughout the text).

Three samples of Titanium (Ti) were employed:

- Ti elemental, 30nm diameter;
- Ti (IV) oxide anatase, 25nm diameter; and
- mixture of Ti (IV) oxide rutile and anatase, 100nm diameter

They are referred to as ‘Ti 30nm’, ‘Ti 25nm’ and ‘Ti 100nm’, respectively, throughout the text.

All nanoparticles were weighed and suspended in α-MEM medium to make a stock suspension of nanoparticles of 5mg/ml. From this stock solution, a number of nanoparticles concentrations (5µg/ml; 12.5 µg/ml; 25 µg/ml and 50 µg/ml) were prepared.

6.3.3 Metabolic activity assay

MTT (3-(4,5-dimethythiazol-2yl)-2,5-diphenyltetrazolium bromide) assay was used to determine the effects of the metal nanoparticles on MSCs viability. It is a colorimetric assay of cell viability and depends on the metabolic activity of the cell as rapidly dividing cells exhibit high rates of MTT reduction. Cells were initially cultured and exposed to nanoparticles as stated above in a 24-wells plate; after the chosen exposure to nanoparticles, the media was replaced with phenol red-free medium and 80 µl of MTT stock solution (5mg/ml) was added to each well and incubated at 37^{o}C in humidified atmosphere containing 5% CO_2 for 2 hour. The metabolised MTT, formazan, was re-suspended with 800 µl of dimethyl sulfoxide (DMSO). 200 µl were transferred to a 96-well plate absorbance at 560nm was read using a spectrophotometer (ELISA Reader Labtech LT-5000MS). All experiments were performed in triplicates with each concentration (5, 12.5, 25 and 50 µg/ml) as well as a control sample of cell suspension not exposed to nanoparticles (untreated cells).

6.3.4 Flow Cytometry

Viability of MSC after exposure to nanoparticles was determined using LIVE/DEAD® Viability/Cytotoxicity Kit, for mammalian cells (Life Technology, UK) through flow cytometry (BD FACSVerse^{TM}). Two fluorescent stains were used: calcein-AM (Excitation 480nm / Emission 520nm) and ethidium homodimer-1 (Excitation 520nm / Emission 615nm); the former returns green fluorescence when interacting with living cells; whilst the latter binds to nucleic acids with red fluorescence only through the compromised membrane as it is cell impermeant.

BD FACSVerse^{TM} was used, with the following red (640nm), blue (488nm) and violet (405nm) lasers and appropriate filters for the chosen dyes. Cells were prepared as described above and after the chosen exposure time elapsed; cells were washed with PBS and trypsinised then re-suspended in sterile PBS. 1 ml of this cell suspension was placed into an Eppendorf and centrifuged at 24 ^{0}C, for 5 minutes at 1800 rpm (363 x g). The supernatant was removed and the pellet of cells in the Eppendorf was resuspended in PBS. 7 μl of both dye solutions, prepared as manufactured recommended were added; then cells were vortexed and left for at least 15 minutes in the dark; after 15 minutes the samples were again centrifuged. Post this centrifugation, the supernatant was removed and the cells re-suspended in PBS, all samples were transferred to FACS tubes prior to sampling. Data collected were then analysed using FlowJo software (LLC, Data Analysis Software, Oregon, USA) to generate four quadrant plots. A gating application is first required to select the cells of interest from the forward and side scatter plot, from this, axis are altered according to

the desired plots and the quadrant application is then selected. These quadrants indicate population fractions of cells that are alive, injured and dead which were calculated according to the distributions in the quadrants.

6.3.5 Zeta potential and size of particles measurements

Particles size was measured through dynamic light scattering (DLS), zeta potential of nanoparticles was measured using laser doppler micro-electrophoresis which calculates the electrophoretic mobility to evaluate the zeta potential. Both characterisations were carried out using Malvern Zetasizer Nano ZS Nano series (Malvern, UK). All measurements were performed on Ti or Co nanoparticles suspensions at 5 µg/ml prepared from a stock solution of 5 mg/ml.

6.3.5.1 Cell nanomechanical property measurements

All AFM force measurements were conducted in an open liquid cell as described in [34], using PBS as the aqueous phase. A triangular tipless cantilever (Bruker, UK) with a nominal spring constants ($K_{cantilever}$) of 0.1 N/m was used; the actual spring constant of the AFM cantilever was determined using the Sader method [35, 36]. Borosilicate glass beads (10 µm in diameter) were glued onto the cantilever and served as cell indentors. In order to prevent indentations depth greater than 400-500 nm, the maximum applied load was set, after preliminary tests, to 1 nN or 2 nN depending on the samples. At least 15 cells were analysed for each sample, at each concentration of particles and at each time point (24, 48, and 72 hours). Cells were first located and then at least 20 approaching and retracting z-piezo coordinates vs. deflection curves

were extracted from randomly selected points on the surface of each cell avoiding the peri-nuclear region. Experiments were performed in triplicates.

6.3.5.2 Cell elasticity and spring constant determination

The approaching part (trace) of the AFM curves was used to calculate the nanomechanical properties of the cells. The Young modulus of the cell surface location under investigation was determined fitting the Hertz model (Eq. 6-1) to the first part of the indentation vs. force curve after contact between AFM tip and cell surface.

$$F = \frac{4}{3}\frac{E}{(1-\nu^2)}\sqrt{R}\delta^{3/2} \quad (6\text{-}1)$$

Where:

F = force recorded by AFM

E = Young modulus

R= radius of the spherical indentor (5 μm)

ν = Poisson ratio (assumed 0.5)

δ = indentation depth

The spring constant of the cell surface in the location probed was determined through the slope of the curve after the Hertzian regime according to:

$$F = k_b \delta \quad (6\text{-}2)$$

Where:

F = force recorded by AFM

K_b = spring constant of the cell

δ = indentation depth

Both models require the determination of the separation between cell surface and AFM tip (δ), this was calculated from the coordinates (z-piezo) of the trace curve assuming that the point of contact corresponded to the local minimum of force; from this:

$$\delta = \left| z - z_0 \right| - d_{cant} \quad (6\text{-}3)$$

Where:

z_0 = z-piezo value of the minimum of the trace curve

z = z-piezo value of the trace curve

d_{cant} = cantilever deflection

δ = indentation depth

and

$$F = K_{Cantilever}\, d_{cant} \quad (6\text{-}4)$$

6.3.5.3 Cell Adhesion force

The adhesion forces between a cell and AFM tip were determined as the minimum value of the retracting (retrace) part of the AFM curve.

6.3.6 Cell metal uptake quantification

Quantification of the cells uptake of the metal nanoparticles was gained by using inductively coupled plasma-mass spectroscopy (ICP-MS). MSCs were grown and exposed to the nanoparticles according to procedure described in section 6.3.1 “Cell Culture”. At the 24 hour period, all media was removed from each well, cells were washed twice with sterile PBS, and 500µl of sub-boiled nitric acid (1:1) was added to each well. The 24-well plate was then placed in an incubator for 24 hours at 60°C in order to digest the cells. After 24 hours in the incubator, from each well 400µl of the solution was transferred into a 15 ml polypropylene tube and filled to a total volume of 8 ml with Milli-Q water. ICP-MS analysis was carried out at sample rate of 1.5ml/min and at characteristic wavelengths of 288.616 nm and 334.940 nm for Cobalt and Titanium ion determination respectively on the Optima 2100DV OES (Perkin Elmer, Waltham, MA, USA) against the Primar 28 element standard.

All experiments were performed independently at least 3 times, and each experiment comprised 3 parallel samples. Results are given as mean ± standard deviation.

6.3.7 Statistical analysis

Comparison of the effect of Ti and Co nanoparticles on mechanical properties of MSCs was performed through ANOVA test followed by Tukey’s *post hoc* test individual pairs of data sets ($p<0.05$). Adhesion forces were compared using the

Kruskal-Wallis test followed by *post hoc* Dunn's with a test for individual pairs of data sets. Statistical analysis was performed using SPSS.

6.4 Results

6.4.1 Size and Charge of nanoparticles

The zeta potentials of nanoparticles in growth media are shown in Table 6-1 along with the pH of each suspension. For all nanoparticles, zeta potentials were negative and Titanium elemental 30nm particles exhibited the lowest negative charge of -44mV, whilst TiO_2 100 nm and 25 nm had the same value ($p<0.05$). Cobalt elemental 25nm and Cobalt oxide (50 nm) had the least negative value at about -20mV and no statistical difference between them ($p<0.05$).

Sizes of nanoparticles did not differ greatly from those stated by the manufacturer i.e. they were consistent.

Table 6-1. Zeta potential of nanoparticles employed and pH of MSC media solution containing them.

Particles	pH	Zeta Potential (mV)	Size (nm)
Co 30nm	8.33	-19.4±1.0	27.3±2.1
CoO_2 50nm	7.19	-20.4±0.8	49.3±0.6
Ti 30nm	7.07	-44.7±1.9	27.7±3.5
TiO_2 100nm	7.15	-28.9±1.7	99.0±2.6
TiO_2 25nm	7.16	-26.8±0.5	27.7±2.3

6.4.2 Metabolic activity

MSC metabolic activity, as assessed through MTT, declined with time over a period of 72 hours regardless of nanoparticle exposure as the control metabolic activity also reduced with time from 1.5 OD to around 1.0 OD (Figure 6-1 and Figure 6-2).

After 24 hours of exposure at each of the concentration tested, Titanium 100nm had the greatest impact on the metabolic activity and Ti 30nm also reduced the viability greater than Ti 25nm (Figure 6-1); furthermore the effect was monotonically growing with growing concentrations.

However, after 48hours Ti 25nm demonstrates a significant impact on the overall metabolic activity of the cells compared to Ti 30nm and Ti 100nm. The effect was also concentration dependent, but at the lowest concentration tested was not statistically different when compared to MSCs not exposed to nanoparticles. Titanium nanoparticles decreased the cell metabolic activity at concentrations greater than 12.5 μg/ml (Figure 6-1) irrespectively of the particles size. Only after 48 hours of exposure the size had an impact on cells viability; the smallest (30 nm) nanoparticles gave the lowest viability and the largest (100 nm) are the highest.

After 72 hours in contact with Ti nanoparticles, MSCs had the same metabolic activity as the cells not exposed to such particles ($p>0.05$).

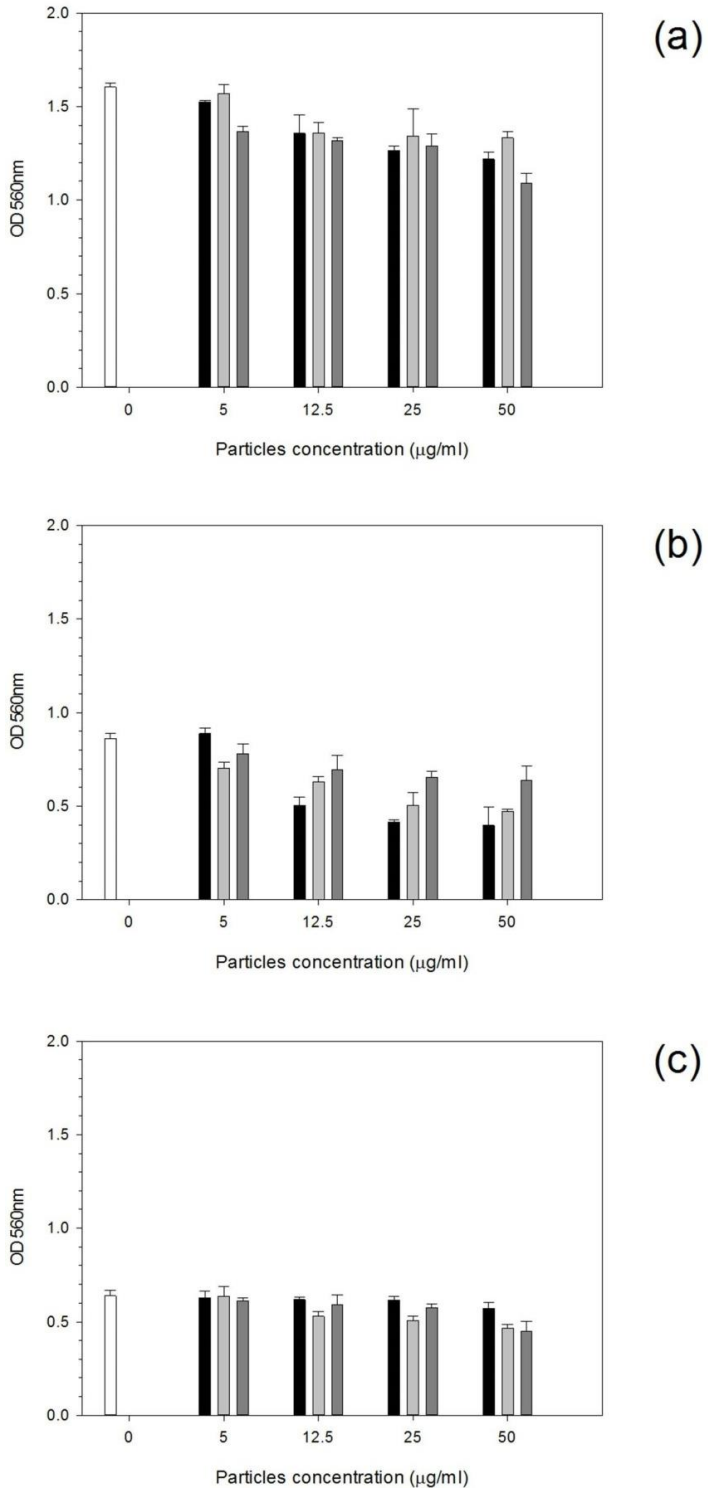

Figure 6-1. MTT results of MSCs exposed to Titanium nanoparticles for (a) 24h, (b) 48 h and (c) 72 h.

Control Ti 30 nm Ti 25 nm Ti 100 nm

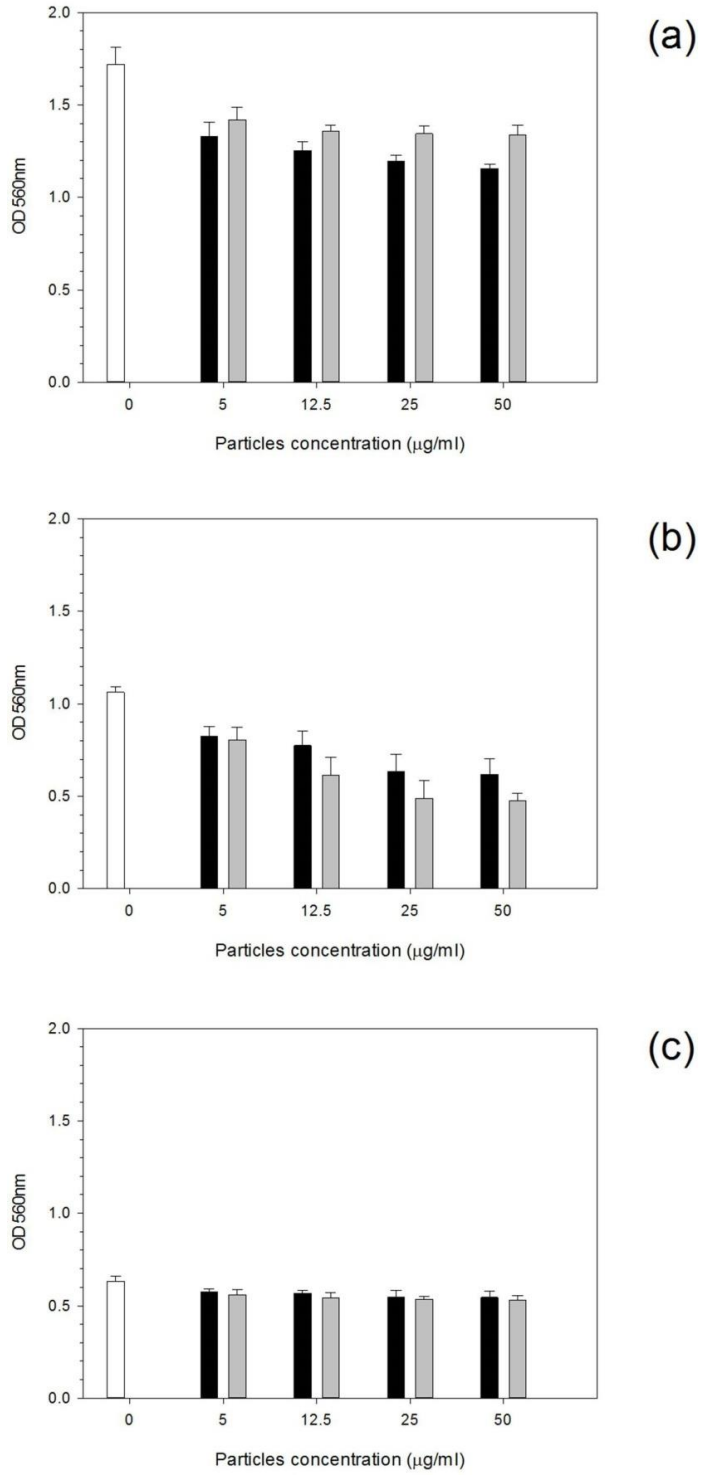

Figure 6-2. MTT results of MSCs exposed to Cobalt nanoparticles for (a) 24h, (b) 48 h and (c) 72 h. Control Co 30 nm Co 50 nm

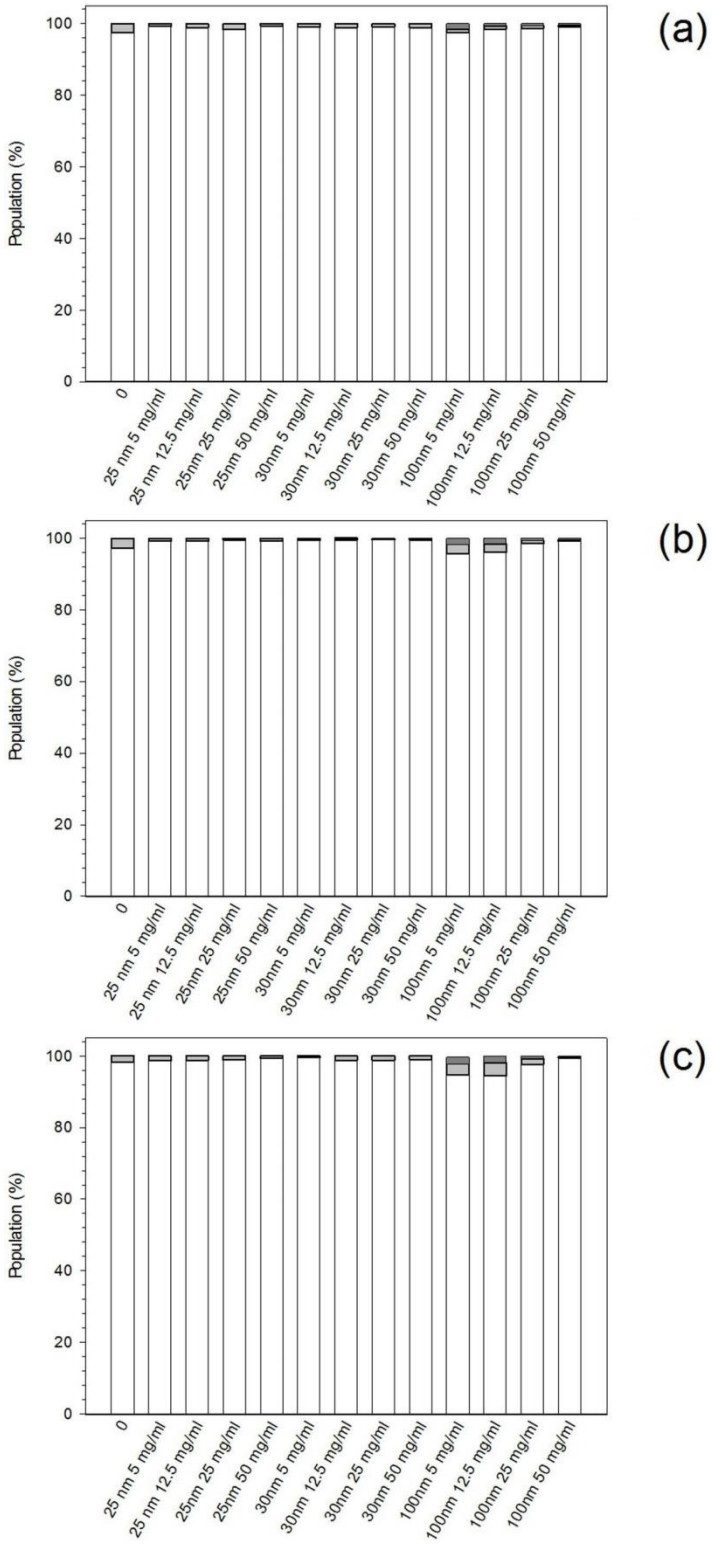

Figure 6-3. Viability of MSCs exposed to Titanium nanoparticles for (a) 24h, (b) 48 h and (c) 72 h. alive injured dead

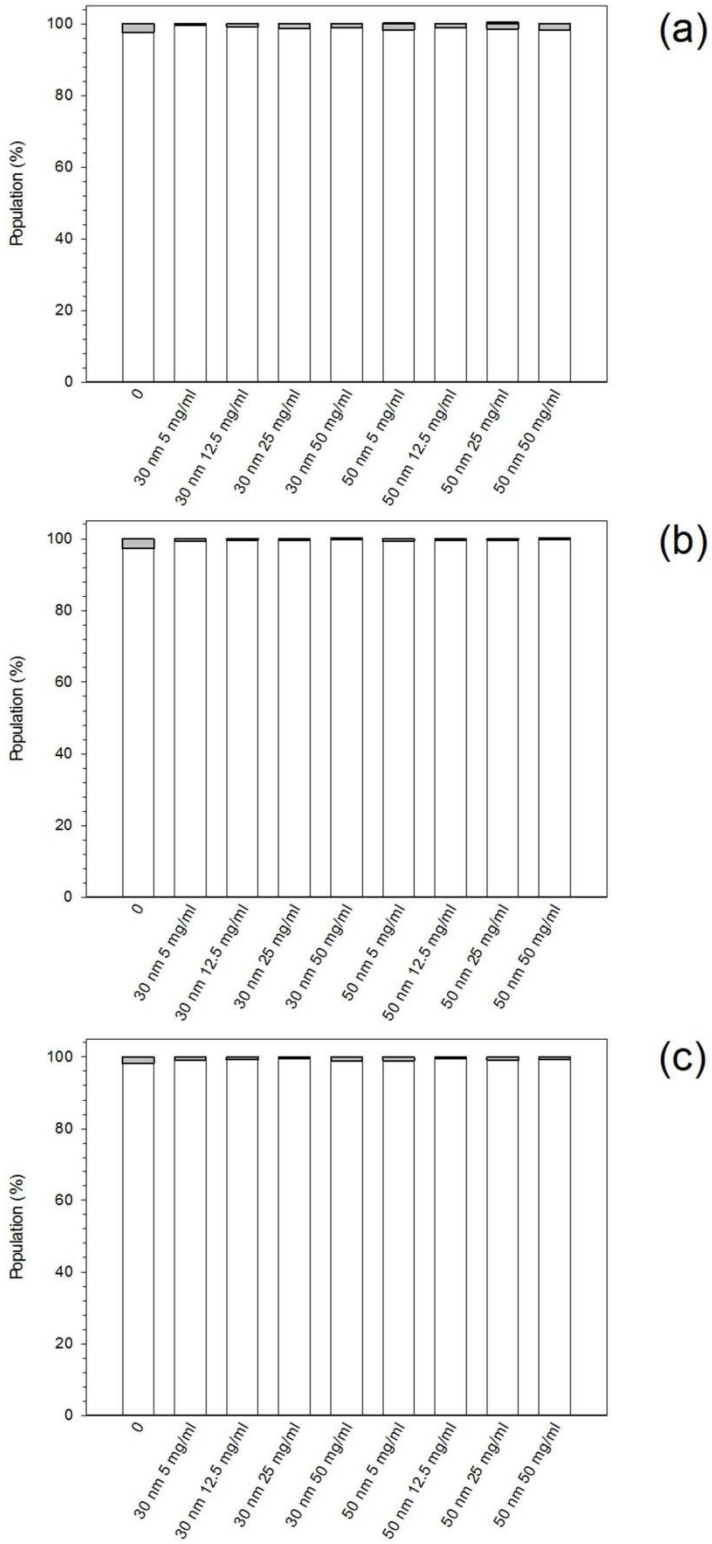

Figure 6-4. Viability of MSCs exposed to Cobalt nanoparticles for (a) 24h, (b) 48 h and (c) 72 h. □ alive ■ injured ▒ dead

Particles of elemental Co 30nm had a lower value of viability compared to the bigger Co oxide 50nm particles after exposure for 24 hour at concentrations higher than 25 μg/ml ($p<0.05$) (Figure 6-2). Moreover, the concentration of both types of nanoparticles did not influence the metabolic activity over the range tested ($p>0.05$). The same was observed after 48 hours for Co 30nm and for Co 50nm at concentrations greater than 12.5 μg/ml. Similar to case with Ti nanoparticles, MSCs had the same metabolic activity, as the cells not exposed to Co nanoparticles after contact for 72 hours regardless of the size, concentration and composition ($p>0.05$).

6.5 Cell structural integrity

Evidence that the cell membrane integrity was not compromised by any type (composition and size) of nanoparticles, regardless of the concentration, could be seen from the results of flow cytometry (Figure 6-3 and Figure 6-4). These demonstrate that the cell population was almost entirely comprised by cells exhibiting high green fluorescence, related to calcein AM uptake, and low red fluorescence, related to ethidium homodimer-1, at any exposure time for any of the particles tested.

6.5.1 Nanomechanical properties

Cell elasticity and turgidity were estimated through modelling the two parts of the AFM indentation curve (Figure 6-5). The initial part of the indentation followed the Hertz model, whilst with greater indentation the force vs. indentation curve appeared linear.

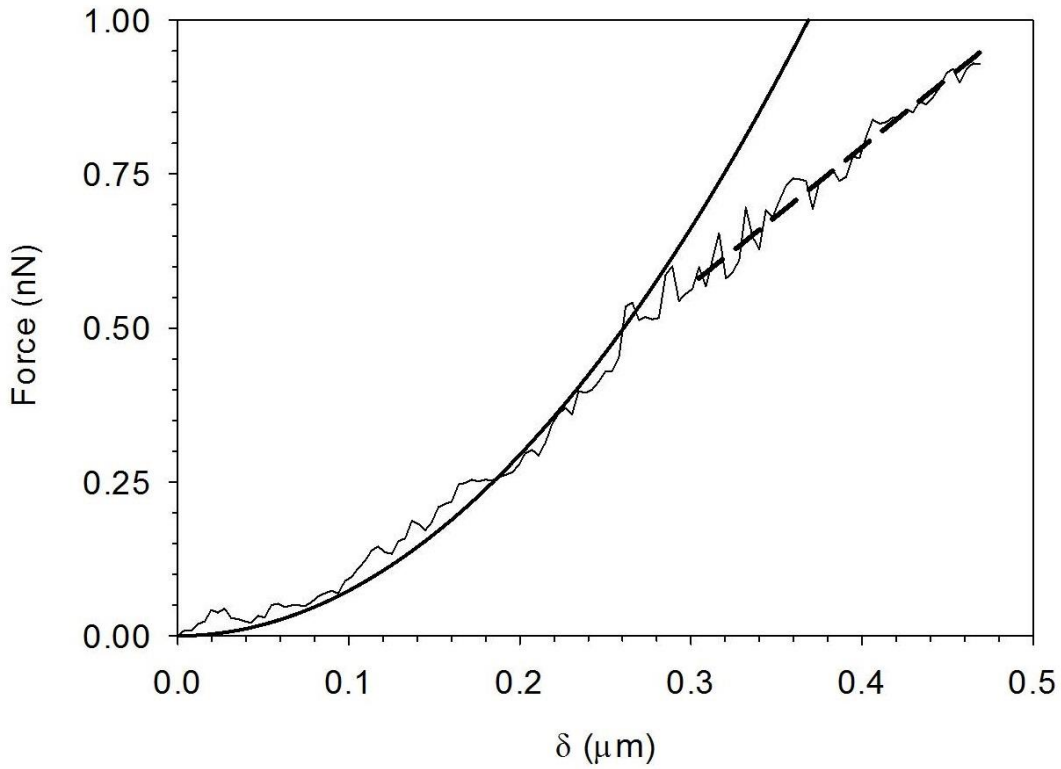

Figure 6-5. Examples of MSCs indentation curve for MSC not exposed to nanoparticles after 24h incubation (———).

——— Hertz model fitting - - - - Hooke model fitting.

The distribution of the MSC nanomechanical properties (elasticity and spring constant) were normally distributed. The elasticity of MSCs not exposed to nanoparticles after 24 hours was about 20 kPa and decreased to about 15 kPa after 2 days and about 10 kPa after 3 days.

MSCs generally exhibited a decrease in elasticity (*E*) as the concentration of all nanoparticles tested increased, even the smallest concentration of 5 μg/ml had a significant effect on the cell elasticity (Figure 6-6 and Figure 6-7). Moreover,

no difference was recorded at concentration greater than 25 μg/ml ($p>0.05$). Elasticity did not change significantly with time for the control sample and for the MSC exposed to nanoparticles ($p>0.05$). The size and chemical composition (elemental or oxide) of Co nanoparticles did not impact on the cell elasticity (Figure 6-7). Elemental Titanium caused a smaller reduction of the cell elasticity than TiO_2 particles (irrespectively of the size) only at the lowest concentration examined (Figure 6-6). Furthermore, MSC exposed to Titanium had higher elasticity than those treated with Cobalt ($p<0.05$).

The turgidity (P_0) of MSCs not exposed to nanoparticles decreased slightly with time from ~0.6 to ~0.4 kPa. When MSCs were exposed to Titanium nanoparticles (

Figure 6-8), either the composition (elemental Ti or Titanium oxide) or the concentrations had a significant effect compared to the control samples ($p>0.05$). Similar behaviour was recorded for Cobalt nanoparticles but the overall cell stiffness was smaller than for the samples in contact with Titanium (Figure 6-9).

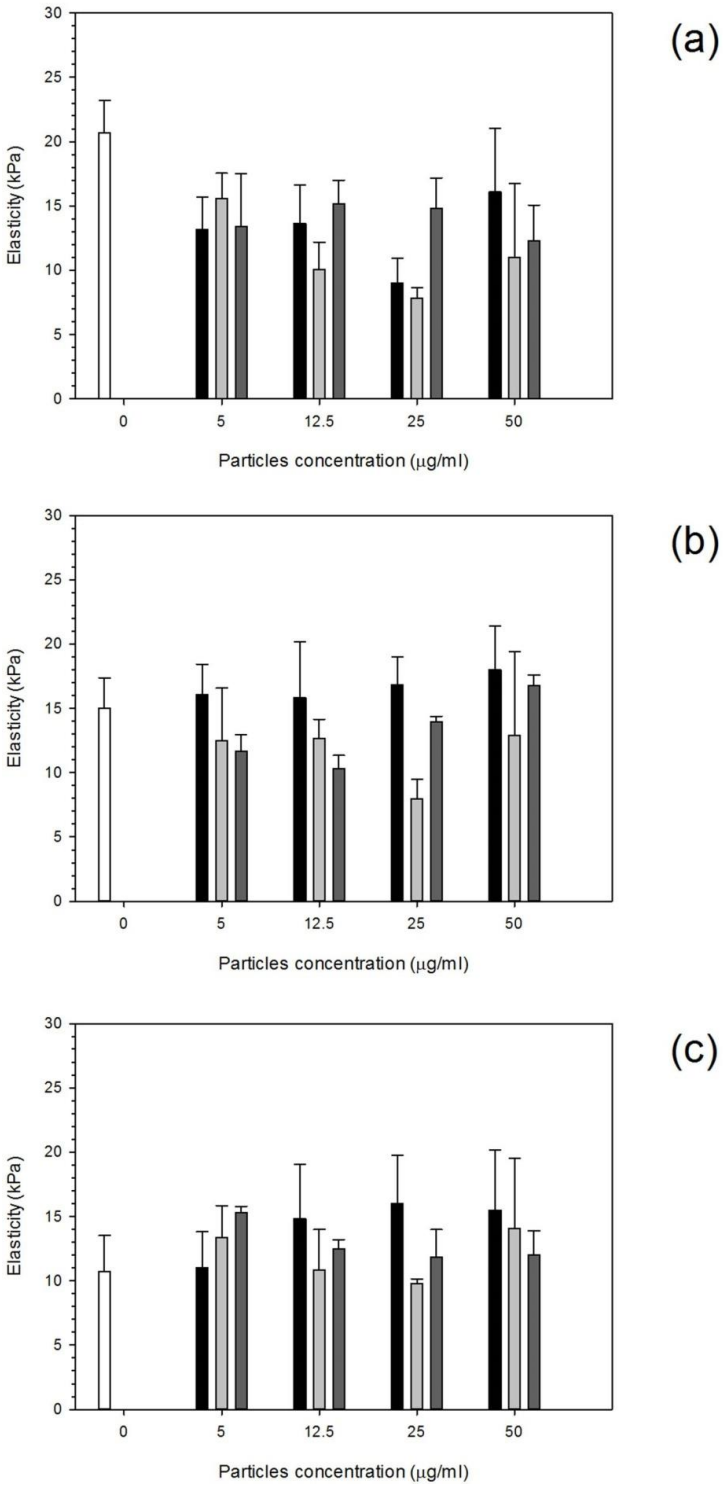

Figure 6-6. Mean cell elasticity of MSCs exposed to Titanium nanoparticles for (a) 24h, (b) 48 h and (c) 72 h. Control Ti 30 nm Ti 25 nm Ti 100 nm

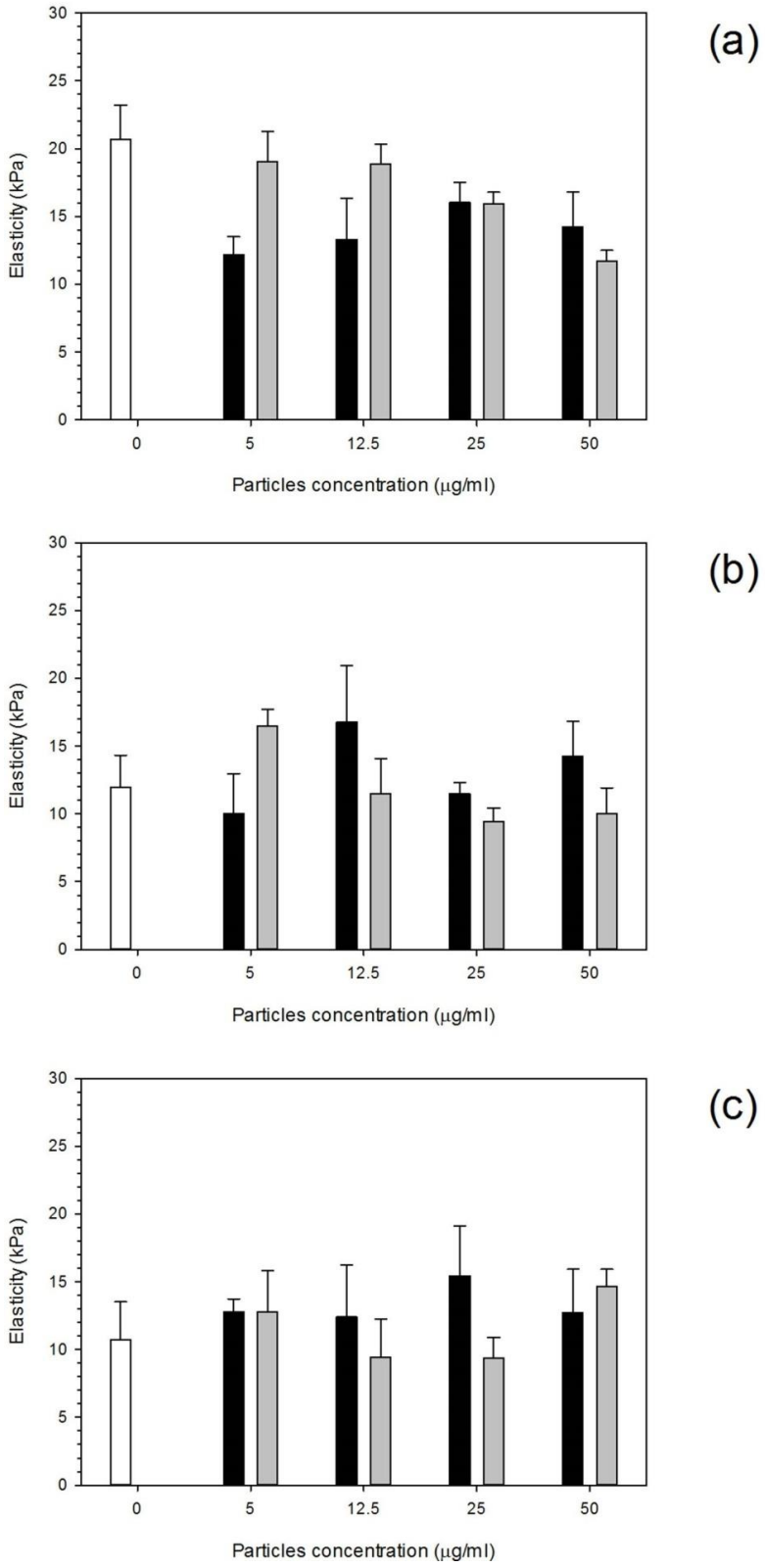

Figure 6-7. Mean cell elasticity of MSCs exposed to Cobalt nanoparticles for (a) 24h, (b) 48 h and (c) 72 h. Control Co 30 nm Co 50 nm

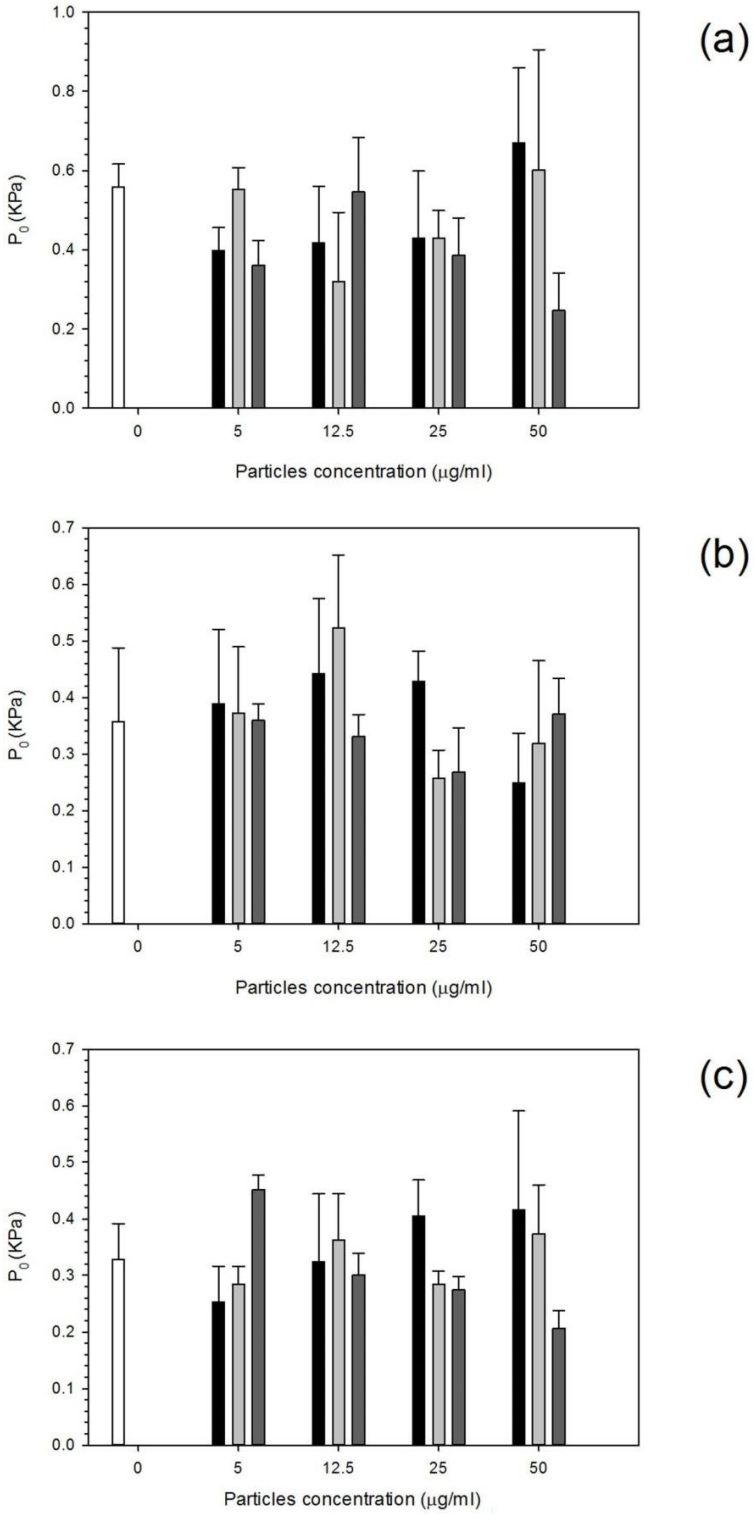

Figure 6-8. Mean turgidity of MSCs exposed to Titanium nanoparticles for (a) 24h, (b) 48 h and (c) 72 h.

Control Ti 30 nm Ti 25 nm Ti 100 nm

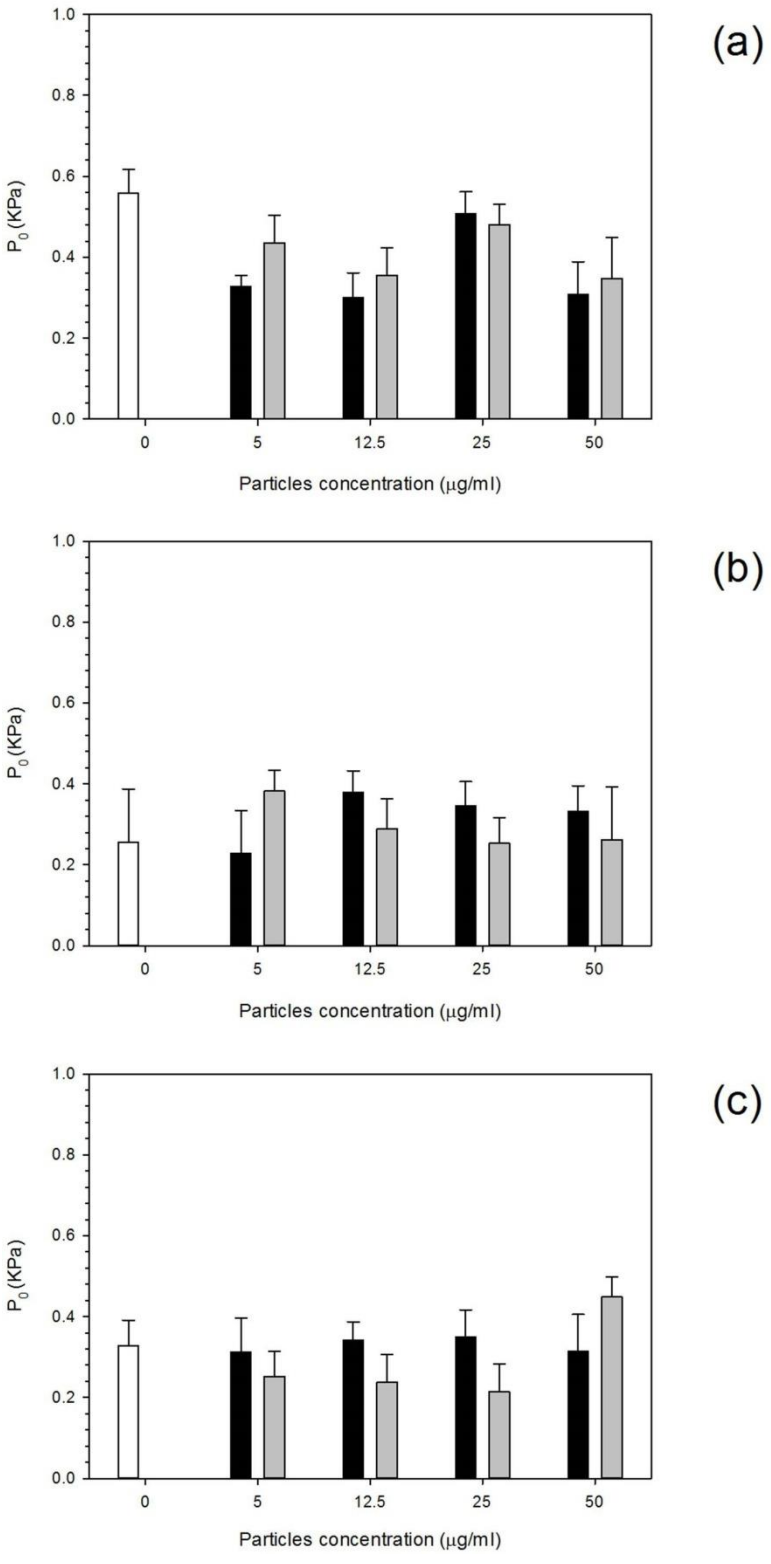

Figure 6-9. Mean turgidity of MSCs exposed to Cobalt nanoparticles for (a) 24h, (b) 48 h and (c) 72 h ☐ Control ■ Co 30 nm ▒ Co 50 nm

6.5.2 Metal uptake

Greater uptake was recorded with increasing concentration; increasing exposure time resulted in higher uptake for lower nanoparticles concentration (Figure 6-10 and Figure 6-11), the composition of the particles seemed to be more important than the size as Ti 25 and 100 nm had similar uptakes while Ti 30 nm had generally lower metal uptake.

Similarly with Co uptake increased with increasing concentration and over time again with the greatest uptake reached after 48 hours; additionally Co 50nm demonstrated the highest uptake at each time point and concentrations ($p<0.05$).

6.5.3 Cell adhesion forces

Generally, MSC exposed either to both types of Co and Ti nanoparticles or not exposed to any nanoparticles exhibited a spatial distribution of the adhesion forces on the cell surface that did not follow a Gaussian distribution (Figure 6-12 and Figure 6-13). No variation in the adhesion forces was detected for the control samples with increasing time; the median was in all 3 cases about 0.9 nN.

Ti nanoparticles generally did not cause variation in the adhesion forces of MSCs for exposure up to 2 days regardless of the size and composition (Figure 6-12) as the distributions of forces were not significantly different from the respective control. Instead, after 3 days of exposure to any of the Ti nanoparticles tested, MSCs exhibited smaller adhesion forces that MSCs that were not exposed to Ti nanoparticles even at the lowest concentration used in this work.

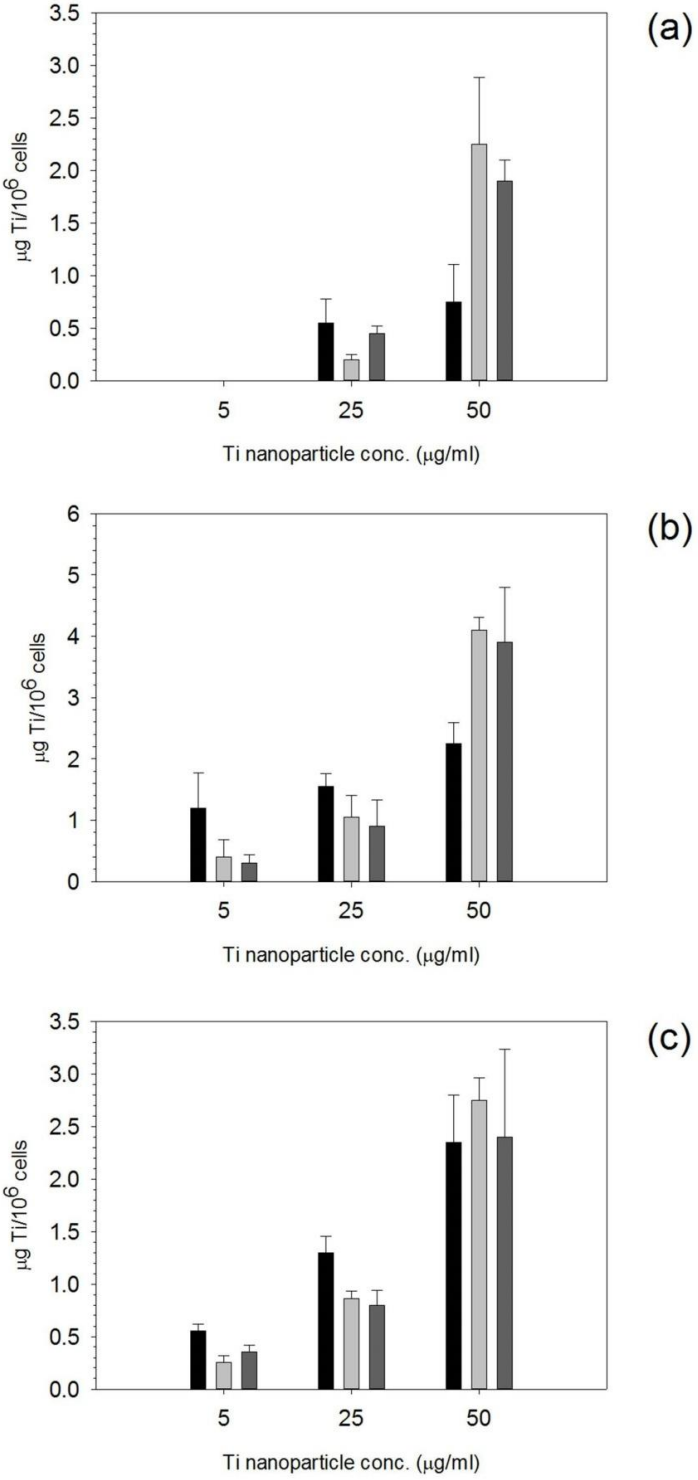

Figure 6-10. Metal uptake of MSCs exposed to Titanium nanoparticles at different concentrations for ■ 24 h ▒ 48 h ▓ 72h.

(a) Ti 25 nm, (b) Ti 30 nm and (c) Ti 100 nm.

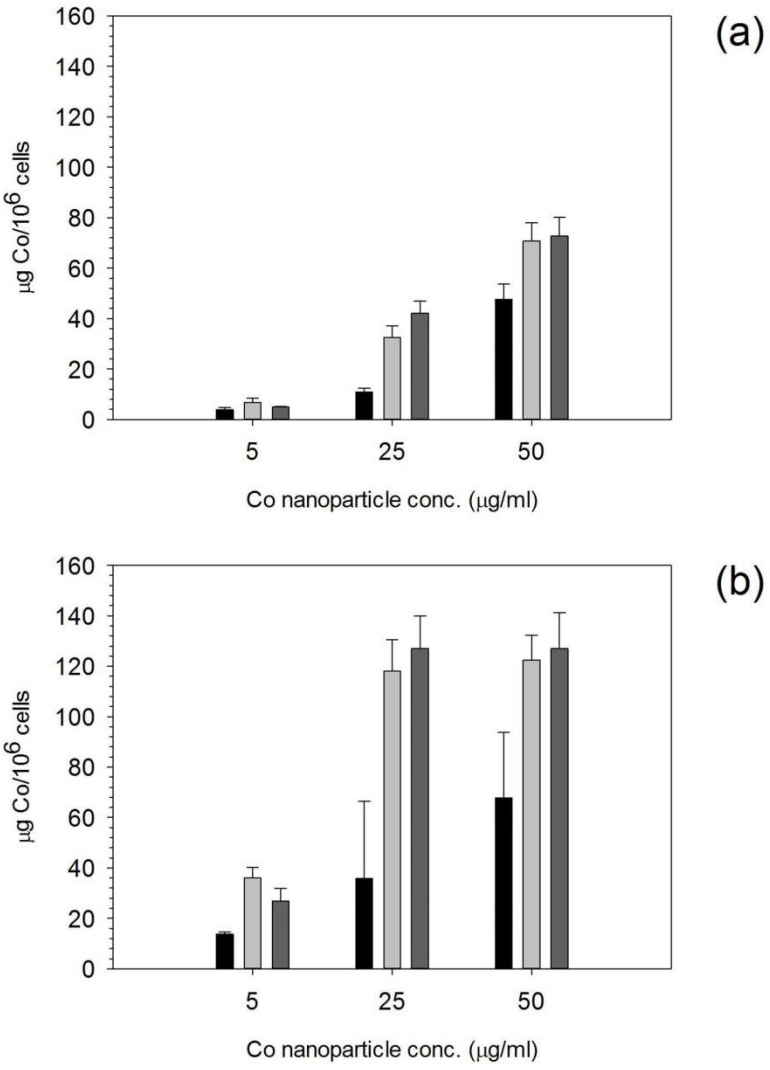

Figure 6-11. Metal uptake of MSCs exposed to Cobalt nanoparticles at different concentrations for ■ 24 h ▯ 48 h ▮ 72h.

(a) Co 30 nm and (b) Co 50 nm.

For Cobalt nanoparticles (Figure 6-13) after 24 hours exposure there was not much difference in the lower quartiles, however, there was a general decrease in mean adhesion values with increasing concentration with the lowest value at 25 μg/ml for both Co 30nm and Co 50nm. Furthermore, the distribution of adhesion forces was narrower for the two greatest concentration of nanoparticles tested. After 48 hours, the range of adhesion decreased for the control but the median remained almost unchanged. Largely, there was a decrease in overall adhesion with increasing concentration similarly to that at 24 hours. However, Co 50nm increased in adhesion at 50 μg/ml; and unlike 24 hours, Co 50nm had a smaller range of adhesion compared to Co 30nm except for the highest concentration. MSCs exposed for 72 hours a similar pattern was observed for the overall adhesion forces that as the concentration of nanoparticles increased the adhesion decreased.

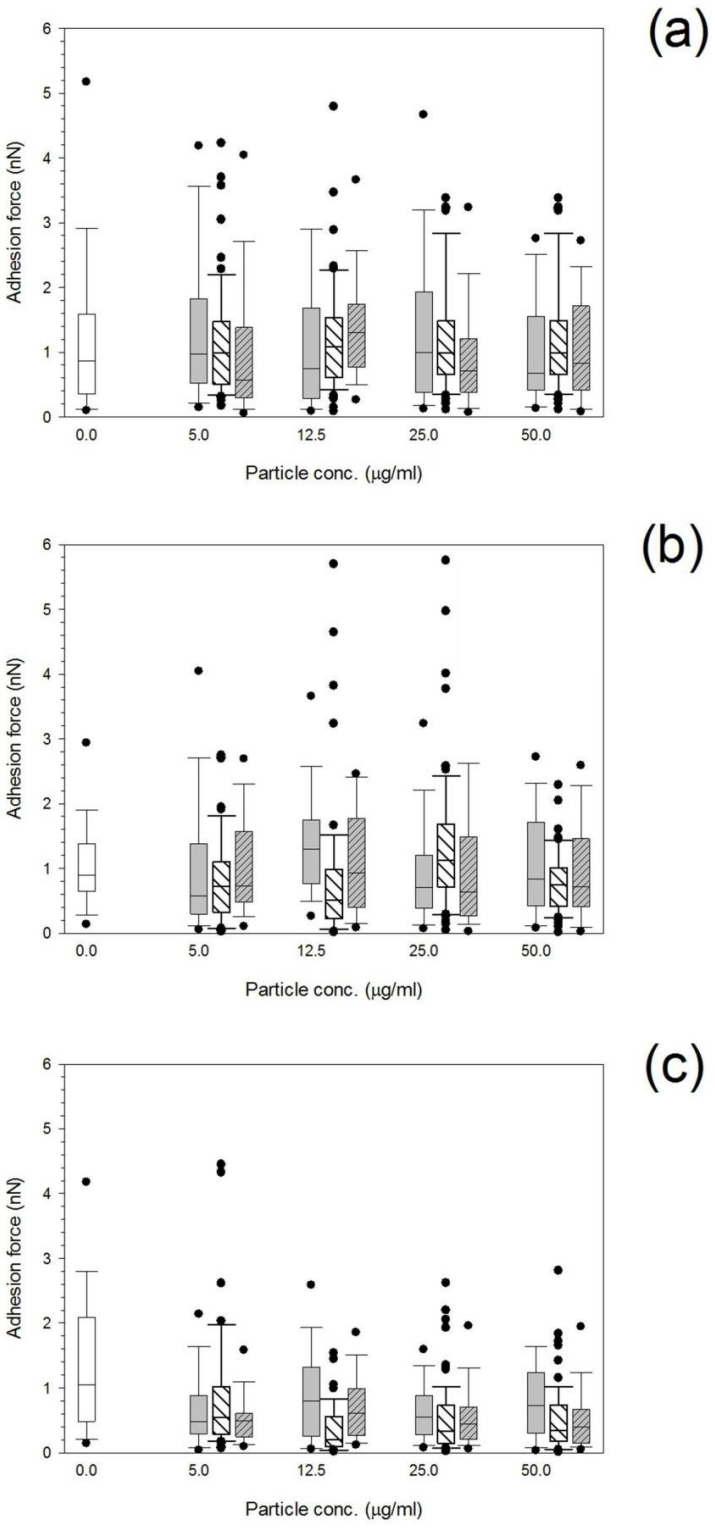

Figure 6-12. Adhesion force distribution of MSC cells exposed to Titanium nanoparticles for (a) 24h, (b) 48 h and (c) 72 h.

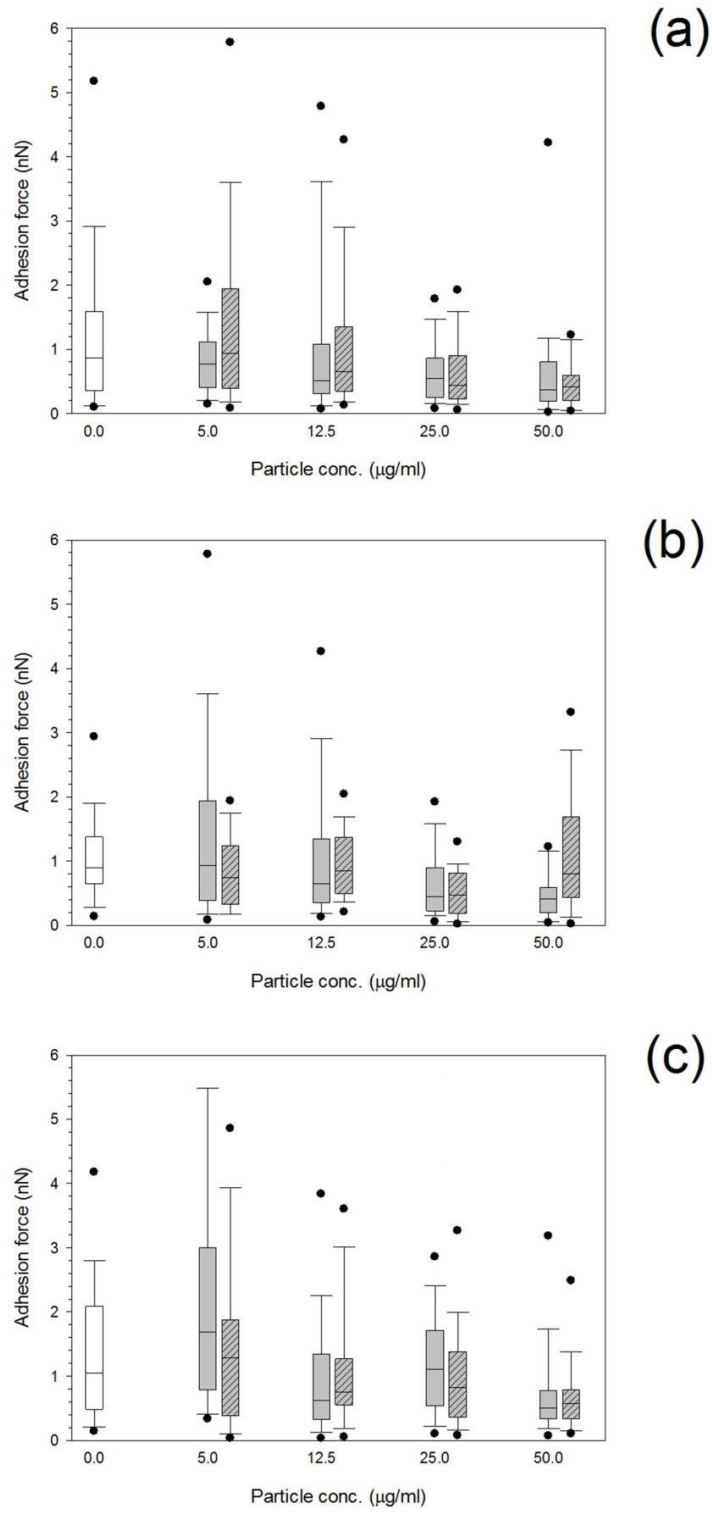

Figure 6-13. Adhesion force distribution of MSC cells exposed to Cobalt nanoparticles for (a) 24h, (b) 48 h and (c) 72 h.

6.6 Discussion

The replacement of a damaged joint with an arthroplasty device (i.e. hip or knee replacement) is a procedure performed in a growing number of cases; one of the leading causes of implant failure is the aseptic loosening caused by the wear debris formed during the device life cycle. During the wear process, particles with a wide range of sizes are generated. It has been found that nano sized particles are the most dangerous ones due to their increase free radicals production and chromosomal damage [15]. Arthroplasty devices can be made from ceramic, metal or plastic materials. Titanium, Cobalt and their oxides are the common materials used, the size, composition and concentration range of the wear particles resulting from these devices have been determined from retrieval studies and found to be around 50 nm for Co and up to few hundreds nanometers for Ti [47]; therefore the particles used in this study are a good model to study the effect of wear debris produced by joint replacement devices.

This work considered the physico-chemical surface parameters of the nanoparticles (such as: particle size and charge), and material (particle chemical composition and its nature) on nanomechanical and adhesive properties of MSCs. Chemical composition and size of metal debris have been found to vary through *in-vivo* studies; these are important parameters to consider when assessing information from *in-vitro* studies [48-50]. A number of studies [51-53] showed nano-sized metal particles decrease viability of MSCs. Cell proliferation and differentiation are affected by the size, shape and chemical composition of the wear particles [47]. Charges of the particles can be influenced by their environment [54, 55]; as Hahn et al (2012) explained,

proteins such as bovine serum albumin adsorb onto the surface of nanoparticles via amino acid groups, for example cysteine [54]. After nanoparticles are coated with such proteins naturally occurring in blood or other body fluids, nanoparticles stabilised and exhibit different zeta potentials compared to the original nanoparticles [54]. The negative zeta potential found in this study, that is the opposite of the positive charge of metal element is in line with many other works [55],[54] and a consequence of the protein adsorption onto the nanoparticles.

MSCs are cells which possess self-renewal and multi-lineage differentiation capacities [56-58]. These non-hematopoietic stem cells may differentiate into tissues such as adipocytes, osteoblasts, chondrocytes, tenocytes, skeletal myocytes and visceral stromal cells [58]; therefore there are many potential therapeutic applications associated with MSCs, for example to treat conditions such as osteogenesis imperfacta; and myocardial infarction [59]. Stem cells are important in bone development and they are present in the early stages of total joint arthoplasty [11] help form new bone; then it is clearly significant to understand if the implanted device has any influence over these cells and if so, whether this would affect the longevity of the biomedical implant and the surrounding bone and tissue. MSCs in trabecular bone [28, 29] and adjacent to implants have osteoprogenitor activities and are critical contributors to maintaining osseous tissue integrity. Perturbation of MSC osteogenic activity may thus affect bony ingrowth and interface stability, leading to increased risk of loosening. It has been observed that exposure to metal wear particles results in reduced osteogenic differentiation and proliferation, and enhanced apoptosis in

human MSCs [18-20]. Endocytosis of Titanium or Cobalt particles is a possible mode of wear particles action on MSCs, which has been previously shown to be necessary for the observed effects on these cells after exposure to these particles [60, 61]. Phalloidin staining revealed that MSCs that have endocytosed Titanium particles display a reduced and highly disrupted cytoskeletal architecture, supported by the irregular distribution and pattern of adherent junctions and concomitant reduction of β-actin expression. Cytoskeletal disruption is thus a likely cause of the inhibition of cellular functions, although the exact mechanisms remain to be analysed [20]. Haleem-Smith et al. 2012 [53] investigated the mechanistic aspects of the endocytosis-mediated responses of MSCs to Titanium particulates. Dose-dependent effects were observed on cell viability, with doses >300 Titanium particles/cell resulting in drastic cell death. To maintain cell viability and analyze particle-induced effects, doses <300 particles/cell were used. Disruptions in cytoskeletal and adherens junction organization were also observed in Titanium particles-treated MSCs [53]. Concentrations of up to 10^5 NP/cell of Titanium nanoparticles were used (assuming each particle is perfect sphere) and did not detect significant impacts; however, in both these studies particles with a median diameter larger than those used here (in the latter about 400 nm, in the former appeared microsize). The lower metabolic activity of cells after exposure to Cobalt nanoparticles we observed (Figure 6-2) has also been presented by Schröck et al. 2014 [60]. The results of the MTT assay, that is based on cellular oxido-reductase enzyme activity, revealed that MSC exposed to nanoparticles had a lower activity (Figure 6-1 and Figure 6-2); however this did not result from the presence of structurally damaged cells as demonstrated by the flow cytometry

data (Figure 6-3 and Figure 6-4). It has been shown that Titanium nanoparticles with size of about 50nm can enter neural stem cells without influencing greatly their viability [61].

It has been recognised that the cell's mechanical properties for example the elasticity, stiffness, membrane tension, cell shape and adhesion strength all have a role in the fate of the cell and affect a number of cell functions such as its differentiation [56, 62, 63], ageing and diseased state [64, 65]. The mechanical properties of the cells are closely linked to its structural integrity. The structural integrity and the mechanical behaviour of cells are mainly controlled by the cell cytoskeleton and actin filaments organisation. Furthermore, because of the involvement of the cytoskeleton in signalling pathways (i.e. mechano-transduction), variations in cell proteomics can result in changes in the mechanical and structural properties of cells [36, 37]. In the last decade there has been an increase in the number of studies investigating mechanical properties of cells and tissues [31-35]. For example, Titushkin et al (2006) [66] studied the membrane properties of mesenchymal stem cells and observed that normal cells had a spring constant anywhere between 0.001-0.1 N/m [66], this correlates well with the values measured in this study using the AFM for all control cells [67][68]. Such variations can also be attributed to different fitting procedures; only the initial part of the indentation curve was modelled with the Hertz model as it is valid only for small indentation depths (up to about 200 nm). This is a consequence of the fact that it was formulated with the assumption of semi-infinite material; in order to operate when this assumption is still valid, an indentation depth of no more than 5-10% of the

average cell height was suggested [69]. At greater indentation depths, a well-known linear relation between indentation depth and force was found and the slope of such relation determined (spring constant). The values of cell elasticity found here (in the order of tens of kPa) are slightly higher than in other works [69, 70], where few kPa, were found; this could be a consequence of the different type of cells and growing conditions; however, in some of this works [71] the full indentation curve was modelled with the Hertz model. The shape of the indentation curve (Figure 6-5) suggested that the smaller Young moduli would be calculated in case the deeper part of the indentation curve is also included in the fitting algorithm.

The results show that particles induce biological responses but not complete cell damage; however the nanomechanical investigation clearly demonstrated that cells exposed to nanoparticles are mechanically affected, mainly for Cobalt nanoparticles, and that the concentration of the nanoparticles is a predominant factor other than size and charge along with metal type (Figure 6-6 to Figure 6-9). On the contrary; for Titanium nanoparticles, our combined results showing unaffected viability and mechanical properties are in agreement with Mao et al. 2015 [72], who reported that neural stem cells structure and viability are unaffected for Titanium nanoparticles at concentrations up to 50 μg/ml. Furthermore, the decrease of metabolic activity (Figure 6-1 and Figure 6-2) of MSCs with longer exposure times was not linked to an increased cell death (Figure 6-3 and Figure 6-4) for both Cobalt and Titanium nanoparticles. Interestingly, the greatest differences in MSC mechanical properties exposed to Cobalt nanoparticles compared to control samples occurred in the first 24

hours; with further exposure the effect of the nanoparticles appeared to decrease and after 3 days of exposure the effect of the nanoparticles was not significant, this is in line with the uptake reaching a plateau after 48 hours of exposure. The distributions of both cell elasticity and spring constant did not exhibit a bimodal behaviour highlighting the homogeneity of MSCs response and is also correlated to the lack of dead cells, who exhibit different mechanical properties (data not shown) among the MSC population.

In addition, the values of turgidity obtained are close to those (up to 0.4 kPa) presented by [73]. As the cell membrane is associated with many functions that are critical for the maintenance of healthy cells, such as adhesion, motility, endocytosis and exocytosis, and signalling then it is important for a cell to regulate the membrane tension [66, 74]. Cells undergo changes in shape and osmolarity which do not affect the tension even with significant variations, however it has been noted that the elasticity of cells can only be stretched by 2-4% before the membrane ruptures [66, 75]. Therefore, it is expected that a reduction in cell elasticity is coupled with a reduction in turgidity in order to minimise the cell volume variation, the results exhibited this anticipated trend.

Adhesion forces originate from interfacial interactions between contacting bodies; the extent of such forces depends on the composition of the materials in contact [76]. Our results generally depicted a trend of reduction of adhesion force when exposed to nanoparticles, particularly for Cobalt. This suggests that the nanoparticles can interfere with stem cell proliferation through preventing or weakening adhesion to a substrate that is the first step into stem cell growth.

The results hint that the lower impact of Titanium nanoparticles on MSC mechanical properties than Cobalt nanoparticles is linked to a lower cell uptake of the former than the latter (Figure 6-10 and Figure 6-11). Also they support the general knowledge of Titanium being more biocompatible than Cobalt [22, 77].

6.7 Conclusion

The effects on cell nanomechanical and adhesive properties were studies for MSCs that are caused by metal nanoparticles, Cobalt and Titanium, closely resembling the wear particles that are originated from commonly used bulk materials in implanted biomedical devices. This is the first time that such an approach was applied to the investigation of the responses of MSCs to wear particles and to identify the role of parameters such as particles size and composition and concentration; usually such investigations are limited to the determination of cytokine production, DNA damage or gene expression. This work is complementary to these results and demonstrate that the MSC response to wear particles involves mechanical changes of the cell.

The results suggest that the higher the concentration of nanoparticles surrounding cells reduces the overall stiffness and turgidity of the cells. Furthermore no evidence of cell structural damage was detected through flow cytometry but a reduction of metabolic activity was noticed. Cell uptake of Cobalt was remarkably higher than Titanium and, at the same time, the impact on mechanical properties was more pronounced for Cobalt. Hence it appeared that changes in mechanical properties are a consequence of nanoparticles endocytosis; moreover the results also support the notion of higher

biocompatibility of Titanium devices compared to Cobalt. Another outcome of nanoparticles was a reduction of the adhesion forces and such possible disruption of MSC growth can results from impeded adhesion.

6.8 References

1. Tee, S.-Y., J. Fu, Christopher s. Chen, and Paul a. Janmey, *Cell Shape and Substrate Rigidity Both Regulate Cell Stiffness.* Biophysical Journal, 2011. **100**(5): p. L25-L27.

2. Tee, S.-Y., A.R. Bausch, and P.A. Janmey, *The mechanical cell.* Current Biology, 2009. **19**(17): p. R745-R748.

3. Guo, Q., Y. Xia, M. Sandig, and J. Yang, Characterization of cell elasticity correlated with cell morphology by atomic force microscope. Journal of Biomechanics, 2012. **45**(2): p. 304-309.

4. Cai, P., Y. Mizutani, M. Tsuchiya, John m. Maloney, B. Fabry, Krystyn j. Van vliet, and T. Okajima, *Quantifying Cell-to-Cell Variation in Power-Law Rheology.* Biophysical Journal, 2013. **105**(5): p. 1093-1102.

5. Bahraminasab, M., B.B. Sahari, K.L. Edwards, F. Farahmand, M. Arumugam, and T.S. Hong, *Aseptic loosening of femoral components – A review of current and future trends in materials used.* Materials & Design, 2012. **42**(0): p. 459-470.

6. Kowandy, C., H. Mazouz, and C. Richard, *Isolation and analysis of articular joints wear debris generated in vitro.* Wear, 2006. **261**(9): p. 966-970.

7. Prokopovich, P., S. Perni, J. Fisher, and R.M. Hall, *Spatial variation of wear on Charité lumbar discs.* Acta Biomaterialia, 2011. **7**(11): p. 3914-3926.

8. Ingham, E. and J. Fisher, *The role of macrophages in osteolysis of total joint replacement.* Biomaterials, 2005. **26**(11): p. 1271-1286.

9. Abu-Amer, Y., I. Darwech, and J.C. Clohisy, *Aseptic loosening of total joint replacements: mechanisms underlying osteolysis and potential therapies.* Arthritis Research & Therapy, 2007. **9**(Suppl 1): p. S6-S6.

10. Tuan, R.S., F.Y. Lee, T.K. Y, J.M. Wilkinson, and R.L. Smith, What are the local and systemic biologic reactions and mediators to wear debris, and what host factors determine or modulate the biologic response to wear particles? J Am Acad Orthop Surg, 2008. **16 Suppl 1**: p. S42-8.

11. Tella, S.H. and J.C. Gallagher, *Prevention and treatment of postmenopausal osteoporosis.* The Journal of Steroid Biochemistry and Molecular Biology, 2014. **142**(0): p. 155-170.

12. Papageorgiou, I., C. Brown, R. Schins, S. Singh, R. Newson, S. Davis, J. Fisher, E. Ingham, and C.P. Case, *The effect of nano- and micron-sized particles of Cobalt–chromium alloy on human fibroblasts in vitro.* Biomaterials, 2007. **28**(19): p. 2946-2958.

13. Naudie, D.D., D.J. Ammeen, G.A. Engh, and C.H. Rorabeck, *Wear and osteolysis around total knee arthroplasty.* J Am Acad Orthop Surg, 2007. **15**(1): p. 53-64.

14. Vermes, C., R. Chandrasekaran, J.J. Jacobs, J.O. Galante, K.A. Roebuck, and T.T. Glant, *The effects of particulate wear debris, cytokines, and growth factors on the functions of MG-63 osteoblasts.* J Bone Joint Surg Am, 2001. **83-a**(2): p. 201-11.

15. Ingham, E. and J. Fisher, *Biological reactions to wear debris in total joint replacement.* Proc Inst Mech Eng H, 2000. **214**(1): p. 21-37.

16. Behl, B., I. Papageorgiou, C. Brown, R. Hall, J.L. Tipper, J. Fisher, and E. Ingham, *Biological effects of Cobalt-chromium nanoparticles and ions on dural fibroblasts and dural epithelial cells.* Biomaterials, 2013. **34**(14): p. 3547-3558.

17. Papageorgiou, I., R. Marsh, J.L. Tipper, R.M. Hall, J. Fisher, and E. Ingham, *Interaction of micron and nano-sized particles with cells of the dura mater.* Journal of Biomedical Materials Research - Part B Applied Biomaterials, 2014.

18. Wang, M.L., L.J. Nesti, R. Tuli, J. Lazatin, K.G. Danielson, P.F. Sharkey, and R.S. Tuan, *Titanium particles suppress expression of osteoblastic phenotype in human mesenchymal stem cells.* Journal of Orthopaedic Research, 2002. **20**(6): p. 1175-1184.

19. Wang, M.L., R. Tuli, P.A. Manner, P.F. Sharkey, D.J. Hall, and R.S. Tuan, *Direct and indirect induction of apoptosis in human mesenchymal stem cells in response to Titanium particles.* J Orthop Res, 2003. **21**(4): p. 697-707.

20. Okafor, C.C., H. Haleem-Smith, P. Laqueriere, P.A. Manner, and R.S. Tuan, *Particulate endocytosis mediates biological responses of human mesenchymal stem cells to Titanium wear debris.* Journal of Orthopaedic Research, 2006. **24**(3): p. 461-473.

21. Tuan, R.S., *Role of adult stem/progenitor cells in osseointegration and implant loosening.* Int J Oral Maxillofac Implants, 2011. **26 Suppl**: p. 50-62; discussion 63-9.

22. Schofer, M.D., S. Fuchs-Winkelmann, A. Kessler-Thones, M.M. Rudisile, C. Wack, J.R. Paletta, and U. Boudriot, *The role of mesenchymal stem cells in the pathogenesis of Co-Cr-Mo particle induced aseptic loosening: an in vitro study.* Biomed Mater Eng, 2008. **18**(6): p. 395-403.

23. Chiu, R., T. Ma, R.L. Smith, and S.B. Goodman, Kinetics of polymethylmethacrylate particle-induced inhibition of osteoprogenitor differentiation and proliferation. Journal of Orthopaedic Research, 2007. **25**(4): p. 450-457.

24. Chiu, R., T. Ma, R.L. Smith, and S.B. Goodman, *Polymethylmethacrylate particles inhibit osteoblastic differentiation of MC3T3-E1 osteoprogenitor cells.* Journal of Orthopaedic Research, 2008. **26**(7): p. 932-936.

25. Chiu, R., T. Ma, R.L. Smith, and S.B. Goodman, *Ultrahigh molecular weight polyethylene wear debris inhibits osteoprogenitor proliferation and differentiation in vitro.* Journal of Biomedical Materials Research Part A, 2009. **89A**(1): p. 242-247.

26. Chiu, R., K.E. Smith, G.K. Ma, T. Ma, R.L. Smith, and S.B. Goodman, Polymethylmethacrylate particles impair osteoprogenitor viability and expression of osteogenic transcription factors Runx2, osterix, and Dlx5. Journal of Orthopaedic Research, 2010. **28**(5): p. 571-577.

27. Song, L., N.J. Young, N.E. Webb, and R.S. Tuan, Origin and characterization of multipotential mesenchymal stem cells derived from adult human trabecular bone. Stem Cells Dev, 2005. **14**(6): p. 712-21.

28. Tuli, R., S. Tuli, S. Nandi, M.L. Wang, P.G. Alexander, H. Haleem-Smith, W.J. Hozack, P.A. Manner, K.G. Danielson, and R.S. Tuan, *Characterization of Multipotential Mesenchymal Progenitor Cells Derived from Human Trabecular Bone.* STEM CELLS, 2003. **21**(6): p. 681-693.

29. Nöth, U., A.M. Osyczka, R. Tuli, N.J. Hickok, K.G. Danielson, and R.S. Tuan, *Multilineage mesenchymal differentiation potential of human trabecular bone-derived cells.* Journal of Orthopaedic Research, 2002. **20**(5): p. 1060-1069.

30. Weissleder, R., M. Nahrendorf, and M.J. Pittet, *Imaging macrophages with nanoparticles.* Nat Mater, 2014. **13**(2): p. 125-138.

31. Helenius, J., C.P. Heisenberg, H.E. Gaub, and D.J. Muller, *Single-cell force spectroscopy.* J Cell Sci, 2008. **121**(Pt 11): p. 1785-91.

32. Cai, X., X. Xing, J. Cai, Q. Chen, S. Wu, and F. Huang, Connection between biomechanics and cytoskeleton structure of lymphocyte and Jurkat cells: An AFM study. Micron, 2010. **41**(3): p. 257-262.

33. Kirmizis, D. and S. Logothetidis, *Atomic force microscopy probing in the measurement of cell mechanics.* International Journal of Nanomedicine, 2010. **5**: p. 137-145.

34. Li, M., L. Liu, N. Xi, Y. Wang, Z. Dong, X. Xiao, and W. Zhang, Atomic force microscopy imaging and mechanical properties measurement of red blood cells and aggressive cancer cells. Sci China Life Sci, 2012. **55**(11): p. 968-73.

35. Yang, R., N. Xi, K.W.C. Lai, K. Patterson, H. Chen, B. Song, C. Qu, B. Zhong, and D.H. Wang, *Cellular biophysical dynamics and ion channel activities detected by AFM-*

based nanorobotic manipulator in insulinoma β-cells. Nanomedicine : nanotechnology, biology, and medicine, 2013. **9**(5): p. 636-645.

36. Radmacher, M., *Studying the Mechanics of Cellular Processes by Atomic Force Microscopy*, in *Methods in Cell Biology*, W. Yu-Li and E.D. Dennis, Editors. 2007, Academic Press. p. 347-372.

37. Xu, W., R. Mezencev, B. Kim, L. Wang, J. Mcdonald, and T. Sulchek, *Cell Stiffness Is a Biomarker of the Metastatic Potential of Ovarian Cancer Cells.* PLoS ONE, 2012. **7**(10): p. e46609.

38. Phinney, D.G., G. Kopen, R.L. Isaacson, and D.J. Prockop, Plastic adherent stromal cells from the bone marrow of commonly used strains of inbred mice: variations in yield, growth, and differentiation. J Cell Biochem, 1999. **72**(4): p. 570-85.

39. Harrington, J., A.J. Sloan, and R.J. Waddington, Quantification of clonal heterogeneity of mesenchymal progenitor cells in dental pulp and bone marrow. Connect Tissue Res, 2014. **55 Suppl 1**: p. 62-7.

40. Preedy, E.C., E. Brousseau, S. Evans, S. Perni, and P. Prokopovich, *Adhesive Forces and Surface Properties of Cold Gas Plasma Treated UHMWPE.* Colloids and Surfaces B: Biointerfaces, 2014.

41. Sader, J.E., J.A. Sanelli, B.D. Adamson, J.P. Monty, X. Wei, S.A. Crawford, J.R. Friend, I. Marusic, P. Mulvaney, and E.J. Bieske, *Spring constant calibration of atomic force microscope cantilevers of arbitrary shape.* Review of Scientific Instruments, 2012. **83**(10): p. 103705-103705-16.

42. Sader, J.E., I. Larson, P. Mulvaney, and L.R. White, *Method for the calibration of atomic force microscope cantilevers.* Review of Scientific Instruments, 1995. **66**(7): p. 3789-3798.

43. Sneddon, I.N., The relation between load and penetration in the axisymmetric boussinesq problem for a punch of arbitrary profile. International Journal of Engineering Science, 1965. **3**(1): p. 47-57.

44. Arnoldi, M., M. Fritz, E. Bauerlein, M. Radmacher, E. Sackmann, and A. Boulbitch, *Bacterial turgor pressure can be measured by atomic force microscopy.* Phys Rev E Stat Phys Plasmas Fluids Relat Interdiscip Topics, 2000. **62**(1 Pt B): p. 1034-44.

45. Boulbitch, A., Deformation of the envelope of a spherical gram-negative bacterium during the atomic force microscopic measurements. J Electron Microsc (Tokyo), 2000. **49**(3): p. 459-62.

46. Polyakov, P., C. Soussen, J. Duan, J.F. Duval, D. Brie, and G. Francius, *Automated force volume image processing for biological samples.* PLoS One, 2011. **6**(4): p. e18887.

47. Prokopovich, P., Interactions between mammalian cells and nano- or micro-sized wear particles: Physico-chemical views against biological approaches. Advances in Colloid and Interface Science, 2014. **213**(0): p. 36-47.

48. Case, C.P., V.G. Langkamer, C. James, M.R. Palmer, A.J. Kemp, P.F. Heap, and L. Solomon, *Widespread dissemination of metal debris from implants.* J Bone Joint Surg Br, 1994. **76**(5): p. 701-12.

49. Doorn, P.F., P.A. Campbell, J. Worrall, P.D. Benya, H.A. Mckellop, and H.C. Amstutz, Metal wear particle characterization from metal on metal total hip replacements: transmission electron microscopy study of periprosthetic tissues and isolated particles. J Biomed Mater Res, 1998. **42**(1): p. 103-11.

50. Catelas, I., P.A. Campbell, J.D. Bobyn, J.B. Medley, and O.L. Huk, *Wear particles from metal-on-metal total hip replacements: Effects of implant design and implantation time.* Proceedings of the Institution of Mechanical Engineers, Part H: Journal of Engineering in Medicine, 2006. **220**(2): p. 195-208.

51. Hou, Y., K. Cai, J. Li, X. Chen, M. Lai, Y. Hu, Z. Luo, X. Ding, and D. Xu, *Effects of Titanium nanoparticles on adhesion, migration, proliferation, and differentiation of mesenchymal stem cells.* International Journal of Nanomedicine, 2013. **8**: p. 3619-3630.

52. Jiang, Y., T. Jia, W. Gong, P.H. Wooley, and S.-Y. Yang, *Effects of Ti, PMMA, UHMWPE, and Co–Cr wear particles on differentiation and functions of bone marrow stromal cells.* Journal of Biomedical Materials Research Part A, 2013. **101**(10): p. 2817-2825.

53. Haleem-Smith, H., E. Argintar, C. Bush, D. Hampton, W.F. Postma, F.H. Chen, T. Rimington, J. Lamb, and R.S. Tuan, *Biological Responses of Human Mesenchymal Stem Cells to Titanium Wear Debris Particles.* Journal of Orthopaedic Research, 2012. **30**(6): p. 853-863.

54. Hahn, A., J. Fuhlrott, A. Loos, and S. Barcikowski, *Cytotoxicity and ion release of alloy nanoparticles.* J Nanopart Res, 2012. **14**(1): p. 1-10.

55. Mohapatra, S., S.R. Rout, S. Maiti, T.K. Maiti, and A.B. Panda, *Monodisperse mesoporous Cobalt ferrite nanoparticles: synthesis and application in targeted delivery of antitumor drugs.* Journal of Materials Chemistry, 2011. **21**(25): p. 9185-9193.

56. Docheva, D., D. Padula, C. Popov, W. Mutschler, H. Clausen-Schaumann, and M. Schieker, Researching into the cellular shape, volume and elasticity of mesenchymal stem cells, osteoblasts and osteosarcoma cells by atomic force microscopy. Journal of Cellular and Molecular Medicine, 2008. **12**(2): p. 537-552.

57. Docheva, D., C. Popov, W. Mutschler, and M. Schieker, Human mesenchymal stem cells in contact with their environment: surface characteristics and the integrin system. J Cell Mol Med, 2007. **11**(1): p. 21-38.

58. Krampera, M., G. Pizzolo, G. Aprili, and M. Franchini, *Mesenchymal stem cells for bone, cartilage, tendon and skeletal muscle repair.* Bone, 2006. **39**(4): p. 678-83.

59. Maloney, J.M., D. Nikova, F. Lautenschlager, E. Clarke, R. Langer, J. Guck, and K.J. Van Vliet, *Mesenchymal stem cell mechanics from the attached to the suspended state.* Biophys J, 2010. **99**(8): p. 2479-87.

60. Schröck, K., H. Schneider, J. Lutz, M.C. Hacker, S. Mändl, M. Kamprad, and M. Schulz-Siegmund, *Cytocompatibility of nitrogen plasma ion immersed medical Cobalt–chromium alloys.* Journal of Biomedical Materials Research Part A, 2014. **102**(6): p. 1744-1754.

61. Wang, Y., Q. Wu, K. Sui, X.X. Chen, J. Fang, X. Hu, M. Wu, and Y. Liu, *A quantitative study of exocytosis of Titanium dioxide nanoparticles from neural stem cells.* Nanoscale, 2013. **5**(11): p. 4737-43.

62. Settleman, J., *Tension precedes commitment-even for a stem cell.* Mol Cell, 2004. **14**(2): p. 148-50.

63. Evans, N.D., C. Minelli, E. Gentleman, V. Lapointe, S.N. Patankar, M. Kallivretaki, X. Chen, C.J. Roberts, and M.M. Stevens, *Substrate stiffness affects early differentiation events in embryonic stem cells.* Eur Cell Mater, 2009. **18**: p. 1-13; discussion 13-4.

64. Suresh, S., *Biomechanics and biophysics of cancer cells.* Acta Biomaterialia, 2007. **3**(4): p. 413-438.

65. Jin, H., X. Xing, H. Zhao, Y. Chen, X. Huang, S. Ma, H. Ye, and J. Cai, *Detection of erythrocytes influenced by aging and type 2 diabetes using atomic force microscope.* Biochemical and Biophysical Research Communications, 2010. **391**(4): p. 1698-1702.

66. Titushkin, I. and M. Cho, Distinct membrane mechanical properties of human mesenchymal stem cells determined using laser optical tweezers. Biophys J, 2006. **90**(7): p. 2582-91.

67. Titushkin, I. and M. Cho, Altered osteogenic commitment of human mesenchymal stem cells by ERM protein-dependent modulation of cellular biomechanics. Journal of Biomechanics, 2011. **44**(15): p. 2692-2698.

68. Simon, A., T. Cohen-Bouhacina, M.C. Porté, J.P. Aimé, J. Amédée, R. Bareille, and C. Baquey, *Characterization of dynamic cellular adhesion of osteoblasts using atomic force microscopy.* Cytometry Part A, 2003. **54A**(1): p. 36-47.

69. Titushkin, I. and M. Cho, Modulation of cellular mechanics during osteogenic differentiation of human mesenchymal stem cells. Biophys J, 2007. **93**(10): p. 3693-702.

70. Kuznetsova, T.G., M.N. Starodubtseva, N.I. Yegorenkov, S.A. Chizhik, and R.I. Zhdanov, *Atomic force microscopy probing of cell elasticity.* Micron, 2007. **38**(8): p. 824-833.

71. Haghi, M., D. Traini, L.G. Wood, B. Oliver, P.M. Young, and W. Chrzanowski, A 'soft spot' for drug transport: modulation of cell stiffness using fatty acids and its

impact on drug transport in lung model. Journal of Materials Chemistry B, 2015. **3**(13): p. 2583-2589.

72. Mao, Z., B. Xu, X. Ji, K. Zhou, X. Han, M. Chen, X. Zhang, Q. Tang, X. Wang, and Y. Xia, *Titanium dioxide nanoparticles alter cellular morphology via disturbing their microtubule dynamics.* Nanoscale, 2015.

73. Stewart, M.P., J. Helenius, Y. Toyoda, S.P. Ramanathan, D.J. Muller, and A.A. Hyman, *Hydrostatic pressure and the actomyosin cortex drive mitotic cell rounding.* Nature, 2011. **469**(7329): p. 226-230.

74. Tan, S.C., W.X. Pan, G. Ma, N. Cai, K.W. Leong, and K. Liao, *Viscoelastic behaviour of human mesenchymal stem cells.* BMC Cell Biol, 2008. **9**: p. 40.

75. Waugh, R.E., Effects of abnormal cytoskeletal structure on erythrocyte membrane mechanical properties. Cell Motility, 1983. **3**(5): p. 609-622.

76. Perni, S., E.C. Preedy, and P. Prokopovich, *Success and failure of colloidal approaches in adhesion of microorganisms to surfaces.* Advances in Colloid and Interface Science, 2014. **206**(0): p. 265-274.

77. Clem, W.C., S. Chowdhury, S.A. Catledge, J.J. Weimer, F.M. Shaikh, K.M. Hennessy, V.V. Konovalov, M.R. Hill, A. Waterfeld, S.L. Bellis, and Y.K. Vohra, *Mesenchymal stem cell interaction with ultra-smooth nanostructured diamond for wear-resistant orthopaedic implants.* Biomaterials, 2008. **29**(24–25): p. 3461-3468.

Chapter 7 - Nanomechanical and surface properties of rMSCs post exposure to CAP treated UHMWPE wear particles

The content of this chapter has been submitted for publication to:

E. Callard Preedy, S. Perni, P. Prokopovich "Nanomechanical and surface properties of rMSCs post exposure to CAP treated UHMWPE wear particles" under review *Nanomedicine: nanotechnology, Biology and Medicine*

7.1 Abstract

Cold atmospheric plasma (CAP) has previously been used (1, 2) to improve the material properties (wear performance) of ultra-high molecular weight polyethylene (UHMWPE) primarily by increasing the cross-linking of the polymer chains and simultaneously enhance hydrophylicity and adhesion.

Wear debris generated by UHMWPE used in joint replacement devices has been of concern for joint replacements due to reductions in longevity of the implanted device, through its effects on the surrounding tissues and cells. Particles of submicron size can be up-taken by new bone cells, osteoblasts, and even change the pathway for differentiation of mesenchymal stem cells. This may have a detrimental effect on the health of the cell disrupting the nanomechanical properties associated with the cells in question.

The aim of this study was to investigate the elastic and adhesive properties of rat mesenchymal stem cells (rMSCs), through atomic force microscopy (AFM), after exposure to UHMWPE wear debris pre and post CAP treatment for 7.5 min and 15min.

The results indicated that the main changes in cell elasticity and spring constant (linked to turgidity) of MSC exposed to wear particles occurred in the first 24 hour of contact and the concentration did not play a significant role (in the range 0.5 to 50 mg/l). Moreover, for UHMWPE treated for 7.5 min, with progression of the wear simulation the results of the CAP treated samples for short periods of time were close to the result of untreated samples highlighting the superficial nature of this treatment. With longer CAP treatment this was not observed.

7.2 Introduction

Total joint arthroplasty and joint replacement surgeries are on the increase, including adjustments to hips, knees, elbows and shoulders. Orthopaedic surgical procedures can replace the whole joint, or commonly the damaged or diseased sections may be replaced with a biomedical prosthesis often including articulating surfaces. Surgery is often the last resort option for many osteoarthritis sufferers and this intervention restores mobility and relieves the debilitating pain thus greatly improving their quality of life. Over time, the implanted devices are subjected to everyday stresses and strains encountered through simple movements and wear debris are inherently produced. Wear debris has become a prevalent topic in the media, and a matter of concern for scientists, medical staff and patients (3-6). It has been noted that wear debris is produced regardless of the original material used in the implanted devices as it is a result of contacting surfaces rubbing and sliding against each other or harder metal based implanted materials (4, 6, 7).

Over the past few decades, Cobalt-chromium alloy alongside ultra-high molecular weight polyethylene (UHMWPE) has been widely employed as a result of their high biocompatibility, low friction coefficients, and high fracture toughness (7). Even so, UHMWPE is prone to generate wear particles after prolonged use (1, 3, 8). The debris formed by UHMWPE has been imaged using atomic force microscopy (AFM), where a range of diameters were observed between 100-500nm, and some as large as 1-2μm (9-11). Due to the size of the wear particles, even a small amount can initiate an inflammatory response which involves osteoblasts, osteoclasts, and macrophages; for

instance, the effect of wear particles on osteoblast cells can cause the cells to differentiate and prevent normal cell synthesis, thereby inhibiting the formation of new bone which in turn increases the resorption of the bone matrix inherently affecting osteoclast cells (12-14). It has been suggested that submicron UHMWPE particles (mean diameter of 0.5μm) greatly increases the induction of osteolysis than metal particles of lesser dimensions (diameter <0.1μm) (15-17).

Bone resorption, or osteolysis is the main culprit for future fracture and aseptic loosening of the surrounding bone and articulating surfaces, respectively. The severity of the bone damage and extent of the loosening of the articulating joint cause depilating pain, including loss of mobility and increased discomfort (3, 4, 7, 18); often resulting in revised surgery and replacement of the biomedical implant. Evidently, a revision operation due to osteolysis has its own issues and complications compared to the initial surgery a patient receives, as well as the mobility of the patient cannot fully recover after the primary operation (7).

Certain treatments have been developed to improve the performance and modify the physicochemical properties of UHMWPE to highly cross-linked polyethylene (XLPE) and carbon fibre reinforced polyethylene employing rapid heavy ion beam irradiation and argon plasma treatment (19-23). XLPE compared to UHMWPE is a denser polymer from an increase in cross-linking of the polyethylene backbone chains as a result of gamma radiation; this is thought to reduce the production of wear debris due to an increase in wear resistance. Despite the minimised generation of wear particles, the increased cross-linking causes a deficiency in the plasticity of the parent material resulting in decreased fatigue crack resistance (20). Apart from increased cross-linking,

UHMWPE and XLPE do not differ greatly when subjected to scratching; furthermore, to date there have been no long term studies on oxidative wear induced by oxygen free radicals produced from the gamma irradiation treatment (20). Presently, UHMWPE is the choice material for articulating surfaces due to its promising properties despite its obvious flaws; yet a lack of *in-vivo* studies and production costs have limited the availability for the exploration of new and/ or improved materials to be investigated as replacements for this polymer (1, 7, 19, 22, 23)

In the last two decades, a non-thermal plasma approach has been used for the sterilisation of heat sensitive materials and dental bleaching, respectively (1, 24). It is a cold atmospheric plasma (CAP) produced at atmospheric pressure and temperature, and is a partly ionised gas which has been more recently been applied to many medical applications including wound cleaning, as well as surface modification for biomedical prosthesis (1, 2, 25-27). CAP is a beneficial technique compared to the more traditional thermal procedures due to the ease of scale up, simple operational set up, and cost effectiveness as there is no need for a vacuum chamber or heating appliances; in addition the process can be applied contact free acting as a sterilisation technique as a result of its broad antimicrobial activity (1, 24). Positive results have been evident for the application of CAP treated material and its potency investigated on UHMWPE and metal surfaces reducing the generation of wear debris (1, 28, 29). CAP treatment has successfully been used to improve the wear performance of UHMWPE, reducing the wear rate by up to half from 2.7×10^{-7} $mm^3/N/m$ to 1.4×10^{-7} $mm^3/N/m$ after only 7 minutes of CAP treatment (1) through increased

cross-linking without detrimental effect on crystallinity. Additionally, the nitrogen group grafted on the material during CAP treatment increased the hydrophylicity and adhesion (whilst no oxygen was detected on the material after exposure to cold gas plasma (1, 2).

Although CAP treatment has proven its reliability in its application to sterilise and strengthen UHMWPE, no investigation has yet delved into its affects towards the surrounding tissues and cells of an implanted biomedical device. Fundamentally, the following investigation is set to explore untreated and CAP treated UHMWPE wear debris with two CAP exposure times (7.5 min and 15 min of He/O_2 gas mixture treatment) and its potential impact on the nanomechanical and adhesive properties of cells. This is achieved by measuring the mechanical (elasticity and turgidity), adhesive properties and metabolic activity of rat mesenchymal stem cells exposed to untreated and CAP treated UHMWPE particles produced at various time points (330k; 660k and 1M cycles of wear); employing the atomic force microscope (AFM). Additionally surface characterisation of the CAP treated surfaces and particles was performed employing SEM, XRD, XPS and Raman spectroscopy measurement techniques respectively.

7.3 Materials and Methods

7.3.1 Polymer

Ultra-high molecular weight polyethylene (UHMWPE) sourced from Germany (GUR 1020, Hoechst).

7.4 Cold Atmospheric Plasma (CAP) source and UHMWPE treatment

Cold atmospheric plasma (CAP) alters gas particles to plasma producing free radicals and ions in the plume to increase cross-linking, sterilisation and surface modification of UHMWPE. The equipment used (Figure 7-1) consisted of two main electrodes: a capillary and ring electrode. The capillary electrode is situated within the quartz tube with an inner diameter of 1.5mm; downstream of this the ring electrode is wrapped around the quartz tube near the nozzle where the plasma jet is emitted. An axially directed electrical field is produced when an external voltage is applied as a result of the axial separation of the electrodes and due to the gas being introduced in an axial direction, therefore this set up is also known as a linear field device (1, 25). A mixture of Helium and Oxygen were mixed before entering the capillary tube with 5 slm (standard litre per minute) of 99.99% Helium, and 10 sccm (standard cubic centimetre per minute) of Oxygen. An alternating voltage supply, at a peak voltage of 8 kV and excitation frequency of 20 kHz, is introduced to the gas mixture entering the capillary electrode in the quartz tubes causing an electrical discharge visualised as a light-emitting plume from the nozzle (1, 25) and is also called as the CAP jet. Under the experimental conditions considered in this study the plasma plume was more than 1 cm long and its gas temperature was always below 27 °C. Samples to be treated were placed on a sample holder which was grounded electrically and the sample was fixed at 1 cm directly downstream of the quartz nozzle. The holder was rotated so that the entire UHMWPE was exposed to the CAP jet plume in turn. The samples were exposed to the plasma plume for 7.5 and 15 min. The treated samples were kept at room temperature and subjected

to material and surface characterization within 1 day. Wear testing was initiated at the same time internal.

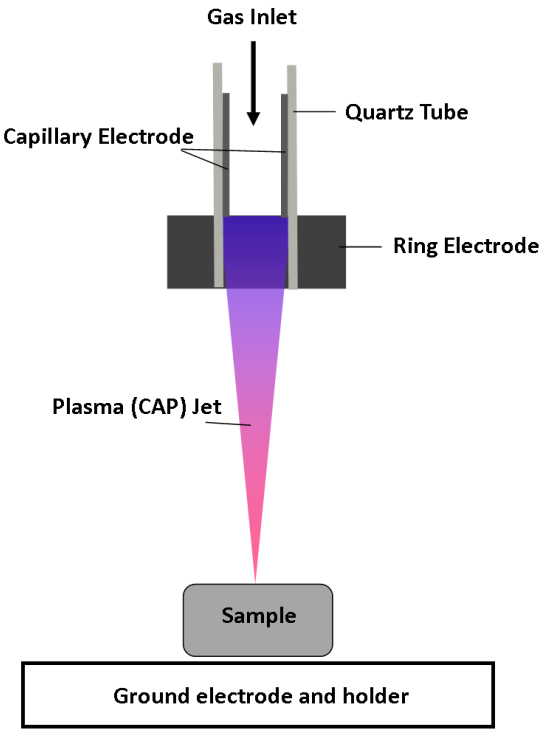

Figure 7-1. CAP equipment set up.

7.4.1 Wear testing

Wear testing of UHMWPE (GUR 1020, Hoechst, Germany) was performed using a single station pin on plate in-house built wear simulator under constant load applied under lubricated conditions. Pins were machined from ram extruded cross-linked (4 Mrad) UHMWPE while metallic plates were made of medical grade wrought Cobalt–chromium alloy (according to ASTM F1537) and polished to an average surface roughness Ra 0.01 µm. Before wear testing all samples were soaked in distilled water at room temperature for 2 weeks, to saturate them. The lubricant employed in all wear tests consisted of 25 % v/v

bovine serum (Harlan Sera-Lab, Loughborough, UK) in sterile water with 0.1% (w/v) sodium azide to inhibit the growth of bacteria. The lubricant was changed every week and serum samples were collected for wear debris analysis. Control pins were soaked in lubricant for the duration of the wear test and were used as a reference for mass change due to water uptake by the UHMWPE. The wear test was performed with multidirectional motion, the pins rotating 30° every 15 mm, and a sliding distance of 60 mm, resulting in a total pin rotation of 120°. The test cycle frequency was 1 Hz. A compressive load of 160 N was applied to an 8 mm diameter area of the pin surface, resulting in a nominal contact pressure of approximately 3.18 MPa. These testing conditions were selected to match the physiological range of contact pressures and lubrication found in human articular joints (30). At least six replicates were obtained for each type of plasma surface modification of UHMWPE.

The serum with wear particles were collected after 333k cycles, 666k cycles and 1M cycles and particles extracted.

7.4.2 Isolation of UHMWPE Wear Debris from Serum

From the lubricant, bovine serum, used in the wear simulator test, the wear particles are isolated by adding 2g of Potassium Hydroxide (KOH) to 100ml of the bovine serum with wear debris. This suspension was placed in a water bath at 60^{o}C with continuous stirring for 48 hours; post 48 hours the solution was removed and allowed to cool to room temperature before placing in the fridge for 30 minutes to reduce the temperature to 4^{o}C. Once cool, a 10ml mixture of chloroform:methanol (2:1) was added to the solution and incubated in a fume cupboard at room temperature for 24 hours. The suspension was then

centrifuged at 2000 rpm (revolutions per minute) at room temperature to remove unwanted proteins and lipids contained in the lubricant for 20 minutes; the supernatant was removed and the process was repeated with the addition of the chloroform:methanol mixture until the supernatant was clear and all proteins and lipids removed. Following the centrifugation of the samples, filtration was required using a Buchner filter and 0.2 µm filter membranes (Whatman, UK), to collect all wear debris remaining in the supernatant solution. The filters were air dried in a fume cupboard overnight in sterile covered petri dishes. All filters membranes were weighed before and after filtration to determine the yield of wear debris.

7.4.3 Surface characterisation

7.4.3.1 SEM analysis

The extracted UHMWPE wear debris on the membrane filters were gold coated and SEM images were acquired. Scanning electron microscopy was performed in a Hitachi filament scanning microscope, using a filament voltage of 5 keV. A minimum of 15 images at random locations were acquired for each filter in secondary electron mode. Wear debris was identified from the images and the shape and size individually determined. This process was performed individually on serum obtained from each of the replicates of the various treated and untreated materials and the results are presented as overall means ± SD.

7.4.3.2 Raman analysis

Raman spectra were obtained using a Renishaw Raman System 1000 (Renishaw plc) with an Ar+ laser (514 nm). The instrument was fitted with an external Olympus BH-2 microscope and the spectra were collected using a

personal computer. The bands at 1080 and 1127 cm^{-1} are due C–C stretching, the band at 1293 cm^{-1} to twisting of crystalline –CH2–, the band at 1365 cm^{-1} is related to amorphous C–C twisting and that at 1440 cm^{-1} to the bending of crystalline C–C (31). Peaks at about 1560 cm^{-1} are characteristic of hydrogenated amorphous carbon found in diamond-like carbon structures (32). Peaks in the regions between 2400 and 2800 and from 3000 to 3300 cm^{-1} can be attributed to nitrogen compounds (31).

7.4.3.3 XRD analysis

X-ray diffraction (XRD) analysis was performed using a Bruker-Axs D8 (GADDS) diffractometer, utilizing a large two-dimensional area detector and a monochromatic Cu X-ray source (Ka1 and Ka2) fitted with a Gobble mirror. The instrumental set-up gave 34° for both h and x, with a resolution of 0.01° and 3–4 mm^2 of sample surface illuminated at any one time. Multiple Debye–Scherrer cones were recorded simultaneously by the area detector with two sections covering a 2h range of 65°. The Debye–Scherrer cones were integrated along x to produce standard one dimensional diffraction patterns of 2h against intensity. Scan data was collected for 800 s to give sufficiently resolved peaks for indexing.

7.4.3.4 XPS analysis

High resolution X-ray photoelectron spectroscopy (XPS) was performed in a Kratos Axis Ultra-DLD photoelectron spectrometer using monochromatic Al Ka radiation. The core peaks for O1s was recorded and analysed.

7.4.4 Cell Culture

28 days old, male Wistar rats were obtained from the colony maintained by Charles River European Suppliers (Charles River UK Ltd., Kent, UK). The animals were housed with free access to water and were maintained with treatment and care protocols conformed to UK Animals (Scientific Procedures) Act 1986, in accordance to the European Convention for the Protection of Vertebrate Animals Used for Experimental and Other Scientific Purposes (Strasbourg, Council of Europe). Bone marrow stem cells were isolated from rat femur and humerus, using plastic adherence (33), followed by fibronectin adherence techniques (34). After 7 days, merged colonies were expanded (passage 0). This study was conducted on cells obtained from early population doubling level.

The cells were routinely cultured in α-MEM (Life Technologies), supplemented with 20% (v/v) FBS, 1% (v/v) of solution penicillin (5000 U/mL) and streptomycin (5000 mg/mL) (Gibco Invitrogen) and 1% (v/v) of L-ascorbic acid 2-phosphate solution at 50 mg/ml (Sigma, UK). Accutase (Gibco Invitrogen) was used when cells were 70% confluent in order to passage and count. The cells were maintained at 37° C in a humidified atmosphere containing 5% CO_2.

For atomic force microscopy experiments, cells were seeded in 24-well plates at a density of 6000 cells per well and cultured for 24 hours on sterilised polystyrene slides placed inside the well before exposure to UHMWPE wear debris. For each type of the wear debris sample a stock solution of UHMWPE particles suspended in culture media was prepared at 5 mg/ml and appropriate amount was added to each well to reach final concentrations of 5; 25 and 50

μg/ml and incubated from 24h up to 3 days. Control samples consisting of cells not exposed to the wear particles and cultured in the same conditions were used for comparison with treated cells.

For the MTT assay, the cells were cultured as described above.

7.4.5 Nanomechanical and adhesive properties of rMSCs measurements

All AFM force measurements were conducted in an open liquid cell as described in [34], using PBS as the aqueous phase. A triangular tipless cantilever (Bruker, UK) with a nominal spring constants ($K_{cantilever}$) of 0.1 N/m was used; the actual spring constant of the AFM cantilever was determined using the modified Sader method [35, 36]. Borosilicate glass beads (10 μm in diameter) were glued onto the cantilever and served as cell indentors. In order to prevent indentations depth greater than 400-500 nm, the maximum applied load was set, after preliminary tests, to 1 nN or 2 nN depending on the samples. At least 15 cells were analysed for each sample, at each concentration of particles and at each time point (24, 48, and 72 hours). Cells were first located and then at least 20 approaching and retracting z-piezo coordinates vs. deflection curves were extracted from randomly selected points on the surface of each cell avoiding the peri-nuclear region. Experiments were performed in triplicates.

7.4.5.1 Cell elasticity and spring constant determination

The approaching part (trace) of the AFM curves was used to calculate the nanomechanical properties of the cells. The Young modulus of the cell surface location under investigation was determined fitting the Hertz model (Eq. 7-1) to

the first part of the indentation vs. force curve after contact between AFM tip and cell surface.

$$F = \frac{4}{3}\frac{E}{(1-\nu^2)}\sqrt{R}\delta^{3/2} \quad (7\text{-}1)$$

Where:

F = force recorded by AFM

E = Young modulus

R= radius of the spherical indentor (5 μm)

ν = Poisson ratio (assumed 0.5)

δ = indentation depth

The spring constant of the cell surface in the location probed was determined through the slope of the curve after the Hertzian regime according to:

$$F = k_b \delta \quad (7\text{-}2)$$

Where:

F = force recorded by AFM

K_b = spring constant of the cell

δ = indentation depth

Both models require the determination of the separation between cell surface and AFM tip *(δ)*, this was calculated from the coordinates (z-piezo) of the trace curve assuming that the point of contact corresponded to the local minimum of force; from this:

$$\delta = |z - z_0| - d_{cant} \quad (7\text{-}3)$$

Where:

z_0 = z-piezo value of the minimum of the trace curve

z = z-piezo value of the trace curve

d_{cant} = cantilever deflection

δ = indentation depth

and

$$F = K_{Cantilever}\, d_{cant} \quad (7\text{-}4)$$

Both Eq. 1 and 2 were fitted to the data using the least squares method through an in-house written FORTRAN code.

Overall surface heterogeneity of nanomechanical properties was studied through the spatial distribution of E and K_b.

7.4.5.2 Cell Adhesion force

The adhesion forces between a cell and AFM tip were determined as the minimum value of the retracting (retrace) part of the AFM curve.

7.4.6 Metabolic activity assay

MTT (3-(4,5-dimethythiazol-2yl)-2,5-diphenyltetrazolium bromide) assay was used to determine the effects of the metal nanoparticles on MSCs viability. It is a colorimetric assay of cell viability and depends on the metabolic activity of the cell as rapidly dividing cells exhibit high rates of MTT reduction. Cells were initially cultured and exposed to nanoparticles as stated above in a 24-wells plate; after the chosen exposure to the wear particles, the media was replaced with phenol red-free medium and 80 µl of MTT stock solution (5mg/ml) was added to each well and incubated at 37^{o}C in humidified atmosphere containing 5% CO_2 for 2 hour. The metabolised MTT, formazan, was re-suspended with 800 µl of dimethyl sulfoxide (DMSO). 200 µl were transferred to a 96-well plate absorbance at 560nm was read using a spectrophotometer (ELISA Reader Labtech LT-5000MS). All experiments were performed in triplicates with each concentration (5, 25 and 50 µg/ml) as well as a control sample of cell suspension not exposed to the wear particles (untreated cells).

7.4.7 Statistical Analysis

All samples were independent of each other, and so the elasticity data was analysed using one-way ANOVA to determine any significant difference between the mean values of the concentrations used. This was followed by Tukey's HSD post-hoc due to the independent nature of the data to determine in which groups the difference if any occurs ($p<0.05$). Adhesion forces were

compared using the Kruskal-Wallis test followed by Dunn's *post hoc* test for individual pairs of data sets. Statistical analysis was performed using SPSS.

7.5 Results

7.5.1 Surface characterisation (Raman, XRD, XPS, SEM)

Raman spectroscopy was employed to investigate the composition of the surface of the samples after treatment. The spectra of the surface of UHMWPE (Figure 7-2) showed two high peaks at about 2800 cm^{-1} that are typical of the bond between carbon and hydrogen. In the range 1000–1500 cm^{-1} four small peaks were evident which are typical of UHMWPE.

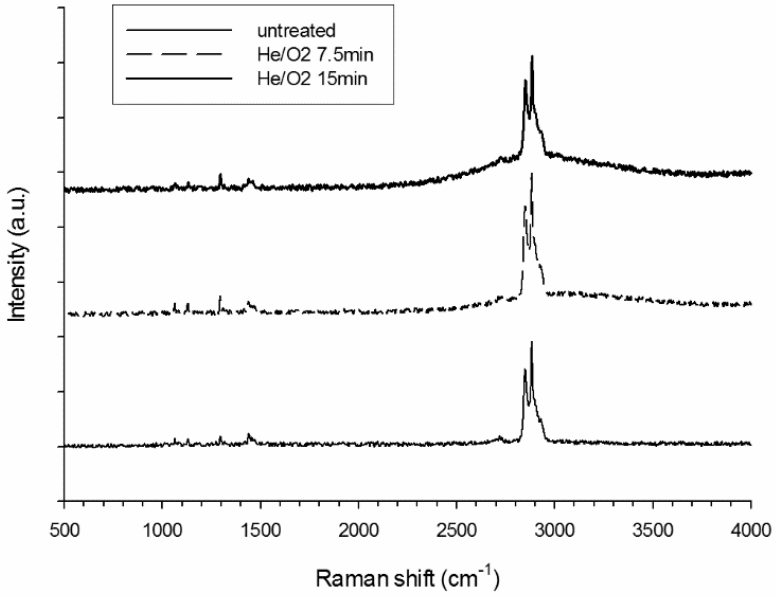

Figure 7-2. Raman spectra of untreated UHMWPE and treated with cold gas plasma for 7.5 and 15 min exposure times

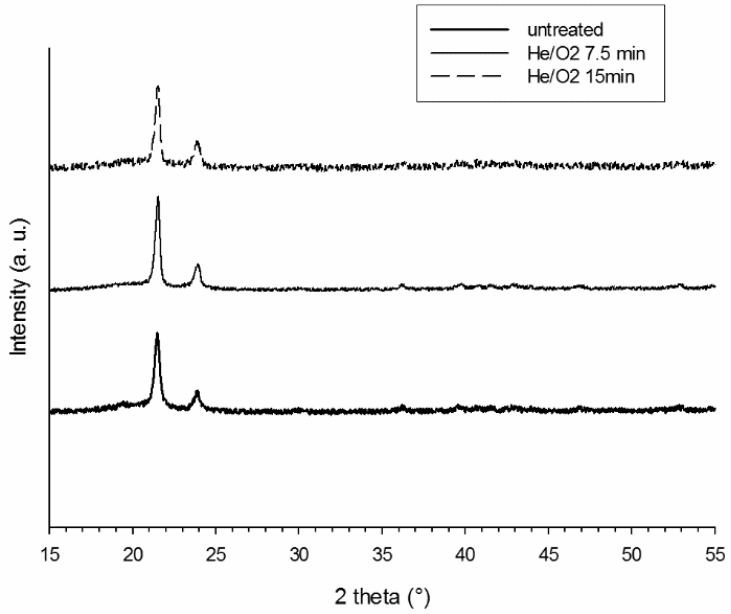

Figure 7-3. XRD diffraction patterns of untreated UHMWPE and treated with cold gas plasma for 7.5 and 15 min exposure times.

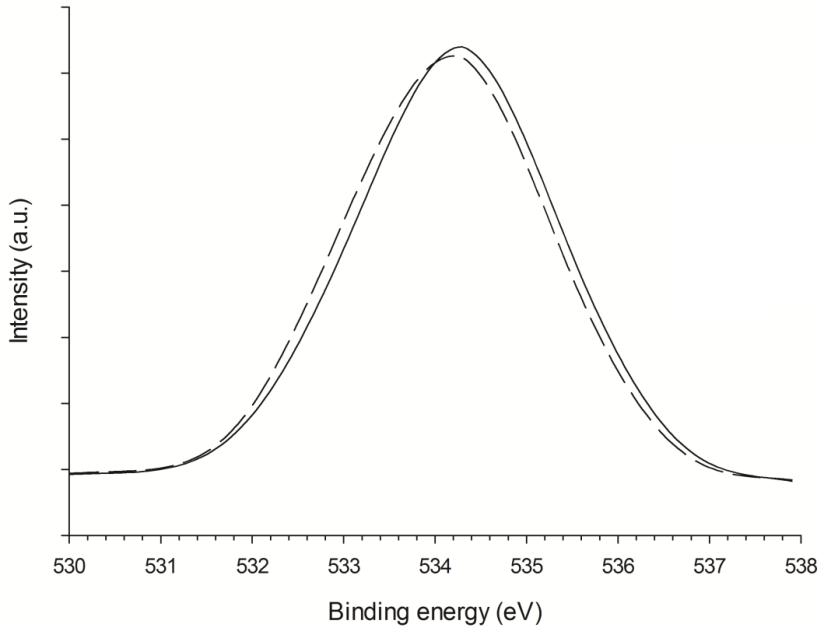

Figure 7-4. XPS spectra acquired for the region O1s.

——— untreated UHMWPE ------ 15 min CAP treated UHMWPE

After 7.5 min of cold plasma treatment the Raman spectra presented a wide peak at a Raman shift between 3000 and 3300 cm^{-1}, which is characteristic of the bond between carbon and nitrogen. A similar peak was also evident in the samples exposed to cold gas plasma for 15 min. The region between 2400 and 2800 cm^{-1} that was altered in the samples treated for 7.5 and 15 min can also be attributed to nitrogen compounds. There was no noticeable difference in terms of the XRD diffraction patterns (Figure 7-3) with and without plasma treatment, demonstrating that the cold atmospheric pressure plasma did not affect the crystallinity of UHMWPE. Moreover, the XPS spectra did not reveal any increase in the level of material oxidation as the peak relative to O1s did not change after 15 min exposure to cold gas plasma Figure 7-4.

Scanning electron microscope was also used to determine size and shape of the UHMWPE wear particles. The UHMWPE debris produced during wear simulation, extracted from the lubricant, were generally circular in shape with some elongated regardless of the CAP treatment, examples are shown in Figure 7-5 and Figure 7-6). From the size distribution data presented in Figure 7-7, it is evident that the great majority (around 70%) of debris had a diameter between 0.2 and 0.6 µm, whilst a small proportion of the debris was between 0.6 and 2 µm, and about 15% of the debris was larger than 2 µm. It is also clear that the CAP treatment had no influence in the size distribution of the wear debris.

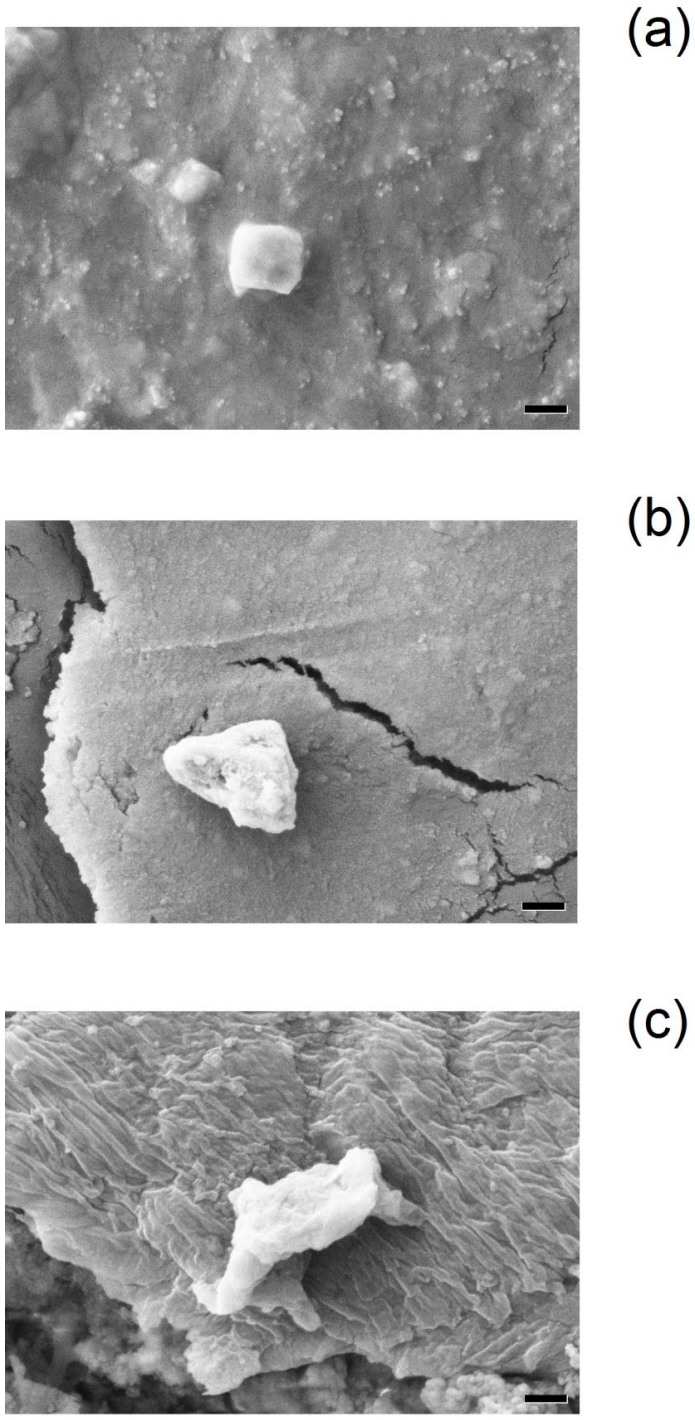

Figure 7-5. SEM of untreated UHMWPE after 333 kC (a), 666 kC (b) and 1 MC. Bar represents 400 nm.

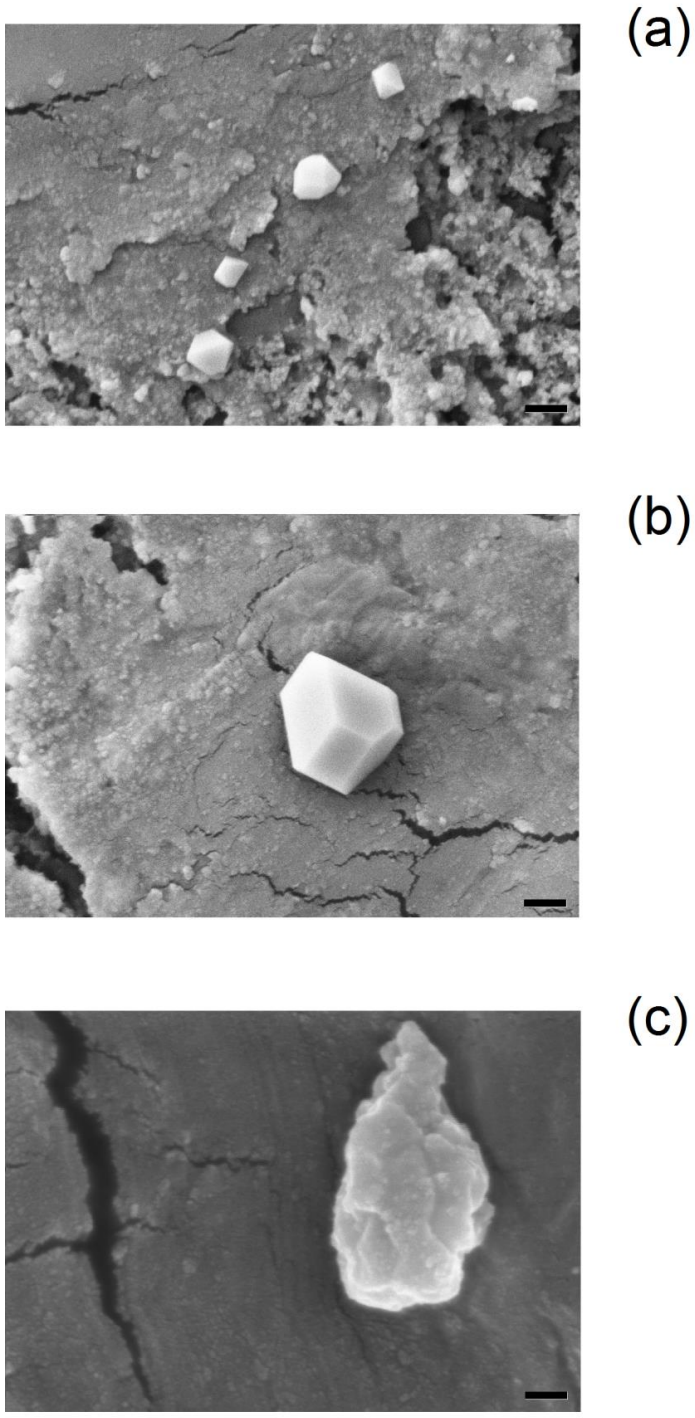

Figure 7-6. SEM of 15 min CAP treated UHMWPE after 333 kC (a), 666 kC (b) and 1 MC. Bar represents 400 nm.

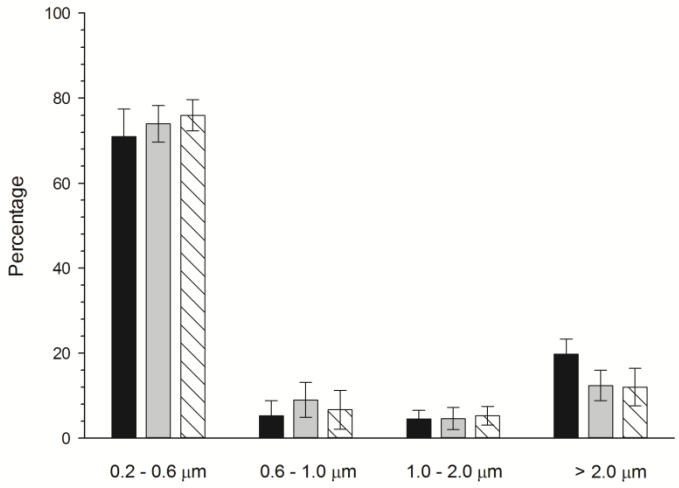

Figure 7-7. Size distribution of the wear debris produced after wear simulation of UHMWPE.

■ untreated UHMWPE ▨ 7.5 min treated UHMWPE ▨ 15 min treated UHMWPE

7.5.2 Metabolic activity

The metabolic activity of MSCs exposed to wear particles of untreated UHMWPE or after CAP treatment did not change with the particles concentration, number of wear cycles and exposure time (Figure 7-8 and Figure 7-9). Furthermore, the CAP treatment had no consequence on the metabolic activity of the cells.

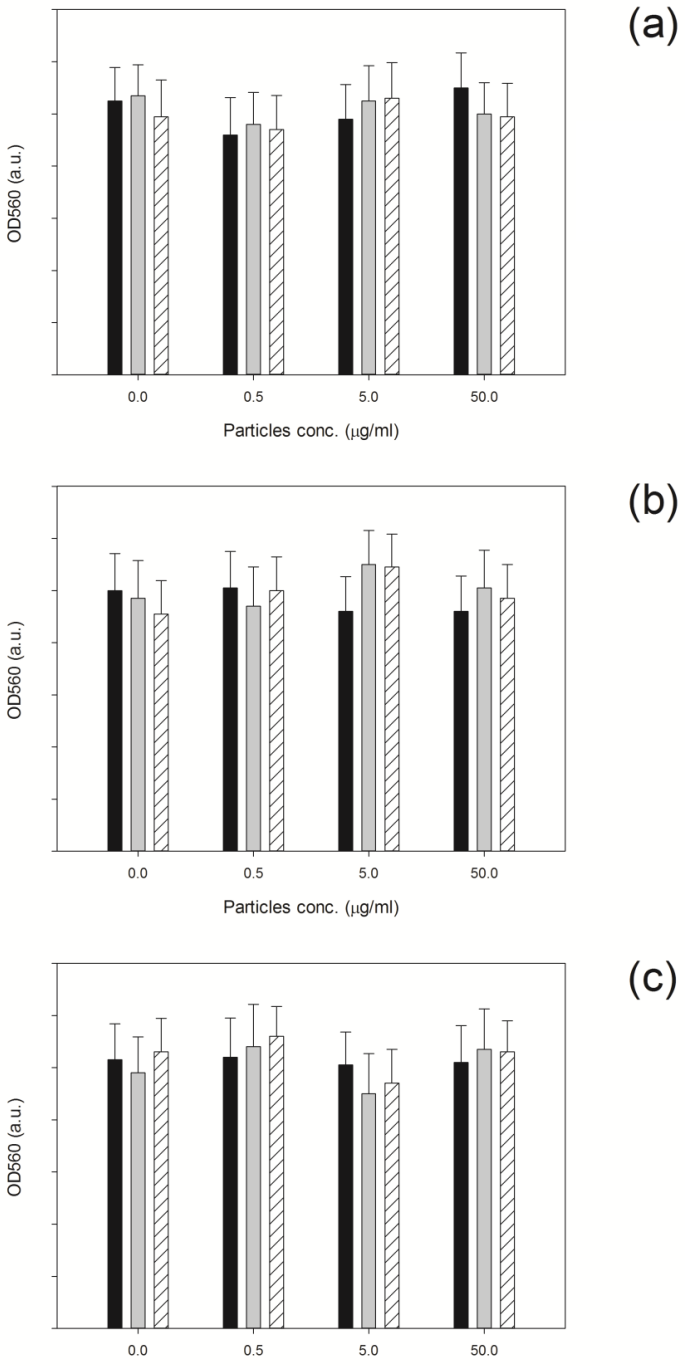

Figure 7-8. MTT results of MSCs exposed for 24 h to UHMWPE wear particles after 333k C (a), 666 kC (b) and 1 MC (c).

■ untreated UHMWPE ▨ 7.5 min treated UHMWPE ▨ 15 min treated UHMWPE

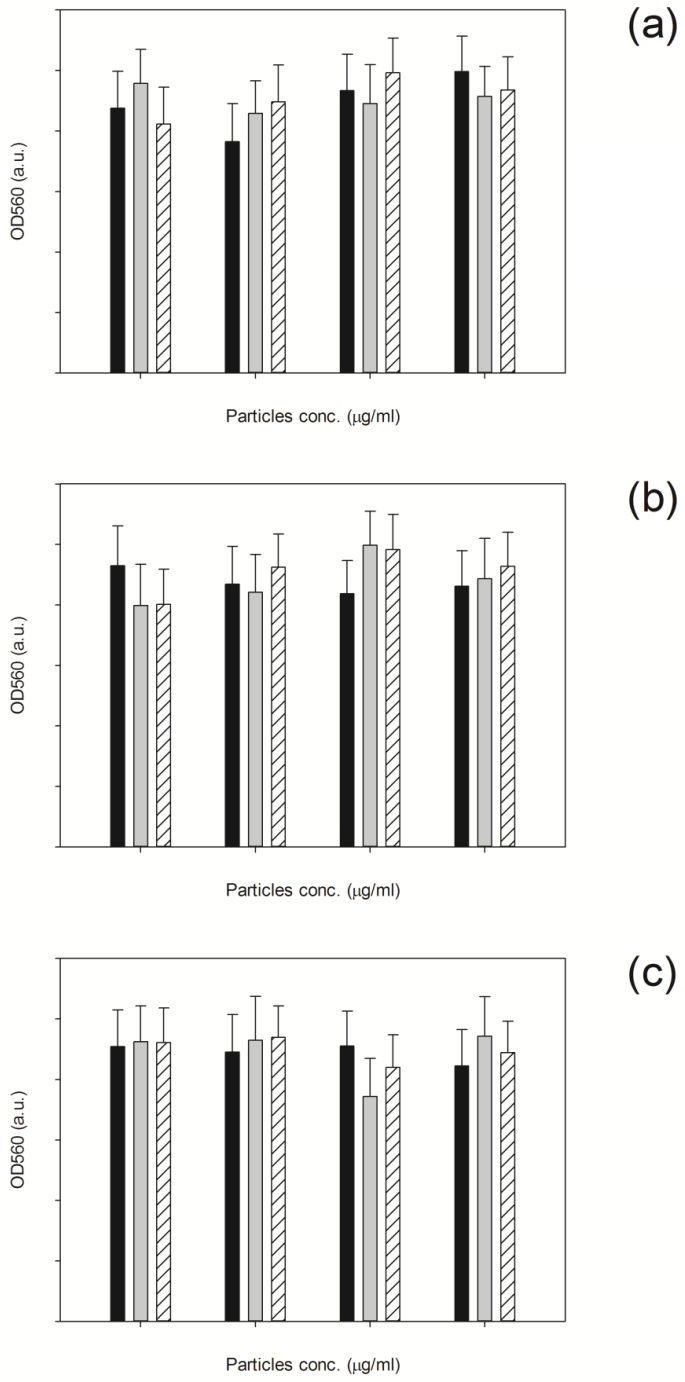

Figure 7-9. MTT results of MSCs exposed for 72 h to UHMWPE wear particles after 333k C (a), 666 kC (b) and 1 MC (c).

■ untreated UHMWPE □ 7.5 min treated UHMWPE ▨ 15 min treated UHMWPE

7.5.3 Elasticity, spring constant and adhesion

Elasticity measurements were conducted using the AFM over 3 days. Cells were exposed to wear debris over time at different concentrations ranging from 0.5 to 50 µg/ml, 9 types of UHMWPE debris were used, untreated UHMWPE (Figure 7-10) along with 333 kC, 666 kC and 1MC CAP treated for either 7.5 min (Figure 7-11) or 15 min (Figure 7-12).

For cells exposed to untreated samples of UHMWPE (Figure 7-10) elasticity was lower compared with the control after 24 hrs exposure, while no difference in elasticity was noted at 48hrs and 72hrs exposure and no effect of concentration was demonstrated. For cells exposed to 7.5min CAP treated samples, Figure 7-11, a reduction in elasticity was recorded after 24hrs exposure compared to cell not exposed to any particle, whilst no difference was noted after 48 hrs and 72hrs compare with control. For cells exposed to 15 min CAP treated samples, Figure 7-12, a decrease of elasticity was observed after 24hrs compared to control samples (cells not exposed to any particle). On the other hand, an increase of elasticity was seen after 48hrs and 72hrs exposure compared to control cells. No effect was observed on cells varying concentration of wear particles or wear rate. Overall elasticity was reduced with lowering rate of wear (at 333kC elasticity is lower than at 666kC and even less at 1MC). No concentration effect was shown. Overall, elasticity of CAP treated wear particles (15min) is higher compared to untreated wear particles especially for 333kC and 666kC wear performance, however at 1MC elasticity of CAP treated and untreated samples do not change significantly. Also there is no difference between untreated and 7.5min treated samples.

For the spring constant values, untreated samples (Figure 7-13), no change was observed for increasing concentration or with time, all spring constant values for cells exposed to the wear debris had a value of around 0.004 N/m. However this was greater than the resulting values for cells not exposed to any particle.

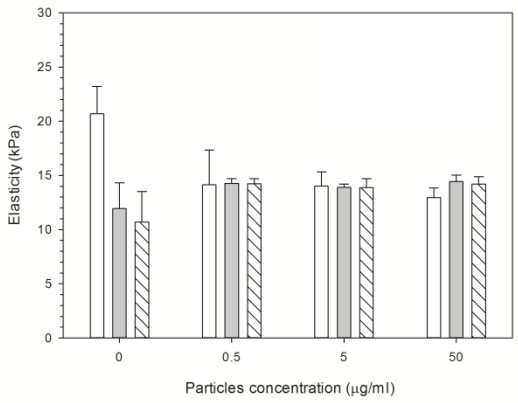

Figure 7-10. Mean cell elasticity of MSCs exposed to untreated UHMWPE wear particles.

□ 24 h ▨ 48 h ▨ 72 h

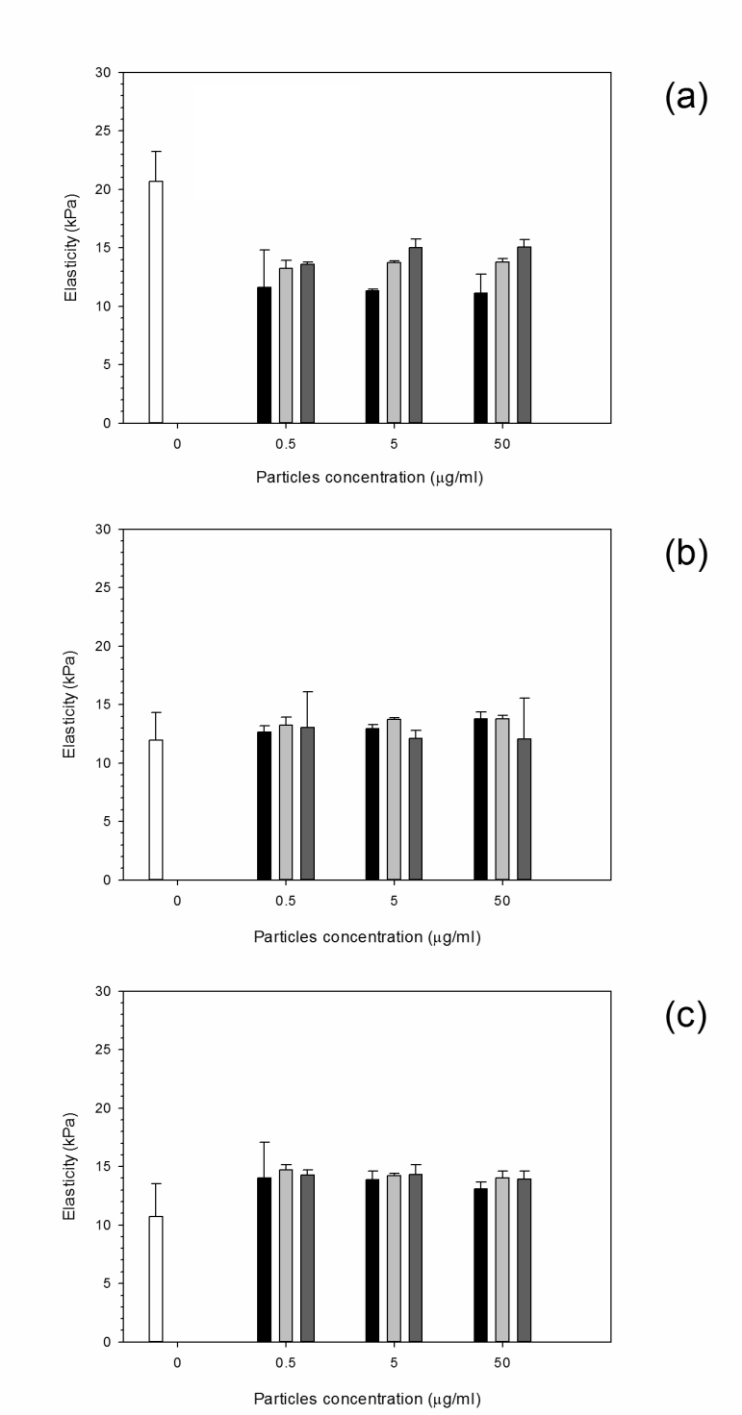

Figure 7-11. Mean cell elasticity of MSCs exposed to UHMWPE wear particles post CAP treatment for 7.5 min for (a) 24h, (b) 48 h and (c) 72 h.

☐ Control ■ UHMWPE 333kC ■ UHMWPE 666kC ■ UHMWPE 1MC

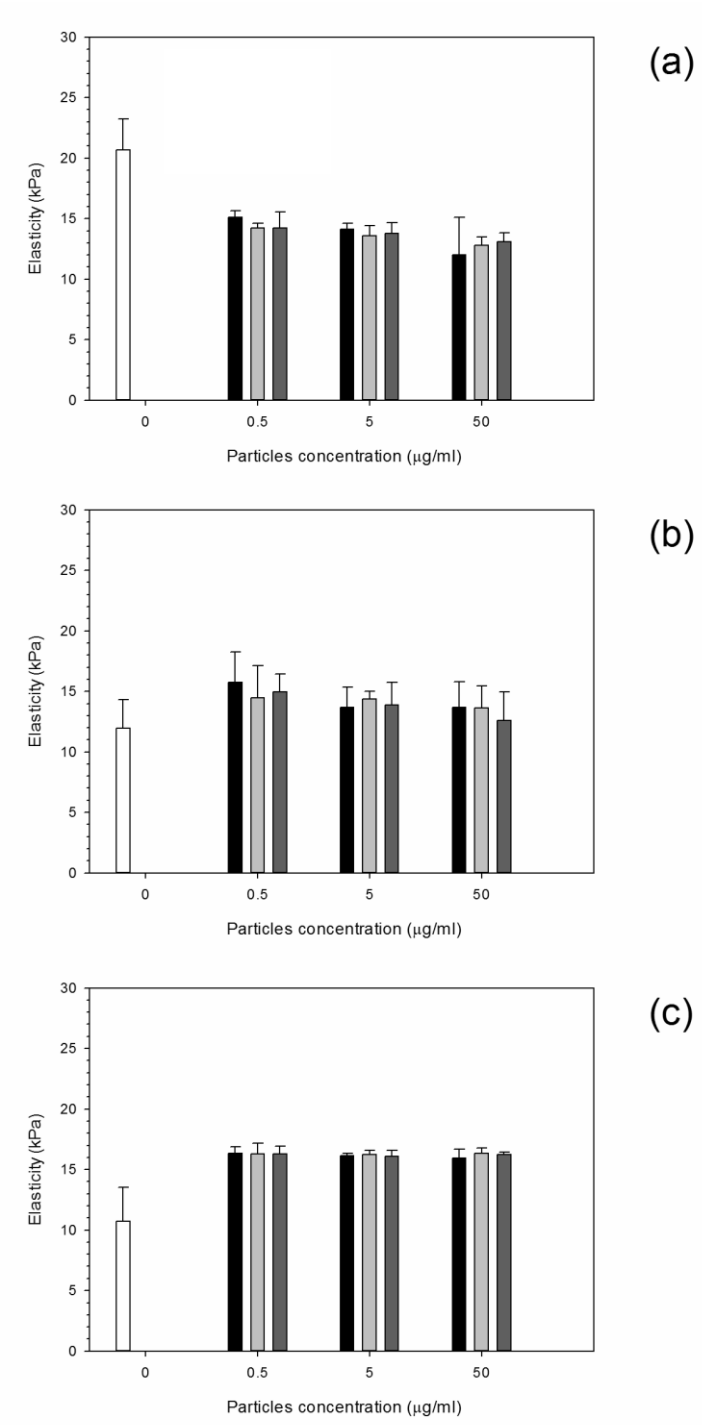

Figure 7-12. Mean cell elasticity of MSCs exposed to UHMWPE wear particles post CAP treatment for 15 min for (a) 24h, (b) 48 h and (c) 72 h.

□ Control ■ UHMWPE 333kC □ UHMWPE 666kC ■ UHMWPE 1MC

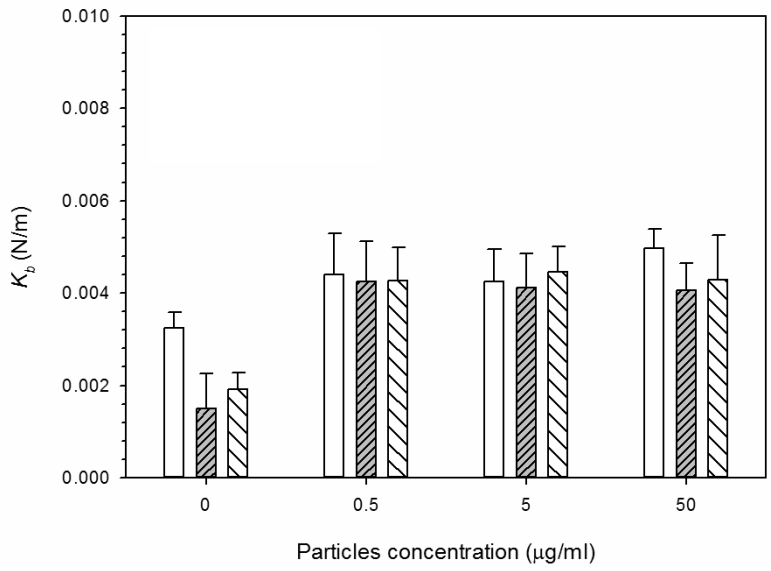

Figure 7-13. Mean spring constant of MSCs exposed to untreated UHMWPE wear particles.

□ 24 h ▨ 48 h ▨ 72 h

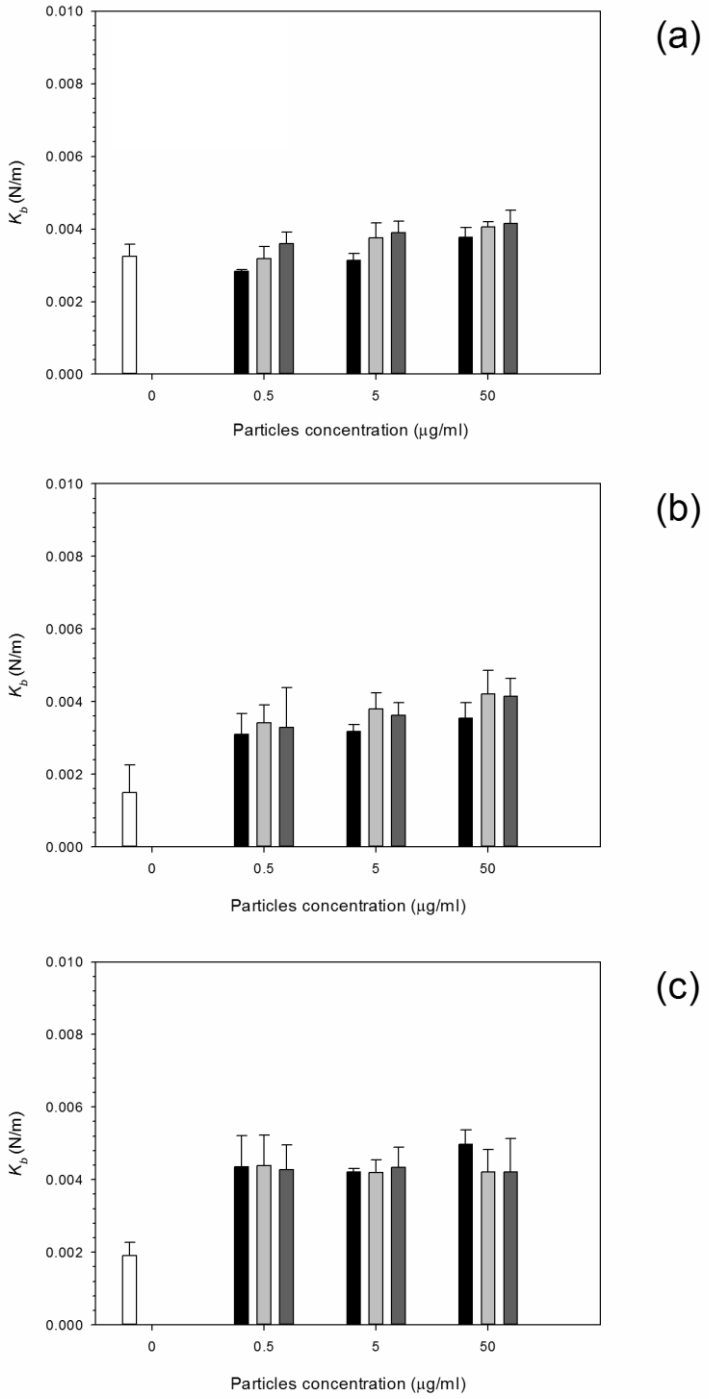

Figure 7-14. Mean spring constant of MSCs exposed to UHMWPE wear particles post CAP treatment for 7.5 min for (a) 24h, (b) 48 h and (c) 72h.

□ Control ■ UHMWPE 333kC □ UHMWPE 666kC ■ UHMWPE 1MC

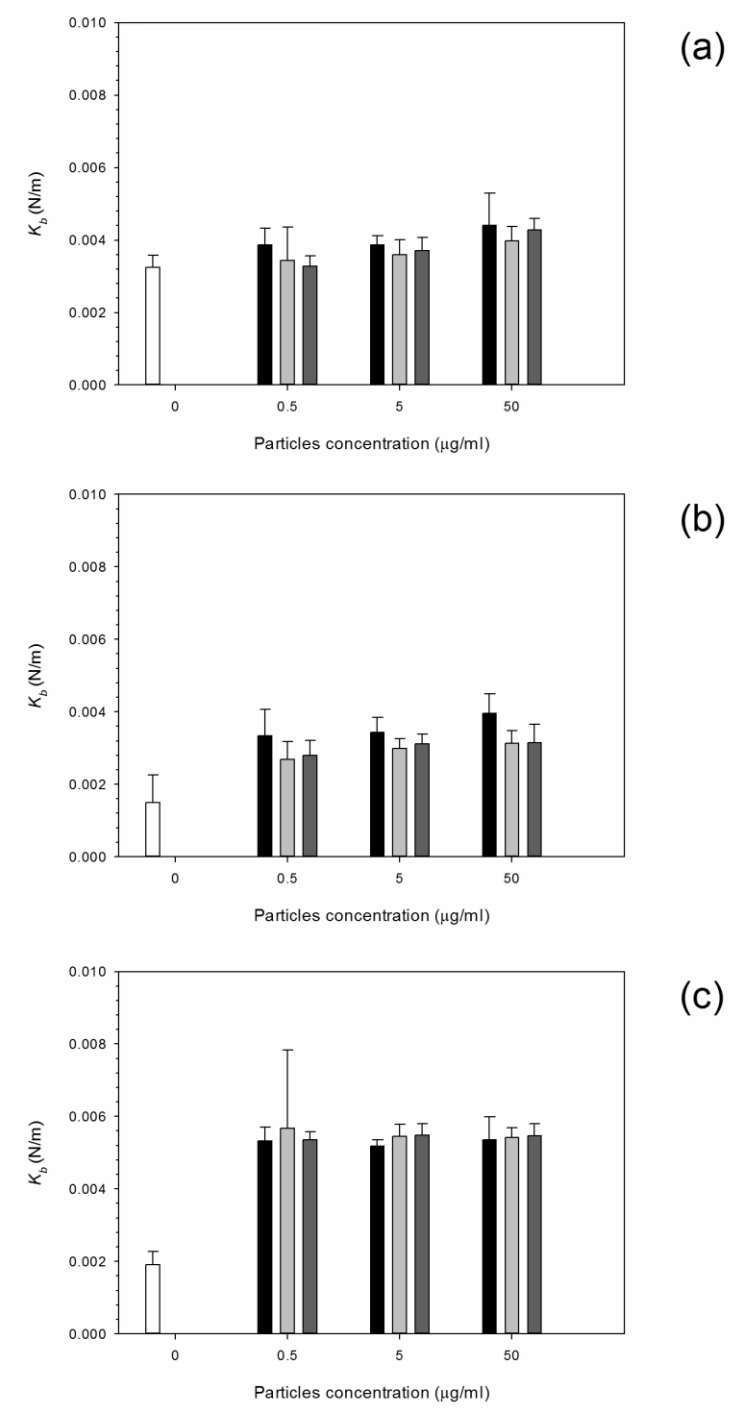

Figure 7-15. Mean spring constant of MSCs exposed to UHMWPE wear particles post CAP treatment for 15 min for (a) 24h, (b) 48 h and (c) 72h.

□Control ■ UHMWPE 333kC □UHMWPE 666kC ■UHMWPE 1MC

For MSC cell exposed to 7.5 min CAP treated UHMWPE samples (Figure 7-14), the spring constant of the cells generally increased with increasing concentration over time. At 24 hours, 666 kC had the lowest spring constant recorded at 0.003 N/m at a concentration of 0.5 µg/ml which increases to 0.004 N/m at a concentration of 50 µg/ml. Similar values for 333 kC and untreated UHMWPE were also observed with slightly higher values for untreated UHMWPE wear debris. At 48 hours exposure, control cells spring constant reduced to below 0.002 N/m, whereas the values for cells exposed to wear debris at a concentration of 0.5 µg/ml spring constant remained at around 0.003 N/m; again an increase in overall spring constant to 0.004 N/m was observed at a concentration of 50 µg/ml. Again for 72 hours, the cell control spring constant remained at 0.002 N/m, whereas the spring constant for all wear debris levelled at 0.004 N/m for all particles at all concentrations.

Spring constant values for cells exposed to wear debris of UHMWPE CAP treated for 15 minutes (Figure 7-15) had a less pronounced increase in spring constant for 24 and 48hours exposure. Yet after 72 hours exposure, all samples plateaued and remained constant at an increased value of around 0.0055 N/m.

For cells exposed for 24hrs to 7.5min CAP treated wear particles no change of spring constant was noted while for cells exposed to 15 min CAP treated particles even at 24hrs there was a pronounced effect at high concentrations of wear particles compared to the control cells. These differences were higher after 48hrs and 72hrs of exposure compared to the control cells with no dependence from the concentration of wear particles and wear rate. In general,

cells exposed to CAP treated UHMWPE gave higher spring constant values than cells exposed to untreated samples.

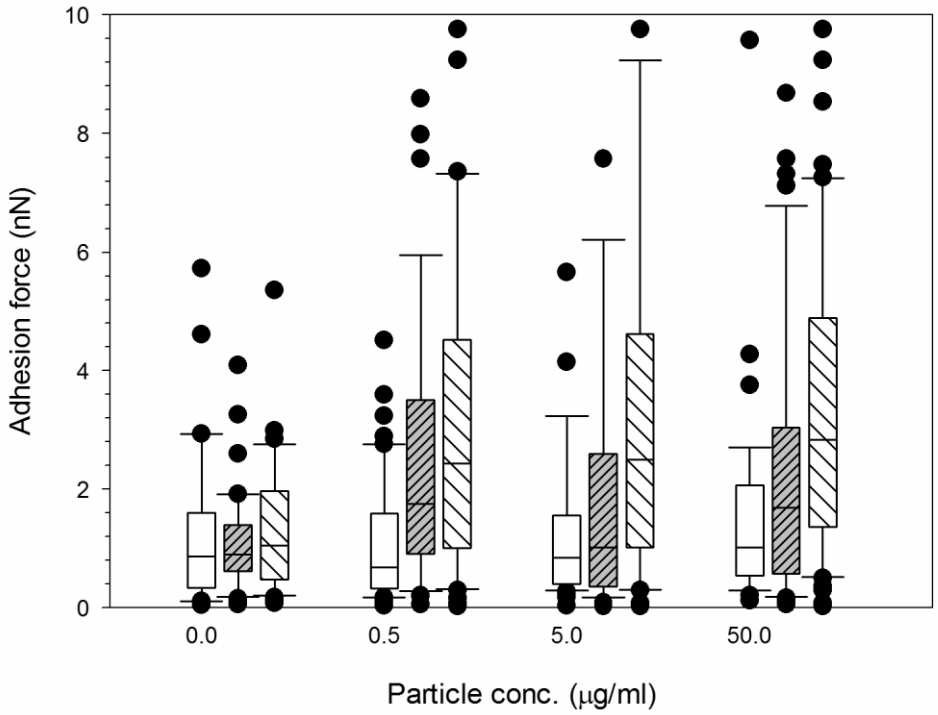

Figure 7-16. Adhesion force distribution of MSC cells exposed to untreated UHMWPE wear particles.

□ 24 h ▨ 48 h ◪ 72 h

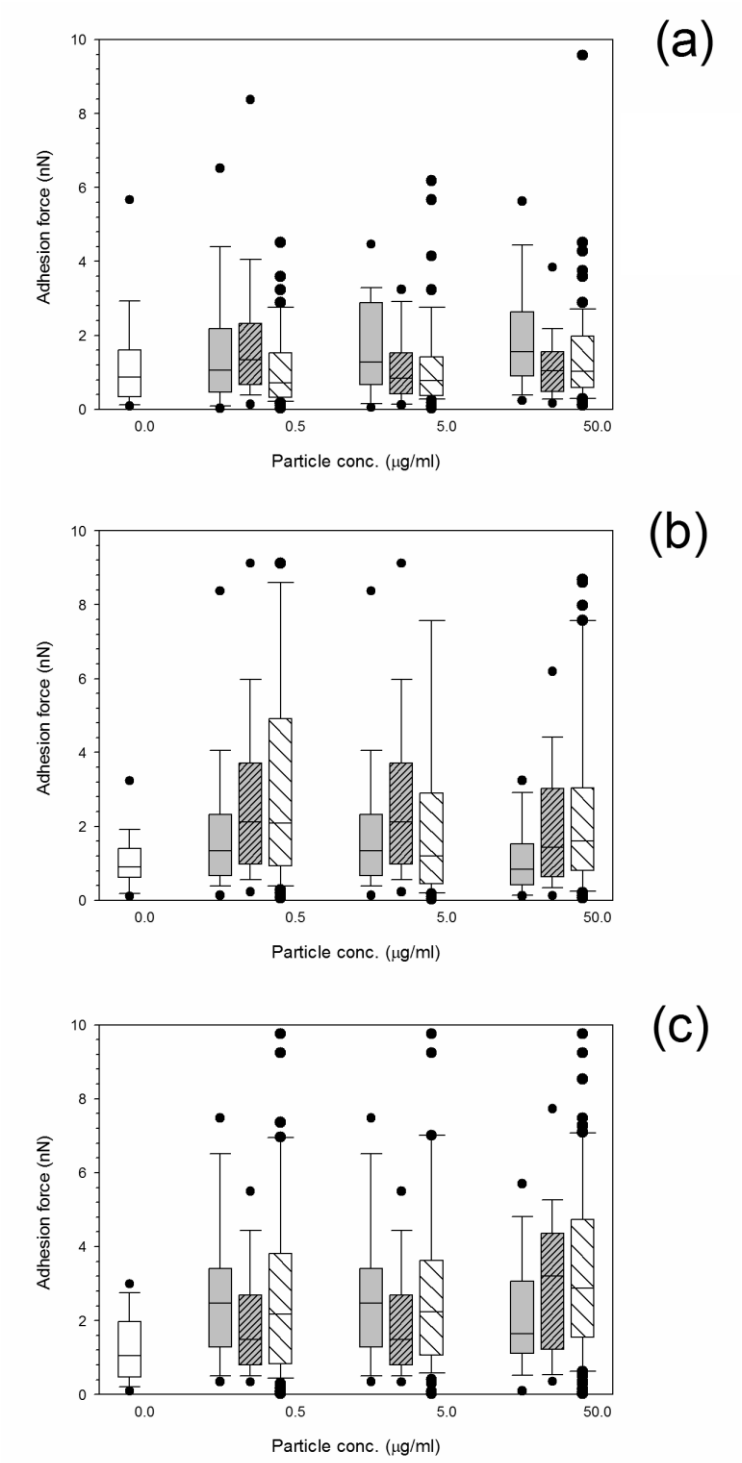

Figure 7-17. Adhesion force distribution of MSC cells exposed to UHMWPE wear particles post CAP treatment for 7.5 min for (a) 24h, (b) 48 h and (c) 72h.

☐ Control ☐ UHMWPE 333kC ☐ UHMWPE 666kC ☐ UHMWPE 1MC

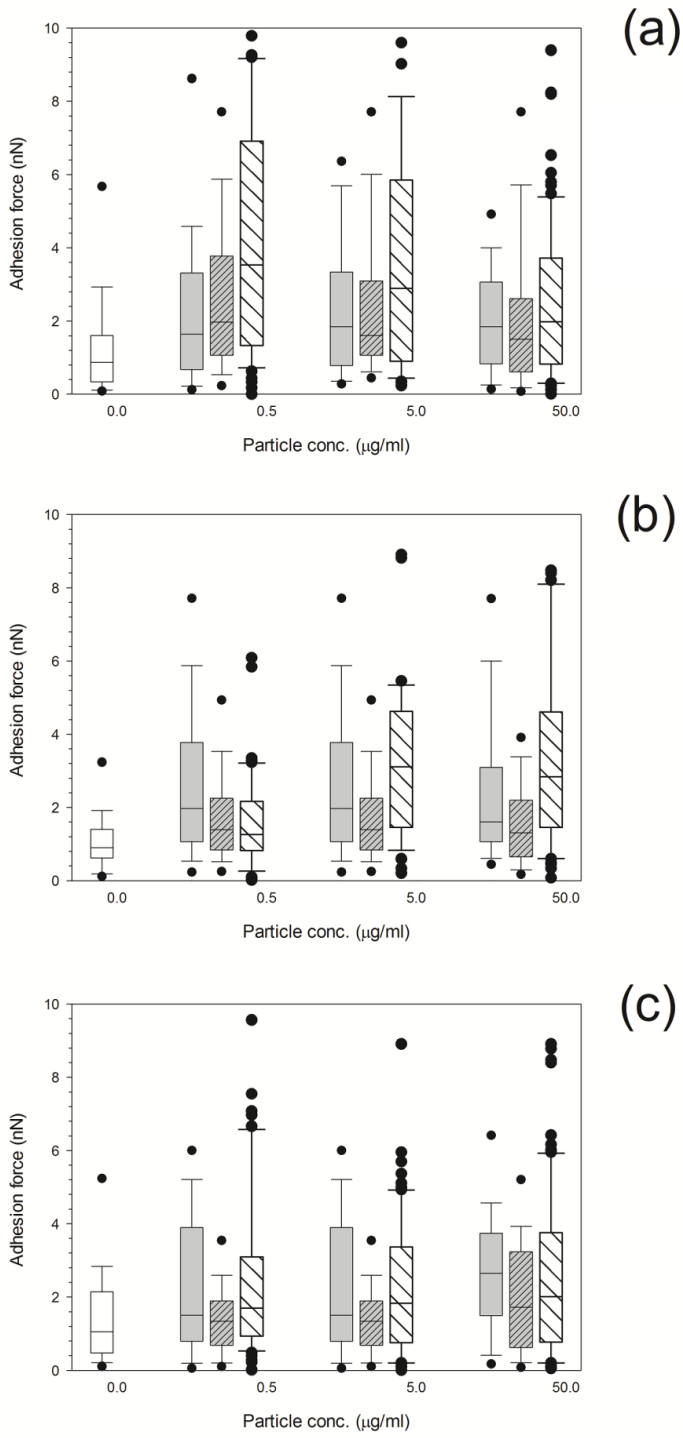

Figure 7-18. Adhesion force distribution of MSC cells exposed to UHMWPE wear particles post CAP treatment for 15 min after (a) 24h, (b) 48 h and (c) 72h.

Control UHMWPE 333kC UHMWPE 666kC UHMWPE 1MC

Another property of the cells that was investigated was the adhesion characteristics of the cells pre and post exposure to CAP treated and untreated wear particles. The wear debris for untreated UHMWPE are presented in Figure 7-16 whilst after CAP treatment for 7.5 minutes and 15 minutes are shown in Figure 7-17 and Figure 7-18 respectively. For untreated UHMWPE the adhesion increased with exposure time and did not change for particle concentration in the range tested in this work. After 24 hours for 7.5 minute CAP treated UHMWPE wear debris (Figure 7-17), an overall reduction in adhesion for all UHMWPE with increasing concentration, however, no change was observed when comparing the control cell with UHMWPE 1MC. For 48 hour exposure of wear debris, an initial increase in adhesion forces were observed for all UHMWPE when compared with the control cell samples, with the greatest increase in the range of data for the 1MC samples, however, a general decrease in adhesion forces were observed with increasing concentration for all UHMWPE samples. At 72 hours exposure, a similar initial increase is demonstrated when compared with the control cells, yet no change was observed with increasing concentration.

UHMWPE wear debris simulated after 15 minutes, also demonstrated a similar pattern of increasing adhesion forces with increasing concentration for 24 hours exposure especially for 1MC. After 48 hours exposure both 333kC and 666kC UHMWPE wear particles a general decrease in adhesion forces with increasing concentration was observed, however, for the 1MC an increase in adhesion was observed with increasing concentration when compared with the control cells. At 72 hours exposure, the 666kC and 1MC remained the same with

increasing concentration, and the 333kC increased with increasing concentrations.

Generally cell adhesion was decreasing after exposure to CAP treated UHMWPE at various time points, 7.5 min and 15min. For cells exposed to 7.5 min CAP treated material adhesion increased with time exposure increase (from no effect at 24hrs to highly effective at 48hrs). Also adhesion increased with increasing of number of wear cycles resulting to cell adhesion after exposure to 1MC CAP treated wear particles similar to cell adhesion after exposure to untreated UHMWPE wear particles. For cells exposed to 15min treated CAP wear particles adhesion increased after 24hrs exposure with similar trends for 48 hrs and 72hrs of exposure indicating that higher adhesion occurs after exposure to materials generated at shorter wear process (333 kC compared to 1 MC).

7.6 Discussion

7.6.1 Effect of CAP modification on UHMWPE

From the Raman data collected in this investigation, it is evident that a shift is observed in C-H, C-N, and N-H bonds as UHMWPE consists of a long chain monomer of ethylene ($(C_2H_4)_n$) with branching of these chains, then these results suggest an increase in cross-linking due to the shift seen between 3000 and 3300 cm^{-1} representing the C-H bonding and branching of the polymer; this cross-linking of the branches and chains effectively increases the density and strength of the polymer (1, 25). It is essential that these changes to UHMWPE do not alter the bulk properties of the material, such as the crystalline and

amorphous phases, as these govern the mechanical behaviour of the polymer (41), yet even though CAP has improved the wear (1, 25) it is not susceptible to changes in its crystallinity, as no changes were observed in the XRD data. The improvements observed with CAP treated UHMWPE come about without the negative effects associated with other thermal and radiated techniques (1, 25, 42, 43); as no oxidation was observed in the Raman spectroscopy results i.e. no shifts observed for oxygen. Oxidation leads to increased abrasion, forming more wear debris inducing an inflammatory response (42, 43). Furthermore, oxygen degradation is commonly seen in other sterilisation techniques such as gamma radiation (41, 44). Oxidative degradation can severely decrease the physical properties of the polymer such as alterations to the fracture toughness, and ductility (41, 43, 44). It has been noted (44) that prolonged oxidation promotes chain scission which eventually leads to long-term degradation of the desired physical, chemical and mechanical properties (44); therefore a further benefit of CAP treatment demonstrates from this investigation that little to no change was observed in the overall bulk material.

Debris are produced as a consequence of wear in joint replacements; it is well known that such debris are present in a wide distribution of sizes and in different shapes. Because many physiological reactions to the generation of wear are influenced by the geometrical properties of the wear, it is important that any new material developed results in wear debris not inducing negative responses in the host.

It has been shown that UHMWPE debris are generally of small sizes, and our result are in agreement with these. Variations of the wear debris size

distribution were not observed with the CAP treatment and at different stages of the wear process (after different periods of wear simulation). This is likely the consequence of the fact that the increased cross-linking between UHMWPE, caused by exposure to cold gas plasma, reduces only the wear rate but does affect the shape and size of the debris.

7.6.2 Effect of exposure to CAP treated UHMWPE wear particles on rMSCs metabolic activity

Because of the different chemical composition of the wear debris after CAP treatment (the presence of nitrogen groups predominante), it is important to determine the possible implication on the metabolism of mammalian cells of this debris. It has been shown that osteoblast cells can grow on UHMWPE unaffected by CAP treatment with He/Oxygen mixtures (45). In this work we determined the effect of the UHMWPE wear particles generated on the metabolic activity of MSC and found that these cells are fundamentally unaffected by UHMWPE at concentrations up to 50 mg/l and CAP treatment does not cause alternation of this (Figure 7-8 and Figure 7-9). Poly-ethylene is a relatively inert material as the results of the MTT test demonstrated that untreated UHMWPE at concentration up to 50 mg/l had the same results as cells not exposed to any wear particle. The added nitrogen groups by the CAP treatment do not cause variation of the level of UHMWPE cytotoxicity.

7.6.3 Effect of exposure to CAP treated UHMWPE wear particles on rMSCs-hydrophilicity, surface properties, adhesion and elasticity/turgidity/spring constant

Previously CAP has been reported to improve the longevity of biomedical devices due to its reduction in the generation of wear by minimising the

asperities of the surface of UHMWPE (25); the determination of the responses of cells when exposed to debris obtained from the treated material was performed in this work as, after exposure to CAP, practically a new material is produced. The surface properties can also influence the overall adhesive characteristics of the UHMWPE such as the hydrophilicity (25), as the interaction between the implanted biomedical device and biological materials is necessary for successful osseointegration (46, 47). Improvement of adhesion in UHMWPE has previously been reported (48, 49) through swelling of the polymer elevates the bonding especially between metal and polyethylene enhancing the ductility when compared to the bulk material (48), and to mouse fibroblasts (49). It is essential for the longevity of the device for positive structural and functional direct contact with living bone and the device (50); as after total joint arthroplasty (TJA) surgery a layer of water forms on the surface which aids in the facilitation of protein adsorption to the surface of the implant i.e. a conditioning film allowing for further cellular adhesion of bone cells (47, 50). CAP treatment evidently improves the hydrophilicity of the surface (25) which inherently leads to enhanced osseointegration (1, 25, 47, 51).

AFM allows for ease of investigation as no sample preparation is required and cells can be imaged and probed in biological conditions minimising damage and potential changes that may occur with other techniques that require fixation of cells (52-54). Previous work conducted on cells using AFM have suggested that an applied force ranging between 1 and 100 nN is sufficient to initiate cellular responses (54), this confirms the selection of a fixed applied load at 4 nN for the

above investigation. The low value of applied force is connected to a small indentation depth that is needed to prevent cell damage.

The change in hydrophobicity of the original material compared to the CAP treated may be attributed to the introduction of free radicals to the surface and the addition of N-H bonds demonstrated using Raman Spectroscopy, and increases the surface energy of UHMWPE; this allows for better interaction with surrounding proteins to form a conditioning layer for osteointegration to take place, improving the chances of new bone formation and minimising rejection of the implanted device. Yet, a general decrease in adhesion properties of the cells was observed when exposed to CAP treated wear debris; this could be due to wear debris interacting with the cells surface altering the overall adhesion mechanisms of the cells as the untreated UHMWPE demonstrated a general increase in adhesion with increasing concentration of particles, but, post CAP treatment the opposite was true and a general decrease in adhesion was observed. This was due to the improved hydrophilicity and surface energy of the treated UHMWPE which enhanced its adhesion to structural components of the cells governing the adhesive characteristics.

Moreover, as the CAP treatment alters the surface characteristics of UHMWPE by improving the hydrophilicity, this could lend itself to increased interactions and uptake with surrounding cells around implantation site. These interactions could affect the important structural features of cells such as the cytoskeleton (55).

Elasticity of cells is an important aspect to consider in the normal function of a cell, it is thought that wear debris may alter the usual differentiation of cells and

can induce osteolysis which affects osteoblasts and osteoclasts (4, 56). Investigating the effects induced to MSCs is essential as these cells can differentiate into a variety of phenotypes including osteoblasts, cartilage, ligaments, adipocytes, muscle and connective tissue (57, 58); differentiation depends on the rigidity of the substrate that cells adhere to. For example, harder surfaces with a matrix stiffness ranging between 25-40 kPa cause MSC differentiation to osteoblast-like cells (59). Owens and Solursh (1981) (60) demonstrated that rat MSCs behave in a similar manner to human MSCs and are often used as an approximation to human cells. Another notion of elasticity is to consider it as the degree of deformation of a cell in response to an applied load; some studies have shown that a relationship exists between the elasticity of cells and their vital functions which include cell differentiation, proliferation, survival and motility (55, 57). Not only are cells probed by an applied load are affected, but also surrounding molecules such as the extracellular matrix (ECM), transmembrane proteins, chromatin, cytoskeleton and lipid bilayer also respond to external as well as internal forces resulting in deformation of the structures of the cells in question (57); therefore, the elastic properties of the MSCs have been measured to determine their effect of wear debris on the cells properties.

The model used to determine the elastic characteristics of the cells is based on the Hertz model, to apply this model seven assumptions must be fulfilled: (i) the material of the contacting bodies is isotropic and homogenous; (ii) the loads applied are static; (iii) the material is linearly elastic in nature; (iv) The curvature of radii of the contacting bodies are much larger than the contact radius; (v) the

dimensions of the bodies are much larger than the dimensions of the contact surface; (vi) the contacting surfaces are smooth; and (vii) the deformations are small (61). As the geometry of the tip satisfies all the above points the Hertz equation can be assumed (62), and all other parameters are known including the tip angle, 35^{o}, indentation depth, δ, and force, F, are determined using the AFM, and the Poisson ratio (when a material is compressed in one way and expanded in another direction perpendicular to the compression) is taken as 0.5 for soft elastic biological samples (62).

Wear debris of UHMWPE have a significant impact on MSC elasticity (Figure 7-10). Without the presence of particles cells exhibit a decreasing elasticity from about 20 kPa to about 10 kPa over the period from 1 to 3 days; when MSC are exposed to UHMWPE debris the elasticity of the cell remains at about 15 kPa regardless of the debris concentration during the same exposure time. The most remarkable fact is the increasing elasticity of MSC exposed to debris obtained from progressive wear (333 kC to 666 kC to 1MC) at debris concentrations greater than 5 µg/l. The elasticity values obtained from the wear simulation between 666kC and 1MC return values closer to pure UHMWPE than the debris generated at the beginning (333kC). This phenomenon is consistent with the fact that the outer layer of the treated samples are more likely to exhibit the effect of the CAP treatment as result of the decreasing penetration of the plasma species. Thus the initial wear generated presents the biggest modification as seen with the lack of response of cells to the debris from the increased wear cycles (i.e. the 666kC and 1MC demonstrate similar outcomes). This hypothesis is also sustained by the observation that the longer

CAP treatment of 15 min (that is resulting in material modification deeper in the samples) does not exhibit such behaviour. It appears that the short treatment improves a thinner layer of UHMWPE.

A study of the cell spring constant (monotonically linked to turgidity) revealed that the presence of UHMWPE causes the cell to exhibit higher pressure. Increased turgidity has been shown to be a mechanism involved in regulating cell uptake and membrane trafficking. Elasticity and turgidity are linked as cell size can only change slightly as result of pressure variation as swelling or shrinking are threats to cell viability. An increase in turgidity can be withstood with increased elasticity.

7.7 Conclusion

Overall, the results demonstrated differences in MSC responses to untreated and CAP treated UHMWPE without alteration of the size distribution of metabolic activity. For untreated there was no change in elasticity over time regardless of increasing the particle concentration; whereas, 7.5 min CAP treatment had a slight reduction in values compared to the untreated, and the 15 minute treatment had a general decrease in elasticity with increasing concentration of wear debris. Similarly, no changes were observed in the spring constant of the cells exposed to untreated UHMWPE, however, 7.5 minute CAP treatment demonstrated an overall increase in spring constant of the cells with increasing concentration; the same was true for 15 minute treatment. These results demonstrate that the cells exposed to CAP treatment become more rigid, which could be attributed to the demise in adhesion post CAP treatment.

The above investigation demonstrates that MSCs physical and not only biological changes take place and these govern the cells characteristics. Thus, this study can aid in further understanding of the role played by wear debris and the reaction of cells near implantations and evaluate the effect of a wear performance enhancing processes such as CAP on the biological consequences of the wear generated.

7.8 References

1. Perni S, Kong MG, Prokopovich P. Cold atmospheric pressure gas plasma enhances the wear performance of ultra-high molecular weight polyethylene. Acta Biomaterialia. 2012;8(3):1357-65.

2. Preedy EC, Brousseau E, Evans SL, Perni S, Prokopovich P. Adhesive forces and surface properties of cold gas plasma treated UHMWPE. Colloids and Surfaces A, Physicochemical and Engineering Aspects. 2014;460:83-9.

3. Brach Del Prever EM, Bistolfi A, Bracco P, Costa L. UHMWPE for arthroplasty: past or future? Journal of orthopaedics and traumatology : official journal of the Italian Society of Orthopaedics and Traumatology. 2009;10(1):1-8.

4. Ingham E, Fisher J. Biological reactions to wear debris in total joint replacement. Proceedings of the Institution of Mechanical Engineers Part H, Journal of engineering in medicine. 2000;214(1):21-37.

5. Lohmann CH, Schwartz Z, Köster G, Jahn U, Buchhorn GH, MacDougall MJ, et al. Phagocytosis of wear debris by osteoblasts affects differentiation and local factor production in a manner dependent on particle composition. Biomaterials. 2000;21(6):551-61.

6. Savio Iii JA, Overcamp LM, Black J. Size and shape of biomaterial wear debris. Clinical Materials. 1994;15(2):101-47.

7. Nine M, Choudhury D, Hee A, Mootanah R, Osman N. Wear Debris Characterization and Corresponding Biological Response: Artificial Hip and Knee Joints. Materials. 2014;7(2):980-1016.

8. van Ooij A, Kurtz SM, Stessels F, Noten H, van Rhijn L. Polyethylene wear debris and long-term clinical failure of the Charite disc prosthesis: a study of 4 patients. Spine (Phila Pa 1976). 2007;32(2):223-9.

9. Gladkis LG, Li RW, Scarvell JM, Smith PN, Timmers H. Exploration of the size, shape and abundance of UHMWPE wear particles using atomic force microscopy. Wear. 2009;267(1–4):632-8.

10. Besong AA, Tipper JL, Ingham E, Stone MH, Wroblewski BM, Fisher J. Quantitative comparison of wear debris from UHMWPE that has and has not been sterilised by gamma irradiation. The Journal of bone and joint surgery British volume. 1998;80(2):340-4.

11. Fang H-W, Su Y-C, Huang C-H, Yang C-B. Influence of biological lubricant on the morphology of UHMWPE wear particles generated with microfabricated surface textures. Materials Chemistry and Physics. 2006;95(2–3):280-8.

12. Chiu R, Ma T, Smith RL, Goodman SB. Ultrahigh molecular weight polyethylene wear debris inhibits osteoprogenitor proliferation and differentiation in vitro. Journal of Biomedical Materials Research Part A. 2009;89A(1):242-7.

13. Purdue PE, Koulouvaris P, Nestor BJ, Sculco TP. The Central Role of Wear Debris in Periprosthetic Osteolysis. HSS Journal. 2006;2(2):102-13.

14. Dean DD, Schwartz Z, Blanchard CR, Liu Y, Agrawal CM, Lohmann CH, et al. Ultrahigh molecular weight polyethylene particles have direct effects on proliferation, differentiation, and local factor production of MG63 osteoblast-like cells. J Orthop Res. 1999;17(1):9-17.

15. Jacobs JJ, Shanbhag A, Glant TT, Black J, Galante JO. Wear Debris in Total Joint Replacements. The Journal of the American Academy of Orthopaedic Surgeons. 1994;2(4):212-20.

16. Green TR, Fisher J, Stone M, Wroblewski BM, Ingham E. Polyethylene particles of a 'critical size' are necessary for the induction of cytokines by macrophages in vitro. Biomaterials. 1998;19(24):2297-302.

17. Campbell P, Ma S, Yeom B, McKellop H, Schmalzried TP, Amstutz HC. Isolation of predominantly submicron-sized UHMWPE wear particles from periprosthetic tissues. J Biomed Mater Res. 1995;29(1):127-31.

18. Fisher J. Wear of ultra high molecular weight polyethylene in total artificial joints. Current Orthopaedics. 1994;8(3):164-9.

19. Kostov KG, Nishime TMC, Castro AHR, Toth A, Hein LRO. Surface modification of polymeric materials by cold atmospheric plasma jet. Applied Surface Science. 2014;314(0):367-75.

20. Waewsawangwong W, Goodman SB. Unexpected failure of highly cross-linked polyethylene acetabular liner. J Arthroplasty. 2012;27(2):323 e1-4.

21. Goodman SB, Ma T. Cellular chemotaxis induced by wear particles from joint replacements. Biomaterials. 2010;31(19):5045-50.

22. Liu H, Pei Y, Xie D, Deng X, Leng YX, Jin Y, et al. Surface modification of ultra-high molecular weight polyethylene (UHMWPE) by argon plasma. Applied Surface Science. 2010;256(12):3941-5.

23. Fasce L, Cura J, del Grosso M, Bermúdez GG, Frontini P. Effect of nitrogen ion irradiation on the nano-tribological and surface mechanical properties of ultra-high molecular weight polyethylene. Surface and Coatings Technology. 2010;204(23):3887-94.

24. Hoffmann C, Berganza C, Zhang J. Cold Atmospheric Plasma: methods of production and application in dentistry and oncology. Med Gas Res. 2013;3(1):21.

25. Preedy EC, Brousseau E, Evans SL, Perni S, Prokopovich P. Adhesive forces and surface properties of cold gas plasma treated UHMWPE. Colloids Surf A Physicochem Eng Asp. 2014;460:83-9.

26. Isbary G, Heinlin J, Shimizu T, Zimmermann JL, Morfill G, Schmidt HU, et al. Successful and safe use of 2 min cold atmospheric argon plasma in chronic wounds: results of a randomized controlled trial. Br J Dermatol. 2012;167(2):404-10.

27. Isbary G, Morfill G, Schmidt HU, Georgi M, Ramrath K, Heinlin J, et al. A first prospective randomized controlled trial to decrease bacterial load using cold atmospheric argon plasma on chronic wounds in patients. Br J Dermatol. 2010;163(1):78-82.

28. Xu W, Huang S, Chen F, Song J, Liu X. Diamond wear properties in cold plasma jet. Diamond and Related Materials. 2014;48(0):96-103.

29. Xu W, Liu X, Song J, Wu L, Sun J. Friction and wear properties of Ti6Al4V/WC-Co in cold atmospheric plasma jet. Applied Surface Science. 2012;259(0):616-23.

30. Saikko V. Effect of contact pressure on wear and friction of ultra-high molecular weight polyethylene in multidirectional sliding. Proceedings of the Institution of Mechanical Engineers Part H, Journal of engineering in medicine. 2006;220(7):723-31.

31. Chen JS, Sun Z, Guo PS, Zhang ZB, Zhu DZ, Xu HJ. Effect of ion implantation on surface energy of ultrahigh molecular weight polyethylene. J Appl Phys. 2003;93(9):5103-8.

32. Marcondes AR, Ueda M, Kostov KG, Beloto AF, Leite NF, Gomes GF, et al. Improvements of ultra-high molecular weight polyethylene mechanical properties by nitrogen plasma immersion ion implantation. Brazilian Journal of Physics. 2004;34:1667-72.

33. Phinney DG, Kopen G, Isaacson RL, Prockop DJ. Plastic adherent stromal cells from the bone marrow of commonly used strains of inbred mice: variations in yield, growth, and differentiation. J Cell Biochem. 1999;72(4):570-85.

34. Harrington J, Sloan AJ, Waddington RJ. Quantification of clonal heterogeneity of mesenchymal progenitor cells in dental pulp and bone marrow. Connective tissue research. 2014;55 Suppl 1:62-7.

35. Sader JE, Sanelli JA, Adamson BD, Monty JP, Wei X, Crawford SA, et al. Spring constant calibration of atomic force microscope cantilevers of arbitrary shape. Review of Scientific Instruments. 2012;83(10):103705--16.

36. Sader JE, Larson I, Mulvaney P, White LR. Method for the calibration of atomic force microscope cantilevers. Review of Scientific Instruments. 1995;66(7):3789-98.

37. Sneddon IN. The relation between load and penetration in the axisymmetric boussinesq problem for a punch of arbitrary profile. International Journal of Engineering Science. 1965;3(1):47-57.

38. Arnoldi M, Fritz M, Bauerlein E, Radmacher M, Sackmann E, Boulbitch A. Bacterial turgor pressure can be measured by atomic force microscopy. Phys Rev E Stat Phys Plasmas Fluids Relat Interdiscip Topics. 2000;62(1 Pt B):1034-44.

39. Boulbitch A. Deformation of the envelope of a spherical gram-negative bacterium during the atomic force microscopic measurements. J Electron Microsc (Tokyo). 2000;49(3):459-62.

40. Polyakov P, Soussen C, Duan J, Duval JF, Brie D, Francius G. Automated force volume image processing for biological samples. PLoS One. 2011;6(4):e18887.

41. Sobieraj MC, Rimnac CM. Ultra high molecular weight polyethylene: Mechanics, morphology, and clinical behavior. Journal of the Mechanical Behavior of Biomedical Materials. 2009;2(5):433-43.

42. Bracco P, Brunella V, Luda MP, Zanetti M, Costa L. Radiation-induced crosslinking of UHMWPE in the presence of co-agents: chemical and mechanical characterisation. Polymer. 2005;46(24):10648-57.

43. Bracco P, Brach del Prever EM, Cannas M, Luda MP, Costa L. Oxidation behaviour in prosthetic UHMWPE components sterilised with high energy radiation in a low-oxygen environment. Polymer Degradation and Stability. 2006;91(9):2030-8.

44. Turos A, Abdul-Kader AM, Grambole D, Jagielski J, Piątkowska A, Madi NK, et al. The effects of ion bombardment of ultra-high molecular weight polyethylene. Nuclear Instruments and Methods in Physics Research Section B: Beam Interactions with Materials and Atoms. 2006;249(1–2):660-4.

45. Perni S, Preedy EC, Prokopovich P. Success and failure of colloidal approaches in adhesion of microorganisms to surfaces. Advances in Colloid and Interface Science. 2014;206(0):265-74.

46. Wang N, Trunfio-Sfarghiu A-M, Portinha D, Descartes S, Fleury E, Berthier Y, et al. Nanomechanical and tribological characterization of the MPC phospholipid polymer

photografted onto rough polyethylene implants. Colloids and Surfaces B: Biointerfaces. 2013;108(0):285-94.

47. Khan SN, Ramachandran M, Senthil Kumar S, Krishnan V, Sundaram R. Osseointegration and more–A review of literature. Indian Journal of Dentistry. 2012;3(2):72-6.

48. Gao P, Mackley MR. Surface treatment of ultra high molecular weight polyethylene to enhance adhesion and conductivity properties. Polymer. 1992;33(19):4075-80.

49. Reznickova A, Novotna Z, Kolska Z, Kasalkova NS, Rimpelova S, Svorcik V. Enhanced adherence of mouse fibroblast and vascular cells to plasma modified polyethylene. Materials Science and Engineering: C. 2015;52(0):259-66.

50. Chug A, Shukla S, Mahesh L, Jadwani S. Osseointegration—Molecular events at the bone–implant interface: A review. Journal of Oral and Maxillofacial Surgery, Medicine, and Pathology. 2013;25(1):1-4.

51. Goda T, Konno T, Takai M, Ishihara K. Photoinduced phospholipid polymer grafting on Parylene film: Advanced lubrication and antibiofouling properties. Colloids and Surfaces B: Biointerfaces. 2007;54(1):67-73.

52. Chen C, Tan J, Tien J. Mechanotransduction at cell-matrix and cell-cell contacts. Annual Review of Biomedical Engineering. 2004;6:275 - 302.

53. Chen Y, Norde W, van der Mei HC, Busscher HJ. Bacterial cell surface deformation under external loading. mBio. 2012;3(6).

54. Chen CS. Mechanotransduction - a field pulling together? J Cell Sci. 2008;121(Pt 20):3285-92.

55. Haleem-Smith H, Argintar E, Bush C, Hampton D, Postma WF, Chen FH, et al. Biological Responses of Human Mesenchymal Stem Cells to Titanium Wear Debris Particles. Journal of Orthopaedic Research. 2012;30(6):853-63.

56. Ren K, Dusad A, Zhang Y, Wang D. Therapeutic intervention for wear debris-induced aseptic implant loosening. Acta Pharmaceutica Sinica B. 2013;3(2):76-85.

57. Janmey PA, McCulloch CA. Cell mechanics: integrating cell responses to mechanical stimuli. Annu Rev Biomed Eng. 2007;9:1-34.

58. Caplan AI. Mesenchymal stem cells. J Orthop Res. 1991;9(5):641-50.

59. Engler AJ, Sweeney HL, Discher DE, Schwarzbauer JE. Extracellular matrix elasticity directs stem cell differentiation. Journal of musculoskeletal & neuronal interactions. 2007;7(4):335.

60. Owens EM, Solursh M. In vitro histogenic capacities of limb mesenchyme from various stage mouse embryos. Developmental Biology. 1981;88(2):297-311.

61. Dintwa E, Tijskens E, Ramon H. On the accuracy of the Hertz model to describe the normal contact of soft elastic spheres. Granular Matter. 2008;10(3):209-21.

62. Neumann T. Determining the elastic modulus of biological samples using atomic force microscopy. JPK Instruments-Application Note2009.

Chapter 8 - Cobalt, Titanium and PMMA Bone Cement particles Influence on Mouse Osteoblasts Cell Elasticity, Spring constant and Calcium Production Activity.

The content of this chapter has been submitted for publication to:

E. Callard Preedy, S. Perni, P. Prokopovich "Cobalt, Titanium and PMMA Bone Cement debris Influence on Mouse Osteoblasts Cell Elasticity, Spring constant and Calcium Production Activity" in press RSC Advances, 2015 DOI:10.1039/C5RA15390E

8.1 Abstract

Periprosthetic osteolysis and implant loosening are the outcomes of wear debris generation in total joint replacements. Although total joint replacement (TJR) are required to withstand impact of daily loading, articulation cycles and even abrasive corrosive environments, wear debris is produced from the continuous abuse of the joint over its lifetime. Wear debris formed from the implanted materials consisting of metals, polymeric, ceramic and bone cement initiate the immune system. Once the immune system has been provoked by the foreign particles, a cascade of major cell types within the interfacial granulomatous fibrous tissue are stimulated to act. Cells including fibroblasts, macrophages, lymphocytes, and foreign-body giants aid in the removal and destruction of external threats. From this immune response, normal cells may be caught in the hysteria of the fray or can even uptake the wear debris. Often osteoblasts, the principal cell type in bone tissue adjacent to the prostheses, are directly impacted. Osteoblasts are responsible for maintaining physiological bone remodelling choreographing a balance of bone formation and resorption with osteoclasts.

In this study, for the first time, the influence of Cobalt, Titanium and PMMA bone cement particles of different sizes, charges and compositions on mouse osteoblast adhesion, nanomechanics (elasticity and spring constant), and metabolic activity (MTT) were investigated. These studies were accomplished by performing osteoblast mineralisation experiments and uptake of particles by the osteoblasts after exposure to particles at defined time points. Understanding

these processes is critical to expanding our knowledge of implant loosening and elucidating the nature of prosthetic joint failure.

8.2 Introduction

Other than the onset of an infection, deterioration of the material components of an implanted biomedical device is a major complication in total joint arthroplasty (TJA), which coincides with a biological response to the particles released from the damaged device. As people are generally living longer, then it is necessary for biomedical implant longevity to also rise with the aging population. Yet, aseptic loosening has been reported to mature within 15-20 years post total joint replacement surgery [1], and is inevitable.

Aseptic loosening is debilitating to patients [2] and results from the subtle wear of the articulating surfaces from every day movements experienced during simple activities such as walking. The major implication of the slow destruction of the materials is that signs and symptoms of the damage do not present clinically until late stages of implant failure. Furthermore, the biological response, or the destruction of the periprosthetic tissue i.e. osteolysis, is a result of an inflammatory response due to the defence mechanisms of the immune system responding to the wear debris [3, 4]. Initially the foreign particles are phagocytosed by macrophages which governs the release of proinflammatory cytokines [5]; as the proinflammatory cascade continues the cellular mediators, cytokines, activate osteoclasts, precursor cells of hemopoietic lineage leading to differentiation, and maturation [5-7]. In turn these defence cells inhibit and suppress differentiation and proliferation of osteoprogentitor cells, and therefore the function of osteoblast cells, even

causing apoptosis [5]. Further resorption occurs due to the release of inflammatory mediators which directly act on bone; this constant bombardment in a hostile environment eventually disrupts the normal homeostatic balance of bone degradation and renewal or formation resulting in osteolysis and aseptic loosening [5, 8, 9] from the accumulation of wear debris.

These biochemical interactions are widely available in the literature [2, 10-12] defining certain cellular pathways; and depend on the type, size, and number of wear particles [13] Simultaneous to these biological responses, cells may undergo mechanotransduction and adhesive changes [14, 15]. These changes will naturally take place within cells as cells are living entities that possess structural, as well as physical properties; there are these characteristics that aid in cells survival enabling them to withstand physiological changes to their native environment, such as mechanical stimuli that may occur internally and externally to the body [16]. Any disruptions to the usual characteristics of the cell will upset its integrity and biological function [14, 16]. For example, osteoprogenitor cells can sense the rigidity of their surroundings responding by regulating their shape, internal cytoskeletal tension, stiffness and thereby proliferation [14]. It is important to note that cells simultaneously detect stress (force/area) and strain (deformation) both internal and external physiological changes [16]; thereby responded to sensitive changes in force, stiffness and adhesion [14]. Yet these physical characteristics have been side lined to biological responses for many years, and only recently have been thought of as contributing factors of pathologies, with the notion that mechanical signals eventually are converted to biological and chemical stimuli in cells governing the

growth, differentiation, migration, and apoptosis of cells, which are also influenced by changes in cell shape and the structural integrity [16].

With enhanced microscopy techniques such as the atomic force microscope (AFM), detailed quantitative analysis of the nanomechanical and adhesive characteristics these characteristics can now been investigated [14, 15]. As cells do not only respond to external forces but internal responses too, some responses may even overcome chemical stimuli which in turn could have similar outcomes to the function, proliferation, differentiation and apoptosis of cells [14, 15, 17].The function and integrity of cells is governed by their cytoskeleton which is responsible for their structural and mechanical properties [15, 18, 19]. For instance, following a TJA bone remodelling cells also adapt not only to the biological changes but to an altered mechanical environment [20], which is a direct effect on the redistribution of load, and inherently stress, especially when the femoral head is replaced in a hip replacement [20]. Stress shielding was introduced by coatings and cemented stems of the implant device, yet this material also produces wear debris as Poly(methylmethacrylate) PMMA a commonly used material for cemented prosthetic implants [20].

Furthermore, bone cells such as osteoblasts are essential in bone remodelling and osseointegration of the biomedical implant [21-23]. Adhesive properties of cells are therefore required to establish this integration is successful, as well as the biocompatibility of the implanted device material which is essentially the substrate for these osteoblast cells [21]. Cells tend to adhere and spread better to rigid substrates [15] but spreading also increases cortical stiffness due to up-regulated cytoskeleton contractiles [15, 24]; moreover, if adhered to rigid and

uniform surfaces then cells sense their shape and may respond in an apoptotic pathway. This ability to determine and maintain a stable form is due to the fact that cells have both elastic and viscous properties [24] which govern the way in which a cell will interact with mechanical signals to aid in its survival and function. For example, cells stiffness will increase non-linearly with large external forces which actively generates internal contractile tension which pulls on its substratum or on neighbouring cells [24-26]. Internal tension control allows cells to finely tune their own stiffness and is determined by the actin cytoskeleton [24]. It is therefore important to produce a quantitative model for cell material properties to gain further understanding in the mechanics and mechanotransduction characteristics [24].

In vitro cultures of rodent osteoblasts are an important method in research in studying the regulation of cells function [27]. For example, murine models are commonly used for studying implant loosening as these models are advantageous in identifying underlying biological mechanisms [5]. These cell types allow for reliable, and simple application for differentiation and bone-forming activities enabling direct studies using mouse osteoblasts [27], and are often applied to in vitro studies due to the limitation of primary human osteoblasts available [28]. Mouse osteoblasts have greatly improved the understanding of cell differentiation, cytokine and hormonal regulation, synthesis of proteins, molecular mechanisms of bone pathologies, as well as cytocompatibility and osteogenicity of biomaterials [28]. For instance murine osteoblast cells can synthesise extracellular matrix under the presence of

phosphate substrates producing a tissue resembling woven bone ultrastructure [28, 29].

This study aims to premier the influence of metal and bone cement particles on mouse osteoblasts to determine their adhesive, nanomechanical and metabolic activity post exposure to these particles of various sizes, charges, compositions and concentrations.

8.3 Methods and Materials

8.3.1 Cell Culture

Murine MC3T3-E1 osteoblasts cells (Sigma, UK) were routinely cultured in α-MEM (Minimum Essential Medium) (Life Technologies), supplemented with 10% (v/v) FBS (Foetal Bovine Serum), 1% (v/v) of solution penicillin (5000 U/ml) and streptomycin (5000 mg/ml) (Gibco Invitrogen). Trypsin (Gibco Invitrogen) was used when cells were 70% confluent in order to passage and count. The cells were maintained at 37° C in a humidified atmosphere containing 5% CO_2.

For atomic force microscopy experiments, cells were seeded in 24-well plates at a density of 6000 cells per well and cultured for 24 hours on sterilised polystyrene slides placed inside the well before exposure to particles. For each type of particles a stock solution of the particles suspended in culture media was prepared at 5 mg/ml and appropriate amount was added to each well to reach final concentrations of 5; 12.5; 25 and 50 µg/ml for Co and Ti nanoparticles and 5; 25, 50, 100 and 200 µg/ml for PMMA bone cement particles and incubated from 24h up to 3 days. Control samples consisting of

cells not exposed to particles and cultured in the same conditions were used for comparison with treated cells.

For the MTT assay, osteoblasts mineralisation ability and cell uptake experiments the cells were cultured as described above.

8.3.2 Particles

Commercially available nanoparticles were obtained of various sizes and compositions from Sigma Aldrich, UK. For Cobalt (Co) nanoparticles (NPs), two samples were employed:

- Co elemental, 30nm diameter (referred as ‘Co 30nm’ throughout the text);
- Co (II,III) oxide, 50nm diameter (referred as ‘Co 50nm’ throughout the text).

Three samples of Titanium (Ti) were employed:

- Ti elemental, 30nm diameter;
- Ti (IV) oxide anatase, 25nm diameter; and
- mixture of Ti (IV) oxide rutile and anatase, 100nm diameter

They are referred to as ‘Ti 30nm’, ‘Ti 25nm’ and ‘Ti 100nm’, respectively, throughout the text.

Polymethyl-methacrylate (PMMA) bone cement particles were generated using a single station pin on plate in-house built wear simulator under constant load applied under lubricated conditions as detailed [30]. PMMA pins for the wear process were prepared from PMMA bone cement formulation according to the

procedure [31, 32]. Briefly it is described here. PMMA bone cement were obtained by manual mixing the powder phase consisting of poly-methyl-methacrylate (4.1 g), barium sulphate (0.46 g), benzoil peroxide (0.1 g) and liquid monomer phase consisting of Methyl-methacrylate (1.96 g) and N-N Dimethyl-p-Toludine (0.04 g) under constant stirring until the powder was fully wetted. The mixture was subsequently inserted into the mould at an approximate dough time of 1 minute. The filled mould was pressed between two glass plates for 1 hour. After the cement had hardened, it was pulled out from the mould and stored under dark, sterile conditions at room temperature. Prior to wear experimentation bone cement specimens were conditioned at 37°C for 24 hours.

All particles were weighed and suspended in α-MEM medium to make a stock suspension of particles of 5mg/ml. From this stock solution, a number of particles concentrations (5 µg/ml; 12.5 µg/ml; 25 µg/ml and 50 µg/ml of Co or Ti nanoparticles or 5 µg/ml; 50 µg/ml; 250 µg/ml; 500 µg/ml and 1000 µg/ml of PMMA bone cement particles) were prepared.

8.3.3 Metabolic activity assay

MTT (3-(4,5-dimethythiazol-2yl)-2,5-diphenyltetrazolium bromide) assay was used to determine the effects of the metal and PMMA bone cement particles on mouse osteoblast (MC3T3) cells viability. It is a colorimetric assay of cell viability and depends on the metabolic activity of the cell as rapidly dividing cells exhibit high rates of MTT reduction. Cells were initially cultured and exposed to particles as stated above in a 24-wells plate; after the chosen exposure to particles, the media was replaced with phenol red-free medium and 80 µl of

MTT stock solution (5mg/ml) was added to each well and incubated at 37^{o}C in humidified atmosphere containing 5% CO_2 for 2 hour. The metabolised MTT, formazan, was re-suspended with 800 µl of dimethylsulfoxide (DMSO). 200 µl were transferred to a 96-well plate absorbance at 560nm was read using a spectrophotometer (ELISA Reader Labtech LT-5000MS). All experiments were performed in triplicates with each concentration (5, 12.5, 25 and 50 µg/ml) for metal nanoparticles and (5 µg/ml; 25 µg/ml; 50 µg/ml; 100 µg/ml and 200 µg/ml) for PMMA bone cement particles as well as a control sample of cell suspension not exposed to particles (untreated cells).

8.3.4 Osteoblast mineralisation

Mouse osteoblast (MC3T3-E1) cells were grown with metal (Co or Ti) nanoparticles or PMMA bone cement particles for the period of 21 days. Particles treatments in medium were changed every 3rd or 4th day. On day 21 all of the media was removed from the wells, and was replaced with 100µl of gluteraldehyde (Sigma Aldrich, UK) 10% (v/v) in phosphate buffer solution (PBS) and incubated for 10mins. The gluteraldehyde was then removed from each well. Each well was washed three times using 100µl of PBS. 100µl of alizarin red staining (ARS) (Sigma Aldrich, UK) 1% (v/v) was pipetted into each well and incubated for 20mins. The ARS was completely removed and each well was washed with Milli-Q water. 100µl of acetic acid 10% (v/v) was added to each well and incubated for 30mins. 50µl samples from each well were taken and transferred into a fresh 96 well plate. The absorbance was measured with Labtech-LT5000MS ELISA reader, the measurement was performed at wavelength 405nm [33].

All experiments were performed in triplicates with each concentration (5, 12.5, 25 and 50 µg/ml) for metal nanoparticles and (5 µg/ml; 25 µg/ml; 50 µg/ml; 100 µg/ml and 200 µg/ml) for PMMA bone cement particles as well as a control sample of cell suspension not exposed to particles (untreated cells).

8.3.5 Zeta potential and size of particles measurements

Particles size was measured through dynamic light scattering (DLS), zeta potential of nanoparticles was measured using laser doppler micro-electrophoresis which calculates the electrophoretic mobility to evaluate the zeta potential. Both characterisations were carried out using Malvern Zetasizer Nano ZS Nano series (Malvern, UK). All measurements were performed on Ti or Co nanoparticles or PMMA bone cement particles suspensions at 5µg/ml prepared from a stock solution of 5mg/ml.

PMMA debris were imaged after gold coating for 15 seconds using a sputter coater from Agar (Model 109A, Standsted, Essex, UK), with a mixture of Gold and Palladium (80% and 20%, respectively) in Argon. Once coated, SEM (XB1540, Carl Zeiss (Gemini, Oberkochen, Germany) was used to obtain images. Size determination was performed using ImageJ software determining the diameter of a circle with the same projected area of the particles.

8.3.6 Cell nanomechanical properties measurements

All AFM force measurements were conducted in an open liquid cell as described in [34], using PBS as the aqueous phase. A triangular tipless cantilevers (Bruker, UK) with a nominal spring constants ($K_{cantilever}$) of 0.1 N/m was used; the actual spring constant of the AFM cantilever was determined using the Sader method [35, 36]. Borosilicate glass beads (10 µm in diameter)

were glued onto the cantilever and served as cell indentors. In order to prevent indentations depth greater than 400-500 nm, the maximum applied load was set, after preliminary tests, to 1 nN or 2 nN depending on the samples. At least 15 cells were analysed for each sample, at each concentration of particles and at each time point (24, 48, and 72 hours). Cells were first located and then at least 20 approaching and retracting z-piezo coordinates vs. deflection curves were extracted from randomly selected points on the surface of each cell avoiding the peri-nuclear region. Experiments were performed in triplicates.

8.3.6.1 Cell elasticity and spring constant determination

The approaching part (trace) of the AFM curves was used to calculate the nanomechanical properties of the cells. The Young modulus of the cell surface location under investigation was determined fitting the Hertz model (Eq. 8-1) to the first part of the indentation vs. force curve after contact between AFM tip and cell surface.

$$F = \frac{4}{3}\frac{E}{(1-\nu^2)}\sqrt{R}\delta^{2/3} \qquad (8\text{-}1)$$

Where:

F = force recorded by AFM

E = Young modulus

R= radius of the spherical indentor (5 μm)

ν = Poisson ratio (assumed 0.5)

δ = indentation depth

The spring constant of the cell surface in the location probed was determined through the slope of the curve after the Hertzian regime according to:

$$\mathrm{F} = k_{\mathrm{b}}\delta \tag{8-2}$$

Where:

F = force recorded by AFM

K_b = spring constant of the cell

δ = indentation depth

Both models require the determination of the separation between cell surface and AFM tip *(δ)*, this was calculated from the coordinates (z-piezo) of the trace curve assuming that the point of contact corresponded to the local minimum of force; from this:

$$\delta = \left|z - z_0\right| - d_{cant} \tag{8-3}$$

Where:

z_0 = z-piezo value of the minimum of the trace curve

z = z-piezo value of the trace curve

d_{cant} = cantilever deflection

δ = indentation depth

and

$$F = K_{Cantilever}\, d_{cant} \tag{8-4}$$

Both Eq. 1 and 2 were fitted to the data using the least squares method through an in-house written FORTRAN code.

Overall surface heterogeneity of nanomechanical properties was studied through the spatial distribution of E and K_b.

8.3.6.2 Cell Adhesion force

The adhesion forces between a cell and AFM tip were determined as the minimum value of the retracting (retrace) part of the AFM curve.

8.3.7 Cell metal (Co or Ti) and Ba uptake quantification

Quantification of the cells uptake of the metal (Co and Ti) nanoparticles and PMMA bone cement (through Ba determination) particles was gained by using inductively coupled plasma-mass spectroscopy (ICP-MS). The cells were grown and exposed to the particles according to procedure described in section “Cell Culture”. At the 24 hour period, all media was removed from each well, cells were washed twice with sterile PBS, and 500µl of sub-boiled nitric acid (1:1) was added to each well. The 24-well plate was then placed in an incubator for 24 hours at 60°C in order to digest the cells. After 24 hours in the incubator, from each well 400µl of the solution was transferred into a 15 ml polypropylene tube and filled to a total volume of 8 ml with Milli-Q water. ICP-MS analysis was

carried out at sample rate of 1.5 ml/min and at characteristic wavelengths of 288.616 nm, 334.940 nm and 233.527 nm for Cobalt, Titanium and barium ion determination, respectively, on the Optima 2100DV OES (Perkin Elmer, Waltham, MA, USA) against the Primar 28 element standard.

All experiments were performed independently at least 3 times, and each experiment comprised 3 parallel samples. Results are given as mean ± standard deviation.

8.3.8 Statistical analysis

Comparison of the effect of Ti, Co and PMMA bone cement particles on mechanical properties of mouse osteoblast (MC3T3-E1) cells was performed through ANOVA test followed *post hoc* by Tukey's test individual pairs of data sets ($p<0.05$). Adhesion forces were compared using the Kruskal-Wallis test followed *post hoc* with a Dunn's test for individual pairs of data sets. Statistical analysis was performed using SPSS.

8.4 Results

8.4.1 Size and Charge of particles

The zeta potentials of all nanoparticles and cells are given Table 8-1. All particles, metals and PMMA, had negative zeta potentials. Both compositions of Cobalt nanoparticles had negative potentials of around -20mV, whilst 30nm Titanium nanoparticles displayed the lowest overall negative charge at -44mV. The smallest sized (25nm) and largest Titanium nanoparticles (100nm) had similar values at around -27mV. PMMA particles also had a negative potential

of -12mV. An example of PMMA wear particles image is shown in Figure 8-1, the shape did not appear spherical and the equivalent diameter was about 5 microns.

Table 8-1. Zeta potential of particles employed and pH of MC3T3-E1 media solution containing them.

Particles	pH	Zeta Potential (mV)	Size (nm)
Co 25nm	8.33	-19.4±1.0	27.3±2.1
CoO_2 50nm	7.19	-20.4±0.8	49.3±0.6
Ti 30nm	7.07	-44.7±1.9	27.7±3.5
TiO_2 100nm	7.15	-28.9±1.7	99.0±2.6
TiO_2 25nm	7.16	-26.8±0.5	27.7±2.3
PMMA bone cement	7.17	-12.1±0.8	5.2 ±1.8 10^3
Mouse Osteoblasts		-9.28±0.7	

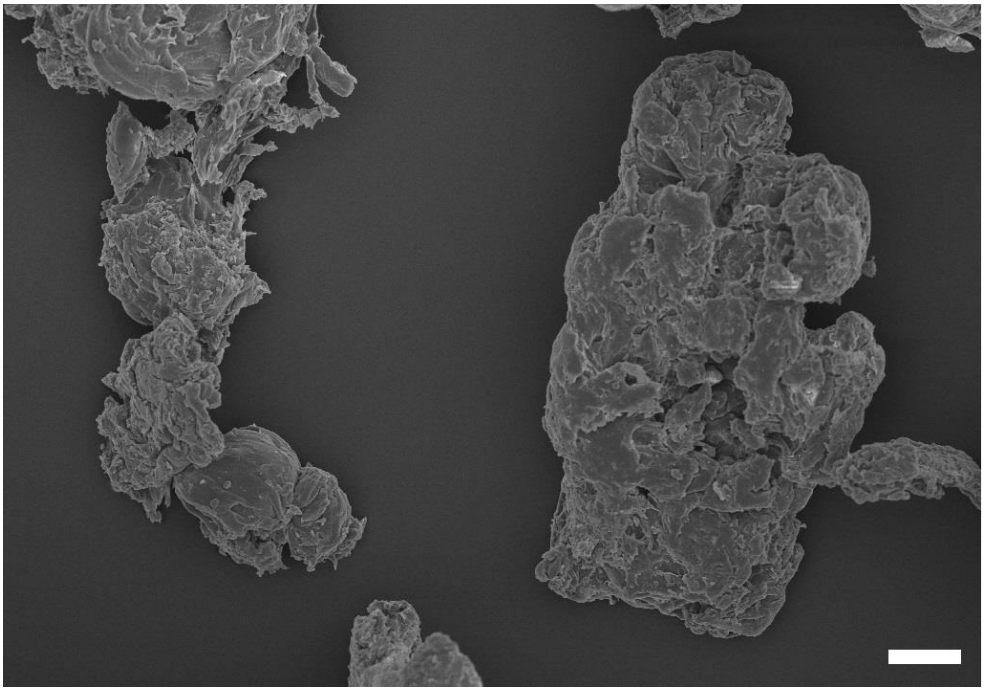

Figure 8-1. Examples of SEM image of PMMA wear debris. Bar correspond to 1 microns.

Mouse osteoblasts in growth medium suspension also exhibited negative zeta potentials of -9mv.

8.4.2 Metabolic activity

MTT was used to assess the metabolic activity of mouse osteoblasts. The metabolic activity gradually declined with time over a 72 hour period with Cobalt nanoparticles, with a greater decrease observed with elemental nanoparticles of Cobalt shown in Figure 8-2. There was a general reduction in overall metabolic activity with increasing concentration for both compositions of Cobalt nanoparticles. Results for the control sample over the 3 days remained consistent at around 1.8 OD; for Co 30nm, there is a deep decline in metabolic activity with the lowest concentration of only 5 μg/ml for all time points, reducing to around 1.3 OD, this reduction continued with increasing concentration to

around 1.0 OD for Co 30nm. For Co 50nm at 24 hours the decrease in metabolic activity was not as pronounced as for Co 30nm; however, for 48 hours and 72 hours metabolic activity for Co 50nm resembled that of Co 30nm.

Similarly with Titanium nanoparticles exposure (Figure 8-3), control samples remained constant over 72 hours at around 1.8 OD; after 24 hours a general decline in metabolic activity was observed with increasing concentration of nanoparticles. Initially at 24 hours the smallest Titanium particle of 25nm had the greatest decrease in metabolic activity to 1.2 OD with the lowest concentration of particles at 5 µg/ml. Titanium 100nm demonstrated the highest overall reduction compared to Titanium 25nm and 30nm, with the lowest metabolic activity of 1.0 OD at a concentration of 50 µg/ml at 24 hours. No effect was observed after 48 hours for Titanium 30nm with a similar metabolic activity to the control; yet both Ti 25nm and Ti 100nm reduced the metabolic activity to 1.4 OD at the lowest particle concentration of 5 µg/ml, with a continued decline with increasing concentration up until 25 µg/ml particle concentration, with an increase at 50 µg/ml to 1.6 OD and 1.7 OD for Ti 25nm and Ti 100nm respectively. For 72 hours the same pattern was demonstrated i.e. a slight reduction was observed from the control cells for all Ti nanoparticles concentrations, however little or no change in metabolic activity was observed.

Metabolic activity for PMMA, Figure 8-4, was also recorded, and control values were all consistent over 3 days at 1.8 OD. A general decrease in metabolic activity is observed with increasing concentration of particles; at 24 hours the lowest decrease of activity was observed at 25 µg/ml particle concentration, with no significant increase thereafter. Similarly, at 48 and 72 hours the lowest

metabolic activity was recorded at 25 µg/ml at around 1.5 OD. Concentrations higher than 25 µg/ml plateaued and no change was observed. This pattern was also displayed at 48 hours with a general reduction in metabolic activity with increasing concentration, however, concentration greater than 25 µg/ml did not further decrease as expected with the metal nanoparticles. At 72 hours PMMA exposure, a similar decline in metabolic activity was observed which continued after a concentration of 25 µg/ml.

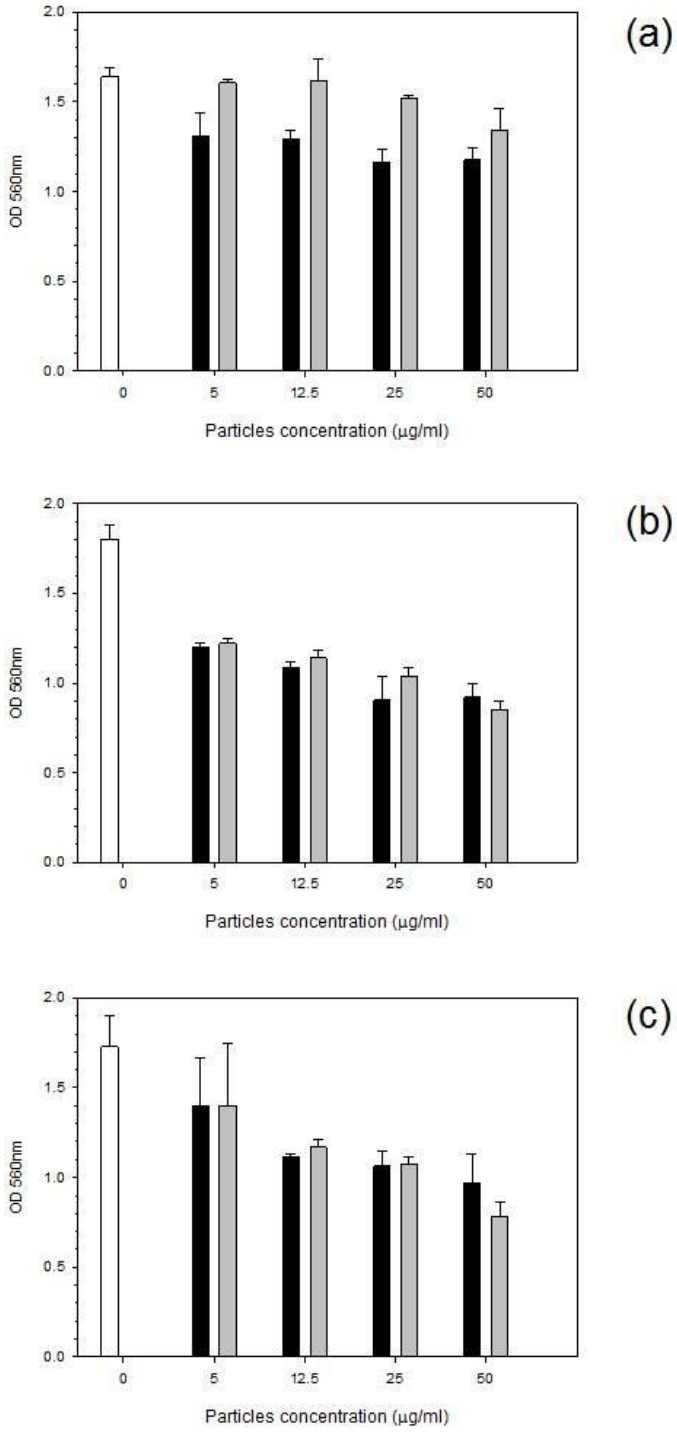

Figure 8-2. MTT results of MC3T3-E1 cells exposed to Cobalt nanoparticles for (a) 24h, (b) 48 h and (c) 72 h.

Control Co 30 nm Co 50 nm

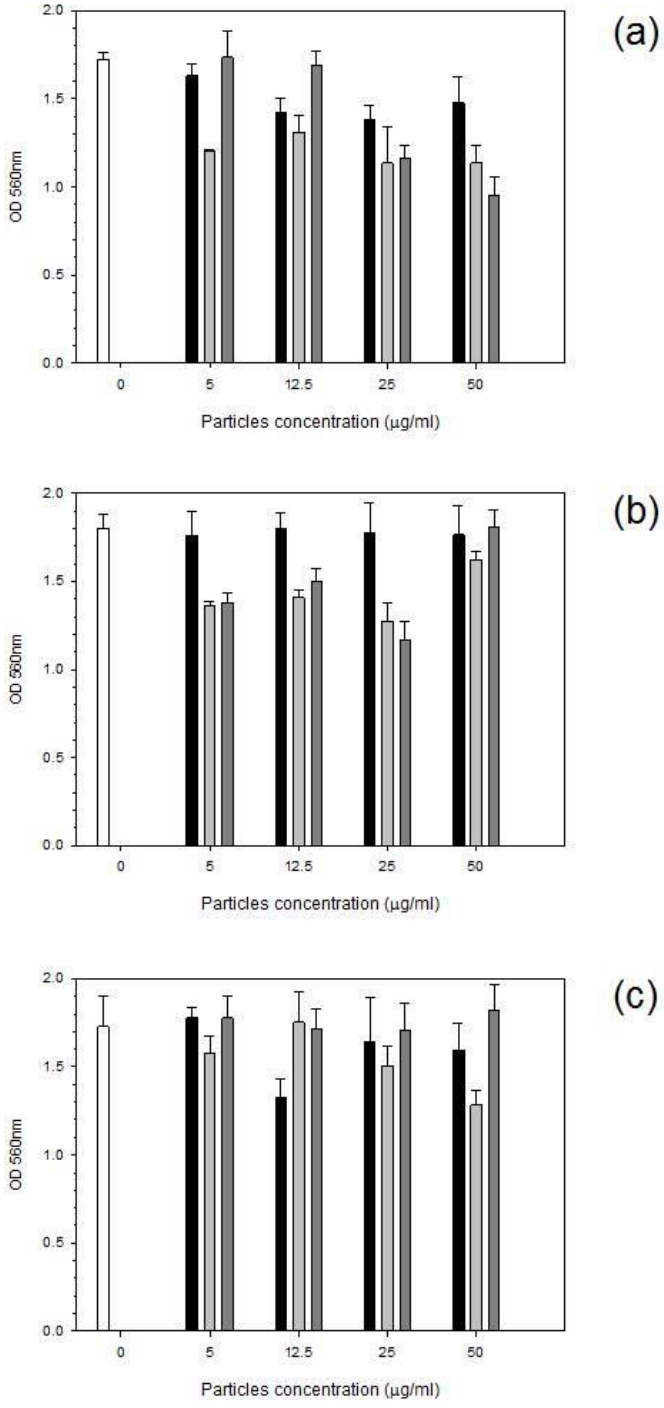

Figure 8-3. MTT results of MC3T3-E1 cells exposed to Titanium nanoparticles for (a) 24h, (b) 48 h and (c) 72 h.

Control Ti 30 nm Ti 25 nm Ti 100 nm

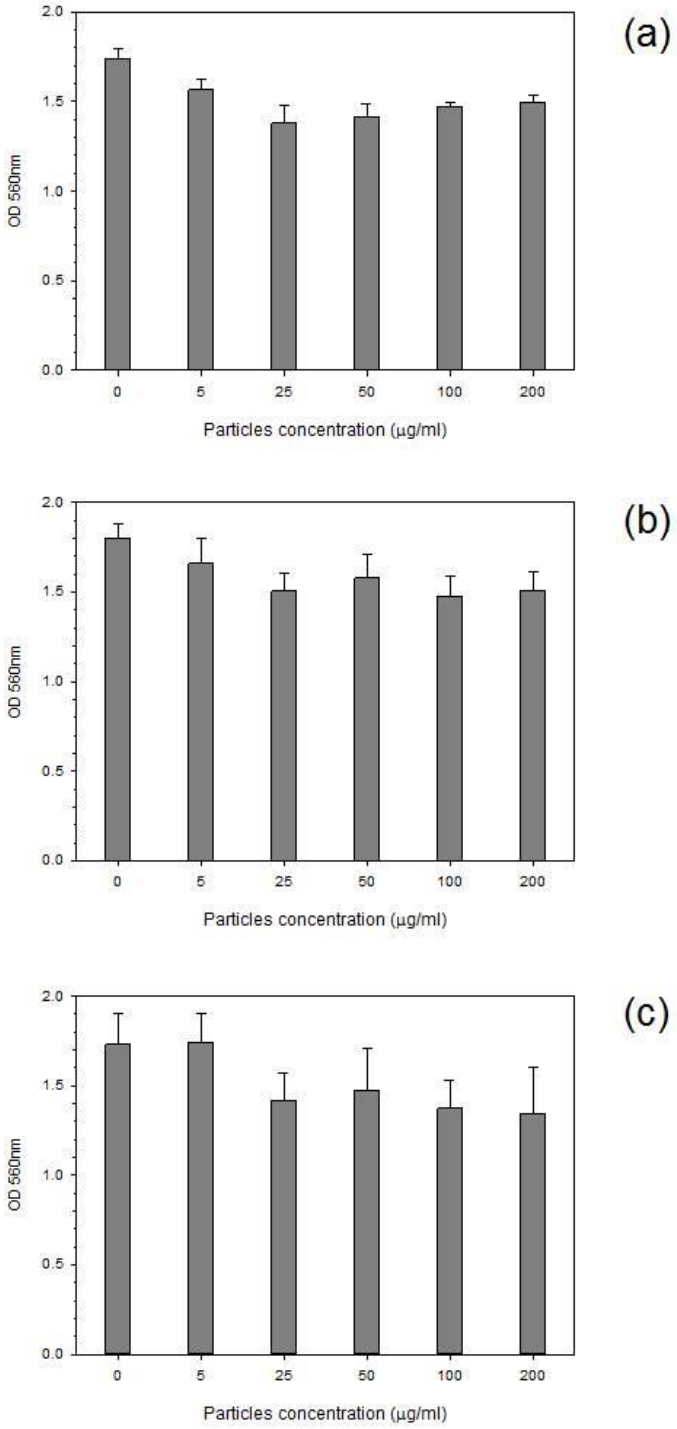

Figure 8-4. MTT results of MC3T3-E1 cells exposed to PMMA particles for (a) 24h, (b) 48 h and (c) 72 h.

8.4.3 Osteoblast mineralisation ability

Alizarin red assay was used to determine the production of calcium after 21 days of particle exposure (Figure 8-5). Control remained at around 1.2 OD. After 21 days, Ti 30nm particles caused a reduction in calcium production with a recorded value at 0.9 OD for particle concentration of 5 µg/ml, which continued to reduce to 0.8 OD at 12.5 µg/ml. Production then increased after a concentration of particles at 25 µg/ml. For Ti 25nm, there was an initial increase in calcium production with a value of 1.3 OD for a particle concentration of 5 µg/ml with a decrease as the concentration increased to 1.0 OD at a particle concentration of 50 µg/ml. Similarly to Ti 30nm particles, the Ti 100nm particles had similar values at a concentration of 5 µg/ml at around 0.9 OD, however, there was a slight increase to 1.1 OD at a concentration of 12.5 µg/ml, and again a reduction in values to 1.0 OD was recorded at 50 µg/ml. Cobalt 30nm particles had no great change on absorbance levels with a slight increase at 12.5 µg/ml particle concentration to 1.3 OD with a continuous decrease with increasing particle concentration of 50 µg/ml to 1.1 OD. Again for Co 50nm, an increase was recorded at 1.3OD at 12.5 µg/ml, however this continued to decrease with increasing concentration to 1.0 OD.

For PMMA wear debris, an initial decrease was observed from around 1.1 OD at 5 µg/ml to 1.0 OD at a particle concentration of 25 µg/ml, from here a spike increase was recorded for 50 µg/ml concentration to over 1.6 OD, however the usual decrease was observed with increasing concentration to 1.2 OD at a particle concentration of 200 µg/ml.

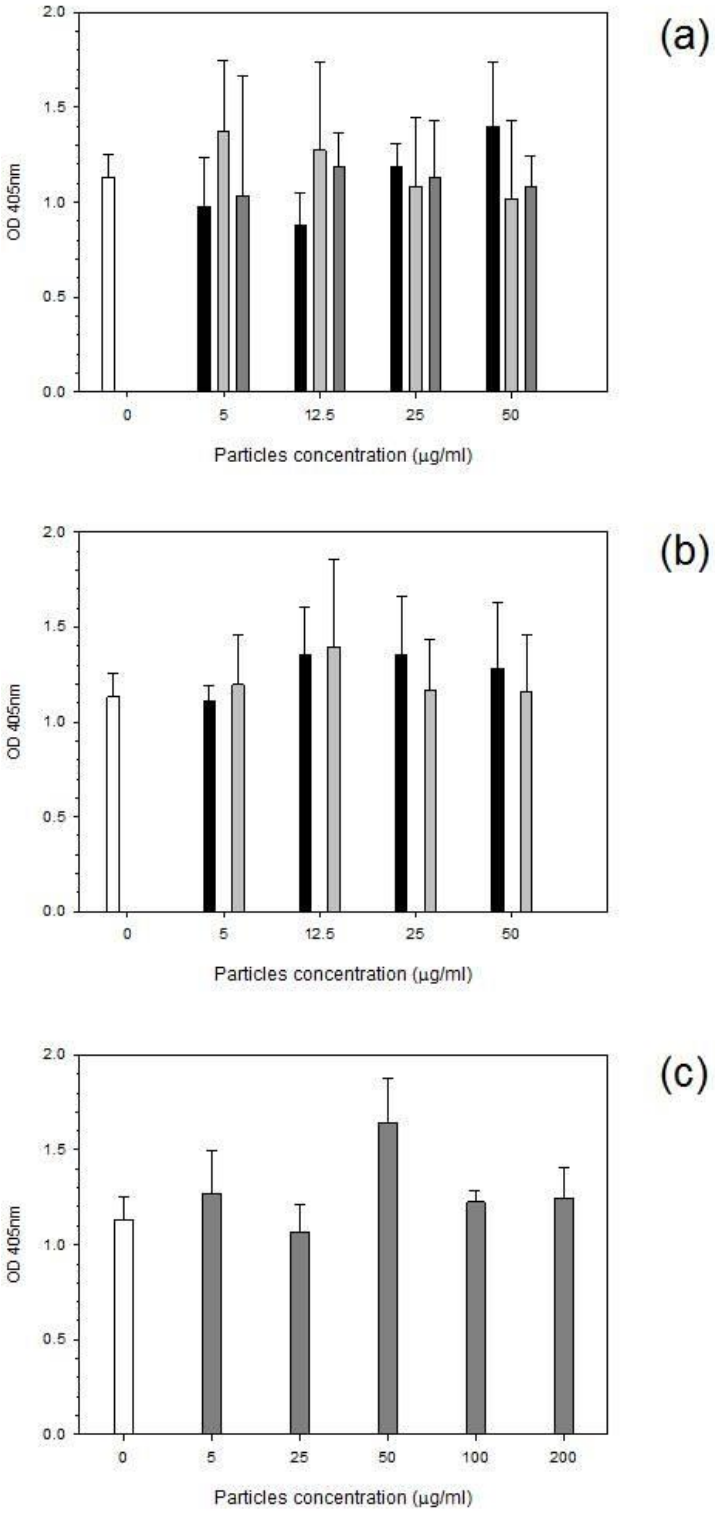

Figure 8-5. Osteoblast mineralisation ability after exposure to Titanium (a) Cobalt (b) and PMMA particles (c).

8.4.4 Nanomechanical properties

Elasticity data for Titanium and Cobalt is given in Figure 8-6 and Figure 8-7, respectively; and the spring constant information for Titanium and Cobalt treatments is shown in Figure 8-9 and Figure 8-10, respectively. Each graph represents all time points that were measured at 24, 48, and 72 hours.

At 24 hours for cells exposed to Titanium (Figure 8-6) the elasticity for all sizes of Titanium particles used generally increased with increasing concentration. All control samples i.e. cells not exposed to any particles remained constant over the 3 day period with an elastic value of around 28 kPa. Comparing each size against this value demonstrated that at the lowest concentration of 5 µg/ml and 12.5 µg/ml for Titanium elemental the elastic values were unchanged at 30 kPa, this dropped slightly at 25 µg/ml to 24 kPa, however, at the highest concentration the elastic modulus increased to 32 kPa. For both Titanium oxide particles, 25nm and 100nm, had a more pronounced increase in elasticity with increasing concentration. For 5 µg/ml, both oxides had an elastic moduli at around 20 kPa, this increased to 36 kPa for Titanium 25nm and to 24 kPa for 100nm at 12.5 µg/ml concentration. At 25 µg/ml the smallest sized particle gave the biggest increase to 40 kPa whereas the Titanium 100nm increased to 36 kPa. The increase continued for Titanium 25nm to 44 kPa, but decreased for Titanium 100nm to around 20 kPa at a concentration of 50µg/ml.

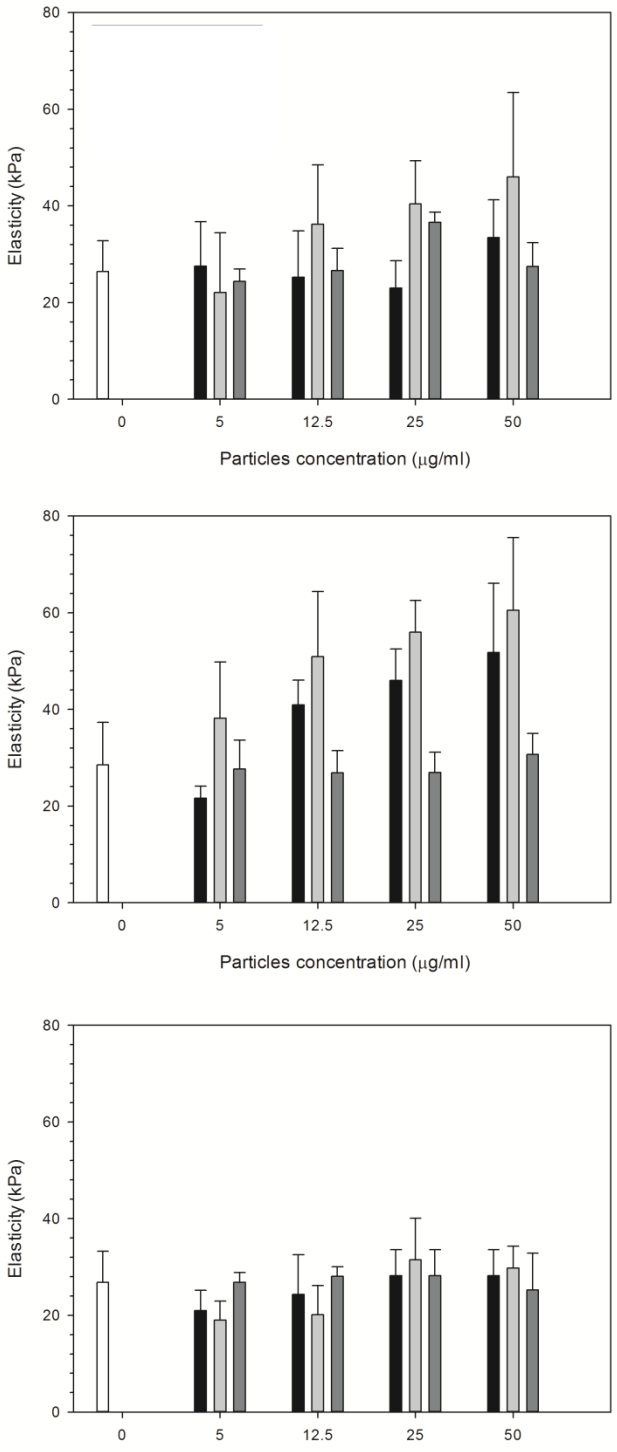

Figure 8-6 Mean cell elasticity of MC3T3-E1 cells exposed to Titanium nanoparticles for (a) 24h, (b) 48 h and (c) 72 h.

Control Ti 30 nm Ti 25 nm Ti 100 nm

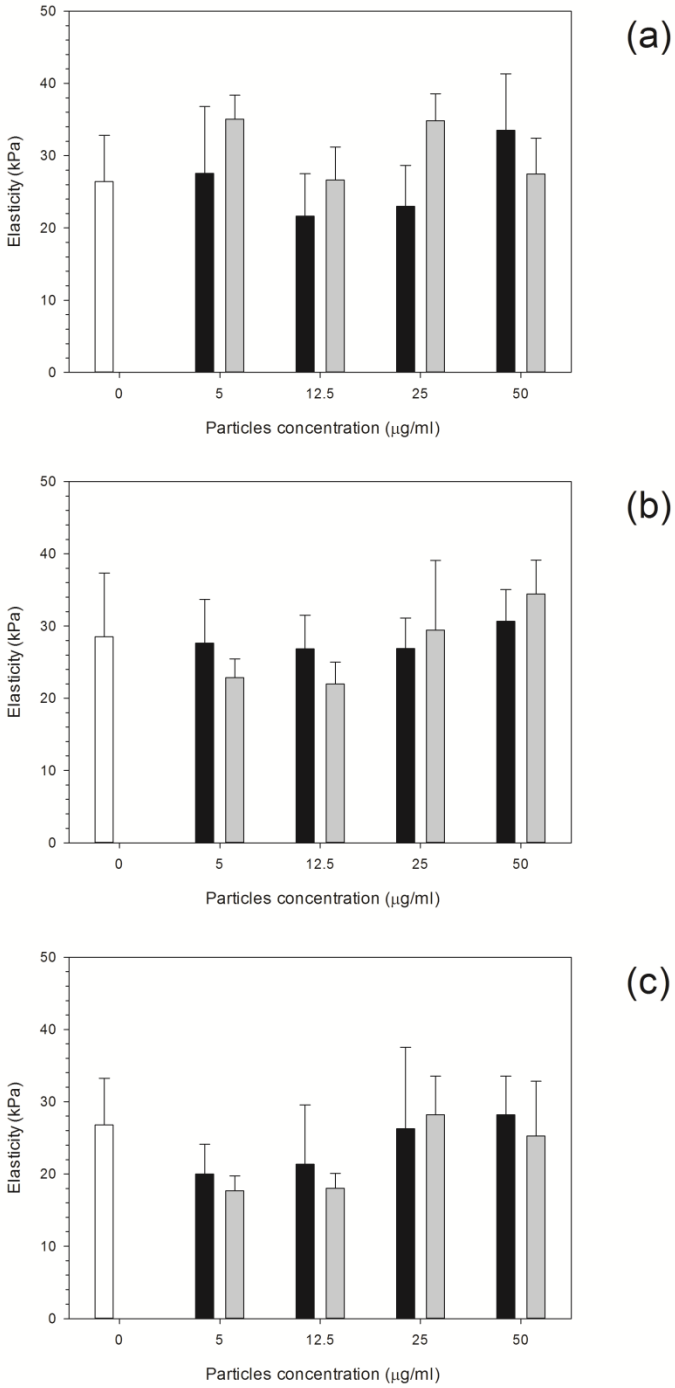

Figure 8-7. Mean cell elasticity of MC3T3-E1 cells exposed to Cobalt nanoparticles for (a) 24h, (b) 48 h and (c) 72 h.

Control Co 30 nm Co 50 nm

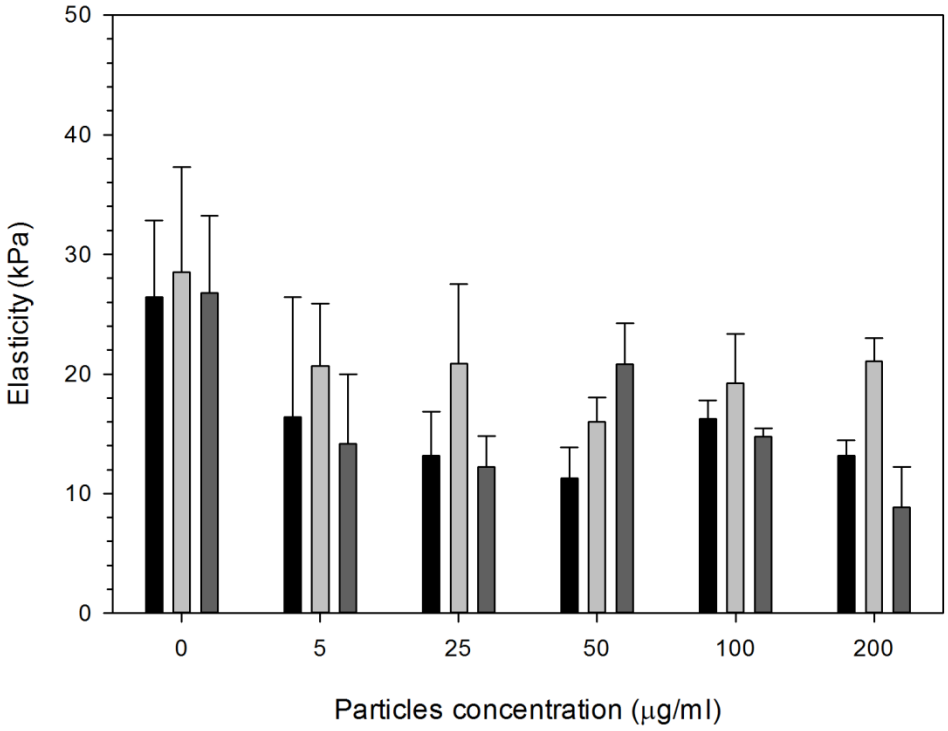

Figure 8-8. Mean cell elasticity of MC3T3-E1 cells exposed to PMMA particles for (■) 24h, (■) 48 h and (■) 72 h.

Over time, at 48 hours, an increase in elasticity is clearly demonstrated especially for Titanium elemental and Titanium 25nm, however little change is seen with the largest particles of 100nm. For Titanium elemental, 30nm particles, there is a slight decrease with the initial concentration with an elastic value at 20 kPa compared to the control, this then increases dramatically to 40 kPa at a concentration of 12.5 µg/ml; at 25 µg/ml a small increase is observed to 48 kPa, and to 52 kPa at a concentration of 50 µg/ml. Similarly, for Titanium

25nm a general increase with increasing concentration is observed, however, the initial value of elasticity at a concentration of 5 µg/ml increases instead of decreases to 40 kPa compared to the control value. This trend continues with another jump in elasticity to 52 kPa at 12.5 µg/ml; 56 kPa at 25 µg/ml, and at the highest concentration at 50 µg/ml had an elastic value of 60 kPa. A different story is seen however with Titanium 100nm as no change is observed with increasing concentration and elastic values remained consistent at 28 kPa. After 72 hours of exposure, an increase in elasticity is seen with increasing concentration but is not as pronounced as 48 hours of exposure. For Titanium 30nm had an elastic value of 20 kpa at 5 µg/ml, which increased slightly to 24 kPa at 12.5 µg/ml; at 25 µg/ml a last increase was observed to 28 kPa which remained for a concentration of 50 µg/ml.

Elasticity results for Cobalt nanoparticles are given in Figure 8-7. Over all three time points: 24, 48, and 72 hours, the elasticity results for the control cells remained consistent at around 25 kPa, shown with white columns. For Cobalt elemental particles at 30nm, there is no change in elasticity at a concentration on 5 µg/ml, following this, a decrease in elasticity was seen with an increase in concentration to 22 kPa at a concentration of 12.5 µg/ml and at 25 µg/ml; however, the elasticity peaks to 34 kPa at the highest concentration at 50 µg/ml. On the other hand for Cobalt 50nm particles, the lowest concentration of 5 µg/ml increased in elasticity to 36 kPa, a reduction in elasticity is observed with increasing concentration to 28 kPa for a concentration of 12.5 µg/ml and 50 µg/ml with a slight increase in elasticity at 25 µg/ml to 35 kPa at 24 hours.

After 48 hours exposure, again the lowest concentration of 5 μg/ml had no change for Cobalt elemental compared to the control, a slight reduction is seen with increasing concentration for 12.5 μg/ml, and 25 μg/ml, and a rise in elasticity to 32 kPa. The larger particles, Cobalt 50nm, demonstrated a reduction in elasticity to 24 kPa for both 5 μg/ml and 12.5 μg/ml, this increased after a concentration of 25 μg/ml to 28 kPa and to 36 kPa for 50 μg/ml.

At 3 days of exposure to the Cobalt nanoparticles, a drop in elasticity values were seen for both sized particles to 20 kPa at 5 μg/ml and 12.5 μg/ml concentrations. After a concentration of 25 μg/ml both elasticity values for both Cobalt nanoparticle sizes increased to 25 kPa and remained at this value for a concentration of 50 μg/ml.

The influence of PMMA bone cement debris on osteoblast nanomechanical properties is shown in Figure 8-8; after 24 hours exposure the elasticity of cell was reduced to about 14 kPa for concentrations greater than 5 μg/ml; no statistical differences were determined for concentrations of PMMA debris in the range 25 to 200 μg/ml. With increasing exposure time the trend was the same as after 24 hours.

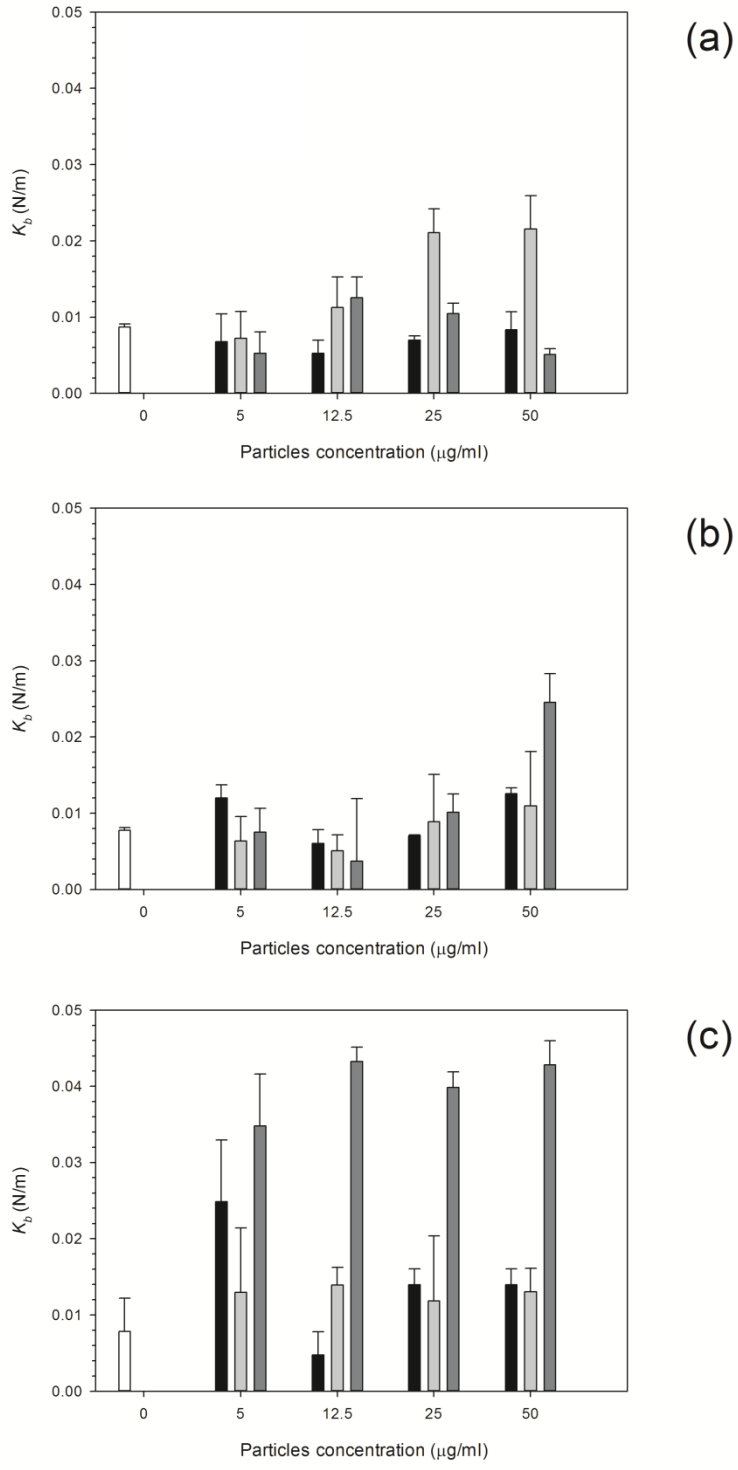

Figure 8-9 Mean spring constant of MC3T3-E1 cells exposed to Titanium nanoparticles for (a) 24h, (b) 48 h and (c) 72 h.

Control Ti 30 nm Ti 25 nm Ti 100 nm

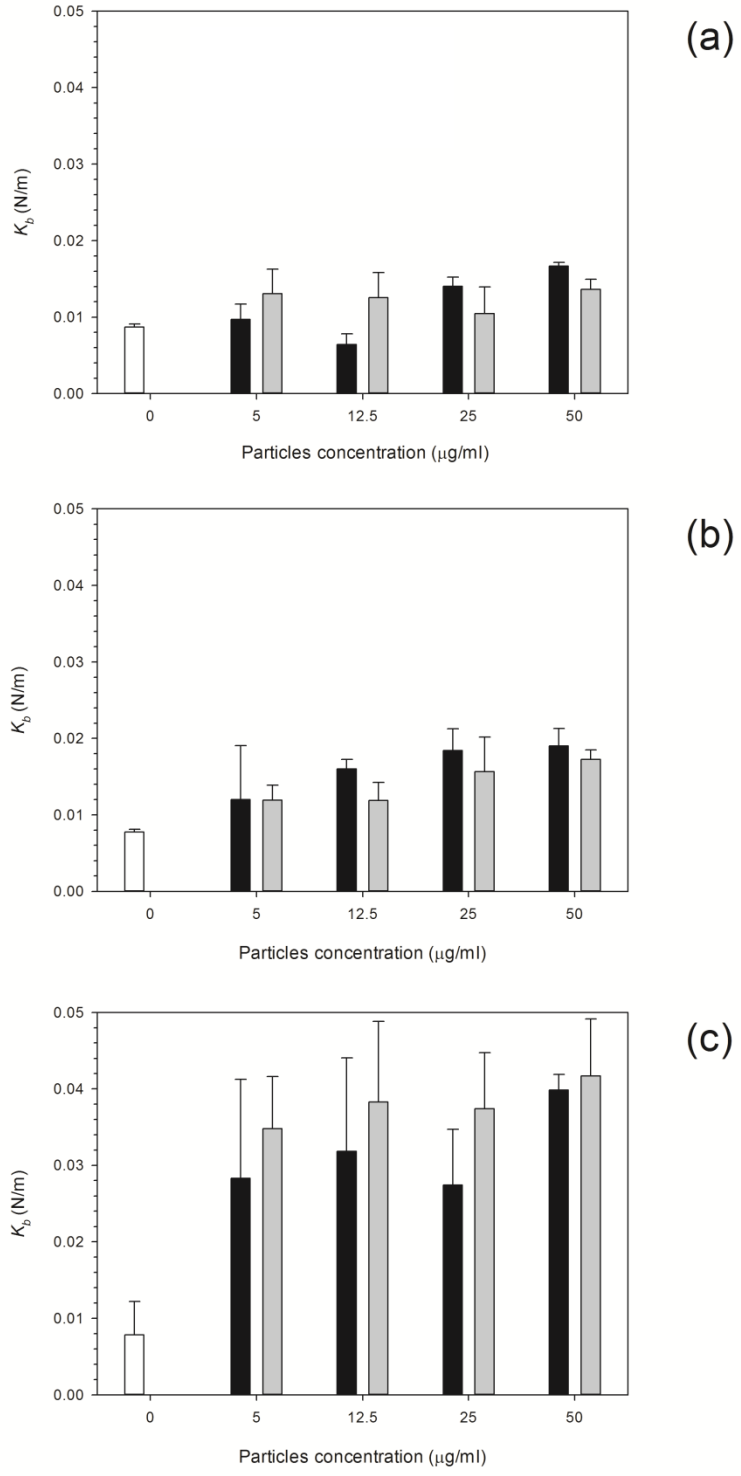

Figure 8-10. Mean spring constant of MC3T3-E1 cells exposed to Cobalt nanoparticles for (a) 24h, (b) 48 h and (c) 72 h.

Control Co 30 nm Co 50 nm

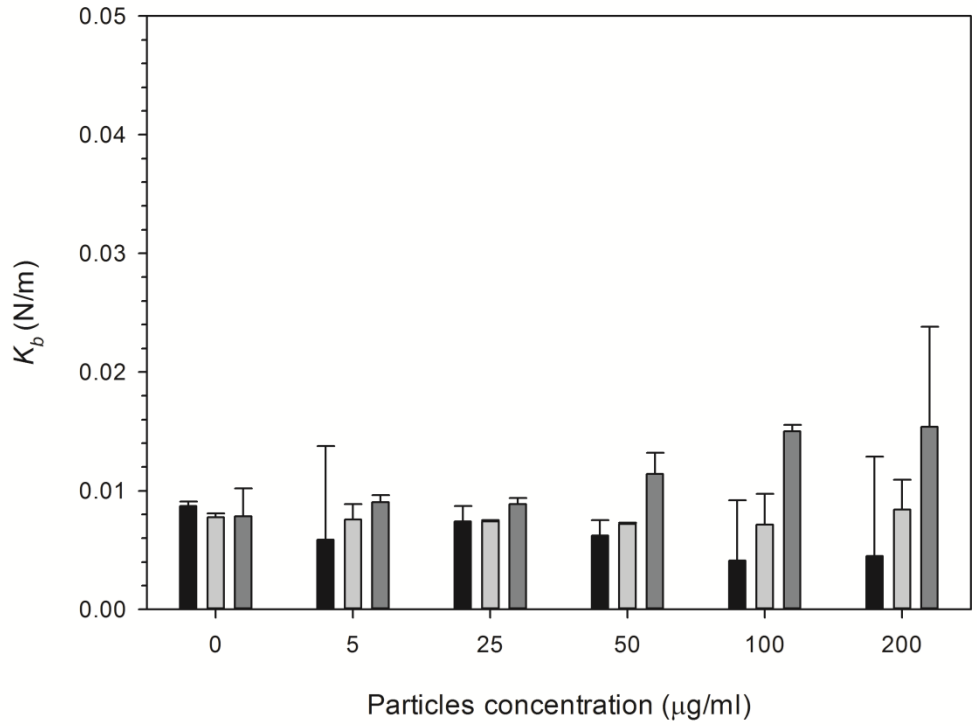

Figure 8-11. Mean spring constant of MC3T3-E1 cells exposed to PMMA particles for (■) 24h, (■) 48 h and (■) 72 h.

For Titanium particles the spring constant values are given in Figure 8-9. Similarly to the elasticity values of Titanium, the spring constant values also increase with increasing concentration. Again the control values of spring constant were consistent over time at around 0.01 N/m. For Titanium elemental, the spring constant did not change with increasing concentration with a value of around 0.08 given for each concentration; Titanium 25nm however, had the same initial value as Ti elemental at 0.08 N/m at 5 μg/ml, this increased to

0.012 N/m at 12.5 µg/ml, a large jump in the spring constant was observed at 25 µg/ml with a value of 0.022 N/m which slightly increased to 0.024 N/m at 50 µg/ml. Titanium 100nm, had an initial increase from 0.006 N/m at 5 µg/ml to 0.012 N/m at 12.5 µg/ml; however, this decreased to 0.01 N/m at 25 µg/ml and again to 0.006 N/m at 50 µg/ml.

At 48 hours of exposure to the Titanium nanoparticles, the spring constant values for Titanium elemental increased slightly from the control to 0.012 N/m at a concentration of 5 µg/ml, which then decreased to 0.006 N/m at 12.5 µg/ml; a small increase to 0.008 was observed at 25 µg/ml, but again increased to 0.012 N/m at 50 µg/ml. For Titanium 25 nm for both 5 and 25 µg/ml the spring constant values remained the same at 0.006 N/m, a rise in the spring constant to 0.01 N/m at 25 µg/ml was observed which again increased to 0.012 N/m at 50 µg/ml.

After 72 hours of exposure, a dramatic increase in the spring constant is observed at 5 µg/ml to around 0.026 N/m for the elemental Titanium, with a sudden drop to 0.004 N/m at a concentration of 12.5 µg/ml; at 25 and 50 µg/ml the concentration increased to 0.014 N/m for both concentrations. For the smallest particle of Titanium at 25nm little to no change was observed with increasing concentration and the spring constant remained at 0.014 N/m. The largest Titanium particles, 100nm, a dramatic increase in the spring constant was demonstrated at the lowest concentration of 5 µg/ml at 0.036 N/m; an increase to 0.044 N/m was shown for the remaining concentrations at 12.5, 25, and 50 µg/ml concentrations.

In Figure 8-10, the spring constant data is seen for all time points for both Cobalt nanoparticles treatments. At 24 hours, the control adhesive forces remained consistent over time at around 0.008 N/m. A slight rise in spring constant was observed for the lowest concentration to 0.009 N/m for Cobalt elemental which declined to around 0.005 N/m at a concentration of 12.5 µg/ml. The spring constant then dramatically increase for the higher concentrations 25 µg/ml and 50 µg/ml at around 0.015 and 0.017 N/m. For the larger particles of Cobalt at 24 hours an increase in spring constant was recorded compared to the control to 0.013 N/m for both 5 and 12.5 µg/ml concentrations, this decreased at 25 µg/ml to 0.010 N/m; for the highest concentration of 50 µg/ml the value increased to that of the lowest concentrations i.e. 0.013 N/m.

At 48 hours, the spring constant values generally increased with increasing concentrations. For the lowest concentration of 5 µg/ml both Cobalt sizes had the same value of 0.012 N/m, this initial value increased for the smaller Cobalt articles to 0.016 N/m but remained the same for the larger particles of Cobalt. Yet for both, spring constant values increased for 25 and 50 µg/ml, for instance, Cobalt elemental to 0.018 N/m and 0.019 N/m respectively; and for Cobalt 50nm to 0.015 N/m and 0.018 N/m, respectively.

At the longest exposure time of 72 hours, the values were much higher than the previous days, for example at 5 µg/ml concentration, the spring constant value was at 0.028 N/m for Cobalt elemental this increased to 0.03 N/m at a concentration of 12.5 µg/ml. This decreased to 0.026 N/m at 25 µg/ml, which again increased to 0.038 N/m at 50 µg/ml. The values for Cobalt 50nm, with an initial value of spring constant of 0.036 N/m for 5 µg/ml, increasing to 0.038 N/m

for 12.5 and 25 µg/ml concentrations, and a slight increase at 50 µg/ml to 0.04 N/m.

The spring constant of osteoblast cells exposed to PMMA debris is presented in Figure 8-11 and revealed that only concentrations higher than 100 µg/ml for 72 hours demonstrated a significant increase of such a parameter.

8.4.5 Metal uptake

Uptake data is shown in Figure 8-12 for Titanium nanoparticles, Figure 8-13 for Cobalt nanoparticles and for PMMA data is shown on Figure 8-14. Generally uptake of nanoparticles increased with increasing concentration, and an increase in exposure time also increased the uptake of nanoparticles. Greater uptake was noted for Cobalt 50nm compared to Cobalt 30nm by almost three fold for the higher concentration of 50 µg/ml after 72 hours of exposure.

For Titanium nanoparticles, overall uptake was far less than for Cobalt nanoparticles, and very little to no uptake was recorded after the initial 24 and 48 hours of exposure for Titanium 25nm at the lower concentrations, with only a small uptake at 50 µg/ml. For Titanium 30nm, uptake was observed by all concentrations, which increased similarly to Cobalt nanoparticles with increasing concentration and increasing time. Yet, for Titanium 100nm, only after 72 hours was any uptake recorded but still followed the same pattern as other particles i.e. increased uptake with increasing concentration.

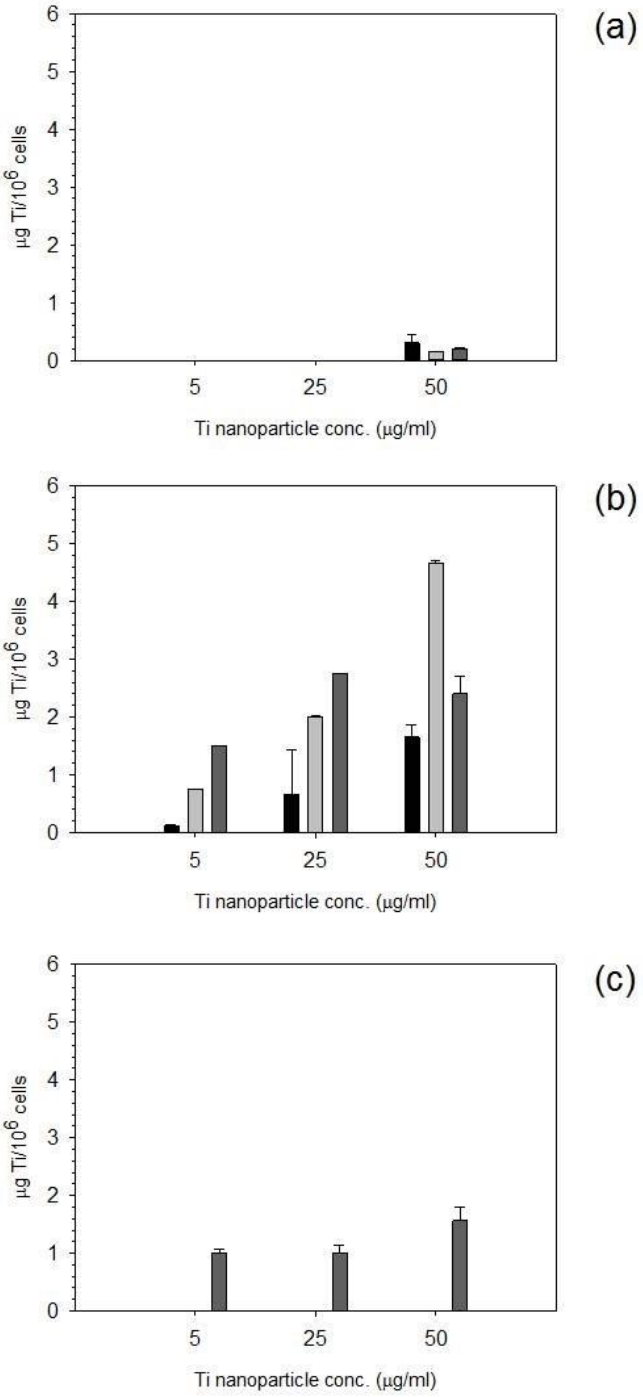

Figure 8-12. Metal uptake of MC3T3-E1 cells exposed to Titanium nanoparticles at different concentrations for ■ 24 h ■ 48 h ■ 72h. (a) Ti 25 nm, (b) Ti 30 nm and (c) Ti 100 nm.

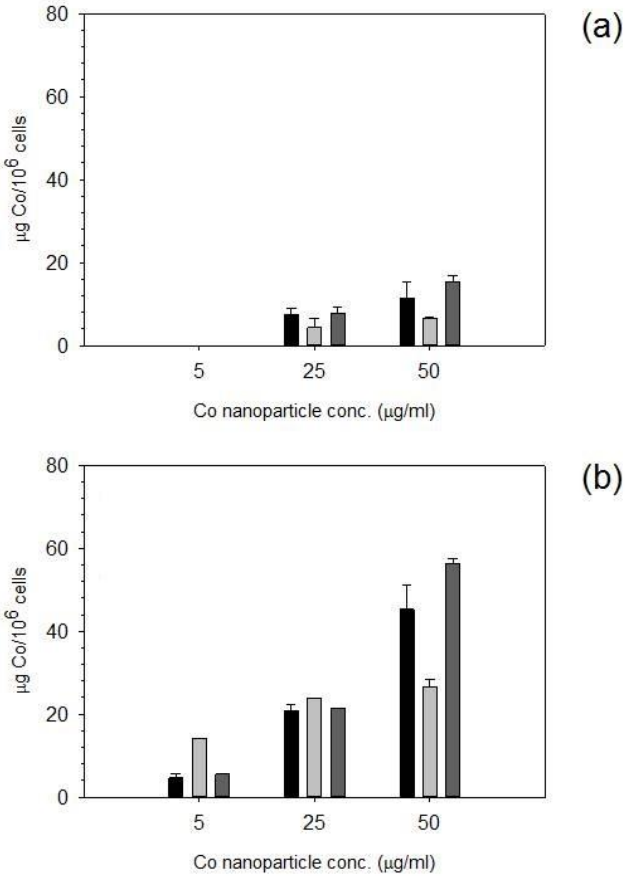

Figure 8-13. Metal uptake of MC3T3-E1 cells exposed to Cobalt nanoparticles at different concentrations for ■ 24 h ■ 48 h ■ 72h.

(a) Co 30 nm and (b) Co 50 nm.

PMMA uptake was measured using concentration of barium, as barium is the only metal in the PMMA bone cement composition. No uptake was recorded at any time point for the lowest concentration of 5 µg/ml. Although, uptake

increased with increasing concentration with increasing time points similarly to both Cobalt and Titanium nanoparticles.

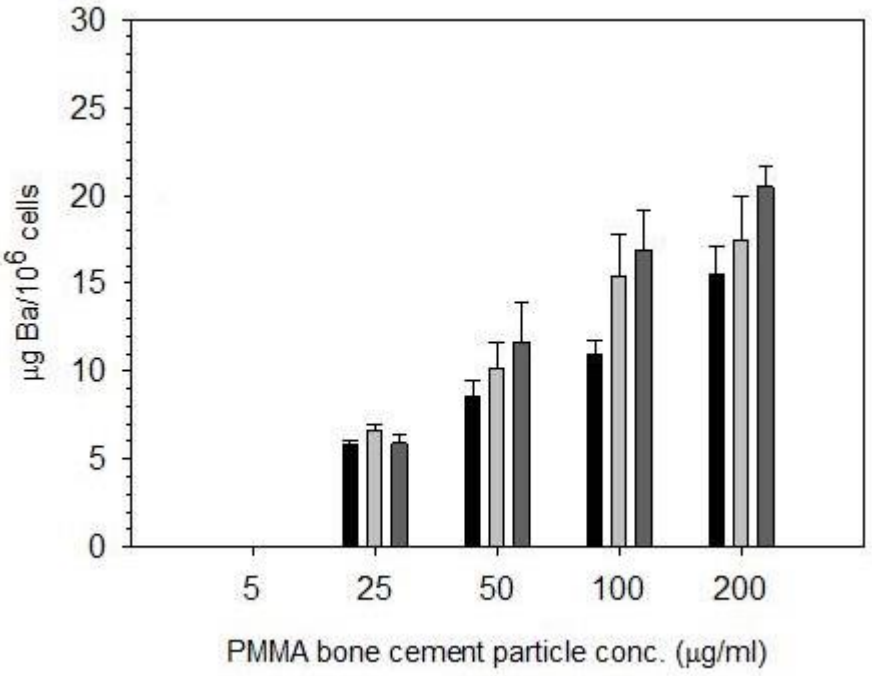

Figure 8-14. Metal uptake of MC3T3-E1 cells exposed to PMMA particles at different concentrations for ■ 24 h ■ 48 h ■ 72h.

8.4.6 Cell adhesion forces

Both treated and non-treated cells i.e. not exposed and exposed cells to particles demonstrated spatial distributions of adhesion forces on the cell surface and were not normally distributed Figure 8-15 and Figure 8-16, for

Titanium and Cobalt nanoparticles, respectively. The control sample median did not vary with increasing time with a consistent value of around 2 nN.

Adhesion forces for Cobalt nanoparticles post 24 and 48 hours exposure did not differ from each other and demonstrated a general decline in adhesive forces with increasing concentration. The lowest values of adhesion were recorded at a concentration of 25 µg/ml for all time points. Generally, there was no change in adhesion after exposure to either Cobalt nanoparticles with increasing concentration as there is little change in the upper and lower quartile range of both Cobalt compositions.

Again, little to no difference in adhesion forces was observed for Titanium after 24 and 48 hours exposure regardless of composition and size of the particles (Figure 8-15). The range of data in this instance did not differ greatly from the control. After three days of exposure a decline in adhesive force is observed for all Titanium compositions up to a concentration of 25 µg/ml.

For PMMA, a general decline in cell adhesion forces were observed with increasing concentrations of PMMA exposed to cells (Figure 8-17). The lowest values of adhesion were observed at the initial 24 hour time point; in this case the values of adhesive forces did not differ with increasing concentration of PMMA at around 0.5nN. An increase in adhesive forces was demonstrated at 48 and 72 hour exposure both recording values at 3nN with the lowest concentration of 5 µg/ml, to 2nN at the highest concentration of 200 µg/ml.

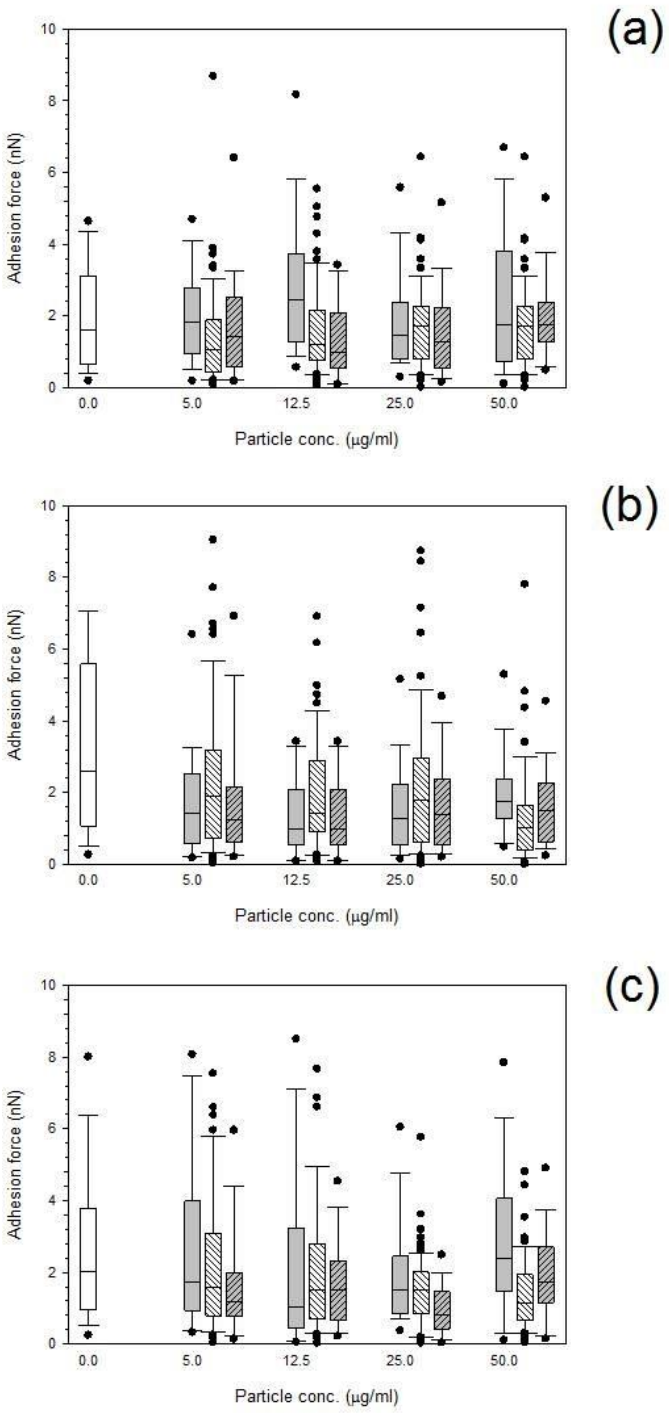

Figure 8-15. Box and whiskers plot of adhesion force distribution of MC3T3-E1 cells exposed to Titanium nanoparticles for (a) 24h, (b) 48 h and (c) 72 h.

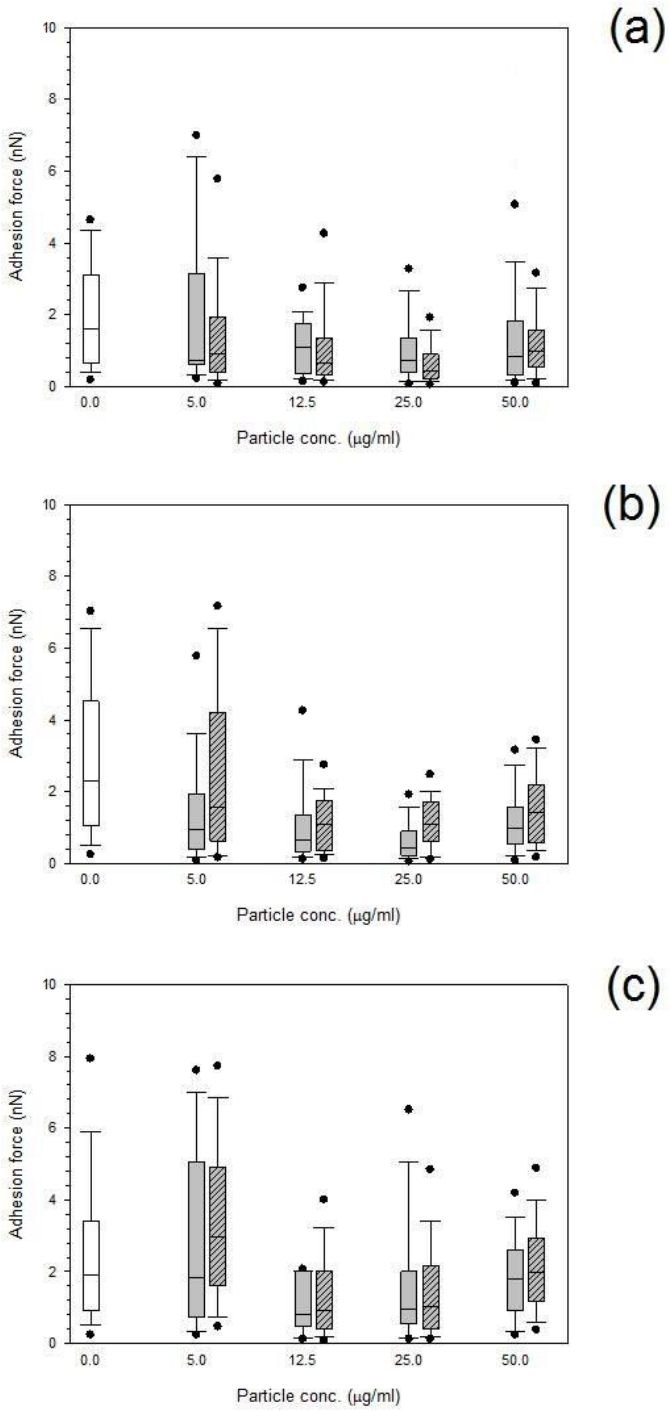

Figure 8-16. Box and whiskers plot of adhesion force distribution of MC3T3-E1 cells exposed to Cobalt nanoparticles for (a) 24h, (b) 48 h and (c) 72 h.

control Co 30 nm Co 50 nm

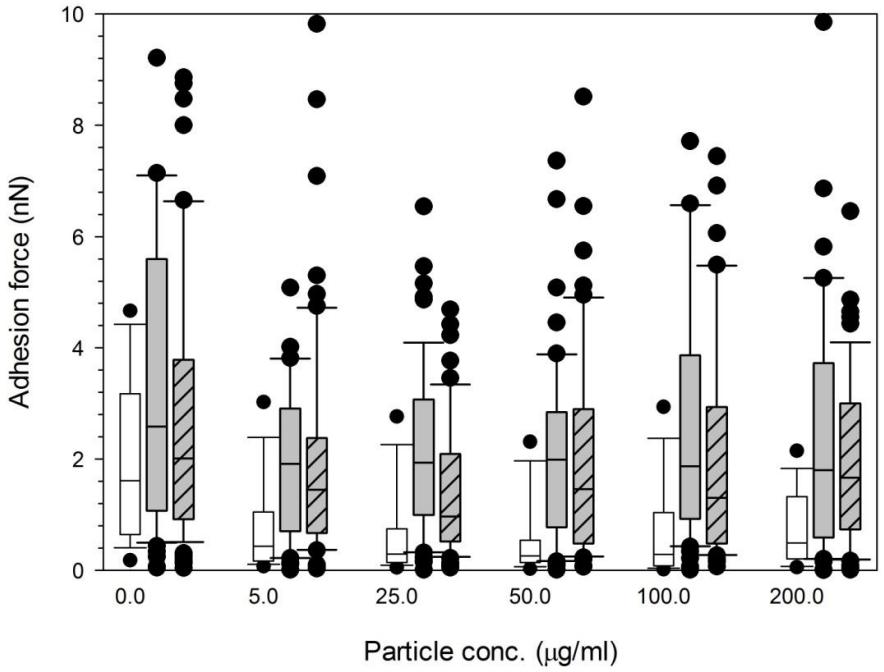

Figure 8-17. Box and whiskers plot of adhesion force distribution of MC3T3-E1 cells exposed to PMMA nanoparticles

24h 48 h 72 h.

8.5 Discussion

Total joint replacement (TJR) is ever increasing in a number of cases [1] yet the leading cause of failure remains as aseptic loosening second to infection problems [1]. Wear debris are the culprit causing aseptic loosening commonly occurring within 15 years of surgery [1-3]; the particles produced range in size from micron to sub-micron, with the majority of wear formed are less than 5 μm in diameter [2], and it's thought that the nano-sized range are potentially the most harmful range due to their increase in free radicals production and chromosomal damage [13, 37]. Commonly, these particles or wear debris

originate from ceramic, metal or polymeric materials [10]; for instance, metals commonly used include Titanium, Cobalt, and their oxides. The size, shape, charge, composition and concentration range of the particles used in this study correspond to retrieved particles from explants, as well as demonstrating cellular response [2]; for example Cobalt wear debris has been noted at around 50nm, and Titanium has been found in a range of sizes up to a few hundred nanometres [38]. From abrasion, adhesion and fatigue, wear particles of PMMA bone cement were found to have a median equivalent circle diameter (ECD) i.e. the diameter of a circle having the same area as the measured feature, was between 0.65 and 1.51 μm [39]; however, many particles were around 10μm, with 67% to be in the submicron range in size. The size of the particles is of importance as it has been previously proposed that phagocytosis has been recognised as an important cellular uptake mechanism [2]. Another study by da Rosa (2013) [40] decided to observe the changes to cells with Titanium particles and the effect of the aggregation may have on the cells [40]. Generally, Titanium is biocompatible, but its length and chemical nature of their aggregates have been linked to toxicity [40, 41].

In this work, we considered physico-chemical, surface parameters of the metal (Co and Ti) and PMMA bone cement particles (such as: particle size and charge) and material (particle chemical composition and its nature) on nanomechanical, adhesive properties and calcium production ability of mouse osteoblasts (MC3T3-E1) cells.

PMMA wear debris have been shown to be larger in size (in the order of microns) than other metal debris and with non spherical shape [38]; so the

PMMA debris generated and employed in this work are in agreement with this previous findings in both size and shape.

Some studies have demonstrated that cells such as osteoblasts have incorporated ionic Cobalt and chromium [42]. This has been achieved through phagocytosis of particles less than 1 μm, suggesting that particles isolated and retrieved from revision tissues including Titanium can incorporate with osteoblast-like MG63 cells [43, 44]. Generally the first stages of initiating an adverse effect begins with the phagocytosis of the particles by the cells, and has been visually demonstrated using polystyrene-based fluorescent particles, such as Fluoresbrite, and are internalised within 24 hours of in vitro exposure, with cells being saturated with around 40-60 particles/cell [44].

Many techniques [21, 45-48] have been used to measure the viscoelastic mechanical properties of single cells which includes micropipette aspiration, cytoindentation, magnetic bead rheometry, optical traps, and AFM [45]. For mesenchymal stem cells, Darling et al. (2008) [45], tested whether elastic and viscoelastic properties indicates the cells phenotype, using AFM with a borosilicate functionalised tip at a similar spring constant to that used in our study, of around 0.04 N/m. Similarly, Bhadriraju and Hansen (2002) [49] used a small spring constant of 0.06 N/m to investigate the stiffness and spreading changes of cells using AFM [49]. In both these work, the elastic modulus was modelled using Hertz model of contact [45] 49], as employed for our investigation. Interestingly, Darling et al. (2008) [45] also found the elastic data to have a not normal distribution and that the osteoblasts demonstrated the

largest elastic moduli and no difference in lineage was noted from the viscoelastic properties.

Generally, when spread, cells are stiffer [45], in this study osteoblasts had the greatest increase in average elastic moduli from spherical to spread. This notion correlates with the increase in the elastic modulus of the cells in our study over time, for example, the control samples had an elasticity value of around 20 kPa which increased to 60 kPa over time with increasing concentration; as well as the alterations in spring constant of the cells from 0.008 N/m for the control cells to around 0.04 N/m for treated cells, demonstrating differences in the mechanical properties of the cell post exposure to nanoparticles. From Darling et al (2008) [45] study has proven useful in utilising these mechanical properties of cells to use as biomarkers for their phenotype and tissue of origin [45]. Two configurations of cells were used short seeding to test the sphericity of the cells and long seeding to understand the morphology of spread cells, but no significant differences were observed which may be due to similarities in cytoskeletal architecture for the spherical cells. However, in the spread morphology demonstrated differences due to the anchored cytoskeleton structures [45]. This has also been observed by Thoumine et al. (1999) [46] who concluded that through analysing the cell rheology and structure assumed that the stiffening of cells upon spreading was due to structural organisation changes of the cytoskeleton [46, 50].

Cell elasticity is closely linked to the cytoskeleton changes [46], and in this study it was observed that that Titanium demonstrated an increase in elasticity suggesting interactions with the network of stress fibres as explained by

Thoumine et al (1999) [46], and disruptions to the membrane integrins of cells, forming complex disturbances to the original form which contributes to the cells rigidity [46, 51]. This could explain the changes observed in the elasticity modulus of the osteoblast cells, with Cobalt and Titanium nanoparticle exposure; there was a general increase in the elastic modulus with time demonstrating that cells become stiffer. Following from this, measurements of the cell rigidity were collected by the amplification of aspiration pressure needed to deform the same length of cytoplasm drawn into the micropipette [51], finding that cells exposed to Titanium required two-fold the amount of aspiration pressure compared to untreated cells, therefore the overall rigidity of the cells exposed to wear debris increased the stiffness of the treated cells. It is explained [52] that disruptions to the cytoskeleton organisation impacts on the expression of transcription factors and osteoblast-specific genes in osteoblasts [52], as well as influencing cell behaviour. Similar values in stiffness were observed [49] when changes in the actin and myosin activity were investigated in relation to the changes in shape of the cell at around 20 kPa [49]. The changes in stiffness are due to the adaptation of the cells to the stress stimuli introduced by the environment when the cells are exposed to the metal nanoparticles [53]. Cells respond to a number of stress factors such as fluid shear stress, strain stimuli and vibration stress; such mechanosensing allows cells to detect adhesion of metal nanoparticles to the outer membrane of the cells [53]. It had also been suggested that the cytoskeleton is the key aspect responsible for sensing the cellular mechanical changes [53, 54].

A study by da Rosa (2013) [40] observed a similar trend in the increasing adhesive forces with time which was thought to be a direct effect of the uptake of the aggregated Titanium nanoparticles which also caused the neutrophil cells to show stronger stiffness after exposure to the metal nanoparticles [40].

Cells also adapt to substrates which can affect the morphology and elasticity of cells [47] due to physical forces exerted on the cell [46]. The AFM has been employed to investigate the adhesion behaviour of osteoblast cells in vitro; Domke et al (2000) [47] were interested in substrates used in implanted materials and highlighted two properties of importance for implantation of synthetic materials. Firstly, the implant should emulate the functionality of the original material; secondly, the implant should be compatible with living organisms [47]. Overall the implant must be biomechanically competent and therefore requires a bioactive interface between the surface of the implant and the surrounding tissue i.e. osseointegration [47]. These interactions involve reactions with extracellular membrane and intracellular molecules and receptors, with osseointegration regulated by cytokines and trophic factors such as protein adsorption, cell attachment, cell proliferation and cell differentiation, proceeded by matrix production and calcification [47]. Influences from physical characteristics also play a role such as the topography and roughness of the implant as well as chemical properties including the hydrophobicity of the surface. Domke et al (2000) [47] used the AFM to study the adhesion behaviour of osteoblasts on substrates by investigating the cytomorphological aspects as a measure of cell adhesion [47]. Cell shape was dependent on the substrate used to culture cells, for example osteoblasts grown on metallic substrates have

an enlarged cross section area whereas cells cultured on glass were rounded and had the largest height, and cells were flat on PS surfaces; with increasing surface roughness, cells become more flat and the mean elasticity differed [47].

The data collected in this study demonstrated a decrease in overall adhesion with increasing particle concentration with increasing exposure time. This is confirmed by the literature, as Kwon et al (2001) [51] investigated the effects of Titanium particles on osteoblast function. Kwon et al (2001) compared the adhesion force of osteoblasts on fibronectin coated glass after exposure to Titanium nanoparticles at incubation times between 0.5 and 72 hours [55], using micro-pipetting single cell manipulation system; particles travelled through the cytoplasm rather than on the cell surface during aspiration. It was shown that only after 4 hours of exposure that there was a significant decrease in adhesion forces, at around 50% reduction at all time points, compared to the control for all seeding times from 15 to 60 minutes; and after 72 hours exposure the adhesion forces were lower than at 4 hours, with cell adhesion inhibited for all seeding times from 15 to 60 minutes [55]. Furthermore, at 72 hours the adhesive forces levelled out which demonstrated no dependence on seeding time, therefore phagocytosis of Titanium particles by osteoblasts significantly alters the rheological behaviour of cells leading to a decrease in adhesion-dependent cellular activity and functions [51, 55].

It is thought that the cytoskeleton of a cell, especially the filamentous actin determine the cells ability to maintain a stable shape, maintaining the function of the cell [24]. In this study it was proposed that the interactions between these actin-filament bundles of the osteoblasts cells within the cytoskeleton could

cause a loss of adhesive function and therefore changes to the adhesion characteristics of the cell could potentially alter the cell's function. A further explanation for the changes in adhesion properties stems from the decrease in cell cytoplasmic spreading and attachment area, stemming from the particles integrating to the actin filaments forming denser networks within the structure [55]. From the addition of Titanium particles to the cell stress fibres reduces the spreading of the cell, a reduction in spreading area of the cell means minimising contact, thereby reducing the overall adhesion. These changes could explain the pathogenesis of peri-prosthetic osteolysis secondary to implant wear debris, with Kwon et al (2001) showing a decrease in adhesion of around 40-60% in spreading attachment [51].

Some of the above studies [11, 24, 40, 41, 44, 47, 48, 50, 51, 55] have demonstrated that orthopaedic wear debris affects the viability of cells, including their proliferation, differentiation, and function. Yet, many of these studies do not coincide featuring many discrepancies such as the choice of cell, cell population, culturing conditions, not to mention the wear debris compositions variances such as the size, composition, dose and aggregation. However, the studies agree that particles and debris of less than 5μm tend to interact with cells and undergo uptake via phagocytosis especially in regards to human, rat, and mouse bone cells. Even though results have been inconsistent for the viability assays, the biological effects are dose-dependent, and the majority of results demonstrate that the higher the concentration or dose the more adverse the effects. Non-toxic particles activate osteoblasts from the up-regulation of pro-inflammatory and bone-resorbing factors, with the down-regulation of bone

forming variables. Interestingly, debris from alumina and polystyrene origins are less harmful in comparison to metals and polymers commonly used in orthopaedic devices [6, 56-58].

From a mechanistic stand point, the presence of foreign particles in direct contact with cells causes an uptake of these particles by osteoblast bone cells. The complete mechanism for damage from this uptake is still unknown; however, once phagocytosis is observed it is unclear whether the physical contact or the uptake or the presence of these particles initiates a cellular response via membrane mediated association.

As literature demonstrates that the bone adjacent to an implanted TJA has a substantial bone resorption surface [59]. It has been assumed that wear debris, especially in regards to this study, contact with bone-forming cells located around loosening implants due to the generation of wear particles. If this contact causes an inhibition or suppression of the function these bone-forming cell, for example, damage to the cells disrupts the normal viability, proliferation, and differentiation of these essential bone forming cells, leads to further loosening of the implant due to a decrease in bone renewal and formation.

It is has been reported that osteoblasts exposed to PMMA particles significantly increased their production of calcium [60, 61], this was also true for our study. Moreover, both Titanium elemental and Cobalt particles increased the calcium formation with increasing concentration. Yet for Titanium 25nm a decrease in calcium production was observed which coincides with other reports [62, 63], which explained that, despite an increase in proliferation, there was a decrease in the calcium production suggesting other mechanisms of damage and that

cellular responses and signalling pathways are altered after nanoparticle exposure [63].

8.6 Conclusion

This study aimed at observing the influence of wear particles on bone cells through an alternative perspective (cells nanomechanical properties) to the usual biological responses previously investigated. Titanium increased the elasticity more than Cobalt nanoparticles even though Titanium demonstrated less cytotoxicity; the smaller nanoparticles had a greater impact on the viability of the cells as well as on the adhesion forces produced by the exposed cells. These mechanical changes are the result of alterations to the cytoskeleton as reported by the literature. Also, the smaller nanoparticles had a higher uptake which may be due to phagocytosis for such smaller particles.

The results lend themselves to a novel idea of the importance of understanding the mechanical changes and their impact on normal cell function which have previously been underestimated. From the results, it is evident that increasing the concentration of wear debris increases the elasticity and spring constant of cells. On the other hand, increasing the number of particles reduces the adhesive properties observed which in turn may affect the spreading and hence proliferation of cells despite an increase in osteocalcin production for both metal nanoparticles as well as PMMA. These results suggest that physical stimulus can alter the normal function of a cell through potential changes in the cytoskeleton of the cell in a similar manner to that of biological responses;

therefore this study points out the importance of an holistically cell analysis i.e. not only from a biological stand point but also through mechanical mechanisms.

8.7 References

1. Sansone, V., D. Pagani, and M. Melato, *The effects on bone cells of metal ions released from orthopaedic implants. A review.* Clin Cases Miner Bone Metab, 2013. **10**(1): p. 34-40.

2. Abu-Amer, Y., I. Darwech, and J.C. Clohisy, *Aseptic loosening of total joint replacements: mechanisms underlying osteolysis and potential therapies.* Arthritis Research & Therapy, 2007. **9**(Suppl 1): p. S6-S6.

3. Kowandy, C., H. Mazouz, and C. Richard, *Isolation and analysis of articular joints wear debris generated in vitro.* Wear, 2006. **261**(9): p. 966-970.

4. Prokopovich, P., et al., *Spatial variation of wear on Charité lumbar discs.* Acta Biomaterialia, 2011. **7**(11): p. 3914-3926.

5. Ren, K., et al., Therapeutic intervention for wear debris-induced aseptic implant loosening. Acta Pharmaceutica Sinica B, 2013. **3**(2): p. 76-85.

6. Goodman, S.B., et al., Cellular profile and cytokine production at prosthetic interfaces. Study of tissues retrieved from revised hip and knee replacements. J Bone Joint Surg Br, 1998. **80**(3): p. 531-9.

7. Fang, H.W., et al., The potential role of phagocytic capacity in the osteolytic process induced by polyethylene wear particles. J Int Med Res, 2006. **34**(6): p. 655-64.

8. Vermes, C., et al., The potential role of the osteoblast in the development of periprosthetic osteolysis: Review of in vitro osteoblast responses to wear debris, corrosion products, and cytokines and growth factors. The Journal of Arthroplasty, 2001. **16**(8, Supplement 1): p. 95-100.

9. Lohmann, C.H., et al., Phagocytosis of wear debris by osteoblasts affects differentiation and local factor production in a manner dependent on particle composition. Biomaterials, 2000. **21**(6): p. 551-561.

10. Bahraminasab, M., et al., Aseptic loosening of femoral components – A review of current and future trends in materials used. Materials & Design, 2012. **42**(0): p. 459-470.

11. Behl, B., et al., Biological effects of Cobalt-chromium nanoparticles and ions on dural fibroblasts and dural epithelial cells. Biomaterials, 2013. **34**(14): p. 3547-3558.

12. Chiu, R., et al., Ultrahigh molecular weight polyethylene wear debris inhibits osteoprogenitor proliferation and differentiation in vitro. Journal of Biomedical Materials Research Part A, 2009. **89A**(1): p. 242-247.

13. Chiu, R., et al., Polymethylmethacrylate particles inhibit osteoblastic differentiation of MC3T3-E1 osteoprogenitor cells. Journal of Orthopaedic Research, 2008. **26**(7): p. 932-936.

14. Tee, S.-Y., A.R. Bausch, and P.A. Janmey, *The mechanical cell.* Current Biology, 2009. **19**(17): p. R745-R748.

15. Tee, S.-Y., et al., *Cell Shape and Substrate Rigidity Both Regulate Cell Stiffness.* Biophysical Journal, 2011. **100**(5): p. L25-L27.

16. Lim, C.T., E.H. Zhou, and S.T. Quek, *Mechanical models for living cells—a review.* Journal of Biomechanics, 2006. **39**(2): p. 195-216.

17. Schmidt, C., A.A. Ignatius, and L.E. Claes, *Proliferation and differentiation parameters of human osteoblasts on Titanium and steel surfaces.* Journal of Biomedical Materials Research, 2001. **54**(2): p. 209-215.

18. Helenius, J., et al., *Single-cell force spectroscopy.* J Cell Sci, 2008. **121**(Pt 11): p. 1785-91.

19. Cai, X., et al., Connection between biomechanics and cytoskeleton structure of lymphocyte and Jurkat cells: An AFM study. Micron, 2010. **41**(3): p. 257-262.

20. Dattani, R., *Femoral osteolysis following total hip replacement.* Postgraduate Medical Journal, 2007. **83**(979): p. 312-316.

21. Anselme, K., *Osteoblast adhesion on biomaterials.* Biomaterials, 2000. **21**(7): p. 667-681.

22. Anselme, K., et al., The interaction of cells and bacteria with surfaces structured at the nanometre scale. Acta biomaterialia, 2010. **6**(10): p. 3824-3846.

23. Hunter, A., et al., Attachment and proliferation of osteoblasts and fibroblasts on biomaterials for orthopaedic use. Biomaterials, 1995. **16**(4): p. 287-295.

24. Kasza, K.E., et al., Filamin A is essential for active cell stiffening but not passive stiffening under external force. Biophys J, 2009. **96**(10): p. 4326-35.

25. Pelham, R.J. and Y.-l. Wang, High Resolution Detection of Mechanical Forces Exerted by Locomoting Fibroblasts on the Substrate. Molecular Biology of the Cell, 1999. **10**(4): p. 935-945.

26. Harris, A.K., P. Wild, and D. Stopak, *Silicone rubber substrata: a new wrinkle in the study of cell locomotion.* Science, 1980. **208**(4440): p. 177-9.

27. Orriss, I., et al., Bone-forming cultures of rat and mouse calvarial osteoblasts: key differences in protocols, in European Calcified Tissue Society Congress 2013, B. Abstracts, Editor. 2013, ECTS: Lisbon, Portugal.

28. Czekanska, E.M., et al., *In Search of an Osteoblast Cell Model for In Vitro Research.* European Cells and Materials, 2012. **24**: p. 1-17.

29. Ecarot-Charrier, B., et al., Osteoblasts isolated from mouse calvaria initiate matrix mineralization in culture. J Cell Biol, 1983. **96**(3): p. 639-43.

30. Perni, S., M.G. Kong, and P. Prokopovich, Cold atmospheric pressure gas plasma enhances the wear performance of ultra-high molecular weight polyethylene. Acta Biomaterialia, 2012. **8**(3): p. 1357-1365.

31. Prokopovich, P., et al., A novel bone cement impregnated with silver-tiopronin nanoparticles: its antimicrobial, cytotoxic, and mechanical properties. Int J Nanomedicine, 2013. **8**: p. 2227-37.

32. Prokopovich, P., et al., *Potent antimicrobial activity of bone cement encapsulating silver nanoparticles capped with oleic acid.* Journal of Biomedical Materials Research Part B: Applied Biomaterials, 2015. **103**(2): p. 273-281.

33. Gregory, C.A., et al., An Alizarin red-based assay of mineralization by adherent cells in culture: comparison with cetylpyridinium chloride extraction. Analytical Biochemistry, 2004. **329**(1): p. 77-84.

34. Preedy, E.C., et al., *Adhesive forces and surface properties of cold gas plasma treated UHMWPE.* Colloids Surf A Physicochem Eng Asp, 2014. **460**: p. 83-89.

35. Sader, J.E., et al., *Spring constant calibration of atomic force microscope cantilevers of arbitrary shape.* Review of Scientific Instruments, 2012. **83**(10): p. 103705-103705-16.

36. Sader, J.E., et al., *Method for the calibration of atomic force microscope cantilevers.* Review of Scientific Instruments, 1995. **66**(7): p. 3789-3798.

37. Ingham, E. and J. Fisher, *Biological reactions to wear debris in total joint replacement.* Proc Inst Mech Eng H, 2000. **214**(1): p. 21-37.

38. Prokopovich, P., Interactions between mammalian cells and nano- or micro-sized wear particles: Physico-chemical views against biological approaches. Advances in Colloid and Interface Science, 2014. **213**(0): p. 36-47.

39. Wimhurst, J.A., R.A. Brooks, and N. Rushton, *The effects of particulate bone cements at the bone-implant interface.* The Journal of Bone and Joint Surgery (Br), 2001. **83**(B): p. 588-92.

40. da Rosa, E.L.S., Kinetic effects of TiO(2) fine particles and nanoparticles aggregates on the nanomechanical properties of human neutrophils assessed by force spectroscopy. BMC Biophysics, 2013. **6**: p. 11-11.

41. Grassian, V.H., et al., Inflammatory response of mice to manufactured Titanium dioxide nanoparticles: Comparison of size effects through different exposure routes. Nanotoxicology, 2007. **1**(3): p. 211-226.

42. Harmand, M.F., In vitro study of biodegradation of a Co-Cr alloy using a human cell culture model. J Biomater Sci Polym Ed, 1995. **6**(9): p. 809-14.

43. Yao, J., et al., *Suppression of osteoblast function by Titanium particles.* J Bone Joint Surg Am, 1997. **79**(1): p. 107-12.

44. Chiu, R. and S.B. Goodman, Biological Response of Osteoblasts and Osteoprogenitors to Orthopaedic Wear Debris, in Osteogenesis - Biochemistry, Genetics and Molecular Biology, L. Yunfeng, Editor. 2012: CC BY.

45. Darling, E.M., et al., Viscoelastic properties of human mesenchymally-derived stem cells and primary osteoblasts, chondrocytes, and adipocytes. Journal of Biomechanics, 2008. **41**(2): p. 454-464.

46. Thoumine, O., O. Cardoso, and J.J. Meister, Changes in the mechanical properties of fibroblasts during spreading: a micromanipulation study. Eur Biophys J, 1999. **28**(3): p. 222-34.

47. Domke, J., et al., Substrate dependent differences in morphology and elasticity of living osteoblasts investigated by atomic force microscopy. Colloids and Surfaces B: Biointerfaces, 2000. **19**(4): p. 367-379.

48. Docheva, D., et al., Researching into the cellular shape, volume and elasticity of mesenchymal stem cells, osteoblasts and osteosarcoma cells by atomic force microscopy. Journal of Cellular and Molecular Medicine, 2008. **12**(2): p. 537-552.

49. Bhadriraju, K. and L.K. Hansen, *Extracellular Matrix- and Cytoskeleton-Dependent Changes in Cell Shape and Stiffness.* Experimental Cell Research, 2002. **278**(1): p. 92-100.

50. Moutzouri, A.G. and G.M. Athanassiou, *Insights into the Alteration of Osteoblast Mechanical Properties upon Adhesion on Chitosan.* BioMed Research International, 2014. **2014**: p. 8.

51. Kwon, S.Y., et al., Alterations in the adhesion behavior of osteoblasts by Titanium particle loading: inhibition of cell function and gene expression. Biorheology, 2001. **38**(2-3): p. 161-83.

52. Alves, R., D, A, M, Osteoblast Differentiation and Bone: Relevant proteins, regulatory processes and the vascular connection, in Department of Internal Medicine. 2012, Erasmus University Rotterdam: Ipskamp Drukkers. p. 166.

53. Bacabac, R.G., et al., *Round versus flat: Bone cell morphology, elasticity, and mechanosensing.* Journal of Biomechanics, 2008. **41**(7): p. 1590-1598.

54. Assoian, R.K. and E.A. Klein, *Growth control by intracellular tension and extracellular stiffness.* Trends in Cell Biology, 2008. **18**(7): p. 347-352.

55. Kwon, S.Y., et al., *Titanium particles inhibit osteoblast adhesion to fibronectin-coated substrates.* Journal of Orthopaedic Research, 2000. **18**(2): p. 203-211.

56. Goodman, S.B., et al., *Effects of orthopaedic wear particles on osteoprogenitor cells.* Biomaterials, 2006. **27**(36): p. 6096-6101.

57. Goodman, S.B. and T. Ma, *Cellular chemotaxis induced by wear particles from joint replacements.* Biomaterials, 2010. **31**(19): p. 5045-5050.

58. Keegan, G.M., I.D. Learmonth, and C.P. Case, Orthopaedic metals and their potential toxicity in the arthroplasty patient: A REVIEW OF CURRENT KNOWLEDGE AND FUTURE STRATEGIES. Journal of Bone & Joint Surgery, British Volume, 2007. **89-B**(5): p. 567-573.

59. Kadoya, Y., et al., Bone formation and bone resorption in failed total joint arthroplasties: histomorphometric analysis with histochemical and immunohistochemical technique. J Orthop Res, 1996. **14**(3): p. 473-82.

60. Anonymous. *Bioactivity of Osteoblasts to Wear Debris Generated From Orthopedic Devices*. 1999; Available from: http://biomed.brown.edu/Courses/BI108/BI108_1999_Groups/THRdebris_Team/gordon.html.

61. Lohmann, C.H., et al., Ceramic and PMMA particles differentially affect osteoblast phenotype. Biomaterials, 2002. **23**(8): p. 1855-1863.

62. Dean, D.D., et al., Ultrahigh molecular weight polyethylene particles have direct effects on proliferation, differentiation, and local factor production of MG63 osteoblast-like cells. J Orthop Res, 1999. **17**(1): p. 9-17.

63. Dean, D.D., et al., The effect of ultra-high molecular weight polyethylene wear debris on MG63 osteosarcoma cells in vitro. J Bone Joint Surg Am, 1999. **81**(4): p. 452-61.

Chapter 9 Cobalt and Titanium nanoparticles Influence on Human Osteoblast-like (Saos-2) Cell Elasticity, Spring constant and Calcium Production Activity-validation approach

9.1 Abstract

Bone cells are dynamic in nature actively adapting to their environment, responding to any damage influenced by wear debris produced over the life time of an artificial hip implant. Wear debris not only causes osteolysis of bone material surrounding an implanted device but also affects the structural integrity of the implanted device resulting in aseptic loosening; aseptic looseing is the primary cause of implantation failure.

It is also essential for successful longevity of an implant for effective osseointegration to take place, through the adhesion and growth of new bone cells produced by osteoblast cells. Alterations to this process affect the normal proliferation, differentiation, survival, and functionality of the osteoblast cells potentially interfering with the integration of mature bone cells interacting with the biomedical implant.

The following study was conducted to investigate the disadvantageous effects that wear debris impact on Saos-2 human osteoblast-like cells, and to validate previous work demonstrating the influence of wear debris on mouse MC3T3-E1 osteoblast cells. Similarly, to the earlier study, both Cobalt and Titanium nanoparticles of the same size will be used to explore the nanomechanical (elastic and spring constant) properties of osteoblasts, as well as the adhesive characteristics of cells after exposure to the metal nanoparticles. For comprehensive data, the viability of cells was also investigated using the MTT and LDH assays; the mineralisation output of the cells was also recorded using alizarin red protocol after 21 days of growth. It is essential to understand whether the prior study on mouse cells was a useful model to predict the

implications of wear debris on the mechanical aspects of cells, as well as investigating these features for the first time on human Saos-2 cell line.

9.2 Introduction

Bone is a unique living tissue with its strength determined by its composition and structure (1). It must be stiff, flexible as well as light enabling movement and to manage the loading processes by resisting deformation (1, 2);interestingly bone is a dynamic material and actively responds to external signals, location and responds to damage by removing or replacing the affected sections (2). The construction (modelling of new bone) and reconstruction (remodelling of damaged bone) of bone modelling is governed by cellular mechanisms changing the characteristic shape and size of the new bone deposited with osteoblasts and osteoclasts being responsible for these actions (1). There are three distinct bone cell types: osteoblasts, osteoclasts, and osteocytes; these are bone forming, resorbing, and osteoblasts that are entombed in the bone matrix (1-3).

Osteoblasts are essential cells for bone remodelling and are involved in the synthesis of bone matrix deposition (4). This is of utmost importance in osseointegration, a procedure of mature bone deposition onto implanted biomedical devices such as those used in total hip arthroplasty (5); and is governed by osteoblasts. These cells originate from mesenchymal cells maturing to osteoblasts which are actively involved in the constantly dynamic process of bone remodelling, especially in bone forming procedures (2, 4). It has also been highlighted that osteoblasts as well as osteoclasts play a role in

the regulation of bone resorption by balancing the differentiation and fusion of osteoclasts (2) to form new bone.

Disruption to this normally balanced well regulated process affects the proliferation, differentiation, function and survival of osteoblasts which inherently can affect the integration of an implanted biomedical device with the surrounding bone (3); often resulting in osteolysis and aseptic loosening of the new joint (6). Although mentioned that bone formation is a multicellular process, yet it is the effects induced to osteoblast cells which ultimately affect the osteoblastic lineage impacting on osseointegration (6). Osteoblasts not only create new bone, but also maintain the structural skeleton of the cells (2).

In this study, Saos-2 cell line was used as a model for human osteoblast-like cells. The cell line was derived from human osteosarcoma cells, and possesses many osteoblastic features useful as a source of bone-related molecules as human osteoblastic-like cells (4, 7, 8). Some features include the expression of certain receptors which aid in the organisation of cell-matrix and alkaline phosphatase (ALP) activity and produce bone matrix proteins (4, 7).

There have been many studies (9-13) into the effect of wear particle exposure on Saos-2 cells. For instance, Allen *et al* (1997) (13) studied the release of cytokines after exposure of two human cell lines (Saos-2 and MG-63) to Cobalt, chromium and Cobalt-chromium alloy. The authors (13) demonstrated that these metal particulates affected the growth and metabolism of osteoblastic cells *in vitro*. It is also suggested that a reduction in osteoblastic activity at the bone-implant interface may induce aseptic loosening affecting the longevity of the device. More recently, another study (14) observed a reduction in

osteoblastic activity through biological responses suggesting that Cobalt and chromium ions are responsible for the altered activity on Saos-2 osteoblast-like cells.

Contrary to all this information available in open literature, regarding the damage caused from the wear debris produced by implanted devices, there is a lack of understanding in the changes of nanoscale, structural and nanomechanical properties of Saos-2 cells post-exposure to wear debris. The present study aims at validating the methods developed in previous chapters concerning the measurement of nanomechanical and adhesive properties of mouse osteoblast cells; and employing these methods to study the elastic and adhesive properties of the human osteoblast-like Saos-2 cells post exposure to Cobalt and Titanium nanoparticles of a fixed size, 30nm. Additionally, metabolic activity (LDH and MTT), calcium production activity of these cells, and the cell uptake were compared with nanomechanical data.

9.3 Materials and Methods

9.3.1 Cell Culture

Saos-2 human osteosarcoma osteoblast-like cells (ATCC® HTB-85) were cultured in Roswell Park Memorial Institute (RPMI)-1640 media, supplemented with 10% (v/v) Heat Inactivated Foetal Bovine Serum (HI-FBS), 1% (v/v) of solution penicillin (5000 U/mL) and streptomycin (5000 mg/mL) (Gibco Invitrogen). To passage and count cells, trypsin (Gibco Invitrogen) was used when the cells were 70% confluent, and cells were maintained at 37^{o}C, with 5% CO_2 humidified atmosphere.

The cells were seeded in 24-well plates at a density of 60,000 cells per well to measure nanomechanical and adhesive properties by the atomic force microscope (AFM), and were cultured for 24 hours on sterilised polystyrene slides situated inside each well before Co or Ti nanoparticle exposure. For cell uptake, osteoblast mineralisation ability, LDH and MTT assay the cell preparations were conducted in the same way.

9.3.2 Nanoparticles

Co and Ti nanoparticles employed in this study were purchased from Sigma Aldrich, UK. Both nanoparticles were elemental with size of 30nm. All nanoparticles were weighed and suspended in Roswell Park Memorial Institute (RPMI)-1640 medium to make a stock solution of 5mg/ml. From the stock solution (5mg/ml), concentrations of 5, 50, 250, 500, and 1000 µg/ml were obtained.

9.3.3 Metabolic activity assay

To determine the effects of the metal nanoparticles on human osteoblast-like (Saos-2) cells viability, MTT (3-(4,5-dimethylthiazol-2yl)-2,5-diphenyltetrazolium bromide) and Lactate dehydrogenase (LDH) assay were used (Sigma, UK). MTT is a colorimetric assay of cell viability and depend on the metabolic activity of the cell. For this assay, cells were cultured as usual and exposed to the various concentrations of metal nanoparticles as stated above in 24-well plates; after the required exposure time, 80 µl of MTT stock solution, a phenol red-free medium, was added to each well and incubated for 4 hours at $37^{o}C$ in a humidified atmosphere containing 5% CO_2. Formazan is the metabolised MTT which is re-suspended with 800 µl of dimethyl sulfoxide (DMSO); 200 µl of this

suspension was transferred to a 96-well plate to read at 560nm absorbance using a spectrophotometer (ELISA Reader Labtech LT-500MS). A cell suspension unexposed to any metal nanoparticles was used as the control i.e. untreated, with all samples performed in triplicates using metal concentrations of Cobalt and Titanium nanoparticles (5, 50, 250, 500, and 1000 µg/ml).

LDH assay is an enzyme which converts sugars into energy for cellular use, damage to cells can therefore be assessed using the total LDH levels, an elevation is a sign of damage to the cells. Initially cells are prepared as usual and exposed to the nanoparticles, at each given time point the LDH levels were analysed. The LDH release levels must first be prepared by removing 25µl of the medium from each well of the 24-well plate and placed into a 96-well plate; an enzymatic assay is then used consisting of 50 µl of the pre-prepared LDH mix. LDH mix is a solution made up of three components: a) LDH assay substrate solution; b) LDH assay dye solution; and c) LDH assay cofactor preparation. Once the LDH mix has been added to each well, the well plate is then placed in the dark for 30 minutes to read the absorbance at 490nm and then at 690nm for correction purposes using a spectrophotometer (ELISA Reader Labtech LT-500MS) . For the total LDH levels, 100 µl of LDH assay lysis is added to each well of the 24-well plate and replaced in an incubator at 37 ^{o}C for 45 minutes; 25 µl of this medium is removed, and placed in a 96-well plate to continue with the enzymatic release.

9.3.4 Osteoblast mineralisation activity

Human osteoblast-like (Saos-2) cells were grown and exposed to the metal nanoparticles (Co and Ti) for a 21 day period. Every three days the medium

was changed and nanoparticles were added. After 21 days, the medium was removed from all wells, 10% (v/v) gluteraldehyde (Sigma Aldrich, UK) in sterile Phosphate Buffer Solution (PBS) (100 µl) was added and incubated for 10 minutes at 37^{o}C. All gluteraldehyde was removed from each well and washed three times with sterile PBS before 1% (v/v) Alizarin red staining (ARS) (Sigma Aldrich, UK) (100 µl) in distilled water was added to each well and placed in the incubator for 20 minutes. At 20 minutes, the ARS was removed and washed with Milli-Q water, and 10% Acetic acid (Sigma Aldrich, UK) (100 µl) and incubated for 30 minutes. After the allotted time, 50 µl from the wells were placed in a 96-well plate for absorbance measurements using a spectrophotometer (ELISA Reader Labtech LT-500MS) at a wavelength of 405nm (15). All mineralisation tests were performed in triplicates for each concentration (5, 50, 250, 500, and 1000 µg/ml) and for unexposed cells.

9.3.5 Zeta potential and size of nanoparticles measurements

Dynamic light scattering (DLS) was used to confirm the Co and Ti nanoparticle sizes and measure nanoparticle charges using Malvern Zetasizer Nano ZS Nano series (Malvern, UK). A stock solution (5mg/ml) for both Cobalt and Titanium nanoparticles was employ for these measurements.

9.3.6 Cell nanomechanical properties measurements

To determine the nanomechanical and adhesive properties of the cells, an Atomic Force Microscope (AFM) (XE-100 Advanced Scanning Probe Microscope (Park Systems, Korea) was used with experiments conducted in an open liquid cell using sterile PBS as the aqueous phase, previously described (16). A triangular tipless cantilevers (Bruker, UK) and a nominal spring

constants ($K_{cantilever}$) of 0.1 N/m were used; the actual spring constant of the AFM cantilever was determined using the Sader method (17, 18). Borosilicate glass beads (10 μm in diameter) were glued onto the cantilever and served as cell indentor. After preliminary tests to prevent indentation depths greater than 400-500 nm, a maximum load of 4nN was applied, with the working load set at 2nN. For each sample, at least 15 cells were analysed at each concentration of nanoparticles (5, 50, 250, 500, and 1000 μg/ml), for each time point (24, 48, and 72 hours). Firstly, cells were located with at least 20 approaching and retracting z-piezo coordinates vs. deflection curves were extracted from randomly selected points on the surface of each cell whilst avoiding the peri-nuclear area, and all experiments were performed in triplicates.

9.3.6.1 Cell elasticity and spring constant determination

The approaching part (trace) of the AFM curves was used to calculate the nanomechanical properties of the cells. The Young modulus of the cell surface location under investigation was determined fitting the Hertz model (Eq. 9-1) to the first part of the indentation vs. force curve after contact between AFM tip and cell surface.

$$F = \frac{4}{3}\frac{E}{(1-\nu^2)}\sqrt{R}\delta^{2/3} \qquad (9\text{-}1)$$

Where:

F = force recorded by AFM

E = Young modulus

R= radius of the spherical indentor (5 μm)

ν = Poisson ratio (set at 0.5)

δ = indentation depth

The spring constant of the cell surface in the location probed was determined through the slope of the curve after the Hertzian regime according to:

$$\mathrm{F} = k_{\mathrm{b}}\delta \tag{9-2}$$

Where:

F = force recorded by AFM

K_b = spring constant of the cell

δ = indentation depth

Both models require the determination of the separation between cell surface and AFM tip *(δ)*, this was calculated from the coordinates (z-piezo) of the trace curve assuming that the point of contact corresponded to the local minimum of force; from this:

$$\delta = \left|z - z_0\right| - d_{cant} \tag{9-3}$$

Where:

z_0 = z-piezo value of the minimum of the trace curve

z = z-piezo value of the trace curve

d_{cant} = cantilever deflection

δ = indentation depth

and

$$F = K_{Cantilever}\, d_{cant} \quad (9\text{-}4)$$

Both Eq. 1 and 2 were fitted to the data using the least squares method through an in-house written FORTRAN code.

Overall surface heterogeneity of nanomechanical properties was studied through the spatial distribution of E and K_b.

9.3.6.2 Cell Adhesion force

The adhesion forces between a cell and AFM tip were determined as the minimum value of the retracting (retrace) part of the AFM curve.

9.3.7 Cell uptake of metal nanoparticles quantification

Using inductively coupled plasma-mass spectroscopy (ICP-MS) Optima 2100DV OES (Perkin Elmer, Waltham, MA, USA) and standard element Primar 28, quantification of cells uptake of metal nanoparticles was determined. Cells were routinely grown and exposed to the relevant nanoparticles for the required time period. After the initial time point, all media was removed from each well and washed three times using sterile PBS; 500 µl of Nitric acid was added to each well, the 24-well plate was then placed in an incubator at 60 ^{o}C for 24

hours to digest the cells. The 24-well plate is then removed from the incubator after 24 hours, 400 µl of the suspension was removed and added to 8 ml of Milli-Q water in a polypropylene tube. The sample rate for the ICP-MS was 1.5 ml/min with characteristic wavelengths for each metal used: 288.616 nm, and 334.940 nm, for Cobalt and Titanium, respectively. Experiments were performed three times independently, and each composed of 3 parallel samples with results given as mean ± standard deviation.

9.3.8 Statistical analysis

Nanomechanical property comparison of the effects of Cobalt and Titanium nanoparticles on Human Osteoblast-like (Saos-2) cells was performed using ANOVA test followed by Tukey's post hoc test of individual pair of data sets ($p<0.05$). The comparison of adhesive force measurements used the Kruskal-Wallis test followed by Dunn's test post hoc for the individual pairs of data sets. All statistical analysis was performed using SPSS.

9.4 Results

9.4.1 Size and Charge of the nanoparticles

All zeta potentials and sizes of the nanoparticles are given in Table 9-1. Both metal nanoparticles had negative zeta potentials with Titanium nanoparticles displaying the lowest overall negative charge at -44mV and with Cobalt nanoparticles having a negative potential of around 20mV. The human osteoblast-like cells in growth medium also had a negative zeta potential of -7mV.

9.4.2 Metabolic activity

The metabolic activity (MTT data) of Saos-2 cells before and after exposure to Co and Ti nanoparticles for various time points is shown in Figure 9-1. After 24 hours all treated cells had a reduction in metabolic activity compared to the control cells, for both Cobalt and Titanium nanoparticles. The decrease was similar for both Cobalt nanoparticles treated and Titanium nanoparticles treated cells, with a drop from 0.3 OD for the controlled cells to 0.28OD at the initial concentration of 5 µg/ml. After the initial decrease in viability, a steady increase in cell viability was observed with increasing concentration of nanoparticle exposure. At 250 µg/ml concentration, the viability for both Cobalt and Titanium nanoparticles was recorded at 0.2 OD, rising to 0.25 OD at a concentration of 500 µg/ml; this level remained the same for Cobalt nanoparticles and slightly higher at 0.29OD for Titanium nanoparticles at the highest concentration of 1000 µg/ml. All values of viability for both nanoparticles were lower than the control cells.

Table 9-1. Zeta potential and size of nanoparticles and zeta potential of Saos-2 cells measured in media solution along with their pH values.

Nanoparticles	pH	Zeta Potential (mV)	Size (nm)
Co 30nm	8.33	-19.4±1.0	27.3±2.1
Ti 30nm	7.07	-44.7±1.9	27.7±3.5
Human Osteoblast-like (Saos-2) cells		-7.70±0.6	

After 48 hours, the overall viability values decreased for both untreated and treated cells, as the control (untreated) also fell to a value of 0.16 OD. A slight decrease was observed in viability for Cobalt nanoparticle at the lowest concentration of 5 µg/ml to 0.14 OD, which remained the same at a concentration of 50 µg/ml. An increase occurred at 250 µg/ml to 0.15 OD the same as the control, which increased again to 0.17 OD at 500 µg/ml, and a big increase to 0.23 OD at the highest concentration of 1000 µg/ml. After exposure to Titanium nanoparticles the optical density (OD) also decreased slightly to 0.19 OD at the lowest concentration of 5 µg/ml, however for 50, 250 and 500 µg/ml the viability increased to 0.15 OD, similar to the control; and for the highest concentration of 1000 µg/ml a very slight increase was observed at 0.16 OD.

At the maximum exposure time of 72 hours, the control viability was 0.18 OD, a decrease was observed for Cobalt nanoparticles at the initial concentration of 5 µg/ml to 0.15 OD. This value remained for 50 µg/ml and 250 µg/ml. At the higher concentrations of 500 and 1000 µg/ml the viability increased dramatically 0.21 OD and 0.22 OD, respectively. After 72 hours the Titanium control was the same at 0.2 OD, this value decreased to 0.15 OD for the concentrations 5, 50, and 250 µg/ml; for both 500 and 1000 µg/ml the viability was the same as the control at 0.16 OD. These values were similar to those at 48 hours.

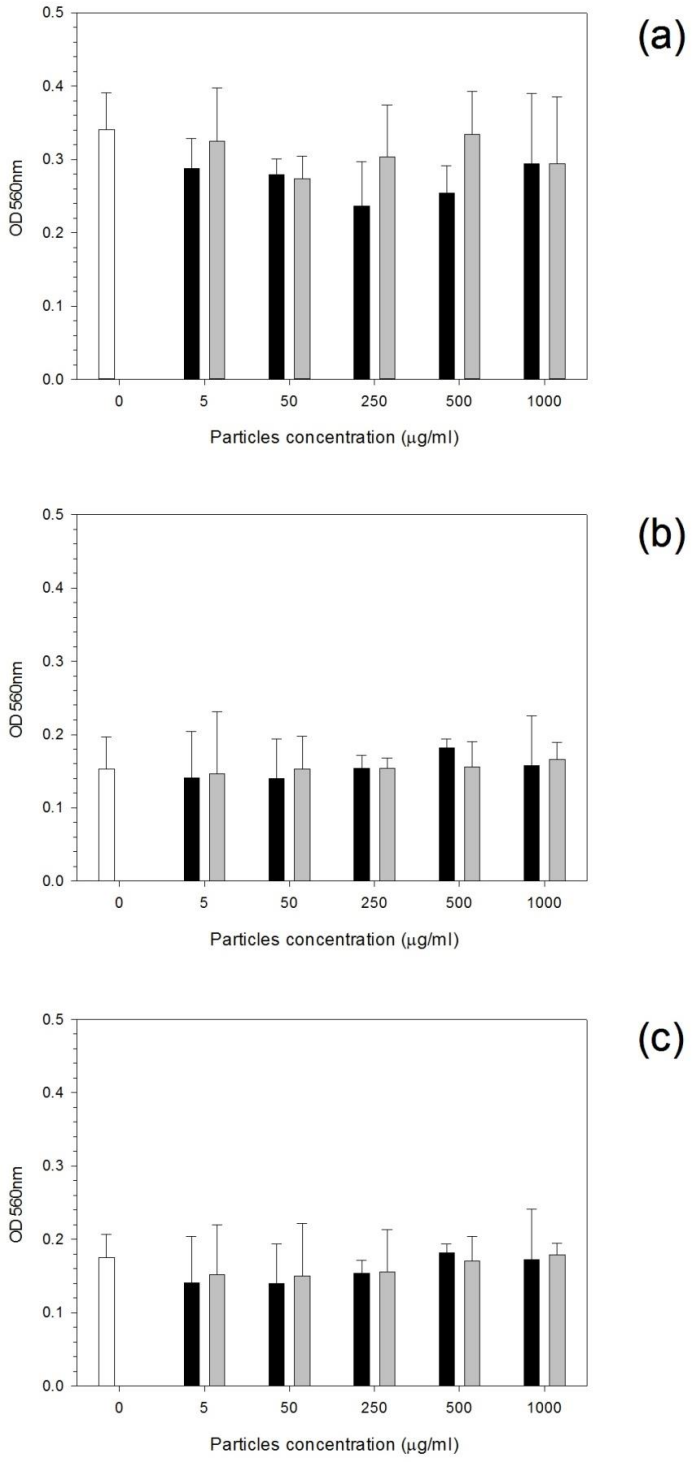

Figure 9-1. Cell Viability results (MTT assay) of Saos-2 cells exposed to Cobalt (black columns) and Titanium (grey columns) elemental nanoparticles at (a) 24h, (b) 48h, and (c) 72h.

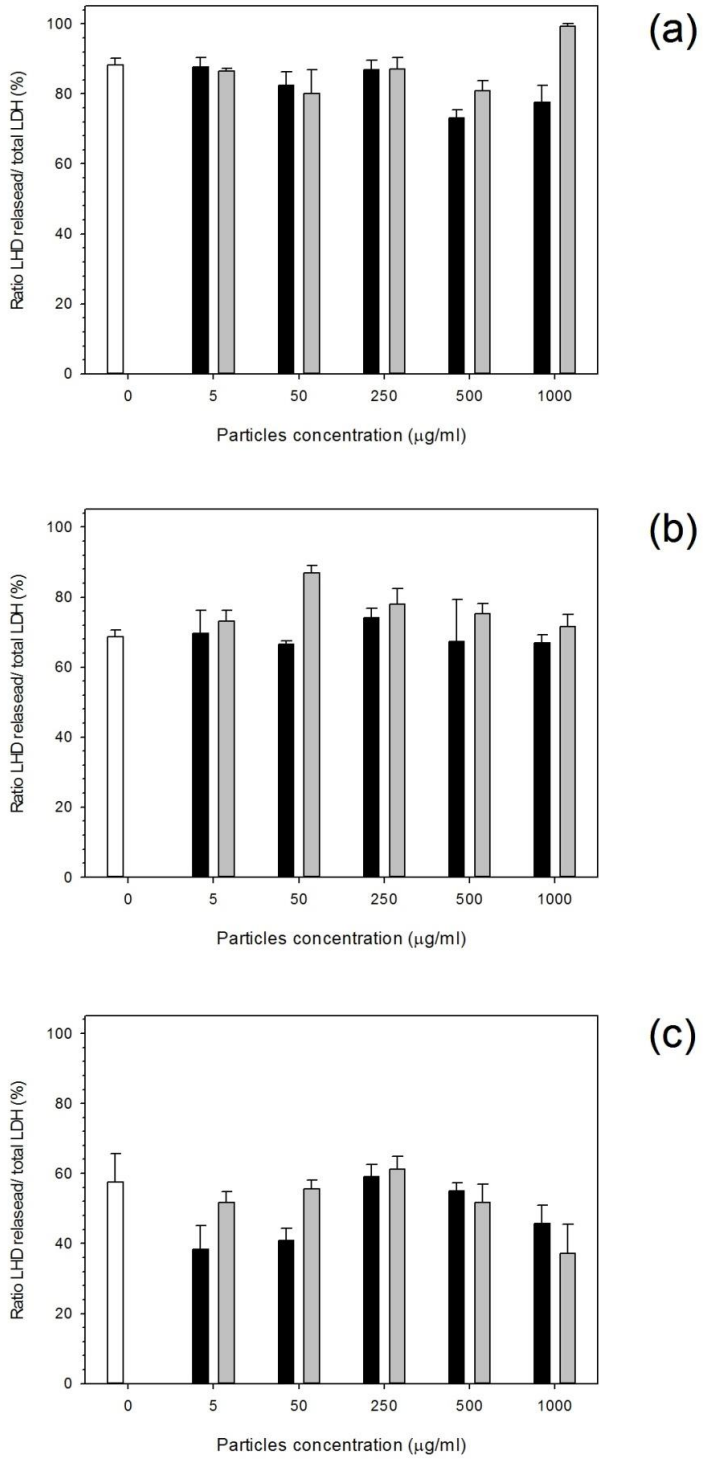

Figure 9-2. Cell Viability results (LDH assay) of Saos-2 cells exposed to Cobalt (black columns) and Titanium (grey columns) elemental nanoparticles at (a) 24h, (b) 48h, and (c) 72h.

LDH levels (Figure 9-2) after 24 hours did not change greatly for either particle: Cobalt or Titanium, with increasing concentration. A slight reduction was however observed with Cobalt nanoparticle exposure especially for the highest concentrations of 500 and 1000 µg/ml, with a reduction from 88% for the control cells to 72% at 500 µg/ml. On the other hand for Titanium, there was also a decrease in LDH level at 500 µg/ml to 80%, however, an elevation in LDH was demonstrated at the highest concentration of 1000 µg/ml to 100%.

At 48 hours, again Cobalt nanoparticle exposure had little to no alterations in LDH compared to the control, which has decreased to 68% this was consistent throughout for Cobalt regardless of concentration. Titanium nanoparticles remained the same as the control for the lowest concentration, but an increase was observed at a concentration of 50 µg/ml to 88%; this elevation decreased slightly with increasing concentration but still remained above the level of the control cells with levels of 80%, 76%, and 72% for 250,500, and 1000 µg/ml.

For 72 hours of exposure, the control cells decreased to 56%. All exposed cells LDH levels had decreased. At 5, and 50 µg/ml the Cobalt nanoparticles caused a decrease to 40%, this increased to 60% just above the control level at a concentration of 250 µg/ml; however the levels declined with increasing concentration of nanoparticles at 500, and 1000 µg/ml the levels were observed at 56% and 44%, respectively. A similar pattern was observed for Titanium nanoparticles, with an initial decline in LDH levels compared to the control cells at 52% and 56% for concentrations of 5 and 50 µg/ml; a peak was recorded at 250 µg/ml to 60% which then decreases with increasing concentrations, with LDH levels at 52% and 36% at 500 and 1000 µg/ml.

9.4.3 Osteoblast mineralisation ability

To determine the mineralisation ability of the cells after exposure to nanoparticles the Alizarin red assay was used after 21 days of nanoparticle exposure. The control cells had an osteocalcin production value of 0.7 OD, shown in Figure 9-3. A general decrease in production was observed for both Cobalt and Titanium nanoparticles treated cells. For Cobalt nanoparticles the decrease began at the lowest concentration with a value of 0.6 OD at 5 µg/ml; at 100 µg/ml recorded the least amount of osteocalcin production at 0.19 OD. Titanium nanoparticles also reduced in osteocalcin production to 0.5 OD at 5 µg/ml, lower than Cobalt nanoparticles; the lowest osteocalcin production also decreased with increasing concentration with the lowest level observed at 0.2 OD at a concentration of 500 µg/ml.

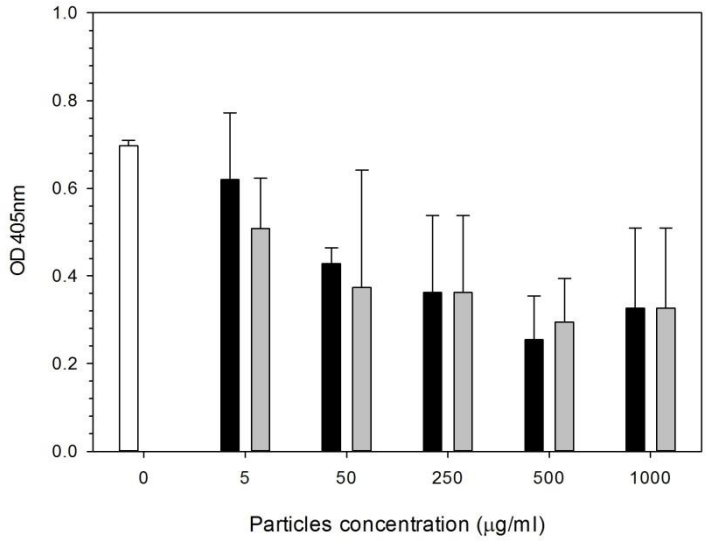

Figure 9-3. Saos-2 cells osteoblast mineralisation ability post exposure to Cobalt (black columns) and Titanium (grey columns) nanopartilces.

9.4.4 Nanomechanical properties

Elasticity and spring constant data are given in Figure 9-4 and Figure 9-5, respectively; each graph represents all time points that were measured at 24, 48, and 72 hours.

At 24 hours of metal nanoparticle exposure demonstrates that there is a general increase in elasticity i.e. the cells get stiffer with increasing concentrations of nanoparticles, and is especially pronounced for Cobalt elemental nanoparticles. The initial elasticity for the control cells were at 9 kPa, for the lowest concentration the elasticity increased to 11 kPa for both Cobalt and Titanium nanoparticles. A dramatic increase was observed at a concentration of 50 µg/ml for both Cobalt and Titanium nanoparticles to 17 kPa. A decrease in elasticity was then recorded for Cobalt nanoparticles, the result was a slight decline to 15kPa and 14kPa at 250 and 500 µg/ml concentrations, respectively, which then had risen to 18kPa at the highest concentration of 100 µg/ml. For Titanium on the other hand, the decline observed was more pronounced dropping to a similar value as the control to 10 kPa for both 250 and 500 µg/ml concentrations, increasing to 15 kPa at the highest concentration of 1000 µg/ml.

With time at 48 hours, the control cells remained consistent with an elastic modulus of 9 kPa, the same as the 24 hours. After exposure to Cobalt elemental nanoparticles the cells demonstrated no change in elasticity at a concentration of 5 µg/ml as observed at 9 kPa; the elastic modulus increased thereafter to 12 kPa for both 50 and 250 µg/ml concentrations. A further increase was then observed to 14OD at a concentrations of 500 µg/ml, then a slight decrease to 13 kPa at the highest concentration of 1000 µg/ml. Titanium

nanoparticles demonstrated a greater initial increase at a concentration of 5 µg/ml to 13 kPa, after this increase, a slight decrease was recorded at an elastic modulus of 12 kPa which remained the same regardless of the concentration the cells were exposed to.

Overall, at 72 hours, the elastic moduli increased. The control cells had an elastic value of 13.5 kPa greater than that recorded for the previous time points. After Cobalt nanoparticle exposure the cells demonstrated that at a concentration of 5 µg/ml increase in the elastic modulus compared to the control of 14 kPa; this continued to increase with higher concentrations of nanoparticles to 19 kPa for 50 µg/ml concentration, 22 kPa at 250 µg/ml, 23 kPa at a concentration of 500 µg/ml which remained the same at a concentration of 1000 µg/ml. Similarly, after Titanium nanoparticle exposure at 48 hours, the exposure at 72 hours had an initial increase in elasticity at 17 kPa with a 5 µg/ml concentration which remained the same for 50 and 250 µg/ml concentrations; however, another increase is recorded for the higher concentrations of 500 and 1000 µg/ml with an observed elasticity of 19 kPa.

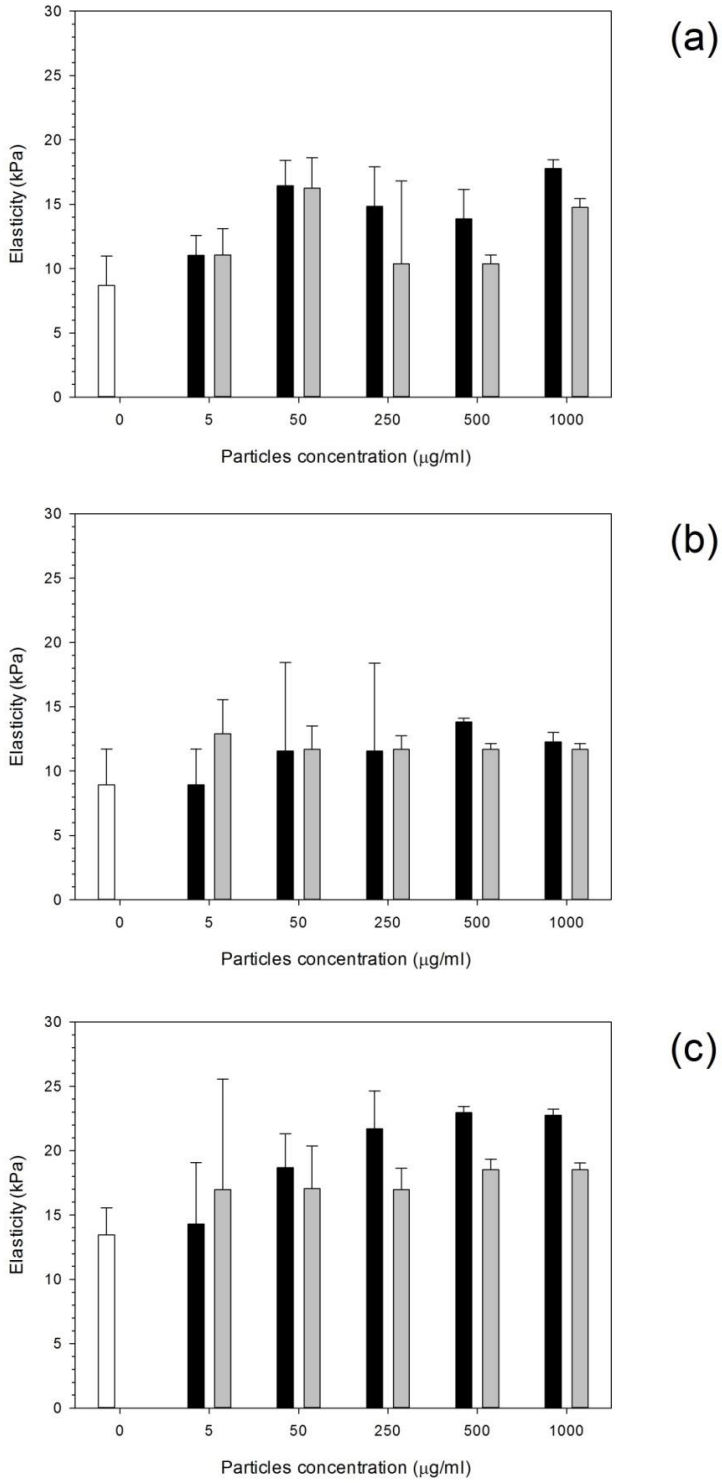

Figure 9-4. Mean cell elasticity of SAOS-2 cells exposed to Cobalt (black columns) and Titanium (grey columns) nanoparticles at three time points: (a) 24h, (b) 48h, and (c) 72h.

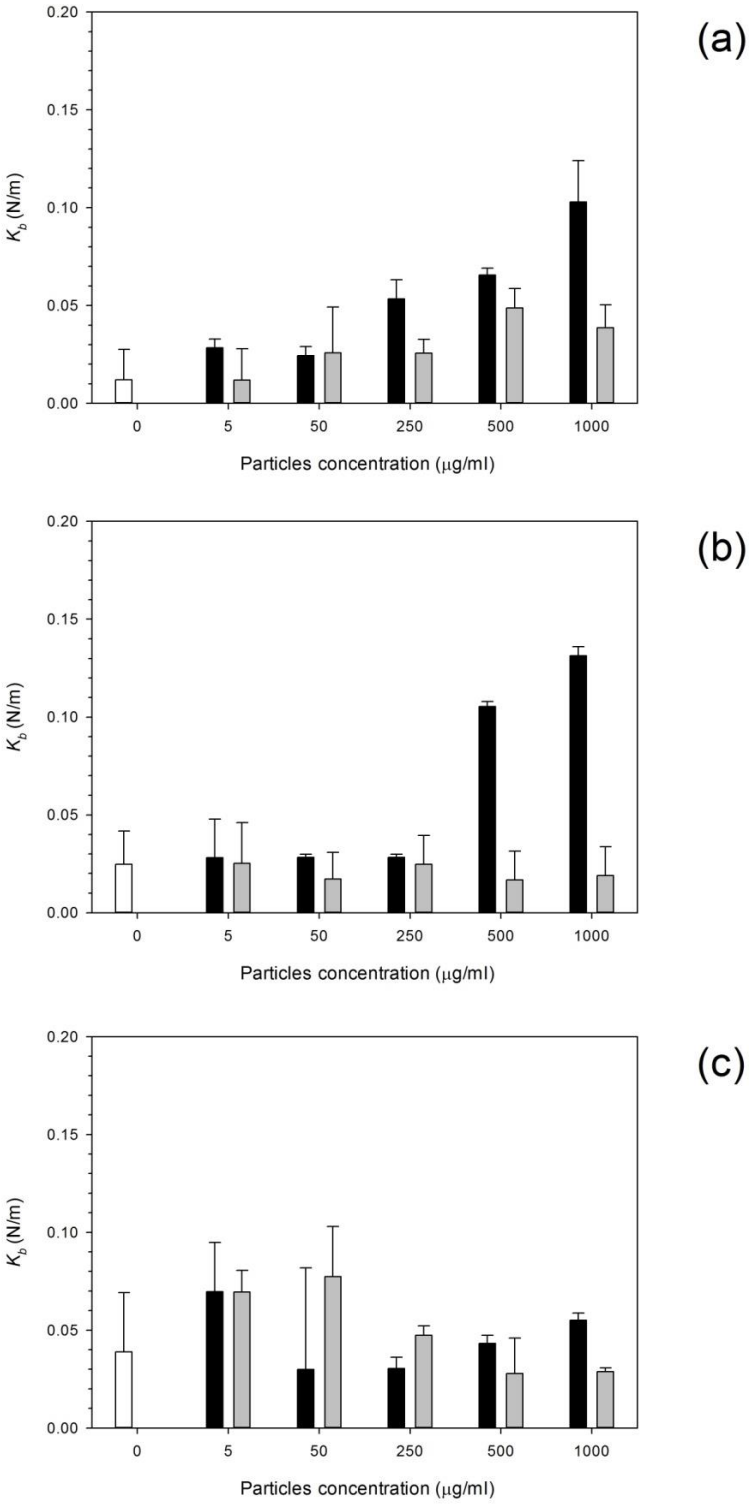

Figure 9-5. Median spring constant of SAOS-2 cells exposed Cobalt (black columns) and Titanium (grey columns) nanoparticles at each time point: (a) 24h, (b) 48h, and (c) 72h.

Figure 9-5 represents the spring constant results for both Cobalt and Titanium nanoparticle exposure. At 24 hours, an obvious increase in spring constant was recorded with increasing concentration for both nanoparticles. The control spring constant was recorded at a value of 0.01N/m; for Cobalt nanoparticles this value increased to 0.03 N/m at a concentration of 5 µg/ml, which remained the same for a concentration of 50 µg/ml. At the highest concentrations of 250, 500, and 1000 µg/ml the spring constant values continued to increase to 0.05, 0.07, and 0.10 N/m, respectively. Titanium nanoparticle exposure also demonstrated a general increase in spring constant values but at smaller values than Cobalt nanoparticles; for 5 µg/ml concentration the spring constant of the exposed cells was the same as the control value of 0.01 N/m, increasing to 0.03 N/m for concentrations of 50 and 250 µg/ml; at 500 µg/ml gave a spike at 0.05 N/m which decreased to 0.04N/m at 1000 µg/ml.

A similar pattern was observed for Cobalt nanoparticles exposed cells after 48 hours, but no change was recorded for Titanium nanoparticles. The control cells spring constant had increased to 0.02 N/m which remained the same value for both Cobalt and Titanium nanoparticles at the lowest concentration of 5 µg/ml. For Cobalt nanoparticles the spring constant of the cells remained at 0.03 N/m for 50 and 250 µg/ml concentrations, and a dramatic increase was demonstrated at a concentration of 500 and 1000 µg/ml at values of 0.11 and 0.13 N/m. For the Titanium nanoparticles treated cells the values for the spring constant with increasing concentration remained between 0.02 and 0.03 N/m.

After 72 hours exposure to nanoparticles, demonstrated a large increase at the initial concentration of 5 µg/ml at 0.07 N/m for both Cobalt and Titanium

nanoparticles, the control cell value also increased compared to the first 2 days of exposure to 0.04 N/m. However, after the initial increase a decline was observed for Cobalt nanoparticle exposure at 50 µg/ml to 0.03 N/m, this value steadily increased with increasing concentration of nanoparticles to 0.035 N/m at 250 µg/ml, to 0.045 N/m at 500 µg/ml and at the highest concentration of 1000 µg/ml to 0.055N/m. Titanium nanoparticles also had the same initial value as Cobalt nanoparticles exposed cells (0.07N/m), this increased slightly to 0.08 N/m at a concentration of 50 µg/ml; however, this spring constant steadily decreased to 0.05 N/m at a concentration of 250 µg/ml, and decreased to a spring constant value of 0.03 N/m for both the highest concentrations of 500 an 1000 µg/ml.

9.4.5 Cell adhesion forces

For all cells, control cells (unexposed to nanoparticles), and exposed cells to Cobalt and Titanium nanoparticles adhesion data are given in Figure 9-6; the data demonstrated spatial distributions of adhesion forces on the cell surfaces.

At 24 hours, the median adhesive force recorded or the control cells was at 2.5 nN, the values for the Cobalt and Titanium nanoparticles exposed cells did not vary greatly from the control. There was an initial decrease in adhesion to 1 nN for both Cobalt and Titanium nanoparticles at the lowest concentration of 5 µg/ml; this value increased to 2 nN for Cobalt nanoparticles for all increased concentrations, however, for Titanium nanoparticles it remained at 1nN. After 48 hours, the control value of adhesion decreased to 1nN compared to 24 hours control; for cells exposed to Cobalt nanoparticles the range of values of adhesion increased with increasing concentration, with the highest adhesion

recorded at a concentration of 500 µg/ml at 2.5 nN. For cells exposed to Titanium nanoparticles, the range of data was less than for cells exposure Cobalt nanoparticles and the greatest adhesion was observed at 2.0 nN at a concentration of 5 µg/ml.

Three days of exposure demonstrated little to no change in adhesion force distribution for neither Cobalt nor Titanium exposed nanoparticles; the control value was the same as 48 hour control cells, and the adhesion forces remained at around 1nN for all Cobalt and Titanium nanoparticles exposed cells with nanoparticle increasing concentrations.

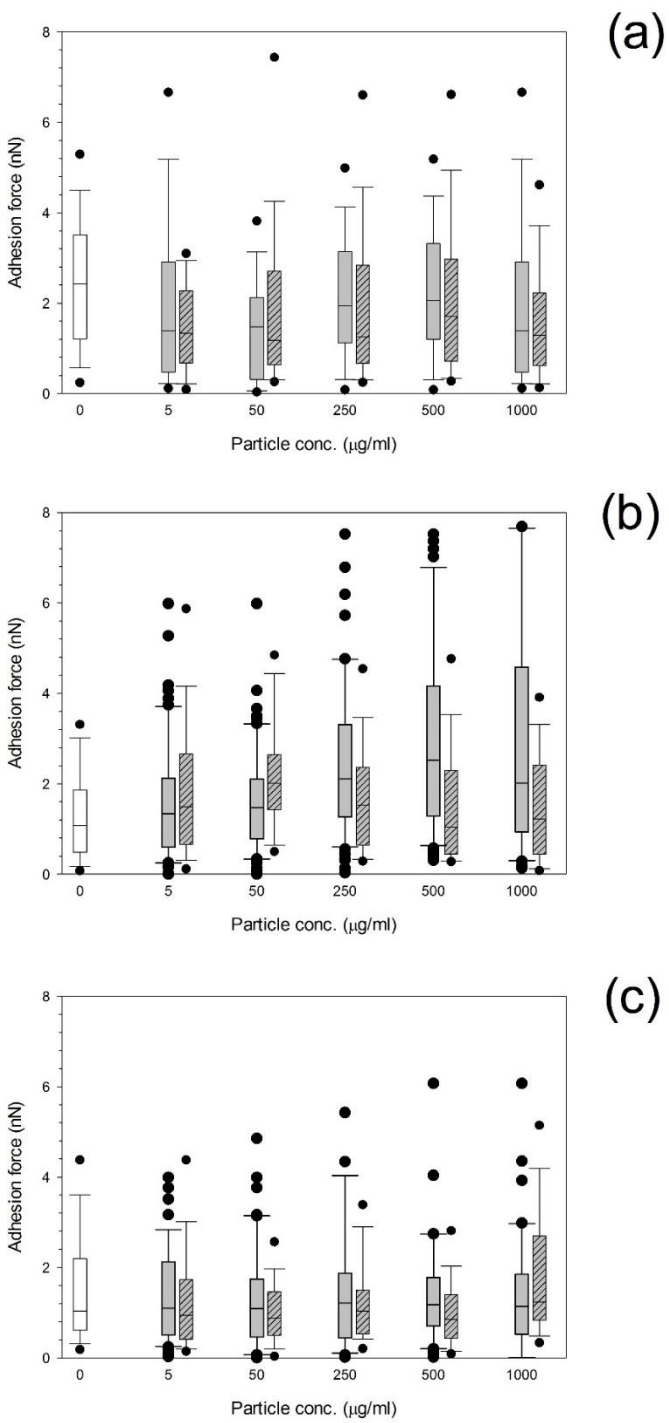

Figure 9-6 Box and whiskers plot of adhesion force distribution of Saos-2 cells exposed to Cobalt (un-patterned columns) and Titanium (patterned columns) nanoparticles for all time points (controls in white columns): (a) 24h, (b) 48h, and (c) 72h.

9.4.6 Metal uptake by cells

Metal uptake by cells data is shown in Figure 9-7. For all uptake data regardless of the metal used, the uptake generally increased with increasing concentration after all three exposure times. For Cobalt nanoparticles, the maximum uptake was observed after 48 hours for 500 and 1000 µg/ml concentrations at around 570 and 700 µg/10^6cell. For Ti nanoparticles, the overall uptake was around six fold smaller than Cobalt nanoparticles, again after 48 hours exposure to the metal particles, demonstarted a peak of uptake especially for a concentration of 500 µg/ml at around 90 µg/10^6cell. After Ti nanoparticles exposure the cells demonstrated the greatest uptake at 24 hours with the greatest concentration at 1000 µg/ml with an uptake of 110 µg/10^6cell. No statistical difference between data after 48 and 72 hours for both types of particles.

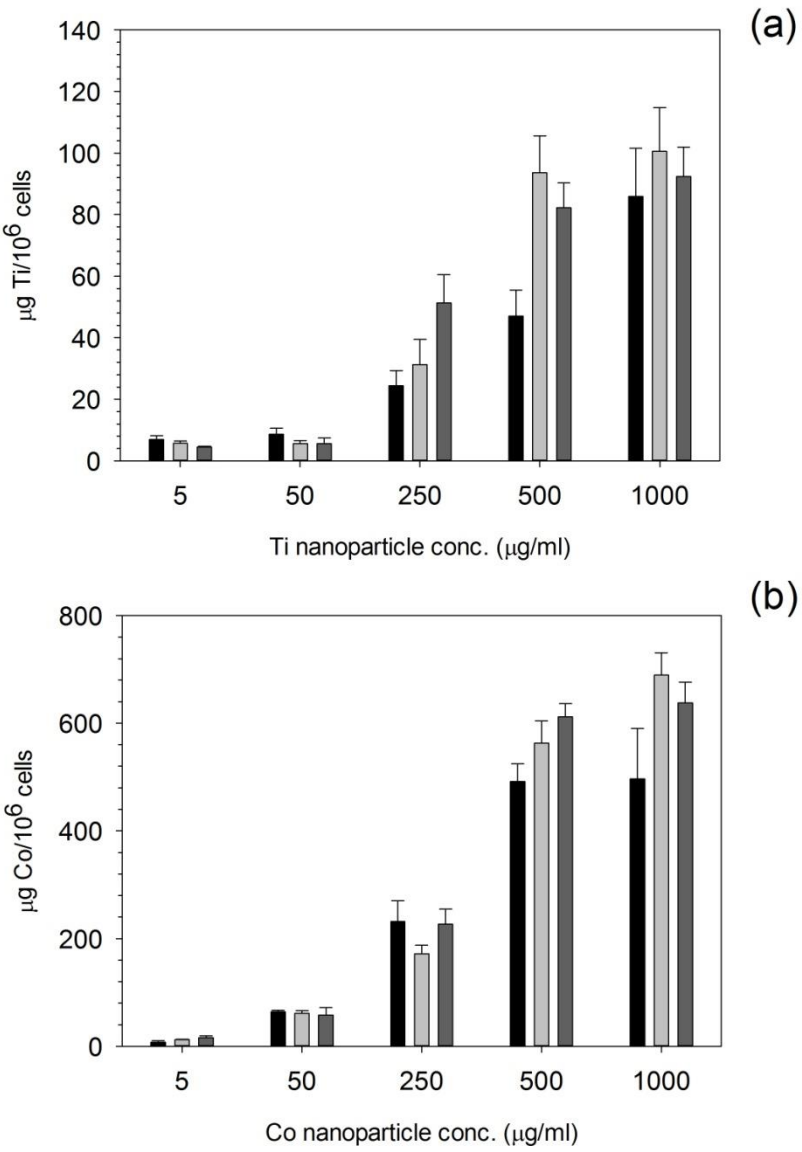

Figure 9-7. SaoS-2 uptake of Titanium (a) and Cobalt (b) ions from corresponding nanoparticles after exposure from 24 h (■), 48 h (■) and 72 h (■) at various nanoparticles concentrations.

9.5 Discussion

Many issues with the longevity of biomedical arthroplasty devices are due to the detection of metal particles that have been retrieved in surrounding tissues from

failed implants (20-22). These wear debris are produced over the lifetime of the device and is the major factor contributing to periprosthetic osteolysis, aseptic loosening (22), as well as increasing the risk of infection (23). Plenty of studies (20, 24-28) have investigated the biological impact of these wear particles on surrounding cells and tissues adjacent to the implantation site (29).

Wear debris originates from the components of an implanted device and often consists of metals, including their oxides (27). Cobalt and Titanium nanoparticles collected from explants resemble those used in this study (26, 30) with many stating sizes of below 100 nm; as well as the size, the shape, charge, composition and concentration range correlate with the literature (30-32). It is important to note the size of the particles as it has been recognized by others (26, 33) that phagocytosis governs the cellular uptake of particles (26). It has been noted (30) that the phagocytosis of particles correlated with the changes in morphology of the particles, and that the proliferation, and differentiation of cells was affected by the size, shape and dose of wear particles present (30). Suggestions have also been made (30) that particles less than 1 μm are more easily phagocytosed compared to larger counterparts, and longer particles induce stronger cellular reactions than round particles (30, 34, 35). Although Titanium is used in hip implants due to its beneficial characteristics such as being biocompatible with robust strength, evidence suggests that the length of the wear produced by Titanium and its chemical composition especially of the aggregated particles have previously been linked to toxicity within osteoblast cells (33, 36). In regards to Cobalt, results have demonstrated less tolerance with nanoparticles which even damage the DNA of osteoblast cells (30, 37) as

the size of the particles at the nanoscale greatly increase the total surface area of the metal. This causes an increase in the tendency for the metals to release ions (37); in turn the damage associated with ions inhibit cellular proliferation, and can induce apoptosis with damage from Cobalt occurring within one hour of exposure (30, 38). The concentrations used in this study (30, 39) was the same as the higher concentrations used in this investigation of 500 µg/ml with changes to the structural aberration taking place within the first 24 hours (38, 39) especially when concerning Co ions.

Previously it has been shown (40) that wear debris originating from Cobalt, Titanium, and Titanium alloys promote the proliferation in the synovial membrane of fibroblasts and so is an important factor in the production of fibrous membranes surrounding the prosthesis(40), demonstrating that metal particles influences the structural integrity of cells; as well as osteolysis occurring due to the phagocytosis of particles (29). In combination, these biological responses can indirectly weaken the mechanical properties and integrity of the implant resulting in aseptic loosening, impact failure and generally requiring revision surgery.

High doses of Titanium were used by Pioletti et al (1999) (29), with concentrations ranging from 0.01, 1.0 and up to 10 mg/ml, even so Titanium had no cytotoxic effect. Yet with chromium and Cobalt-chromium of similar concentrations did induce a cytotoxic effect (29); from this evidence, the notion that the viability of osteoblasts is adversely influenced by wear debris can be assumed, and so it is assumed that the rate of bone formation will also decrease. Expectantly, this was true for the results shown in this investigation,

for both Cobalt and Titanium exposed cells, as the bone mineralisation decreased with increasing concentration of nanoparticles after 21 days of growth. This loss of bone material formation around the implantation is the root cause of aseptic loosening due to the combination of bone loss and increased bone resorption when wear debris is present.

Pioletti et al. (1999) studied the direct and indirect effects of different Titanium particle concentrations on the viability of neonatal calvarial rat osteoblast cells (29) as well as identifying the type of cell death i.e. necrosis or apoptosis. The author observed a cytotoxic effect on osteoblasts using Titanium particles less than 5 µm in size; the cell viability was affected when the cells were in direct contact with the Titanium particles in a concentration-dependent manner. Also the authors found that particles in direct contact with cells began the process of phagocytosis, and the shape of the cells changed according to the size and number of particles ingested (29). Pioletti observed that the majority of particles were phagocytosed in the first 24 hours. This was true for Cobalt nanoparticles in the investigation of human osteoblasts, however, there was no great change in the viability of the cells exposed to Titanium and is supported by findings from Vandrovcova et al (2014) (41) using Titanium debris and its effects on the viability of Saos-2 cells; this could be dependent on their size as Pioletti et al. (1999) used particles less than 5 µm, whereas the above study only observed nanoparticles and not micro sized particles.

As Titanium is a commonly used material in biomedical implantations along with their alloys, due to its advantageous mechanical properties, resistance to corrosion (42) as well as its biocompatibility of the bulk material (22). Post

implantation, inflammatory cascades are initiated which stimulates the proliferation, differentiation and bone synthesis of bone forming osteoblasts, these cells are found in the tissues adjacent to the prosthesis and govern the preliminary stages of osseointegration, essential for the longevity of the device (22, 43). The metal particles; or wear debris also directly impact on the bone-implant interface reducing the activity of new bone formation which in turn lends itself to aseptic loosening. According to Dorr et al. (1996), retrieved particles are within the phagocytosable range of 1-10 μm (43).

Also, Pioletti et al (1999) observed rat osteoblast cells not human; this could have a difference due to the difference in growth rates of rat and human cells. It has been highlighted (44) that mouse and rat cells are affected by the age of the original specimen, with a study (45) discussing the differences in osteocalcin synthesis; the investigation demonstrated that younger models (taken 30-36 hours after birth) had 6 times more osteocalcin compared to older models (samples taken 78-84 hours after birth) (45). Similarly, mouse cells produced greater levels of osteocalcin compared to rat and human cells (44, 45). This could explain the elevated levels demonstrated by the mouse MC3T3-E1 osteoblasts in previous work as Cobalt and Titanium both induced an increase the production of osteocalcin, whereas a decrease in osteocalcin levels were recorded in this investigation using human osteoblast-like Saos-2 cells.

Interestingly, surface properties often govern the osseointegration of an implant (42). Osseointergration is essential for the longevity of a successful and stable implanted biomedical device, this interfacial interaction often depends on the

topography, roughness and chemical composition of the implanted device (23). The charge of all metal particles had a negative zeta potential, and it has been demonstrated (41) that negatively charged surfaces increased the attachment of osteoblasts, namely Saos-2, therefore the charge of all particles would have aided in the interactions between the wear debris and cells. Osteoblasts cells are the essential cells involved in their osseointegration as they synthesize and produce extracellular matrix (ECM) and control its mineralisation (23). Attachment and spreading of osteoblasts is the initial interactions of cells to implanted devices; and cellular behaviour is regulated by the attachment of cells especially when concerned with osteoblast and fibroblasts as these are anchorage dependent cells and need adherence for survival (23, 46). In this study the osteosarcoma cell line Saos-2 was used as a model to study the nanomechanical and adhesive properties of these cells to further understand the potential damage caused by the exposure of the cells to wear debris; this cell line has been previously used to model osteoblast-like behaviours such as cell attachment, spreading, proliferation, and differentiation (47-50). Others (51) suggest that the nanotopography of cells have an influence on cell behaviour governing the integrin clustering and focal adhesion assembly (51).

The mechanical properties of single cells have been measured using various techniques (52-55), some of which include rheometry with magnetic beads, optical traps, and AFM (52) techniques employed in this study. It has also been postulated that the overall function of osteoblasts is dependent on their adhesive interactions; these are governed by the binding integrins to the extracellular matrix (ECM) made of fibronectin and collagen type 1.

Furthermore, the ECM signals anchorage dependent cells by changing the local matrix stiffness (51), evidence of this has previously been observed using mesenchymal stem cells causing differentiation into specific lineage, for example, softer matrix induces neurogenic routes whereas stiffer matrices cause developments of myogenic and osteogenic phenotypes (51, 56, 57). Alterations to the ECM can influence further mechanical stimuli which impact on the cellular function for example, the growth, motility, survival, adhesion and contractility (58).

The cellular adhesion, spreading, and migration depend on these integrins (23) which rapidly bind to the actin cytoskeleton via focal adhesions which control the behaviour of the cells (59, 60). Not only do focal adhesion kinases (FAK) provide structural support which is essential to maintain adhesion to substrates, yet FAK also transduce stimuli to regulate adhesion, motility, proliferation, differentiation and survival (22, 59-61). Reorganisation of the actin cytoskeleton and microtubule stabilisation will take place in integrin-mediated activation of FAK, which are both essential for cell adhesion, motility and morphology. It is evident that osteoblasts maintain the structural integrity of the cells (2), and it has been noted that the elastic properties of these cells is directly linked to the cytoskeleton of osteoblasts (62, 63).

So, Saldana et al (2009) investigated the influence of metal particles on cell adhesive interactions using Titanium micro particles (1-15um) at a concentration of 10 ng/cell or 50 ng/cell. AlamarBlue is redox reaction which changes colour in response to metabolic activity and quantifies the cell proliferation as a function of viability using Saos-2 cells (22). It was also

stipulated that Titanium decreases the number of attached cells in a dose-dependent response at all time points measured. Titanium was also internalised by the Saos-2 cells (22), the actin and tubulin cytoskeleton were also disorganised, shortening the stress fibres, and disassembled the microtubules reducing the density of the tubulin. From the disruption to the structural integrity of the cells this inherently reduces the focal adhesion size (22). The micrometric size particles of Titanium decrease the osteoblast adhesion force, proliferation and production of procollagen and alkaline phosphate (22, 64), reducing the cell spreading thereby inhibiting cell migration and proliferation especially for Saos-2 cells. Moreover, this reduction in adhesive properties was also evident in this study.

Vandrovcova et al. (2014) also noted that the proliferation of human Saos-2 cells was lower when exposed to Titanium wear debris compared to the primary human cells, furthermore, the actin-cytoskeleton was more pronounced and better-developed with exposure to wear debris demonstrating that cells become stiffer and were also associated with less proliferation compared to mouse osteoblast cells (41). Other studies have also used AFM techniques to investigate the stiffness of cells (65) and reported that a cantilever spring constant of 0.06N/m was sufficient to approach cellular samples of mammalian origin, correlating to the spring constant used for human osteoblasts in this study. Generally it is accepted that differentiating cells are stiffer (52), for example the control cells of Saos-2 had a mean elastic modulus of around 10 kPa with Cobalt exposed cells having an elastic modulus twice that of the control samples illustrating that metal nanoparticles do alter the cells

mechanical properties. The elastic modulus of cells is of importance as clinically it has been suggested that changes to cellular stiffness indicate pathological disorders, for instance increased liver stiffness indicates a cirrhotic liver (58); attributions of stiffness are therefore an important characteristic to explore as it indicates damage to the cells by changes to the cytoskeletal organisation sensed by mechanosensors of the cells (58, 66). It is believed that cells not only respond to chemical stimuli but can adapt due to stress factors (66), and that the cytoskeleton is the main component of sensing mechanical changes (58, 66, 67).

9.6 Conclusion

The idea behind this study was to validate the previous findings of the influence of wear debris on mouse osteoblast, MC3T3-E1 cells nanomechanical and adhesive properties. It was observed that human cells proliferation was less than that of the mouse cells which had an impact on the growth rate and therefore viability results. Little to no change was observed in the MTT viability results for Saos-2 human osteoblast-like cells for both Cobalt and Titanium nanoparticle exposure, even though the same sized particles of Cobalt had a greater impact on the viability of the mouse MC3T3-E1 cells. Interestingly, both Cobalt and Titanium nanoparticles increased the osteocalcin production in the mouse osteoblast cells but clear decreases in osteocalcin productions were observed for human Saos-2 osteoblast-like cells; the decrease in production suggests that damage to the cells viability of human osteoblast like cells must be present and was supported by the LDH viability assay.

Similarly, the elasticity of both Cobalt and Titanium exposed cells increased, demonstrating that cells become stiffer post exposure to metal wear debris validating the results concluded using mouse MC3T3-E1 osteoblast cells; yet Cobalt in both cellular cases, MC3T3-E1 and Saos-2 had elevated spring constants of the cells greater than that produced by Titanium. Also, the results data regarding the adhesive forces in this study increased with increasing concentration of nanoparticles, the same can be said for MC3T3-E1. From the comparison of data, it can be assumed that the nanomechanical and adhesive findings from this study using the human Saos-2 osteoblast-like cells validate the data collected using the mouse MC3T3-E1 osteoblast cells confirming the mouse cells as a good model for alterations to the mechanical properties of cells. Both studies demonstrate a more adverse effect on cells is observed with increasing concentrations of nanoparticles that are evident over the lifetime of the wear and tear produced by hip implants. The presence therefore of wear debris affects the normal function of the cells by the potential alterations to the essential cytoskeletal organisation which governs both the nanomechanical sensing and adhesive properties of living cells.

9.7 References

1. Seeman E, Delmas PD. Bone Quality - The Material and Structural Basis of Bone Strength and Fragility. The New England Journal of Medicine. 2006;54(3):2250-61.

2. Caetano-Lopes J, Canhao H, Fonseca JE. Osteoblasts and bone formation. Acta Reumatol Port. 2007;32(2):103-10.

3. Chiu R, Goodman SB. Biological Response of Osteoblasts and Osteoprogenitors to Orthopaedic Wear Debris. In: Yunfeng L, editor. Osteogenesis - Biochemistry, Genetics and Molecular Biology. CC BY2012.

4. Saldaña L, Bensiamar F, Boré A, Vilaboa N. In search of representative models of human bone-forming cells for cytocompatibility studies. Acta Biomaterialia. 2011;7(12):4210-21.

5. Ahmad M, McCarthy M, Gronowicz G. An in vitro model for mineralization of human osteoblast-like cells on implant materials. Biomaterials. 1999;20(3):211-20.

6. Goodman SB, Ma T, Chiu R, Ramachandran R, Lane Smith R. Effects of orthopaedic wear particles on osteoprogenitor cells. Biomaterials. 2006;27(36):6096-101.

7. Rodan SB, Imai Y, Thiede MA, Wesolowski G, Thompson D, Bar-Shavit Z, et al. Characterization of Human Osteosarcoma Cell Line (Saos-2) with Osteoblastic Properties. American Association for Cancer Research. 1987;47:4961-6.

8. Pautke C, Schieker M, Tischer T, Kolk A, Neth P, Mutschler W, et al. Characterization of Osteosarcoma Cell Lines MG-63, Saos-2 and U-2 OS in Comparison to Human Osteoblasts. Anticancer Research. 2004;24:3743-8.

9. Ahmad M, Gawronski D, Blum J, Goldberg J, Gronowicz G. Differential response of human osteoblast-like cells to commercially pure (cp) Titanium grades 1 and 4. Journal of Biomedical Materials Research. 1999;46(1):121-31.

10. Degasne I, Basle MF, Demais V, Hure G, Lesourd M, Grolleau B, et al. Effects of roughness, fibronectin and vitronectin on attachment, spreading, and proliferation of human osteoblast-like cells (Saos-2) on Titanium surfaces. Calcif Tissue Int. 1999;64(6):499-507.

11. Harmand MF. In vitro study of biodegradation of a Co-Cr alloy using a human cell culture model. J Biomater Sci Polym Ed. 1995;6(9):809-14.

12. Lohmann CH, Schwartz Z, Köster G, Jahn U, Buchhorn GH, MacDougall MJ, et al. Phagocytosis of wear debris by osteoblasts affects differentiation and local factor production in a manner dependent on particle composition. Biomaterials. 2000;21(6):551-61.

13. Allen MJ, Myer BJ, Millet PJ, Rushton N. The Effects of Particulate Cobalt, Chromium and Cobalt-Chromium Alloy on Human Osteoblast-like cells *in vitro*. British Editorial Society of Bone and Joint Surgery. 1997;79-B(3):475-82.

14. Zijlstra WP, Bulstra SK, van Raay JJ, van Leeuwen BM, Kuijer R. Cobalt and chromium ions reduce human osteoblast-like cell activity in vitro, reduce the OPG to RANKL ratio, and induce oxidative stress. J Orthop Res. 2012;30(5):740-7.

15. Gregory CA, Grady Gunn W, Peister A, Prockop DJ. An Alizarin red-based assay of mineralization by adherent cells in culture: comparison with cetylpyridinium chloride extraction. Analytical Biochemistry. 2004;329(1):77-84.

16. Preedy EC, Brousseau E, Evans SL, Perni S, Prokopovich P. Adhesive forces and surface properties of cold gas plasma treated UHMWPE. Colloids Surf A Physicochem Eng Asp. 2014;460:83-9.

17. Sader JE, Larson I, Mulvaney P, White LR. Method for the calibration of atomic force microscope cantilevers. Review of Scientific Instruments. 1995;66(7):3789-98.

18. Sader JE, Sanelli JA, Adamson BD, Monty JP, Wei X, Crawford SA, et al. Spring constant calibration of atomic force microscope cantilevers of arbitrary shape. Review of Scientific Instruments. 2012;83(10):103705--16.

19. Sneddon IN. The relation between load and penetration in the axisymmetric boussinesq problem for a punch of arbitrary profile. International Journal of Engineering Science. 1965;3(1):47-57.

20. Buly RL, Huo MH, Salvati E, Brien W, Bansal M. Titanium wear debris in failed cemented total hip arthroplasty: An analysis of 71 cases. The Journal of Arthroplasty. 1992;7(3):315-23.

21. Margevicius KJ, Bauer TW, McMahon JT, Brown SA, Merritt K. Isolation and characterization of debris in membranes around total joint prostheses. The Journal of bone and joint surgery American volume. 1994;76(11):1664-75.

22. Saldaña L, Vilaboa N. Effects of micrometric Titanium particles on osteoblast attachment and cytoskeleton architecture. Acta Biomaterialia. 2010;6(4):1649-60.

23. Li C-y, Gao S-y, Terashita T, Shimokawa T, Kawahara H, Matsuda S, et al. In vitro assays for adhesion and migration of osteoblastic cells (Saos-2) on Titanium surfaces. Cell Tissue Res. 2006;324(3):369-75.

24. Dillon J, Waring-Green V, Taylor A, Wilson PM, Birch M, Gartland A, et al. Primary Human Osteoblast Cultures. In: Helfrich MH, Ralston SH, editors. Bone Research Protocols. Methods in Molecular Biology. 816: Humana Press; 2012. p. 3-18.

25. Brien WW, Salvati EA, Betts F, Bullough P, Wright T, Rimnac C, et al. Metal levels in cemented total hip arthroplasty. A comparison of well-fixed and loose implants. Clinical orthopaedics and related research. 1992(276):66-74.

26. Abu-Amer Y, Darwech I, Clohisy JC. Aseptic loosening of total joint replacements: mechanisms underlying osteolysis and potential therapies. Arthritis Research & Therapy. 2007;9(Suppl 1):S6-S.

27. Bahraminasab M, Sahari BB, Edwards KL, Farahmand F, Arumugam M, Hong TS. Aseptic loosening of femoral components – A review of current and future trends in materials used. Materials & Design. 2012;42(0):459-70.

28. Cadosch D, Chan E, Gautschi OP, Filgueira L. Metal is not inert: Role of metal ions released by biocorrosion in aseptic loosening—Current concepts. Journal of Biomedical Materials Research Part A. 2009;91A(4):1252-62.

29. Pioletti DP, Takei H, Kwon SY, Wood D, Sung KL. The cytotoxic effect of Titanium particles phagocytosed by osteoblasts. J Biomed Mater Res. 1999;46(3):399-407.

30. Nine M, Choudhury D, Hee A, Mootanah R, Osman N. Wear Debris Characterization and Corresponding Biological Response: Artificial Hip and Knee Joints. Materials. 2014;7(2):980-1016.

31. Prokopovich P. Interactions between mammalian cells and nano- or micro-sized wear particles: Physico-chemical views against biological approaches. Advances in Colloid and Interface Science. 2014;213(0):36-47.

32. Howling GI, Sakoda H, Antonarulrajah A, Marrs H, Stewart TD, Appleyard S, et al. Biological Response to Wear Debris Generated in Carbon Based Composites as Potential Bearing Surfaces for Artifical Hip Joints. Biomed Mater Res Part B: Appl Biomater. 2003;67(B):758-64.

33. da Rosa ELS. Kinetic effects of TiO(2) fine particles and nanoparticles aggregates on the nanomechanical properties of human neutrophils assessed by force spectroscopy. BMC Biophysics. 2013;6:11-.

34. Ingham E, Fisher J. The role of macrophages in osteolysis of total joint replacement. Biomaterials. 2005;26(11):1271-86.

35. Callaghan JJ, O'rourke MR, Saleh KJ. Why knees fail: Lessons learned. Journal of Arthroplasty. 2004;19:31-4.

36. Grassian VH, Adamcakova-Dodd A, Pettibone JM, O'shaughnessy PI, Thorne PS. Inflammatory response of mice to manufactured Titanium dioxide nanoparticles: Comparison of size effects through different exposure routes. Nanotoxicology. 2007;1(3):211-26.

37. Papageorgiou I, Brown C, Schins R, Singh S, Newson R, Davis S, et al. The effect of nano- and micron-sized particles of Cobalt–chromium alloy on human fibroblasts in vitro. Biomaterials. 2007;28(19):2946-58.

38. Lewis G. Properties of crosslinked ultra-high-molecular-weight polyethylene. Biomaterials. 2001;22(4):371-401.

39. Papageorgiou I, Yin Z, Ladon D, Baird D, Lewis AC, Sood A, et al. Genotoxic effects of particles of surgical Cobalt chrome alloy on human cells of different age in vitro. Mutation Research/Fundamental and Molecular Mechanisms of Mutagenesis. 2007;619(1–2):45-58.

40. Maloney WJ, Smith RL, Castro F, Schurman DJ. Fibroblast response to metallic debris in vitro. Enzyme induction cell proliferation, and toxicity. The Journal of bone and joint surgery American volume. 1993;75(6):835-44.

41. Vandrovcova M, Jirka I, Novotna K, Lisa V, Frank O, Kolska Z, et al. Interaction of human osteoblast-like Saos-2 and MG-63 cells with thermally oxidized surfaces of a Titanium-niobium alloy. PLoS One. 2014;9(6):e100475.

42. Uggeri J, Guizzardi S, Scandroglio R, Gatti R. Adhesion of human osteoblasts to Titanium: A morpho-functional analysis with confocal microscopy. Micron. 2010;41(3):210-9.

43. Dorr LD, Hilton KR, Wan Z, Markovich GD, Bloebaum R. Modern metal on metal articulation for total hip replacements. Clinical orthopaedics and related research. 1996(333):108-17.

44. Czekanska EM, Stoddart MJ, Richards RG, Hayes JS. In Search of an Osteoblast Cell Model for *In Vitro* Research. European Cells and Materials. 2012;24:1-17.

45. Carpenter TO, Moltz KC, Ellis B, Andreoli M, McCarthy TL, Centrella M, et al. Osteocalcin production in primary osteoblast cultures derived from normal and Hyp mice. Endocrinology. 1998;139(1):35-43.

46. Baxter LC, Frauchiger V, Textor M, ap Gwynn I, Richards RG. Fibroblast and osteoblast adhesion and morphology on calcium phosphate surfaces. European cells & materials. 2002;4:1-17.

47. Kilpadi KL, Sawyer AA, Prince CW, Chang P-L, Bellis SL. Primary human marrow stromal cells and Saos-2 osteosarcoma cells use different mechanisms to adhere to hydroxylapatite. Journal of Biomedical Materials Research Part A. 2004;68A(2):273-85.

48. Degasne I, Baslé MF, Demais V, Huré G, Lesourd M, Grolleau B, et al. Effects of Roughness, Fibronectin and Vitronectin on Attachment, Spreading, and Proliferation of Human Osteoblast-Like Cells (Saos-2) on Titanium Surfaces. Calcified Tissue International. 1999;64(6):499-507.

49. Mayr-Wohlfart U, Fiedler J, Gunther KP, Puhl W, Kessler S. Proliferation and differentiation rates of a human osteoblast-like cell line (SaOS-2) in contact with different bone substitute materials. J Biomed Mater Res. 2001;57(1):132-9.

50. Postiglione L, Di Domenico G, Ramaglia L, di Lauro AE, Di Meglio F, Montagnani S. Different Titanium surfaces modulate the bone phenotype of SaOS-2 osteoblast-like cells. Eur J Histochem. 2004;48(3):213-22.

51. Yim EKF, Darling EM, Kulangara K, Guilak F, Leong KW. Nanotopography-induced changes in focal adhesions, cytoskeletal organization, and mechanical properties of human mesenchymal stem cells. Biomaterials. 2010;31(6):1299-306.

52. Darling EM, Topel M, Zauscher S, Vail TP, Guilak F. Viscoelastic properties of human mesenchymally-derived stem cells and primary osteoblasts, chondrocytes, and adipocytes. Journal of Biomechanics. 2008;41(2):454-64.

53. Thoumine O, Cardoso O, Meister JJ. Changes in the mechanical properties of fibroblasts during spreading: a micromanipulation study. European biophysics journal : EBJ. 1999;28(3):222-34.

54. Domke J, Dannöhl S, Parak WJ, Müller O, Aicher WK, Radmacher M. Substrate dependent differences in morphology and elasticity of living osteoblasts investigated by atomic force microscopy. Colloids and Surfaces B: Biointerfaces. 2000;19(4):367-79.

55. Docheva D, Padula D, Popov C, Mutschler W, Clausen-Schaumann H, Schieker M. Researching into the cellular shape, volume and elasticity of mesenchymal stem cells, osteoblasts and osteosarcoma cells by atomic force microscopy. Journal of Cellular and Molecular Medicine. 2008;12(2):537-52.

56. Discher DE, Janmey P, Wang YL. Tissue cells feel and respond to the stiffness of their substrate. Science. 2005;310(5751):1139-43.

57. Engler A, Sen S, Sweeney H, Discher D. Matrix elasticity directs stem cell lineage specification. Cell. 2006;126(4):677 - 89.

58. Wells RG. The role of matrix stiffness in regulating cell behavior. Hepatology. 2008;47(4):1394-400.

59. Mitra SK, Hanson DA, Schlaepfer DD. Focal adhesion kinase: in command and control of cell motility. Nat Rev Mol Cell Biol. 2005;6(1):56-68.

60. Parsons JT. Focal adhesion kinase: the first ten years. J Cell Sci. 2003;116(Pt 8):1409-16.

61. Siebers MC, ter Brugge PJ, Walboomers XF, Jansen JA. Integrins as linker proteins between osteoblasts and bone replacing materials. A critical review. Biomaterials. 2005;26(2):137-46.

62. Tee S-Y, Fu J, Chen Christopher S, Janmey Paul A. Cell Shape and Substrate Rigidity Both Regulate Cell Stiffness. Biophysical Journal. 2011;100(5):L25-L7.

63. Kasza KE, Nakamura F, Hu S, Kollmannsberger P, Bonakdar N, Fabry B, et al. Filamin A is essential for active cell stiffening but not passive stiffening under external force. Biophys J. 2009;96(10):4326-35.

64. Kwon SY, Lin T, Takei H, Ma Q, Wood DJ, O'Connor D, et al. Alterations in the adhesion behavior of osteoblasts by Titanium particle loading: inhibition of cell function and gene expression. Biorheology. 2001;38(2-3):161-83.

65. Bhadriraju K, Hansen LK. Extracellular Matrix- and Cytoskeleton-Dependent Changes in Cell Shape and Stiffness. Experimental Cell Research. 2002;278(1):92-100.

66. Bacabac RG, Mizuno D, Schmidt CF, MacKintosh FC, Van Loon JJWA, Klein-Nulend J, et al. Round versus flat: Bone cell morphology, elasticity, and mechanosensing. Journal of Biomechanics. 2008;41(7):1590-8.

67. Assoian RK, Klein EA. Growth control by intracellular tension and extracellular stiffness. Trends in Cell Biology. 2008;18(7):347-52.

Chapter 10 Summary and Future Work

Chapter 4 – The bacteria that cause infections post-surgery of biomedical devices from dental to hip implantations have been investigated for their adhesive interactions with relevant substrates. CAP treatment was used on a commonly employed polymer, UHMWPE, often found in the acetabular cup of the hip. This treatment can be utilised as an alternative sterilisation technique from the commonly adopted but expensive gamma radiation; as this process requires no vacuum and uses the environmental Nitrogen freely available to modify the surface chemistry of the polymer without any detrimental effects to the bulk properties. CAP also increases the cross-linking of the polymer. Initially, Helium and Helium Oxygen mix are used to generate the plasma. The results from this plasma treatment demonstrated both a reduction in asperity height as well as the asperity density by half that of the untreated UHMWPE. Previously, it was noted that CAP reduces the wear factor by half therefore potentially increasing the longevity of the implanted device as less wear is produced after this treatment. Moreover, the surface chemistry was altered with CAP treatment from the introduction of Nitrogen free radicals to the surface which improved its hydrophilicity by reducing the contact angles of water, allowing for better osseointegration.

Chapter 5 – Surface characteristics of a material is important to consider for the adhesion of bacteria and whether or not it can inhibit or assist in establishing an infectious colony on an implanted biomedical device. Chapter 5 indicated just how important the surface roughness characteristics are and that it is a scale dependent parameter, as better correlations for bacterial adhesion and the

borosilicate glass were observed when areas comparable with the bacterial size were employed. It was also crucial to consider the surface topography along with the conditioning layer, made up of proteins and glycoproteins that formed the extracellular matrix (ECM) which can effectively mask the original surface modulations and also alter the surface hydrophobicity i.e. protein coating is hydrophilic. This change in the hydrophobic properties of the surface can assist hydrophilic bacteria to attach whilst deterring hydrophobic bacteria, this could also lead to improved cell adhesion in combination with the reduction in contact angle of water, and the roughness as a scale dependent parameter which directly influences the extent of adhesion.

The investigations from Chapters 6 through to 9 focused on the relevant cells exposed to wear debris and the influence these foreign particles have on the nanomechanical and adhesive properties of these cells.

Chapter 6 – For the first time it has been demonstrated that metal wear debris have more of a detrimental effect on cells compared to UHMWPE or PMMA. Initially, MSCs, progenitor cells were observed for changes to the nanomechanical and adhesive properties, along with alterations if any to the metabolic activity after exposure to various Cobalt, and Titanium nanoparticles. This preliminary investigation demonstrated a reduction in metabolic activity for both metal nanoparticles, and that their size or composition did not alter for Cobalt nor Titanium, but Cobalt lowered the metabolic activity greater than Titanium. This was evident throughout regardless of the cell type, which supported the claims that Titanium is more biocompatible than Cobalt. Generally, the elasticity for MSCs exposed to Cobalt increased, whereas it

decreased for Titanium, however, the adhesion properties decreased for both metal nanoparticles when compared with the control. Therefore, any alterations in the initial adhesion of cells to a surface govern the outcome of that cells growth and differentiation.

Chapter 7 - Furthermore, this notion of improvements of CAP treatment was extended to chapter 7 for the investigation of UHMWPE wear debris and its effect on MSCs nanomechanic and adhesive properties before and after CAP treatment. The wear debris was produced for wear cycles representative of up to a year worth of wear in a relatively sedentary patient (333kC, 666kC and 1MC). Chemical analysis using Raman spectroscopy demonstrates the fact that only Nitrogen attaches to the surface of UHMWPE, and no Oxygen was present as the XPS results had no shift for Oxygen; more importantly there was no change in the crystallinity of the polymer therefore retaining its beneficial qualities of choice for its application in biomedical implants. Images of the wear debris revealed no changes in size and shape. However, with increased wear cycles that the polymer undergoes, it gradually returns to its original surface properties. It is noteworthy to state that all the benefits of CAP treatment do not damage MSCs greater than or less than untreated UHMWPE. In other words the cells reactions are consistent so no further damage is applied to the cells.

Chapter 8 – When applying the same methods to Osteoblast cells exposed to nanoparticles, similar detrimental results were observed as for MSCs exposed to wear debris. For example the metabolic activity reduced for both Cobalt and Titanium nanoparticles, as well as for PMMA, bone cement often used as a fixative. The elasticity increased for both metals, but decreased for PMMA, and

the adhesion forces also decreased for Cobalt and PMMA wear particles, while no change were observed in Titanium. A further biological investigation into the mineralisation properties of cells was conducted and the results were different from that of the control. Indeed, Cobalt, Titanium and PMMA all increased the Calcium production due to the nanomechancial changes caused by the exposure of cells to wear particles.

Chapter 9 – A comparison and validation of the methods was also required against human osteoblast cells. For these cells, their metabolic activity decreased for Cobalt and Titanium nanoparticles with increasing concentration. Moreover, the elasticity also increased for Cobalt but no change was observed for Titanium nanoparticles. The adhesion increased slightly for Cobalt and again no changes were noted for Titanium nanoparticles. Conversely to the mouse osteoblasts, the mineralisation decreased for both metal nanoparticles.

It is evident from the work conducted in this thesis that a number of nanomechanical changes to cells have taken place due to the exposure to foreign particles. Especially, these changes are more prominent for Cobalt nanoparticles than for Titanium. Greatest impact was observed after the initial 24 hours, yet some changes were observed up until 72 hours which coincides with the increase in metal particle uptake by the cells. Cobalt had the greatest uptake from all cells which supports its greater influence on the cells nanomechanical, adhesive and metabolic activity. All results obtained here are aimed at complementing previous literature on the detrimental impact of metal debris on the biological aspects of cellular damage which may affect the cells proliferation, differentiation and growth. It is noteworthy that CAP treated

materials reduce the production of wear, maintain sterility, and uphold the integrity of the bulk material that makes UHMWPE beneficial for its application in biomedical devices.

For the first time the impact of this treated polymer as wear debris, as well as the impact of metal nanoparticles impact on cellular nanomechanical processes has been explored with scope to expand these studies to greatly improve the holistic approach to hazardous changes that are present when cells are exposed to nano sized debris at/near biomedical implants.

This thesis lends itself to applying and expanding these methods to other materials and cells that are relevant at/near biomedical implants, for example, further studies that may be of benefit for a more rounded approach would be to:

- Expand nanomechanical and adhesive cell properties study pre and post exposure to metal alloy nanoparticles (like CoCr) and microparticles;
- Study these nanomechanical effects on cells pre and post exposure to metal ions in solution;
- Characterise cellular structural elements (such as actin filaments) pre and post exposure to wear particles;
- Optimise CAP technology to further improve material performance of UHMWPE;
- Determine nanomechanical and adhesive properties of other cell lines such as fibroblasts, osteoclasts and macrophages (both rodent and human origin);
- Investigate the impact of surface roughness on cell adhesion of other orthopedically relevant materials.